GEMS & GEMOLOGY

WINTER 2020
VOLUME LVI

THE QUARTERLY JOURNAL OF THE GEMOLOGICAL INSTITUTE OF AMERICA

Low-Temperature Heating of Pink Sapphire from Madagascar

Rose-Cut Colored Stones from the Baroque Era

Fluorescence Characteristics of Blue Amber

Mineral Inclusions in Vietnamese Sapphire

GEMS & GEMOLOGY®
Winter 2020
VOLUME 56, No. 4


p. 449


p. 470


p. 500


p. 527

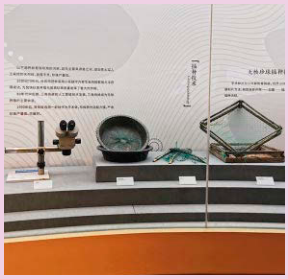
p. 553

Editorial

Feature Articles

Regular Features

GEMS & GEMOLOGY

gia.edu/gems-gemology

Subscriptions
Copies of the current issue may be purchased for $29.95 plus shipping. Subscriptions are $79.99 for one year (4 issues) in the U.S. and $99.99 elsewhere. Canadian subscribers should add GST. Discounts are available for renewals, group subscriptions, GIA alumni, and current GIA students. To purchase print subscriptions, visit store.gia.edu or contact Customer Service. For institutional rates, contact Customer Service.

Database Coverage
Gems & Gemology's impact factor is 0.767, according to the 2019 Thomson Reuters Journal Citation Reports (issued July 2020). *G&G* is abstracted in Thomson Reuters products (Current Contents: Physical, Chemical & Earth Sciences and Science Citation Index—Expanded, including the Web of Knowledge) and other databases. For a complete list of sources abstracting *G&G*, go to gia.edu/gems-gemology, and click on "Publication Information."

Manuscript Submissions
Gems & Gemology, a peer-reviewed journal, welcomes the submission of articles on all aspects of the field. Please see the Author Guidelines at gia.edu/gems-gemology or contact the Managing Editor. Letters on articles published in *G&G* are also welcome. Please note that Field Reports, Lab Notes, Gem News International, Micro-World, Diamonds from the Deep, and Charts are not peer-reviewed sections but do undergo technical and editorial review.

Gems & Gemology is published quarterly by the Gemological Institute of America, a nonprofit educational organization for the gem and jewelry industry.

Postmaster: Return undeliverable copies of *Gems & Gemology* to GIA, The Robert Mouawad Campus, 5345 Armada Drive, Carlsbad, CA 92008.

Our Canadian goods and service registration number is 126142892RT.

About the Cover

The lead article in this issue examines the effects of low-temperature heat treatment on inclusions in pink sapphires from Madagascar. The six pink sapphires on the cover are from Ilakaka, Madagascar. The top three range from 1.06 to 1.17 ct and were treated using a low-temperature process. The bottom three range from 1.15 to 1.29 ct and did not receive heat treatment. Photo by Robert Weldon/GIA; courtesy of Jeffrey R. Hapeman, Earth's Treasury.

Printing is by L+L Printers, Carlsbad, CA.
GIA World Headquarters The Robert Mouawad Campus 5345 Armada Drive Carlsbad, CA 92008 USA

ISSN 0016-626X

Pink Sapphires from Madagascar, Rose-Cut Colored Stones from the Baroque Era, Separating Blue Amber Localities, and More…

Welcome to the Winter 2020 issue of *Gems & Gemology!* This issue brings an exciting conclusion to the volume year with a study on low-temperature heat treatment of pink sapphire, a characterization of rose cuts that adorn rare artifacts of a bygone era, and the means to separate the three principal localities for blue amber.

In the lead article, a team led by Sudarat Saeseaw examines the effects of low-temperature heat treatment on inclusions in pink sapphire from Ilakaka, Madagascar. The detailed characterization of these samples before and after heating will help laboratories develop treatment detection criteria. This study also presents a useful technique using Fourier-transform infrared (FTIR) spectroscopy to detect low-temperature heat treatment of this material.

"A characterization of rose cuts that adorn rare artifacts of a bygone era…"

In the second article, researcher Karl Schmetzer returns to the pages of *G&G* with an evaluation of seventeenth-century colored stones fashioned as rose cuts, which richly decorate rare artifacts once belonging to archbishops and prince-electors of Trier and Cologne. This article seeks to fill a gap in the historical record, as rose-cut colored stones have been mainly overlooked in favor of their diamond counterparts.

Next, Zhiqing Zhang and a team from the Gemmological Institute, China University of Geosciences in Wuhan use observation, UV-Vis-NIR spectroscopy, and excitation-emission mapping to separate blue amber mined from the Dominican Republic, Mexico, and Myanmar. This widely loved organic gemstone may be grouped according to very strong blue fluorescence and distinct emission and excitation wavelengths.

In the final article, Doan Thi Anh Vu from Vietnam National University heads an investigation of mineral inclusions in basaltic sapphire from southern Vietnam. The team analyzes inclusion chemistry using EPMA to understand the formation model of these sapphires in relation to the basaltic volcanism of this locality.

As always, our regular columns feature an array of interesting gemological findings. Highlights of from *Lab Notes* include a large "all-American" diamond from Arkansas and artificial glass prisms masquerading as Paraíba tourmaline. *Micro-World* enchants with the inner beauty of gems: lazurite and snowflakes in Burmese ruby from Mogok and Mong Hsu, respectively, and sapphires exhibiting elongated rutile. Stay up to date in the *Gem News International* section with a new emerald locality in Southern California and the use of rhodium plating on etched iron meteorites. *Diamonds from the Deep* returns with a unique perspective on how diamond ages can help us understand continent evolution spanning billions of years.

Finally, we include a reprint of the Spring 2020 article by Emily Dubinsky et al. ("A Quantitative Description of the Causes of Color in Corundum") to correct the color of several photos and areal color density circles. We regret these errors and have used the opportunity to produce a new wall chart displaying the corundum chromophores from this article.

We hope you enjoy our Winter issue!

Duncan Pay | Editor-in-Chief | dpay@gia.edu

Low-Temperature Heat Treatment of Pink Sapphires from Ilakaka, Madagascar

Sudarat Saeseaw, Charuwan Khowpong, and Wim Vertriest

Low-temperature heat treatment is often applied to gem corundum to improve its appearance. Pink sapphires from Madagascar, one of the most important sapphire-producing countries, are no exception. Therefore, characterizing Madagascan pink sapphire before and after heat treatment helps laboratories develop criteria for treatment detection. This study showed that after heat treatment at 800ºC, a subtle blue tint was removed, making the color a purer pink. Only slight alterations of monazite inclusions and iron stains in fissures were observed following these heating conditions. Other common inclusions such as needles, particles, etch tubes, and mica and zircon crystals remained unaffected. Interestingly, the monazite crystal inclusions changed color from orange-brown to near-colorless after heat treatment. Raman spectroscopy was used to detect the effect of heat treatment on zircon and monazite crystals. While the Raman spectra of zircon remained unchanged, except in the region of 1000 cm^{-1} after heating at 1000°C, the Raman peaks of monazite crystals became sharper with increasing temperature. We measured full width half maximum at ~976 cm^{-1} (ν_1, related to the PO_4 group of monazite) after all annealing steps. The results showed that the width decreased around 5 cm^{-1} after heating at 1000°C. This study also showed that Fourier-transform infrared (FTIR) spectroscopy, specifically the peak at 3232 cm^{-1}, is a useful technique to detect low-temperature heat treatment in pink sapphires from Madagascar.

Heat treatment has been used to improve the color and/or clarity of corundum for more than a thousand years. Various parameters such as temperature, heating and cooling time, and oxidizing or reducing atmosphere will affect the final color (Emmett and Douthit, 1993; Emmett et al., 2003; Hughes et al., 2017). The border between high- and low-temperature heat treatment has been defined by Emmett (in Hughes et al., 2017) as the temperature needed to dissolve second-phase microcrystals, which is somewhere between 1200° and 1350°C. Heating at high temperatures will damage most inclusions in ruby and sapphire and is often detectable by trained gemologists. In contrast, heating corundum at low temperatures, sometimes below 700°C, will only subtly affect their internal inclusions, making the treatment much more challenging to detect without advanced instrumentation (figure 1).

Previous studies on the effect of low-temperature heat treatment on inclusions have focused on rubies from Mozambique (Pardieu et al., 2015; Sripoonjan et al., 2016; Saeseaw et al., 2018) and blue sapphires from Madagascar (Krzemnicki, 2010; Hughes and Perkins, 2019). In these studies, rubies showed slight inclusion alterations when heated to 900°C and developed clear

In Brief

- The subtle blue tint in many pink sapphires from Madagascar can be lightened or removed by heating at 800°C for 120 minutes in air.
- FTIR spectroscopy is a crucial technique to detect low-temperature heat treatment. The presence of the 3232 cm^{-1} peak is an indicator of heat treatment in Madagascan pink sapphire.
- Careful observation of monazite crystal inclusions showed a change in color from orange-brown to near-colorless after low-temperature heat treatment.
- Raman spectroscopy can be used to detect the annealing of monazite during low-temperature treatment.

See end of article for About the Authors and Acknowledgments.
Gems & Gemology, Vol. 56, No. 4, pp. 448–457,
http://dx.doi.org/10.5741/GEMS.56.4.448

Figure 1. These pink sapphires from Ilakaka, Madagascar, underwent low-temperature heat treatment. From top to bottom, they weigh 1.16 ct, 1.17 ct, and 1.06 ct. Photo by Robert Weldon/GIA; courtesy of Jeff Hapeman, Earth's Treasury.

FTIR signatures after heat treatment. This article focuses on the effects of low-temperature heat treatment on inclusions, such as zircon and monazite, and the FTIR spectra of pink sapphire from Madagascar. This is the first study to report the use of Raman spectroscopy to analyze monazite inclusions in corundum during heat treatment experiments.

MATERIALS AND METHODS

Samples and Instruments. Fourteen samples reportedly from Ilakaka, Madagascar, were selected and polished with at least two windows for data analysis. Sample sizes ranged from 0.41 to 2.15 ct. The first set of samples (PS01–PS11) consisted of 11 pink sapphires (table 1). Samples PS01–PS08 and PS11 were purchased directly from the miner, but not at the mine site near the Taheza River in Ilakaka. These samples are classified as C-type samples in GIA's colored stone reference collection (Vertriest et al., 2019). Sample PS09 was acquired from a trader in the Ilakaka market and was reportedly from the Ambala-

TABLE 1. Color-calibrated photos of samples PS01–PS11 before (left) and after (right) heat treatment at 800°C for 160 minutes.

Sample ID	Before heating	After heating
PS01		
PS02		
PS03		
PS04		
PS05		
PS06		
PS07		
PS08		
PS09		
PS10		
PS11		

TABLE 2. Color-calibrated photos of samples PS21–PS23 for the secondary experiment (samples were kept at the maximum temperature for 120 minutes).

Sample ID	Before heating	After heating at 200°C	After heating at 400°C	After heating at 600°C	After heating at 800°C	After heating at 1000°C
PS21[a]						
PS22						
PS23						

[a]*Sample PS21 is not zoned. The darker part is the reflection of a polished window on the side of the stone to improve observation of the inclusions.*

vihy mining area. This sample is classified as an E-type sample. PS10 was purchased from miners at the Sakameloka washing site, which makes it a B-type sample.

A second set of three pink sapphires, containing zircon and monazite inclusions (PS21–PS23), was used for a follow-up heating experiment (table 2). Sample PS21 was purchased from the miners at the Ambarazy mine; therefore, it is C-type. GIA field gemologists witnessed the mining of samples PS22 and PS23 in the Esoki and Besatra areas, respectively. These samples are classified as B-type (Vertriest et al., 2019).

To compare the true color of the samples before and after treatment, we used a Canon EOS 5D camera with a Canon Macro MP-E 65 mm lens to produce consistent results. Photographs were taken under identical lighting conditions, with the reference samples placed in a Logan Electric Tru-View 810 color-corrected lightbox (5000 K lamp). A neutral-density filter was used to calibrate the camera/lightbox combination to produce a neutral gray background.

Photomicrographs of internal inclusions were captured at different magnifications with a Nikon SMZ18 system and under different types of illumination, together with a fiber-optic light source.

Non-polarized FTIR spectra were collected using a Thermo Fisher Nicolet 6700 FTIR spectrometer equipped with an XT-KBr beam splitter and a mercury-cadmium-telluride (MCT) detector operating with a 4× beam condenser accessory. The resolution was set at 4 cm^{-1} with 1.928 cm^{-1} data spacing. Infrared spectra were collected in the same area of each sample before and after heat treatment.

Raman spectra were obtained using a Renishaw inVia Raman microscope fitted with a Stellar-REN Modu Ar-ion laser producing highly polarized light at 514 nm. For internal inclusion analysis, the system was operated in confocal mode with 20× and 50× objectives. Calibration using neon emission lines and the silicon signal at 520 cm^{-1} provided wavenumber accuracy within ±0.5 cm^{-1}. Spectra were collected in the 1500–200 cm^{-1} region.

Heating Experiment. The pink sapphires were separated into two experimental groups. First, 11 samples (PS01–PS11) were subjected to heat treatment in air at 800°C for 160 minutes to study the effect on color, inclusions, and infrared spectroscopy. The second set consisted of three samples (PS21–PS23) that were heated at 200°, 400°, 600°, 800°, and 1000°C for 120 minutes at each step to study the changes in monazite and zircon inclusions using Raman spectroscopy.

Samples were placed on an alumina ceramic felt (99.8% Al_2O_3) in a Thermo Scientific FB1400 Thermolyne benchtop 1100°C muffle furnace and heated to the desired temperature at a rate of 5°C/min. At the end of each heating cycle, the furnace was switched off. When the temperature of the furnace dropped

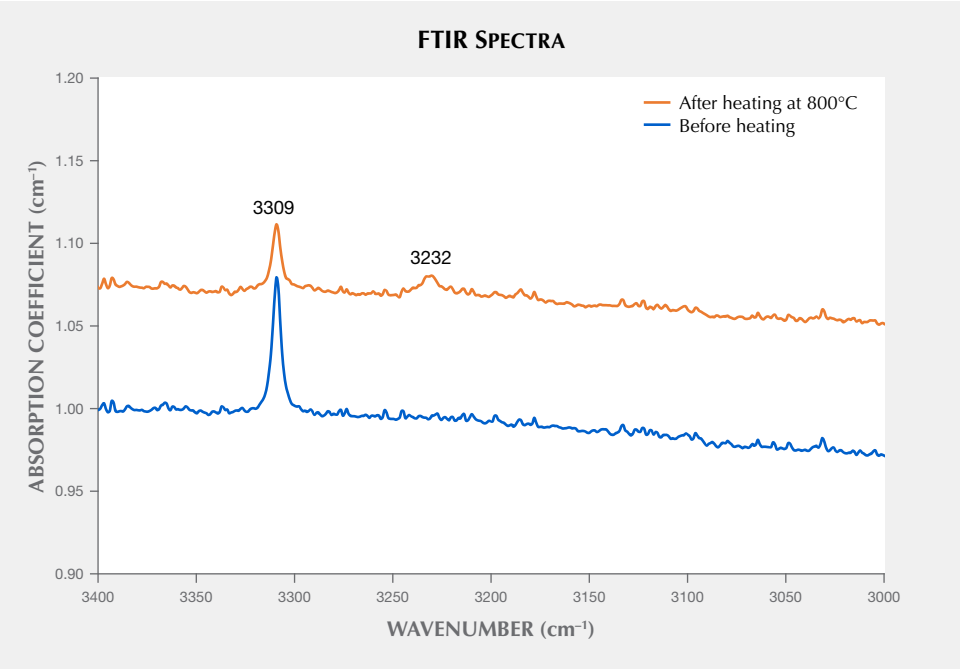

Figure 2. Comparison of non-polarized FTIR spectra before (blue) and after (orange) heat treatment at 800°C for 160 minutes on an unoriented pink sapphire from Madagascar. Spectra are offset vertically for clarity.

below 600°C, the samples were removed and allowed to cool to room temperature. Samples were analyzed at room temperature after each heating cycle.

RESULTS AND DISCUSSIONS

Color Appearance and Gemological Properties. Before heating, most of the samples in the first set were purplish pink. After the heat treatment process, they changed to a purer pink (table 1). These sapphires showed a significant reduction in the blue color component when heated at 800°C for 160 minutes, which had also been observed in rubies from Mozambique. Gemological properties were consistent for corundum and did not change during the heating experiment. Fluorescence was strong to medium red under long-wave and medium to weak under short-wave UV light, both pre- and post-treatment. Chalky white fluorescence is sometimes observed in heated sapphire, caused by a charge transfer between O^{2-} and Ti^{4+} ions (Emmett et al., 2017); however, none of the samples studied showed chalky fluorescence after treatment.

Infrared Spectroscopy. Previous studies on Mozambican rubies (Pardieu et al., 2015; Saeseaw et al., 2018) have shown that only samples with a single peak at 3309 cm^{-1} will develop a 3309 series (3309, 3232, and/or 3185 cm^{-1}), which can be used as an indication of heat treatment. This criterion is effective for some blue sapphires (Hughes and Perkins, 2019) but is not valid for basalt-related blue sapphires.

In this study, we selected Ilakaka samples that had an obvious peak at 3309 cm^{-1}. All samples in the first set showed a decreased 3309 cm^{-1} peak after heating, while 9 out of 11 samples developed a peak at 3232 cm^{-1}, as shown in figure 2 and table 3. No 3185 cm^{-1} peak was observed in this experiment. This observation has been previously reported (Saeseaw and Khowpong, 2019). The strength of the OH absorption bands at 3309, 3232, and 3185 cm^{-1} is re-

TABLE 3. Comparison of FTIR peak heights before and after heat treatment at 800°C for 160 minutes.

Sample ID	Before heating	After heating	
	3309 cm^{-1}	3309 cm^{-1}	3232 cm^{-1}
PS01	0.04	nd	nd
PS02	0.04	0.02	0.005
PS03	0.07	0.04	0.01
PS04	0.07	0.04	0.01
PS05	0.04	0.02	nd
PS06	0.05	0.02	0.01
PS07	0.05	0.03	0.01
PS08	0.06	0.03	0.01
PS09	0.06	0.03	0.01
PS10	0.06	0.03	0.01
PS11	0.04	0.01	0.005

Abbreviation: nd = not detected

lated to the orientation of the crystal and the polarization of the light used to analyze the sample. They are strongest when collected perpendicular to the c-axis and are related to the presence of certain trace elements. The peak height absorption coefficient of the 3185 cm^{-1} peak is only one-third that of the peak at 3232 cm^{-1}; therefore, it rarely presents on small stones (Beran, 1991).

However, it is worth noting that only when the peak height absorption coefficient of the 3309 cm^{-1} peak is greater than or equal to 0.04 cm^{-1} before heating will it develop a 3232 cm^{-1} peak after treatment. Absorption coefficient or cm^{-1} is related to the thickness of a sample. Therefore, a small sample might not show the 3232 cm^{-1} peak since the path length of the light through the stone is much shorter. This means that the feature is easier to detect in larger stones, while smaller stones will have "no indication of heat treatment" based on FTIR spectra.

We also collected FTIR spectra on 250 additional unheated pink sapphires reportedly from Madagascar. The results showed 130 samples with only the single 3309 cm^{-1} peak, and none of these samples showed a 3309 series. Therefore, it is important to ensure that spectra are either collected perpendicular to the c-axis, taken in multiple directions, or collected using a diffuse reflectance (DRIFT) accessory to obtain high sensitivity of the 3232 cm^{-1} peak.

Internal Features. *Visual Observations.* Pink sapphires from Madagascar commonly contain numerous zircon crystals (figure 3A). Zircon crystals typically have a rice grain shape and can occur as clusters or single crystals (figure 3B), sometimes with tension halos, similar to discoid fractures that develop around crystals after heat treatment (figure 3C). Needles, particles, thin films, etch tubes, and twinning can also be observed (figure 3D and 3E), as can

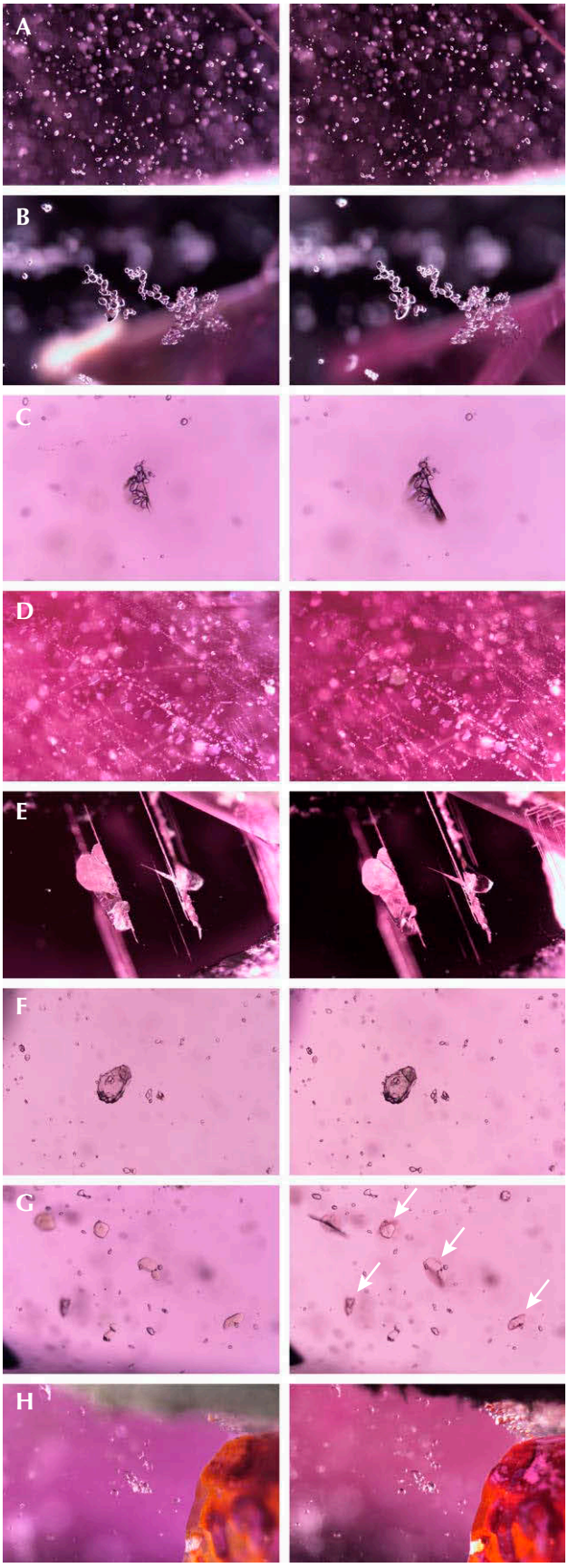

Figure 3. Typical inclusion scenes in pink sapphire from Madagascar before (left) and after (right) heat treatment at 800°C for 160 minutes. Numerous zircon crystals (A) and clusters of zircon crystals (B). C: Zircon with tension halos; the fracture expanded slightly after heating. D: Minute particles, needles, and platelets. E: Etch tubes with natural fractures. F: Large mica crystal and smaller isolated zircon crystals. G: Monazite crystals that altered from orange-brown to near-colorless, some developing tension fractures after heat treatment (see arrows). H: Zircon and fracture with iron stains. Photomicrographs by Charuwan Khowpong. Fields of view 2.85 mm (A), 1.05 mm (B–C, H), 1.75 mm (D, F–G), and 3.65 mm (E).

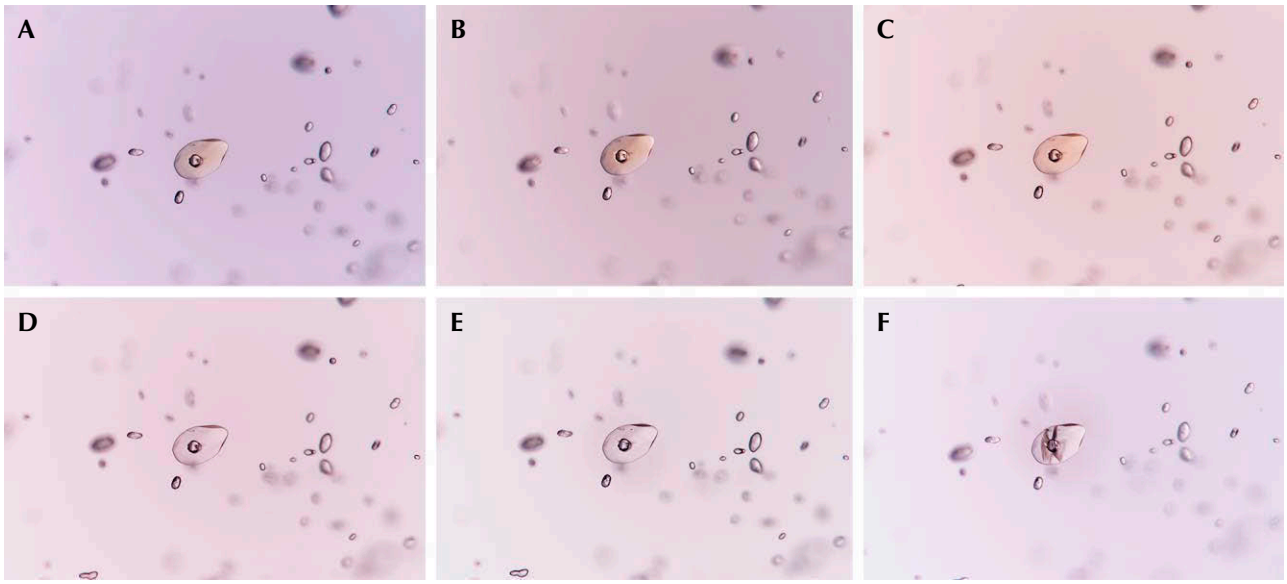

Figure 4. Reaction of a monazite crystal prior to heating and after being heated to 200°, 400°, 600°, 800°, and 1000°C (A–F). The orange-brown color of the crystal disappeared after heating to 600°C (D), and it developed a tension crack at 1000°C (F). The small crystal visible inside the monazite was identified by Raman spectroscopy as zircon. Photomicrographs by Charuwan Khowpong; field of view 1.05 mm.

crystals of mica (figure 3F) and monazite (figure 3G). The monazite crystals typically have an orangy color; this is due to natural radiation damage caused by a relative enrichment in radioactive elements such as uranium and thorium (Ruschel et al., 2012). A few stones featured inclusions within inclusions, with zircon crystals embedded in monazite or mica crystals (figure 3F).

During the first experiment with samples PS01–PS11, most of the inclusions, including zircon, showed no change when heated at 800°C for 160 minutes. After treatment, orange epigenetic iron stains in surface-reaching fissures became darker due to the oxidation and dehydration of iron minerals at higher temperatures (figure 3H). Typically the orange iron stains consist of limonite (α-FeO(OH)) and convert to brownish red hematite (α-Fe_2O_3) during heat treatment (Koivula, 2013; Sripoonjan et al., 2016). The other observed change was seen in monazite crystals, which changed color from orange-brown to near-colorless after heat treatment. In some cases, tension fractures also formed (figure 3G).

Focus on Monazite and Zircon. The most likely explanation for the change of color in the monazite inclusion is the annealing of the radiation damage caused by radioactive elements that substituted in the crystal lattice. Monazite is a phosphate mineral rich in rare earth elements such as cerium, lanthanum, and neodymium (Clavier et al., 2011). It is radioactive due to the presence of thorium and, to a lesser degree, uranium. Other minerals such as zircon and baddeleyite can also contain radioactive elements. These elements are of great interest in geological studies since they can be used to date minerals based on the radioactive decay of those trace elements. Age dating research is mostly focused on zircon, where small amounts of uranium are common in the lattice (Dickin, 2018).

A side effect of radioactivity is the slow damage to the crystal structure, which is seen as the orange-brown color in the monazite inclusions. The term *metamict* indicates that a gem (most often zircon) has strongly altered properties (RI, SG, toughness, etc.) because of its internal radiation damage. Such radiation damage can distort the crystalline structure to such a degree that it becomes non-crystalline (amorphous). An example is "low" zircon from Sri Lanka.

The initial heat treatment experiment strongly suggests that heat treatment can undo this radiation damage, healing the crystal lattice to its original undamaged state (Meldrum et al., 1998; Nasdala et al., 2002).

To further study the potential healing of radiation damage in inclusions, we continued our heating experiment on selected samples (table 2) containing monazite and zircon inclusions. Both of these minerals commonly include radioactive elements and

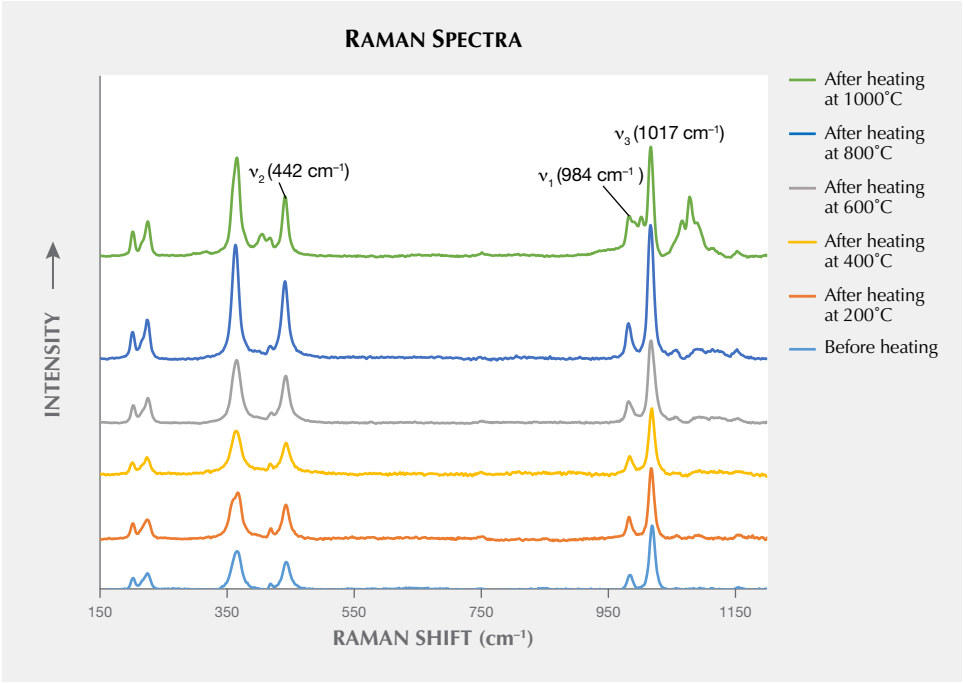

Figure 5. Stacked Raman spectra of a zircon inclusion in sample PS23 before and after heat treatment at each step. Peaks in the 1000–1100 cm^{-1} region are due to luminescence observed in the sample after heating to 1000°C. FWHM measured by GRAMS software.

potentially have crystal structure damage induced by radioactivity. They may also be annealed at higher temperatures.

In this heating experiment, the temperature was increased from 200°C to 1000°C at 200°C intervals with a two-hour heating duration. Data was collected between every step. Results showed that the color of a monazite crystal did not change when heated at 200°C and 400°C, but started to fade after heating above 600°C (figure 4D). A tension fracture developed after heating at 1000°C (figure 4F).

Raman spectroscopy was introduced in 1995 as a method to estimate the degree of radiation damage in minerals, such as in zircon and monazite (Nasdala et al., 1995). In this study, we used Raman to analyze zircon and monazite inclusions in Madagascan pink sapphires. The results will be discussed separately.

Zircon. We analyzed 31 randomly chosen zircon inclusions with and without tension halos from the three sapphires in the second set. Raman spectra (figure 5) showed characteristic zircon peaks at 201.3, 223.8, 364.5, 442.2 (ν_2), 984.0 (ν_1), and 1016.8 (ν_3) cm^{-1}. It is well known that the three main peaks at 442.2, 984.0, and 1016.8 cm^{-1} are related to internal SiO_4 vibration modes, and the three other peaks at 201.3, 223.8, and 364.5 cm^{-1} are lattice vibrational modes involving interactions between SiO_4 tetrahedra and the Zr atom. The peak at 1016.8 cm^{-1} or ν_3 (SiO_4) is

TABLE 4. Results of Raman analyses of zircon inclusions or ν_3 (SiO_4) in pink sapphire, reported in average ± SD (n = number of analyzed crystals).

Annealing temperature (°C)	Sample PS21 (n = 15)		Sample PS22 (n = 8)		Sample PS23 (n = 8)	
	Peak position (cm^{-1})	Measured FWHM (cm^{-1})	Peak position (cm^{-1})	Measured FWHM (cm^{-1})	Peak position (cm^{-1})	Measured FWHM (cm^{-1})
–	1009.9 ± 1.7	11.3 ± 2.5	1011.8 ± 3.1	10.4 ± 1.5	1016.8 ± 3.0	10.4 ± 1.5
200	1009.7 ± 1.9	11.2 ± 2.7	1012.0 ± 2.2	9.9 ± 1.7	1016.0 ± 3.1	9.9 ± 1.7
400	1009.5 ± 1.9	10.8 ± 2.8	1010.8 ± 2.8	9.4 ± 1.3	1015.5 ± 4.1	9.4 ± 1.3
600	1009.6 ± 1.5	9.9 ± 1.8	1011.7 ± 2.1	9.4 ± 2.0	1015.6 ± 3.1	9.4 ± 2.0
800	1010.1 ± 1.2	8.6 ± 1.0	1009.0 ± 1.5	9.8 ± 1.6	1015.4 ± 3.3	9.8 ± 1.6
1000	1010.2 ± 1.3	10.4 ± 2.3	1008.8 ± 1.0	8.6 ± 2.0	1014.6 ± 1.1	8.2 ± 1.3

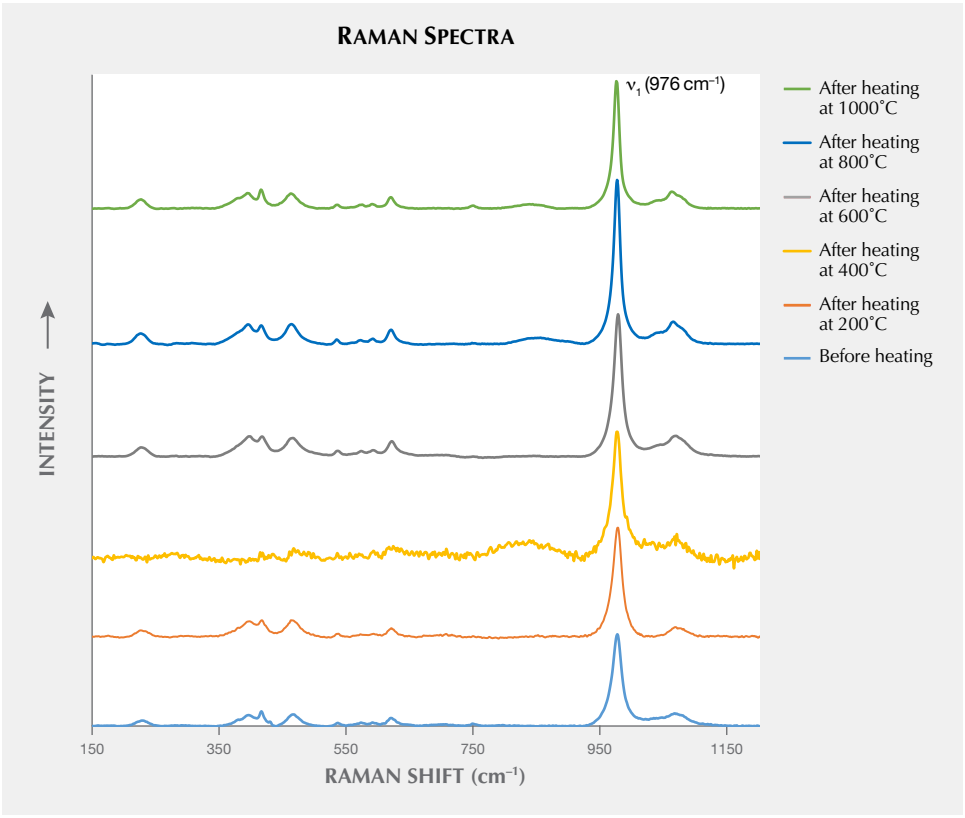

Figure 6. Stacked Raman spectra of one monazite crystal in sample PS23 before and after heat treatment. FWHM was measured by GRAMS software.

the most sensitive to the accumulation of radiation damage, and therefore it is commonly used to compare the structural state of radiation.

Before heating, ν_3 peak positions were at about 1009.9 and 1011.8 cm^{-1} on average for samples PS21 and PS22, respectively. The peak of zircon crystals in sample PS23 was at a slightly higher wavenumber, around 1016.8 cm^{-1}; see table 4. The differences in peak position are affected by many factors, such as chemical composition, pressure, and temperature. However, those differences are beyond the scope of this study.

After heating, we found insignificant changes to Raman peaks where FWHM of the ν_3 peak ranged from 8.6 to 11.3 cm^{-1}. These numbers were reported as a partially metamict state (Nasdala et al., 1995; Palenik et al., 2003). At 1000°C, we found 10 out of 31 zircons developed peaks in the range of 950 and 1150 cm^{-1} (which might be luminescence features (Krzemnicki, 2010). However, these features were not observed when the Raman spectra were collected using a laser with 488 nm wavelength instead of 514 nm.

Significant changes in the Raman spectra of these inclusions have been reported when heated at higher temperatures (Rankin and Edwards, 2003; Wang et al., 2006). When heated above 1400°C, the Raman spectra of these inclusions start to show baddeleyite peaks, indicating that zircon becomes unstable in these conditions and breaks down into oxides.

Monazite. Fifteen monazite inclusions from the three sapphires in the second set were studied. The Raman spectrum of monazite is presented in figure 6 and shows distinct vibrational bands in the ranges 970–1075 cm^{-1} and below 620 cm^{-1}. The former is assigned to the internal PO_4 stretching vibrations, whereas the latter is due to the PO_4 bending and external vibrations of the Ce^{3+} ions and the $[PO_4]^{3-}$ units, respectively (Ruschel et al., 2012). The most prominent peak in the Raman spectrum of monazite is at about 976 cm^{-1} or ν_1 (PO_4). We measured the peak position and FWHM, as shown in table 5.

The results showed the effect of heat treatment on the peak position to be insignificant in all samples. Samples PS21 and PS22 showed a lower wavenumber of peak position and narrower peaks than those of the monazite crystals in sample PS23.

All samples showed sharper ~976 cm^{-1} peaks during progressive heating at higher temperatures. Sample PS21 displayed decreasing width, from 14.2 ± 0.5 cm^{-1} unheated to 8.8 ± 0.2 cm^{-1} after heating at

TABLE 5. Results of Raman analyses of monazite inclusions or ν_1 (PO_4) in pink sapphire, reported in average ± SD (n = number of analyzed crystals).

Annealing temperature (°C)	Sample PS21 (n = 6)		Sample PS22 (n = 6)		Sample PS23 (n = 2)	
	Peak position (cm^{-1})	Measured FWHM (cm^{-1})	Peak position (cm^{-1})	Measured FWHM (cm^{-1})	Peak position (cm^{-1})	Measured FWHM (cm^{-1})
–	974.0 ± 0.8	14.2 ± 0.5	974.0 ± 1.3	15.9 ± 0.3	976.5 ± 0.3	18.4 ± 0.1
200	973.9 ± 0.8	14.3 ± 0.3	974.1 ± 1.3	15.8 ± 0.4	976.2 ± 0.5	18.1 ± 0.5
400	974.0 ± 0.5	12.5 ± 1.1	974.0 ± 1.1	14.9 ± 0.2	976.2 ± 0.4	17.5 ± 0.4
600	974.1 ± 0.3	11.2 ± 0.5	974.6 ± 0.8	12.9 ± 0.2	976.9 ± 0.4	15.4 ± 0.6
800	974.6 ± 0.2	9.6 ± 0.2	973.9 ± 0.5	11.4 ± 0.3	975.9 ± 0.1	13.3 ± 0.4
1000	974.8 ± 0.3	8.8 ± 0.2	974.5 ± 0.5	9.8 ± 0.4	975.8 ± 0.2	13.3 ± 0.4

1000°C. Sample PS23 also decreased in width from 18.4 ± 0.1 cm^{-1} unheated to 13.3 ± 0.4 cm^{-1} after heating at 800°C. The width did not change during the heating step from 800°C to 1000°C (see figure 7). The differences between these two sets of results may be caused by chemical composition or differential degrees of initial radiation damage (which is not included in this study). Our results corresponded with previous work in which Raman spectra showed distinctly narrower bands on annealed monazite than on untreated monazite (Seydoux-Guillaume et al., 2002).

CONCLUSIONS

It has long been known that heat treatment at low temperatures helps to improve color in pink sapphires. Detecting this treatment remains challenging since inclusions such as zircon, needles, and particles are often not affected by low-temperature heat treatment. Using advanced analytical instruments such as FTIR spectrometers is necessary to help gemologists detect heat treatment. In this study on Madagascar pink sapphire, we have shown that the presence of the 3232 cm^{-1} peak is related to heat treatment. While this peak is only found in heated stones, its absence is not an indicator of an unheated stone. This peak will only develop if the initial 3309 cm^{-1} peak is strong enough. This is exactly the same behavior that has been observed in rubies from Montepuez, Mozambique.

Another possible indicator of heat treatment is the observation of monazite crystals, even though they are less common in pink sapphire than zircon crystals. Monazite typically has an orange-brown color that will fade to near-colorless after heat treatment at relatively low temperatures. This alteration can be explained by annealing radiation damage to monazite inclusions due to the increasing temperature. This also results in narrower peaks in the

Figure 7. The relative difference between FWHM of monazite at ν_1 (PO_4) at ~974–976 cm^{-1} and heating temperature on sample PS22 (n = 6; left) and sample PS23 (n = 2; right). Different dots represent different monazite inclusions analyzed in each sample (n=number of analyzed crystals).

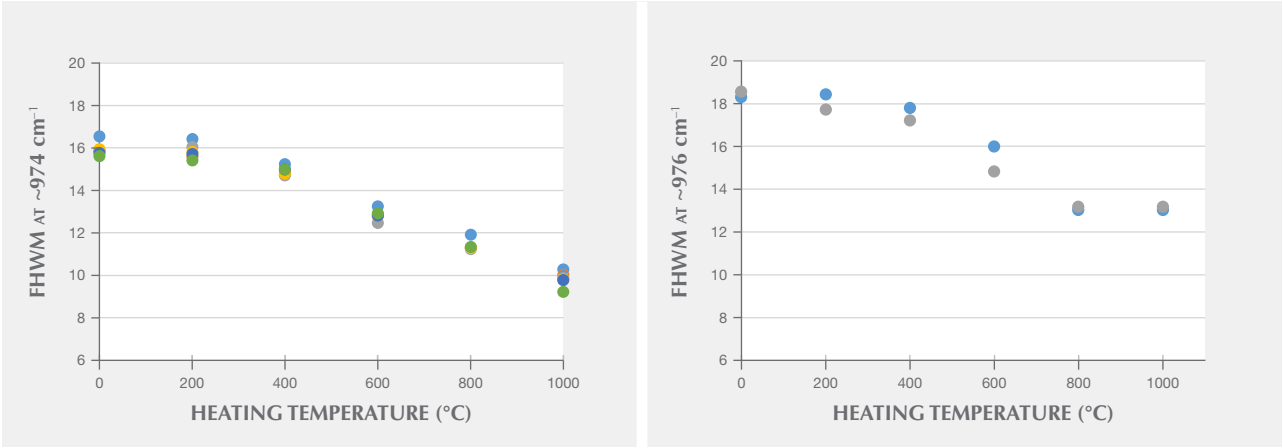

Raman spectrum. The presence of a near-colorless monazite inclusion suggests the gem has been heated, but its color is sometimes masked by the bodycolor of the host.

In order to use FWHM and other Raman spectra features as an indication of low-temperature heat treatment, more samples will be required to complete a statistically relevant analysis.

ABOUT THE AUTHORS

Ms. Saeseaw is senior manager of colored stone identification, Ms. Khowpong is an analytics technician, and Mr. Vertriest is supervisor of field gemology, at GIA in Bangkok.

ACKNOWLEDGMENTS

The authors would like to give thanks to GIA's Bangkok lab staff, especially Suwasan Wongchacree for photomicrography, Polthep Sukpanish for FTIR data, and Sasithorn Engniwat for photo calibration. Also, thanks to Aaron Palke and Shane McClure for their useful suggestions. We also thank the peer reviewers for valuable comments that improved this article.

REFERENCES

Beran A. (1991) Trace hydrogen in Verneuil-grown corundum and its colour varieties: An IR spectroscopic study. *European Journal of Mineralogy*, Vol. 3, No. 6, pp. 971–976, http://dx.doi.org/10.1127/ejm/3/6/0971

Clavier N., Podor R., Dacheux N. (2011) Crystal chemistry of the monazite structure. *Journal of the European Ceramic Society*, Vol. 31, No. 6, pp. 941–976, http://dx.doi.org/10.1016/j.jeurceramsoc.2010.12.019

Dickin A.P. (2018) *Radiogenic Isotope Geology*. Cambridge University Press, Cambridge, UK, https://doi.org/10.1017/9781316163009

Emmett J.L., Douthit T.R. (1993) Heat treating the sapphires of Rock Creek, Montana. *G&G*, Vol. 29, No. 4, pp. 250–272, http://dx.doi.org/10.5741/GEMS.29.4.250

Emmett J.L., Scarratt K., McClure S.F., Moses T., Douthit T.R., Hughes R., Novak S., Shigley J.E., Wang W., Bordelon O., Kane R.E. (2003) Beryllium diffusion of ruby and sapphire. *G&G*, Vol. 39, No. 2, pp. 84–135, http://dx.doi.org/10.5741/GEMS.39.2.84

Emmett J.L., Dubinsky E.V., Hughes R.W., Scarratt K. (2017) Color, spectra & luminescence. In R.W. Hughes, Ed., *Ruby & Sapphire: A Gemologist's Guide*. Bangkok, pp. 107–163.

Hughes E.B., Perkins R. (2019) Madagascar sapphire: Low-temperature heat treatment experiments. *G&G*, Vol. 55, No. 2, pp. 184–197, http://dx.doi.org/10.5741/GEMS.55.2.184

Hughes R.W., Manorotkul W., Hughes E.B. (2017) *Ruby & Sapphire: A Gemologist's Guide*. RWH Publishing/Lotus Publishing, Bangkok.

Koivula J.I. (2013) Useful visual clue indicating corundum heat treatment. *G&G*, Vol. 49, No. 3, pp. 160–161, http://dx.doi.org/10.5741/GEMS.49.3.160

Krzemnicki M.S. (2010) How to get the "blues" out of the pink: Detection of low-temperature heating of pink sapphires. *SSEF Facette*, No. 17, p 12.

Meldrum A., Boatner L.A., Weber W.J., Ewing R.C. (1998) Radiation damage in zircon and monazite. *Geochimica et Cosmochimica Acta*, Vol. 62, No. 14, pp. 2509–2520, http://dx.doi.org/10.1016/S0016-7037(98)00174-4

Nasdala L., Irmer G., Wolf D. (1995) The degree of metamictization in zircon: A Raman spectroscopic study. *European Journal of Mineralogy*, Vol. 7, No. 3, pp. 471–478, http://dx.doi.org/10.1127/ejm/7/3/0471

Nasdala L., Lengauer C.L., Hanchar J.M., Kronz A., Wirth R., Blanc P., Kennedy A.K., Seydoux-Guillaume A.-M. (2002) Annealing radiation damage and the recovery of cathodoluminescence. *Chemical Geology*, Vol. 191, No. 1-3, pp. 121–140, http://dx.doi.org/10.1016/S0009-2541(02)00152-3

Palenik C.S., Nasdala L., Ewing R.C. (2003) Radiation damage in zircon. *American Mineralogist*, Vol. 88, No. 5-6, pp. 770–781, http://dx.doi.org/10.2138/am-2003-5-606

Pardieu V., Saeseaw S., Detroyat S., Raynaud V., Sangsawong S., Bhusrisom T., Engniwat S., Muyal J. (2015) "Low temperature" heat treatment of Mozambique ruby. *GIA Research News*, https://www.gia.edu/gia-news-research-low-temperature-heat-treatment-mozambique-ruby

Rankin A.H., Edwards W. (2003) Some effects of extreme heat treatment on zircon inclusions in corundum. *Journal of Gemmology*, Vol. 28, No. 5, pp. 257–264.

Ruschel K., Nasdala L., Kronz A., Hanchar J.M., Többens D.M., Škoda R., Finger F., Möller A. (2012) A Raman spectroscopic study on the structural disorder of monazite–(Ce). *Mineralogy and Petrology*, Vol. 105, No. 1-2, pp. 41–55, http://dx.doi.org/10.1007/s00710-012-0197-7

Saeseaw S., Khowpong C. (2019) Gem News International: The effect of low-temperature heat treatment on pink sapphire. *G&G*, Vol. 55, No. 2, pp. 290–291.

Saeseaw S., Kongsomart B., Atikarnsakul U., Khowpong C., Vertriest W., Soonthorntantikul W. (2018) Update on "low-temperature" heat treatment of Mozambican ruby: A focus on inclusions and FTIR spectroscopy. *GIA Research News*, https://www.gia.edu/ongoing-research/update-low-temperature-heat-treatment-mozambican-ruby-focus-on-inclusions-and-ftir-spectroscopy

Seydoux-Guillaume A.M., Wirth R., Nasdala L., Gottschalk M., Montel J.M., Heinrich W. (2002) An XRD, TEM and Raman study of experimentally annealed natural monazite. *Physics and Chemistry of Minerals*, Vol. 29, No. 4, pp. 240–253, http://dx.doi.org/10.1007/s00269-001-0232-4

Sripoonjan T., Wanthanachaisaeng B., Leelawatanasuk T. (2016) Phase transformation of epigenetic iron staining: Indication of low-temperature heat treatment in Mozambique ruby. *Journal of Gemmology*, Vol. 35, No. 2, pp. 156–161.

Vertriest W., Palke A.C., Renfro N.D. (2019) Field gemology: Building a research collection and understanding the development of gem deposits. *G&G*, Vol. 55, No. 4, pp. 490–511, http://dx.doi.org/10.5741/GEMS.55.4.490

Wang W., Scarratt K., Emmett J.L., Breeding C.M., Douthit T.R. (2006) The effects of heat treatment on zircon inclusions in Madagascar sapphires. *G&G*, Vol. 42, No. 2, pp. 134–150, http://dx.doi.org/10.5741/GEMS.42.2.134

Baroque-Era Rose Cuts of Colored Stones: Highlights from the Second Half of the Seventeenth Century

Karl Schmetzer

Colored stones from the Baroque era fashioned as rose cuts have received little attention to date. Even the colored stone rose cuts incorporated in notable collections, such as the Cheapside Hoard discovered in London in 1912, have not been studied in detail, and only very limited further examples are depicted and described in gemological texts. Recent work with five objects of liturgical insignia and electoral regalia belonging originally to the archbishops and prince-electors of Trier and Cologne has thus offered an opportunity to augment available information. All of these pieces date to the second half of the seventeenth century. Although the table cuts from that era were still quite simple, consisting of an upper flat table facet surrounded by one or two rows of step-cut facets, the rose cuts were enormously varied and complex while still generally following a symmetrical pattern in the facet arrangement. The goal of the study was to contribute to filling a gap in the historical information on gem cuts by offering an overview of the many rose cuts used for colored stones in the second half of the seventeenth century.

Rose cuts encompass a variety of faceting arrangements, all of which lack a flat table (figure 1). In contrast to the considerable literature on the use of rose cuts in diamonds, there has been a dearth of information regarding their use in colored stones.

The story of diamond fashioning started with the polishing and/or slight modification of the crystal faces of natural diamond octahedra, creating what is known as the point cut. Thereafter, simple table cuts were developed from the fifteenth century onward, becoming more complex over time (Lenzen, 1966; Falk, 1975; Tillander, 1995; Klein, 2005; Gilbertson, 2007; Ogden, 2018). Diamonds with rose cuts came later as a typical product of the sixteenth and seventeenth centuries, employing a cutting process that began with a rough cleavage fragment from a diamond octahedron. The standard appearance generally consisted of a flat base topped by a dome with six triangular facets at the center. Between the dome top and the base was an intervening layer with six, 12, or 18 additional facets (figure 2). Despite some inconsistency in terminology, these cuts are primarily denoted as Antwerp roses (6 + 6 facets), half-Dutch roses (6 + 12 facets), and full-Dutch roses (6 + 18 facets), respectively (Eppler and Eppler, 1934; Stranner, 1953).

Visual evidence of the foregoing historical progression in diamond cuts is readily found in references depicting jewelry objects from bygone eras and in seventeenth-century sketchbooks of goldsmiths or jewelry designers such as T. Cletcher (1629) or G. Légaré (1663) (figure 3; see, e.g., Gans, 1961; Walgrave, 1993a,b; Scarisbrick, 1993). Political and economic circumstances related to the development of rose-cut diamonds are discussed by Kockelbergh et al. (1992) and De Bie (2014).

In the decidedly less voluminous literature on colored stones cut without flat tables, the first appearance of such a faceted gemstone in art is found in a sixteenth-century painting by A. Bronzino (1542) portraying Venus, Cupid, Folly, and Time (an allegory of lust) (see Prim, 2018). The oval gemstone in that work shows a crown covered by multiple facets in the form of elongated rhombuses. Other isolated art and jewelry pieces from the second half of the sixteenth century and the seventeenth century likewise offer several examples (see, e.g., Prim, 2019). A notable influx of items displaying colored stones cut without flat tables then occurred with the 1912 discovery of the so-called Cheapside Hoard, dated before the Great Fire of London in 1666. Exemplars are contained in the catalog prepared for the 2014 exhibition

See end of article for About the Authors and Acknowledgments.
Gems & Gemology, Vol. 56, No. 4, pp. 458–482,
http://dx.doi.org/10.5741/GEMS.56.4.458

Figure 1. In the present study, five richly decorated liturgical insignia from the second half of the seventeenth century were examined. This photo shows part of the monstrance from the Treasury of Cologne Cathedral decorated mainly with larger garnets, peridots, blue sapphires, and quartz with yellow foil backing. The smaller stones are diamonds, amethysts, and emeralds. Many of the gemstones used to decorate the insignia are rose cuts without flat tables, showing a great variety of cutting styles. The large blue sapphire below measures 26 × 14 mm. Courtesy of the Treasury of Cologne Cathedral.

at the Museum of London (Forsyth, 2013), and a further selection of objects is depicted by Ogden (2013, 2014).

Although today the interested gemologist, art historian, or jeweler might be able to find various photographs or drawings of art objects exhibiting

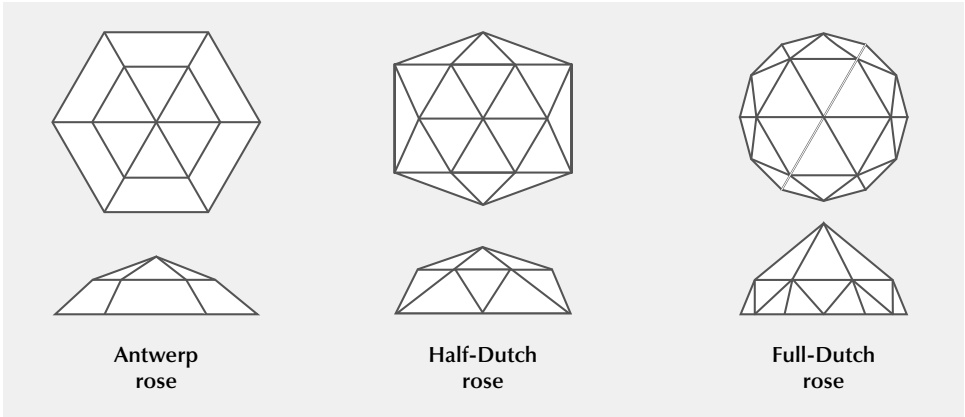

Figure 2. Sketches of the most common rose cuts used for diamonds, all consisting of a flat base, a dome topped by six triangular facets, and several additional facets between the dome top and the base. Top row: View looking down on the dome, parallel to the six-fold axis. Bottom row: View perpendicular to the six-fold axis. After Eppler and Eppler (1934).

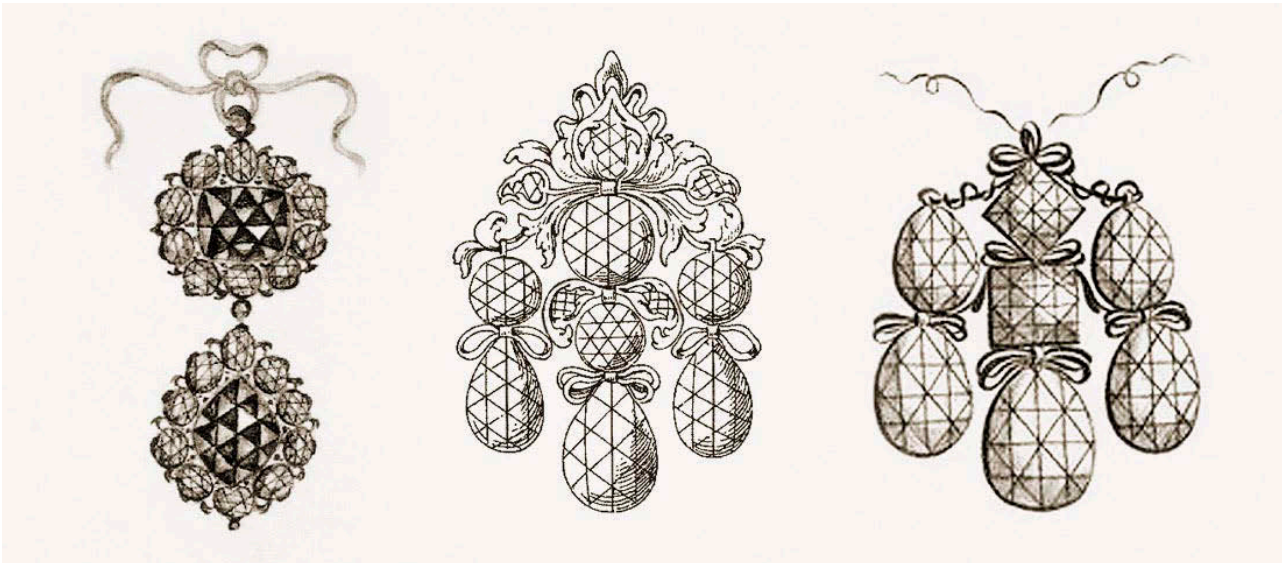

Figure 3. Jewelry designs from the seventeenth century using various types of rose-cut diamonds. Illustrations by (left to right) T. Cletscher (1629; from Walgrave, 1993a); P. Bourdon (ca. 1660; from Walgrave, 1993b); and G. Légaré (right, 1663).

rose-cut colored stones, no systematic evaluation of such cuts is available in the literature. While nineteenth-century texts may present a broad selection of table cuts, along with covering the three traditional rose cuts for diamonds, other gem cuts without flat tables are not shown or described as being commonly available. Presumably such objects were not known to the authors of these treatises and were thus considered extremely rare, an estimation borne out by their treatment in Schrauf (1869). There, a

Figure 4. Sketch of the so-called cross-rose cut consisting of a flat base, a dome topped by eight rhombuses, and additional triangular and step-cut facets between the dome top and the base. Top: view looking down upon the dome, parallel to the eight-fold axis. Bottom: view perpendicular to the eight-fold axis. After Schrauf (1869).

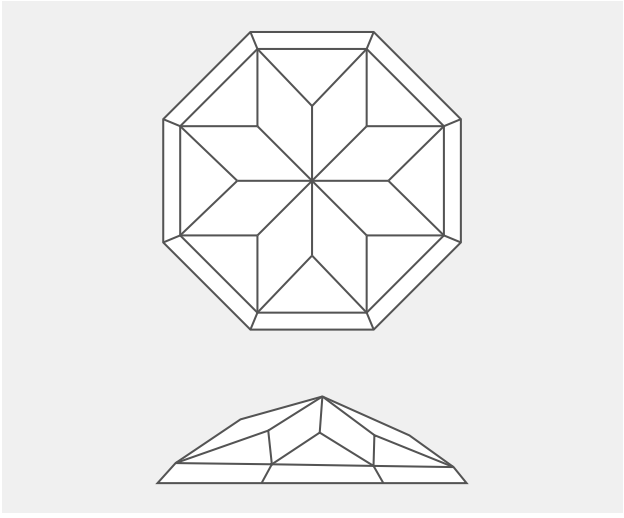

In Brief

- Colored stone rose cuts from the second half of the seventeenth century present widely varied and complex facet arrangements while generally following a symmetrical pattern.
- Five objects of liturgical insignia and electoral regalia originally belonging to the archbishops and prince-electors of Trier and Cologne were richly decorated with colored stones, including numerous rose cuts reflecting the broad variety of patterns available during the era.
- Rose-cut gems embellishing the pieces were fashioned from corundum (ruby and sapphire), peridot, garnet (pyrope-almandine and hessonite), and quartz (rock crystal and amethyst), in addition to diamond.
- The colored stone rose cuts studied can be characterized by the symmetry of the dome's center (e.g., four-fold, six-fold, eight-fold) and by the shape of the central facet (e.g., triangular, rhombus, kite).
- Cuts referred to as half-Dutch and full-Dutch roses, also seen in diamonds, and expanded Dutch roses were most common. The creativity displayed with colored stones resulted in a number of more complicated patterns that far exceeded what is known in diamonds.

Figure 5. Stones with rose cuts are still found frequently in the trade using garnet and quartz material. Left: Garnets displaying traditional patterns formed by multiple triangles, with the largest measuring 14 × 10 mm. Samples courtesy of Hermann Lind II, Idar-Oberstein. Center: Garnets where the rose pattern is created using rhombuses (upper left, 16 × 12 mm), squares (upper right, 14 × 14 mm), or triangles (all others). Samples courtesy of Hermann Lind II, Idar-Oberstein. Right: Quartz varieties with the rose pattern formed by rhombuses (upper left), triangles (lower left), or squares (upper and lower right), with the amethyst at the lower right measuring 10 × 10 mm. The samples were purchased at the Sainte-Marie-aux-Mines Mineral and Gem show in 2019. Photos by K. Schmetzer.

rose-cut garnet with a flat base and eight rhombus-shaped facets forming a central dome (figure 4) was drawn and characterized as a unique gem fashioned in the eighteenth century or before, and a similar stone with eight kite-shaped facets topping the central dome was also described as unique and very rare.

Rose cuts are still produced from multiple gem materials, primarily garnet (figure 5, left and center) and quartz (figure 5, right), and thousands of facet designs including numerous rose cuts can be found by interested users and cutters in modern texts (e.g., Long and Steele, 1979–1989) and online databases (e.g., FacetDiagrams.org). However, these are mainly cuts developed in the nineteenth or twentieth century, and the publications are silent as to whether the designs find any analogue in objects of eras past.

The colored stone rose cuts featured in the current study came to light during examination of five objects of liturgical insignia and electoral regalia. Four were from what is known as the Trierer Kurschatz (the treasury of the archbishops and prince-electors of Trier, who were one of the seven electors of the Holy Roman Empire[1]). The work began principally with gemstone identification at the time the collection was publicly presented in October 2017 ("The Munich Show," 2017). The investigation continued at the Diözesanmuseum Limburg (Museum of the Roman Catholic Diocese of Limburg), where the treasury is normally exhibited, with the focus turning in part to the cuts of the stones. It soon became apparent that these artifacts, dated to the second half of the seventeenth century, contained numerous colored stones with rose cuts differing markedly from the standard cuts presented for diamonds in gemological texts (again, see figure 2).

The study was then augmented by the addition of a seventeenth-century monstrance from the Domschatzkammer Köln (the Treasury of Cologne Cathedral, the Roman Catholic cathedral of the former archbishop and prince-elector of Cologne, another one of the seven electors of the Holy Roman Empire).

HISTORY OF THE LITURGICAL INSIGNIA AND ELECTORAL REGALIA

Trier/Limburg. The four pieces from the Limburg museum were crafted by different goldsmiths during the terms of two archbishops and prince-electors of Trier: Carl Caspar von der Leyen (Karl Kaspar von der Leyen), reigning 1652–1676, and Johann Hugo von Orsbeck, reigning 1676–1711 (figure 6; see also Kloft, 2016, for a synopsis of the history of the Limburg cathedral and museum). Information about the age and production of the various masterpieces, and the artisans responsible, derives primarily from accounts remaining from the respective periods of production, which were examined in detail by Michel (1925).

The monstrance (figure 7, top) was created in 1667 by the goldsmith Christian Schweling from Cologne. The crosier (figure 8, top) was made in 1672 by Johann Daniel Treudel from Frankfurt, and the processional cross (figure 8, bottom) was produced by the same goldsmith one year later, in 1673. The miter (figure 7, bottom) was started by Christian

[1]The seven prince-electors constituted the electoral college that selected the emperor of the Holy Roman Emperor. In addition to the archbishops of Cologne, Trier, and Mainz, there were four secular electors: the King of Bohemia, the Count Palatine of the Rhine, the Duke of Saxony, and the Margrave of Brandenburg.

Figure 6. The liturgical insignia and electoral regalia now in the collection of the Museum of the Diocese of Limburg were commissioned in the second half of the seventeenth century by Carl Caspar von der Leyen, archbishop and prince-elector of Trier (left, reigning 1652–1676), and his successor, Johann Hugo von Orsbeck (right, reigning 1676–1711).

Schweling in 1674. After his death in 1675, his son Cornelius Schweling took over and pursued the project until 1678. Following a decade-long interval, work on the miter was continued by Peter Boy from Frankfurt in 1688 and finished in 1691. Attribution of the various aspects of the miter's ornamentation to a particular craftsman has remained a subject of discussion (Clasen, 1993). The ensemble, together with other objects no longer extant such as a ceremonial sword, is referred to collectively as the Landrentamtspretiosen and contains some of the most richly decorated liturgical insignia and electoral regalia known. For instance, the miter alone is embellished with more than 3,300 gemstones, while the monstrance displays more than 3,100 gems.

During the reign of Johann Hugo von Orsbeck, the main residence of the archbishops and prince-electors of Trier was moved from Trier to the city of Koblenz, where the Ehrenbreitstein fortress was located. With the end of the Electorate of Trier, which took place between 1801 and 1803, and the resignation of the last archbishop, Klemens Wenzeslaus, the territories on the right bank of the Rhine were annexed by Duke Friedrich Wilhelm of Nassau-Weilburg, who reigned from 1788 to 1816. In 1806 the Duchy of Nassau was established, and in 1822, Duke Wilhelm of Nassau, who reigned from 1816 to 1839 as Friedrich Wilhelm's successor, donated the Landrentamtspretiosen collection to the Diocese of Limburg (Luthmer, 1907; Kuhn, 1976).

In connection with this donation, the different objects underwent conservation work by a goldsmith from the city of Mainz, but gemstones, mainly diamonds from the miter, were stolen and replaced with other materials. After the manipulation was detected and most of the stolen gemstones were found, the miter was fully restored. In 1906, all the pieces were the beneficiary of additional conservation, this time performed carefully without altering the gemstone embellishment. Thus, while the documented history

Figure 7. Among the insignia and regalia from the treasury of the archbishops and prince-electors of Trier were a monstrance (top, 66 × 29 cm) created by goldsmith Christian Schweling from Cologne in 1667 and a miter (bottom, 44 × 31 cm) started by Schweling and his son Cornelius from 1674 to 1678 and later completed by Peter Boy of Frankfurt between 1688 and 1691. Courtesy of the Museum of the Diocese of Limburg.

Figure 8. Included within the insignia and regalia from the treasury of the archbishops and prince-electors of Trier were a crosier (top, 38 × 21 cm) crafted by Johann Daniel Treudel of Frankfurt in 1672 and a processional cross (bottom, 39.5 × 32.0 cm) fabricated by the same goldsmith in 1673. Courtesy of the Museum of the Diocese of Limburg.

Figure 9. Several inscriptions on a monstrance in the collection of the Treasury of Cologne Cathedral indicate that the object was donated in 1657 and 1658 by Maximilian Heinrich von Bayern, archbishop and prince-elector of Cologne (left, reigning 1650–1688), and his prime minister Franz Egon von Fürstenberg (right, serving 1650–1674).

would appear to suggest that only limited restorative work and substitution of damaged materials was undertaken, this does not exclude the possibility that single stones were lost through simple usage and replaced without explicit documentation (see Beitz, 1928).

Cologne. The monstrance in the collection of the Treasury of Cologne Cathedral bears two inscriptions evidencing its donation to the cathedral through transactions in 1657 and 1658. Maximilian Heinrich von Bayern, archbishop and prince-elector of Cologne (figure 9), who reigned from 1650 to 1688, is believed to have been the principal donor. Per the inscriptions, he was joined in the donation by Franz Egon von Fürstenberg (Clasen, 1983, 1989), his friend and the prime minister from 1650 to 1674. Filling multiple roles, Franz Egon also became the bishop of Strassburg in 1663. Creation of the monstrance (figure 10) has been attributed to Christian Schweling, primarily through comparison with the Limburg piece, because contemporaneous documentation or accounts identifying the goldsmith responsible were not preserved (Beitz, 1928).

In 1975, the Cologne monstrance was stolen along with several other objects from the treasury. After an intensive police investigation in several countries, some of the stolen objects were found and returned, albeit partially damaged. The monstrance's return, with the remains having been located in five countries, was accompanied by detached portions of its decoration ranging from single loose stones to single stones within their gold settings and larger sections of the gold mounting holding several stones (e.g., a rosette with a central stone surrounded by a number of smaller gems). The state of disrepair revealed that most of the gold framework had been melted following removal of the stones.

Figure 10. On the basis of its design and craftsmanship, the monstrance (52 × 21 cm) from the Treasury of Cologne Cathedral has been attributed to the goldsmith Christian Schweling of Cologne (compare with figure 7, top). This photo of the Cologne monstrance was taken shortly before its theft in 1975. Courtesy of the treasury of Cologne Cathedral.

The monstrance was reconstructed using the original stones (approximately 85% of the original decoration consisting of more than 3,100 gemstones), with and without the original settings, and from the original gold. The work was performed by the goldsmith Peter Bolg from 1978 to 1987, spending two days per week on the project (Peter Bolg, pers. comm. 2020; see also Clasen, 1983, 1989; Mösch, 1995; Bolg and Zieleskiewicz, 1995). Most of the larger colored stones, with the exception of two peridots and certain garnets and emeralds, were returned after the theft. Comparison of photographs taken before (fig-

Figure 11. Photos of the Cologne monstrance in its present state reflect the high quality of the goldsmith's work in the reconstruction with gemstones even being restored to their original locations (compare with figure 10). Photos by K. Schmetzer.

ure 10) and after (figure 11) the theft shows that the goldsmith succeeded in a reconstruction remarkably close to the seventeenth-century original.

Gemstone Provenance and Origin. Original documents concerning the provenance of the gemstones used in the artifacts contain limited information. Accounts available in the archives of the archbishops of Trier demonstrate that, in the majority of cases, the archbishops and prince-electors purchased the gemstones from local stone dealers or goldsmiths and, once the group of gems intended for a particular object was completed, submitted the collection to the goldsmith commissioned to prepare the masterpiece (Beitz, 1928).

A less frequent alternative is evidenced by financial records reflecting that the goldsmith was paid by the archbishops and prince-electors for both the artwork and the stones (Kuhn, 1989, 1999). This suggests that the goldsmith had to purchase the stones, either from local middlemen or from a foreign cutter or dealer. Schweling is known to have taken both approaches, even traveling to Antwerp—a city hosting a large cutting industry at the time—to acquire gemstones (Beitz, 1930). Only one example is documented where gems were purchased by the archbishop and prince-elector of Trier directly from a foreign stone cutter or dealer in Antwerp and were then provided to Schweling for a chalice.

A high percentage of the rose-cut gems in the various regalia and insignia from Limburg and Cologne were garnets (see below), a fact that offers certain insights regarding potential origin, given the historical context. With respect to Germany, the art of cutting

Figure 12. Gemstones decorating the Limburg pieces, such as the monstrance shown here, were identified using energy-dispersive X-ray fluorescence (EDXRF) spectroscopy. Photo by H.A. Gilg.

garnet as rose cuts was brought to Nuremberg in 1590 by the Frenchman Claudius de la Croix. Competition thereby ensued between the cutting industries in Nuremberg and Freiburg and Waldkirch, a pair of cities neighboring one another in the Rhine Valley and the Black Forest. The resulting dispute was eventually resolved through the granting in 1601 of a privilege by Rudolf II, Holy Roman Emperor, in favor of Freiburg and Waldkirch.

The privilege stipulated that Bohemian garnets were to be cut and polished solely in Freiburg and Waldkirch. Nonetheless, available references indicate that only the relatively small Bohemian chromium-bearing pyropes, mainly up to 6 mm in size, were cut there during the seventeenth century, and the industry's importance declined with the French occupation of Freiburg from 1677 to 1697 (Trimborn, 1940; Kaiser, 2003). Thus, it is unlikely that the much larger pyrope-almandines and hessonites in the objects examined for this study came from the production at Freiburg and Waldkirch.

MATERIALS AND METHODS

The present study of colored stone rose cuts was based upon examination of five objects of liturgical insignia and electoral regalia: the miter, monstrance, processional cross, and crosier in the collection of the Museum of the Diocese of Limburg and the reconstructed monstrance in the collection of the Treasury of Cologne Cathedral. As mentioned above, the evaluation began when the author and Professor H. Albert Gilg (Technical University of Munich) were invited to examine the pieces from Limburg during their presentation at the 2017 Munich Show. On that occasion, work was restricted to determining gemstone identity, primarily through energy-dispersive X-ray fluorescence (EDXRF) spectroscopy in combination with Raman spectroscopy. Examination subsequently continued in Limburg in February 2018. At that time, Professor Gilg proceeded with identifying the gem materials (figure 12) while the author, together with Heidi and Helmut Bürger, gem cutters and cut designers, started to evaluate the various cuts employed. It soon became apparent that several thousand of the colored stones decorating the four objects were fashioned as different table and rose cuts.

The rose cuts were examined for further visual detail during April 2019 in Limburg by the Bürgers and the author using the unaided eye, a loupe, and optical microscopy at low magnification (figure 13). Sizes of gemstones in settings were estimated with a simple caliper. In general, sketches were drawn by the author and reviewed for accuracy by the Bürgers, and photos of the rose cuts were taken. Using the sketches and information from the photos, the author then prepared final drawings showing approximately 40 different cuts. In November 2019, those drawings were verified by the author through comparison with the objects at Limburg, and several ad-

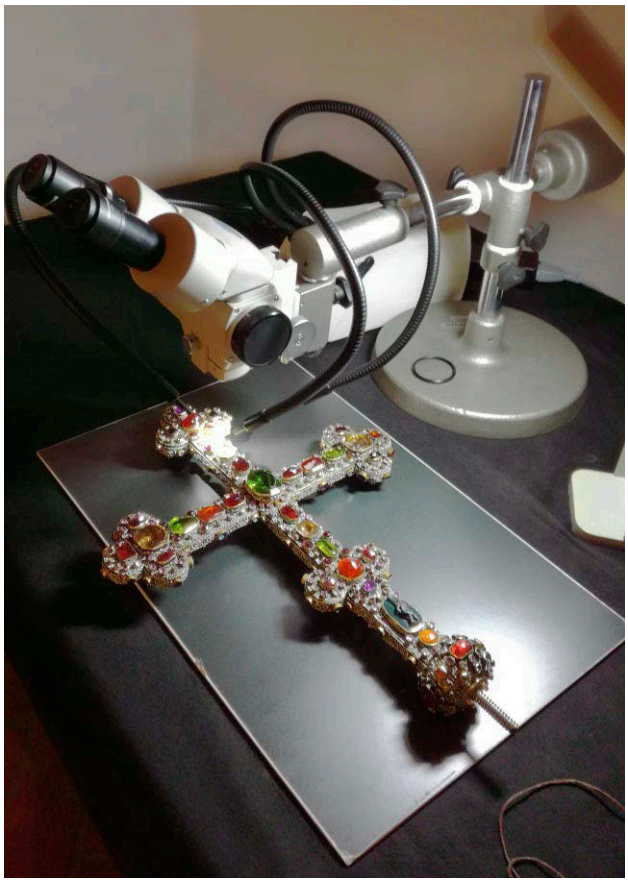

Figure 13. The cuts of the colored stones decorating the Limburg artifacts, including the processional cross, were examined by optical microscopy at low magnification. Photo by K. Schmetzer.

ditional sketches were prepared for gemstones that had proven to be of interest in the photos but had not previously been examined in detail.

In connection with restorations done in the nineteenth and twentieth century (see above), some lost gemstones were replaced, but without any detailed documentation. This was obvious for a limited number of stones with modern faceting styles such as table cuts and mixed cuts. There is, however, no indication that historical rose cuts were studied and gemstones were cut in the "old style" to replace lost stones.

The monstrance at Cologne was examined visually by the author in November 2019. As noted above, the monstrance was reconstructed after the 1975 theft, making extensive use of the original gem material recovered (Clasen, 1983, 1989; Bolg and Zieleskiewicz, 1995). To ensure that the study focused on historical gems cut prior to the 1658 donation to the cathedral, rather than material purchased for the reconstruction, the author in 2020 consulted with the goldsmith Peter Bolg and the gem merchant August Wintermantel, who supplied all the diamonds and colored stones for Bolg's reconstruction. Visiting the Wintermantel firm in Waldkirch in 2020, the author was also able to review and copy a list of missing stones, several hand-drawn sketches identifying their position within the piece, and notes and invoices in the archives of the company.

The insight obtained may be summarized as follows:

- Missing rose-cut diamonds were replaced with rose-cut diamonds of appropriate sizes taken from other historical jewelry pieces or cut to the sizes needed.
- Missing colored stones were either selected from the stock of the A. Wintermantel firm (e.g., garnets of appropriate size and shape) or cut from rough to the desired form (e.g., cabochon sapphires and garnets or table-cut emeralds).
- Invoices indicate that five garnets cut as standard full-Dutch roses (10 mm or smaller) with a crown of 24 facets were used to replace missing stones.
- The more complex rose cuts of the original colored stones remaining were not examined in detail in the reconstruction years from 1978 to 1987, and no attempt was made to facet any similar examples to replace missing materials.

The information collected in Munich, Limburg, and Cologne is expected to lead to three distinct works. The present paper is focused on describing the rose cuts found in the regalia and insignia from Limburg and Cologne. These results also stimulated developments in modern cut design, especially rose cuts that use pavilion facets for gemstones with high brilliancy (H. Bürger, in preparation). A comprehensive description of the four Limburg objects is likewise anticipated (H.A. Gilg, in preparation).

RESULTS

Overview of Embellishment and Gemstone Properties—Limburg Objects. For purposes of understanding the context that frames the detailed discussion of rose cuts to follow, a broad overview of the general appearance of the objects is given below. As noted previously, further specifics are not within the scope of this study and will be published elsewhere.

Figure 14. The gemstones embellishing the pieces from the Limburg museum and the Cologne treasury were grouped in decorative assemblages and mounted in closed bezel settings. Left: From the Limburg monstrance: table-cut peridots, together with a rose-cut garnet (center, 35.0 × 12.5 mm) and smaller faceted and cabochon garnets. Right: From the Cologne monstrance: table-cut peridots, together with a rose-cut amethyst (center, 23 × 18 mm) and faceted garnets of varying sizes, including rose cuts. Photos by K. Schmetzer.

Gem Varieties. The minerals and gem varieties, as well as any significant modification such as foil backing, that were identified by a combination of EDXRF, Raman spectroscopy, and visual examination most commonly included:

- Diamond
- Corundum: ruby, sapphire
- Emerald
- Peridot
- Garnet: pyrope-almandine, hessonite
- Quartz: rock crystal (colorless, yellow with foil backing, and orange with foil backing), amethyst
- Pearl

The foregoing formed the vast majority of the thousands of colored stones decorating the pieces. A few far rarer materials comprised two pink spinel cabochons, one faceted colorless topaz (presumably a replacement stone) surrounded by smaller diamonds, and several samples of glass in various colors.

Mounting and Sizes. The gemstones were secured in the mountings with a closed bezel setting (figure 14). No part of the girdle or, if present, pavilion was visible, rendering it impossible to evaluate the degree to which the bases might be flat, curved, or faceted. Definitive measurement of dimensions was similarly restricted, so only approximate sizes will be given in the figure captions. Such will afford a general impression of the sizes of gems available and used in the second half of the seventeenth century.

Diamond Cuts. The diamonds had been faceted in a variety of styles. Pyramidal point cuts, quadratic and rectangular table cuts, cuboids, full-Dutch roses, trihedral roses, and pear-shaped roses were observed. Each such type is known from the literature on diamond cutting conventions (e.g., Tillander, 1995; see also for nomenclature and definitions).

Colored Stone Cuts. The colored stones incorporated those with table facets, those shaped as cabochons, and those fashioned as rose cuts. The samples with table facets presented a multitude of outline shapes (again, see figure 14):

- Irregular forms
- Octagons
- Hexagons
- Quadrilateral forms: squares, rectangles, rhombuses, kites, isosceles trapezoids
- Three-sided forms: equilateral triangles, isosceles triangles
- Pear-shaped forms

Only the relatively small faceted rubies, about 5–6 mm in size, showed table cuts with somewhat irregular shapes. The tables were surrounded by a row of small step-cut facets (figure 15).

The other colored stones (blue sapphire, emerald, peridot, garnet, and quartz) displayed regular symmetrical cuts. Most exhibited step cuts with one or two rows of eight, six, four, or three crown facets each, parallel to the edges of the table. A few stones with more complex, modern faceting styles (e.g., mixed cuts) are thought to be nineteenth- and twentieth-century replacements of gems lost during usage. A similar assumption of later replacement might apply to the single faceted topaz and the few glass simulants.

Faceted stones without tables (i.e., rose cuts) were found only in a subset of the colored stone varieties seen in the Limburg pieces:

- Corundum: ruby, sapphire
- Peridot
- Garnet: pyrope-almandine, hessonite
- Quartz: rock crystal (colorless, yellow with foil backing, and orange with foil backing), amethyst

Cabochons with a round or oval shape also made an appearance among the colored stones, particularly the garnets.

Previous Use and Surface Indentations. There were only a small number of stones with drill holes indicating previous use in other jewelry items (figure 16, left). Samples with surface indentations were also present (figure 16, right), reflecting a technique used since the Middle Ages in India and Sri Lanka to remove impurities (see, e.g., Schmetzer and Gilg, 2020). The facet edges of some stones were highly abraded, which might indicate previous use in other pieces of jewelry.

Consideration of Embellishment for Comparative Purposes—Cologne Object. Insofar as the Cologne monstrance is thought to have been crafted by the same goldsmith as the Limburg piece, the general style paralleled that described above. The forms and facet style of gemstones with table facets were comparable with the colored stones from Limburg. Some of the gemstones that returned after the theft in an unmounted state showed faceted pavilions, but the cuts were not studied in detail (Peter Bolg and August Wintermantel, pers. comms., 2020).

As specifically relevant to this study, the rose cuts were fashioned from:

Figure 15. Rubies from group 1 are found as rose cuts with a somewhat irregular surface pattern (left column), as table cuts with large tables and one row of step-cut facets (middle column), or as irregularly shaped, polished pebbles (right column). The larger stones measure about 5.5 to 6.0 mm in diameter.

- Corundum: blue sapphire
- Garnet: pyrope-almandine
- Quartz: rock crystal (colorless, yellow with foil backing), amethyst

Detailed Description of Rose Cuts. The various rose cuts observed in the five objects studied are grouped and presented according to the form of the central facets (e.g., triangular, lozenge, kite) in combination with the number of central facets present. This reflects the symmetry of the dome's center (e.g., four-fold, six-fold, and eight-fold, or somewhat distorted four-fold, six-fold, and eight-fold). In addition, visually similar cuts were added to some of the main groups, even if the individual example did not belong to that particular main group in a strict sense. The author wants to underline that this is one of the alternatives to group the various cuts observed and present the results of the study. The accompanying line drawings are schematic representations and should help to understand the cuts shown in the different photos.

Non-Symmetrical Cuts (Group 1). While the great majority of the colored stone rose cuts displayed highly symmetrical fashioning, a few stones had no symmetrical pattern. These outliers consisted of one garnet and several rubies—the only faceted rubies without a table, approximately 5.5 to 6.0 mm in diameter—that showed facets of different sizes and no symmetrical surface pattern (again, see figure 15). Rather, the appearance was consistent with an irregularly shaped pebble that had simply been covered with random facets. It has already been mentioned that, different from all the other gemstones, the rubies with tables also did not show completely symmetrical cuts but, in some examples, only some irregular facets inclined to the table. Furthermore, some rubies were irregularly shaped pebbles with polished surfaces. These results indicate that only small rough rubies were available in the second half of the seventeenth century and that cutters tried to keep the rough as large as possible.

Domes Topped with Six Triangular Faces: Half-Dutch and Full-Dutch Roses (Group 2). A small subset of the garnets was cut as half-Dutch roses (figure 17, A and B), while a large number took the form of full-Dutch roses (figure 17, C and D). The samples were characterized by six-fold symmetry with a dome centered on six triangular faces. Round or near-round to slightly oval shapes were widespread (figure 17, A and C), but examples of elongated ovals through stretching of the triangles in certain directions were also common (figure 17, B and D).

Expanded Dutch Roses (Group 3). Larger samples often expanded on the standard Dutch rose forms with additional rings or rows of triangular facets. Round or near-round samples resulted from retaining six triangular facets at the center of the dome but increasing the number of circumscribing rings of triangles (figure 18A). More oval-shaped forms were derived if the number of triangular facets differed in two perpendicular directions (figure 18B). Yet another variation to produce larger oval stones featured the addition of trapezoidal faces between the center and girdle (figure 18C).

Figure 16. Drill holes were seen in a small number of stones, as here in a 12 × 10 mm blue sapphire (left), indicating prior use in other jewelry items. Also present on occasion were polished surface indentations, here demonstrated in a 19 × 17 mm garnet (right), reflecting a technique used since the middle ages to remove impurities. Photos by K. Schmetzer.

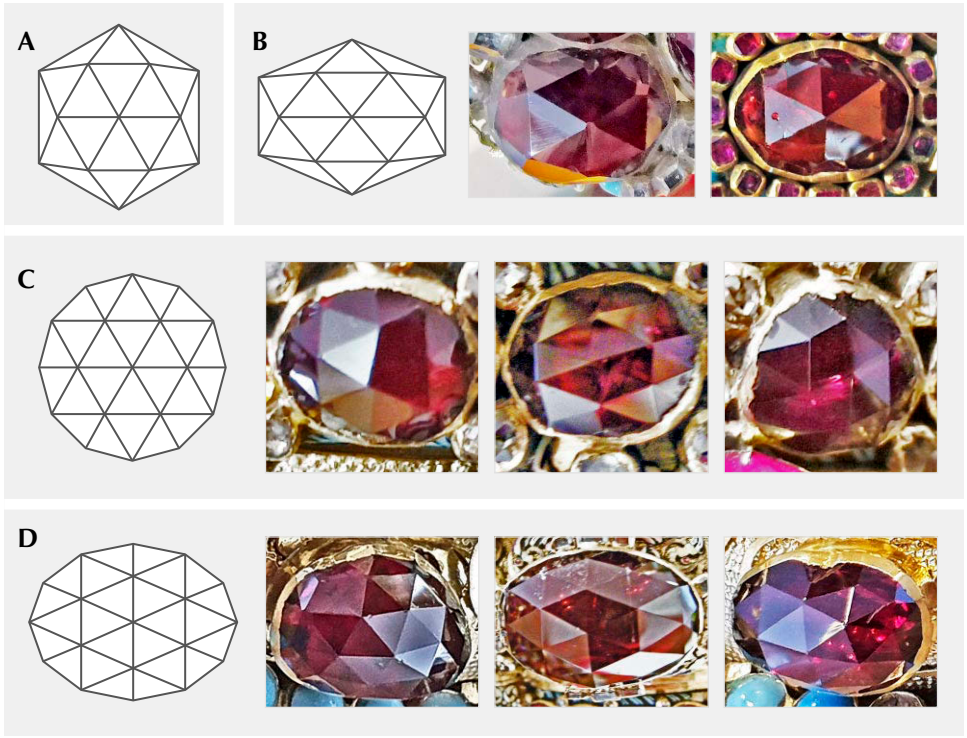

Figure 17. Group 2 garnets with half-Dutch (A, B) and full-Dutch rose cuts (C, D) from the Limburg and Cologne insignia displayed outlines approximating round, almost round to slightly oval (A, C) or oval (B, D). B: Both 15 × 11 mm. C (left to right): 8 × 7 mm, 8 × 7 mm, and 7 × 7 mm. D (left to right): 20 × 16.5 mm, 30 × 21 mm, and 9 × 7 mm. Drawings and photos by K. Schmetzer.

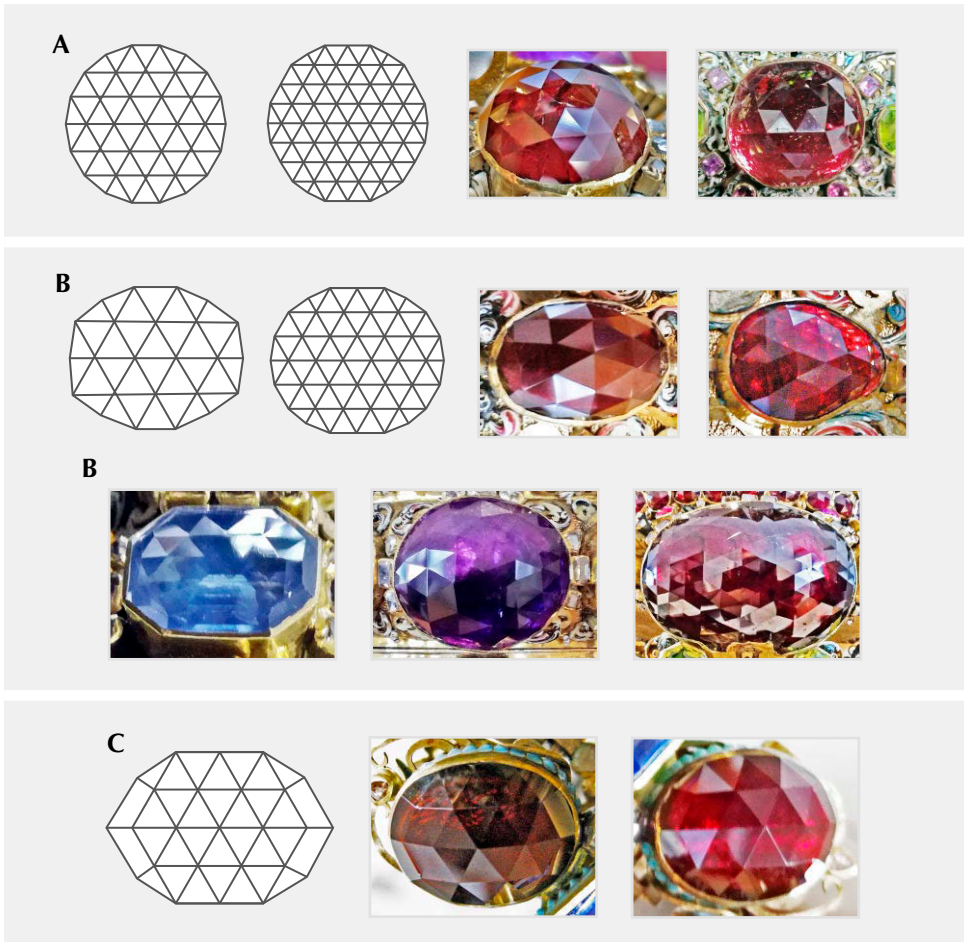

Figure 18. Larger garnet, quartz, and sapphire samples from group 3 exhibited expanded Dutch rose forms with additional rings or rows of triangular facets. Round outlines resulted from simply increasing the number of circumscribing rings (A). More oval stones derived from the addition of different numbers of facets in perpendicular directions in the horizontal and vertical rows of facets running through the center (B) or the addition of trapezoidal facets at two ends of the samples (C). A: 16.0 × 14.5 mm garnet (left) and 28 × 27 mm foil-backed quartz (right). B, upper row: 9 × 7 mm and 13 × 9 mm garnets. B, lower row: 12 × 8 mm sapphire (left), 34 × 29 mm amethyst (center), and 56 × 38 mm garnet (right). C: Two garnets, each measuring 18 × 15 mm. Drawings and photos by K. Schmetzer.

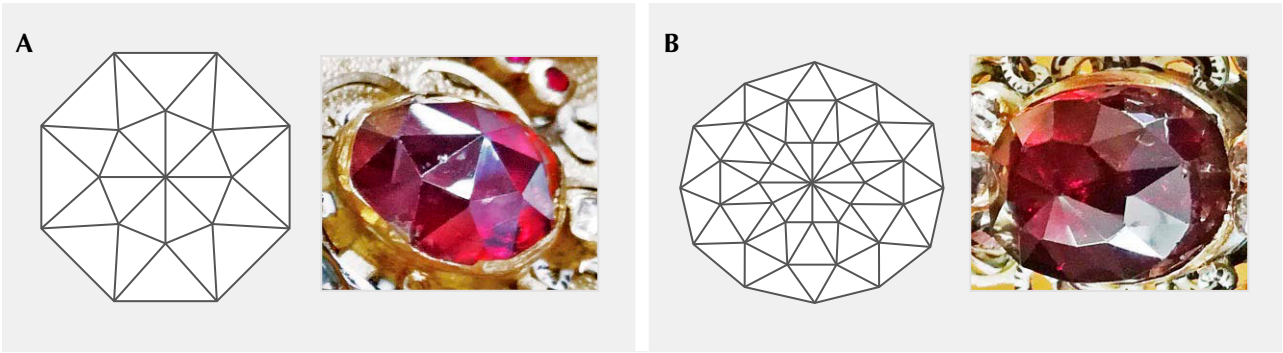

Figure 19. Group 4 consisted of a small number of samples presenting domes topped by either eight (A) or 12 (B) identical triangles. Additional triangles extended toward the girdles. A: 13 × 11 mm garnet. B: 13.0 × 11.5 mm garnet. Drawings and photos by K. Schmetzer.

Domes Topped with Eight or 12 Triangles (Group 4). A few samples incorporated a pattern where the domes centered on eight or 12 triangles and where the consequent overall symmetry was either eight-fold (figure 19A) or six-fold (figure 19B), respectively.

Domes Topped with Four Triangles Meeting at Right Angles (Group 5). Certain gems featured four triangular facets meeting at right angles in the center and grouped into a square or rhombus. That pattern could be repeated several times to produce a nearly circular (figure 20A) or octagonal (figure 20B) outline, among others. Step-cut facets might also be added along the girdle, resulting in a range of octagonal shapes, depending on the arrangement and number of faces (figure 20, C and D). A sample with an analogous cut shifted the pattern to place two triangles at the center (figure 20E).

Domes Topped with Four or Eight Triangles Not Meeting at Right Angles (Group 6). The domes of

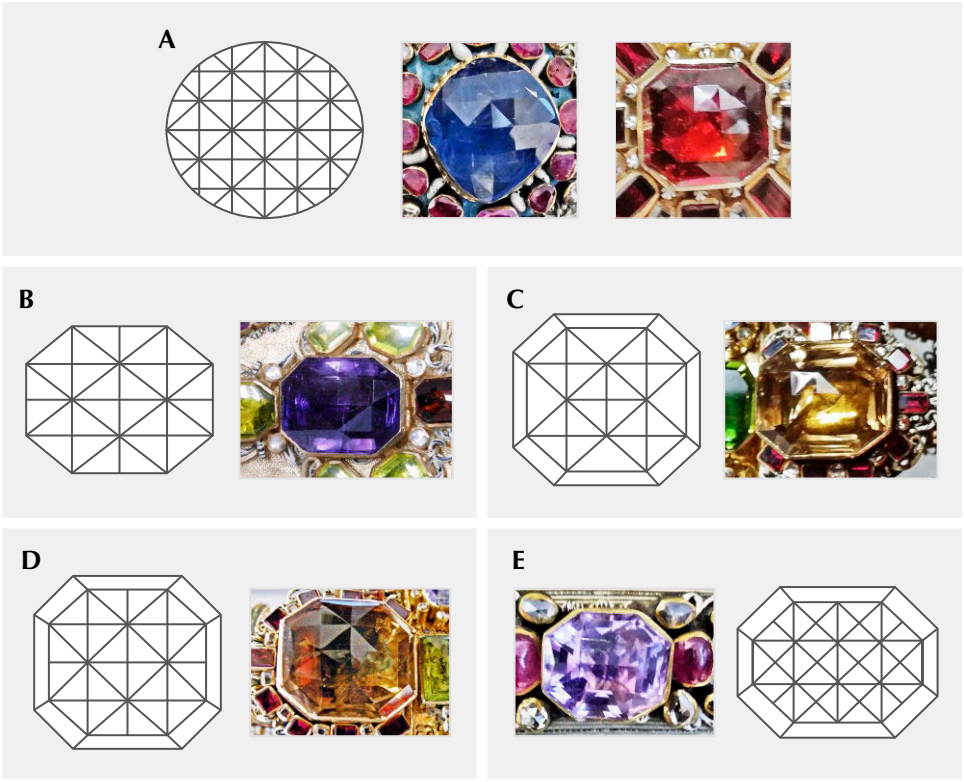

Figure 20. In group 5, the domes centered on four triangular facets meeting at right angles. The pattern then generally repeated outwards (A, B) and could also be augmented by the addition of step-cut facets close to the girdle (C, D). An analogous sample shifted the pattern so that just two triangles met at the central point (E). A: 28 × 25 mm sapphire (left) and 19 × 19 mm garnet (right). B: 23 × 18 mm amethyst. C: 30 × 25 mm foil-backed quartz. D: 28 × 25 mm foil-backed quartz (left) and 12 × 10 mm amethyst (right). Drawings and photos by K. Schmetzer.

some samples were topped with four or eight triangular facets not meeting at right angles and grouped into a rectangle or rhombus. The simpler form used four triangles (figure 21A), while the splitting of each of those four triangles led to eight triangles (figure 21, B–E). Beyond the central rectangle or rhombus, the outer patterns varied widely, with some relying entirely on different arrangements of triangles (figure 21, B–D) and others combining triangles, trapezoids, and a step-cut facet close to the girdle (figure 21A). An example of a rather complex pattern is seen in figure 21E. A sample with a similar cut showed only two triangles meeting at the center (figure 21F). This cut could also be assigned to group 13 (domes cut with mirror symmetry).

Domes Topped with Three or Four Rhombuses or Kites (Group 7). Some gemstones exhibited a dome topped by three (figure 22A) or four (figure 22B) identical rhombuses. Between those rhombuses and the girdle, a range of different trapezoidal, triangular, or quadrilateral facets could be used. The outer perimeter might also incorporate four or eight additional step-cut facets to form a rectangular (figure 22C) or octagonal (figure 22D) outline. A related variation used four kites in the center (figure 22, E and F), as opposed to rhombuses.

Domes Topped with Six Rhombuses or Kites in Three Different Orientations (Group 8). In another group of samples, the central pattern consisted of six rhombuses or kites forming a six-rayed star (figure 23A). That pattern could be expanded outward through repetition of rhombuses oriented in three directions (figure 23B). Together with triangular or quadrilateral facets on the perimeter, oval or almost rectangular gemstones could result (figure 23, C and D). Hexagonal outlines were created when step-cut facets abutted the girdle (figure 23, E and F).

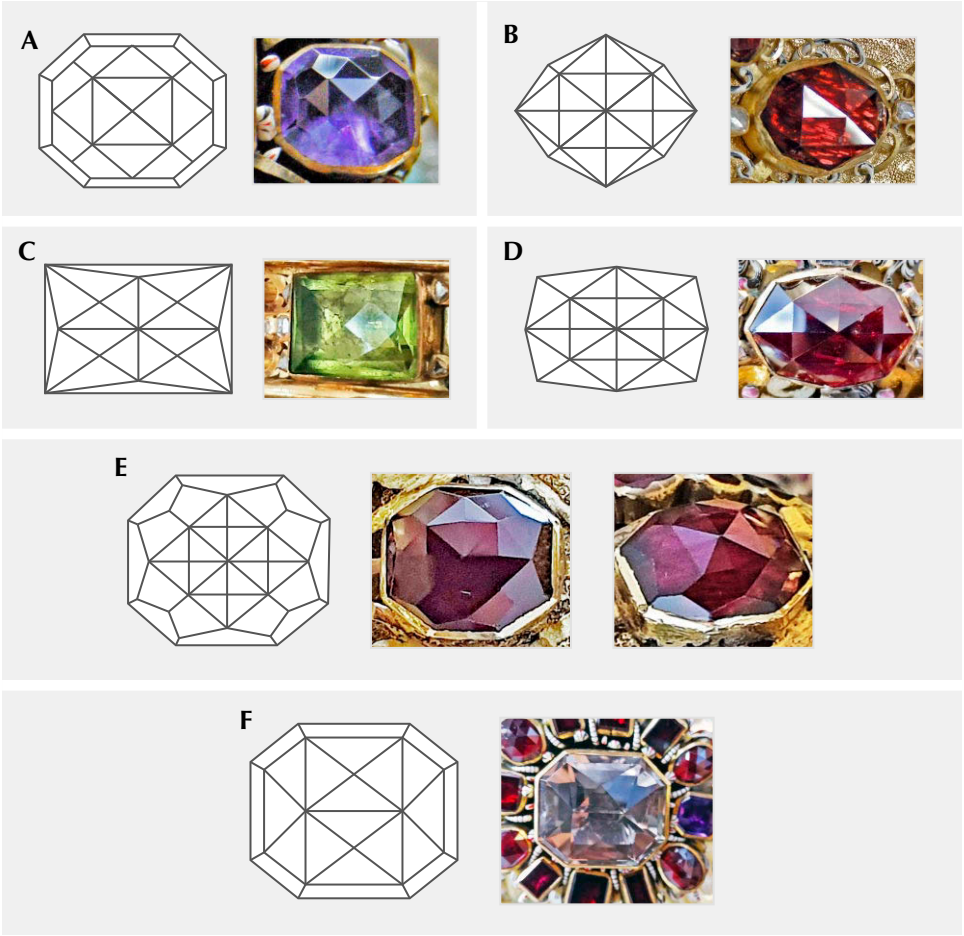

Figure 21. Group 6 stones featured at the apex of their domes, either four (A) or eight (B–E) triangular facets not meeting at right angles. Surrounding those facets were further triangles (B–D) or triangles plus trapezoids (A), and the pattern could become rather complex (E). A variation with a similar appearance had been cut such that only two triangles topped the dome (F). A: 8 × 8 mm amethyst. B: 19 × 14 mm garnet. C: 16 × 11 mm peridot. D: 19 × 14 mm garnet. E: Two garnets, each measuring 11 × 8 mm. F: 19 × 17 mm quartz. Drawings and photos by K. Schmetzer.

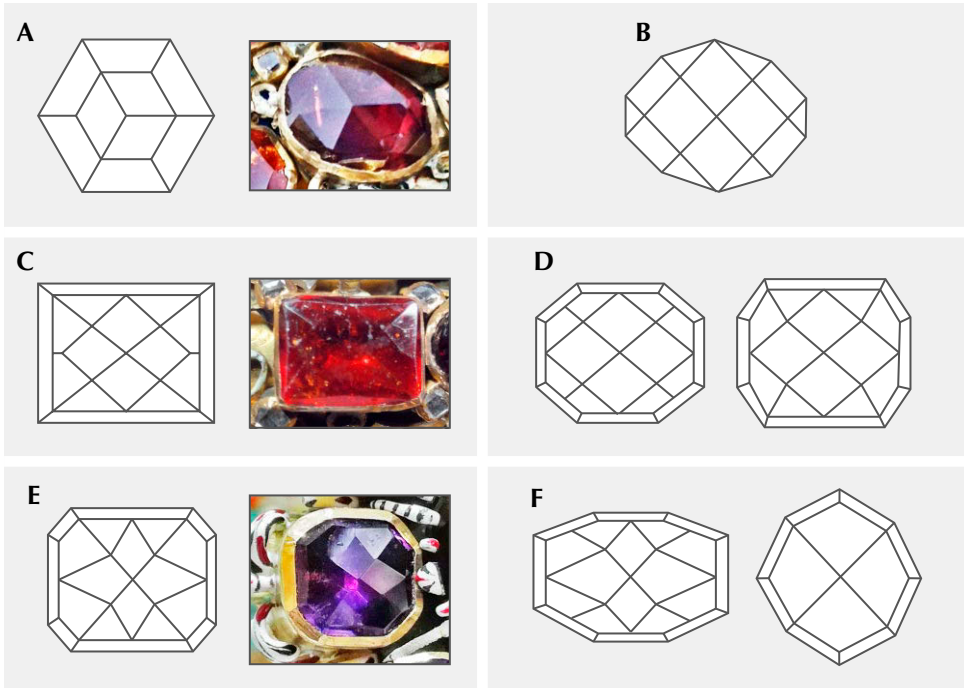

Figure 22. Samples in group 7 displayed domes topped by three or four rhombuses (A–D) or kites (E, F). A: 10 × 9 mm garnet. C: 11 × 8 mm garnet. E: 7 × 6 mm amethyst. Drawings and photos by K. Schmetzer.

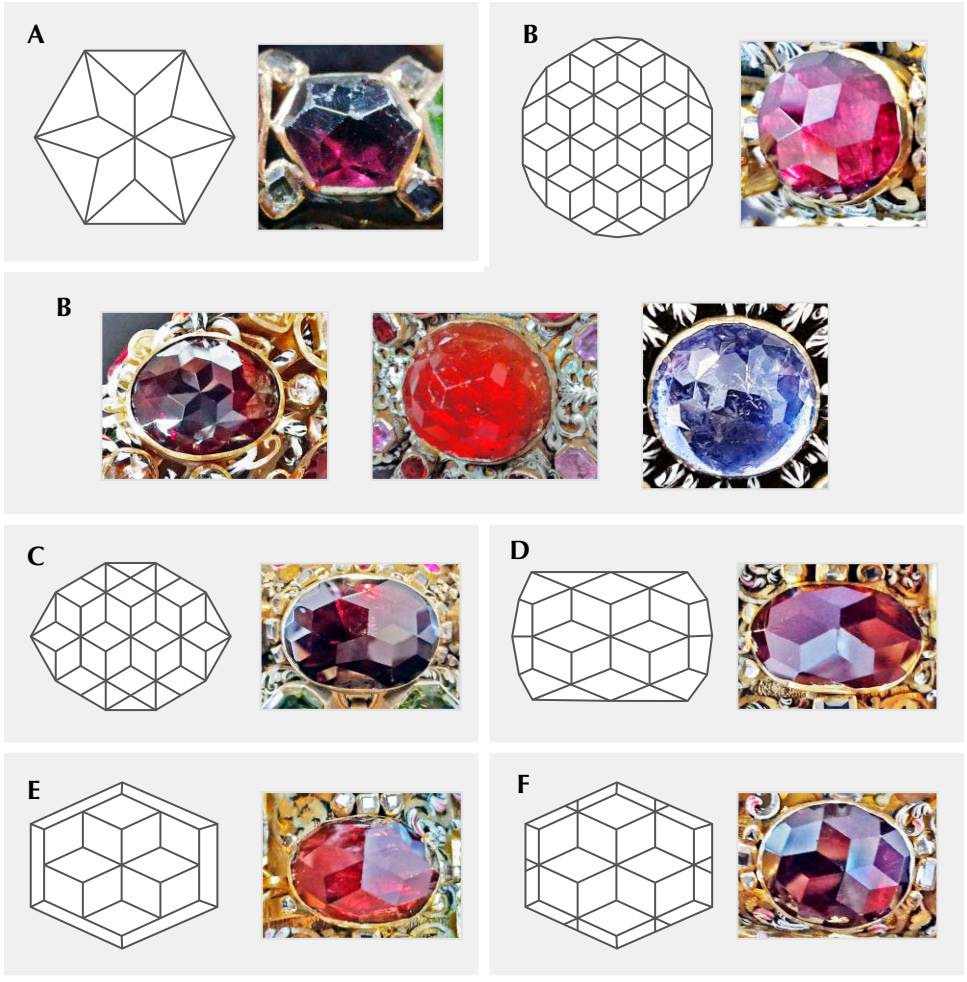

Figure 23. In group 8, a pattern of six rhombuses or kites in three orientations resulted in gemstones centered on a six-rayed star (A, B). The addition of other facet shapes as the design radiated could lead to oval or almost rectangular outlines (C, D), while augmentation with step-cut facets abutting the girdle produced hexagonal outlines (E, F). A: 7 × 7 mm garnet. B, upper row: 8 × 7 mm garnet. B, lower row: 28 × 22 mm garnet (left), 21 × 19 mm foil-backed quartz (center), and 12 × 12 mm sapphire (right). C: 28 × 22 mm garnet. D: 22.0 × 13.5 mm garnet. E: 20 × 15 mm garnet. F: 20 × 17 mm garnet. Drawings and photos by K. Schmetzer.

Domes Topped with Six Rhombuses in Three Different Orientations, Some or All Further Split (Group 9). More complex patterns could also be derived from the basic concept of domes topped by six rhombuses through the splitting of some or all of such facets into two components. In some samples, the rhombuses oriented in just one direction were split (figure 24, A and B). In others, the splitting occurred in all three possible directions (figure 24, C–E). A similar concept and appearance could be derived by splitting the triangles of expanded Dutch roses (figure 24F), particularly in round or oval samples (figure 24, G and H).

Domes Topped with Eight Rhombuses or Parallelograms (Group 10). Another group of stones comprised domes topped by eight rhombuses or parallelograms (figure 25, A and B), for an appearance resembling the so-called cross roses described by Schrauf (1869). Between the dome top and girdle, additional step-cut facets were frequently included (figure 25, C–E). The outline shapes were octagonal (figure 25, A–D) or rectangular (figure 25E), with varying ratios of length to width. A comparable but more complex pattern with an additional ring of triangular facets is shown in figure 25F.

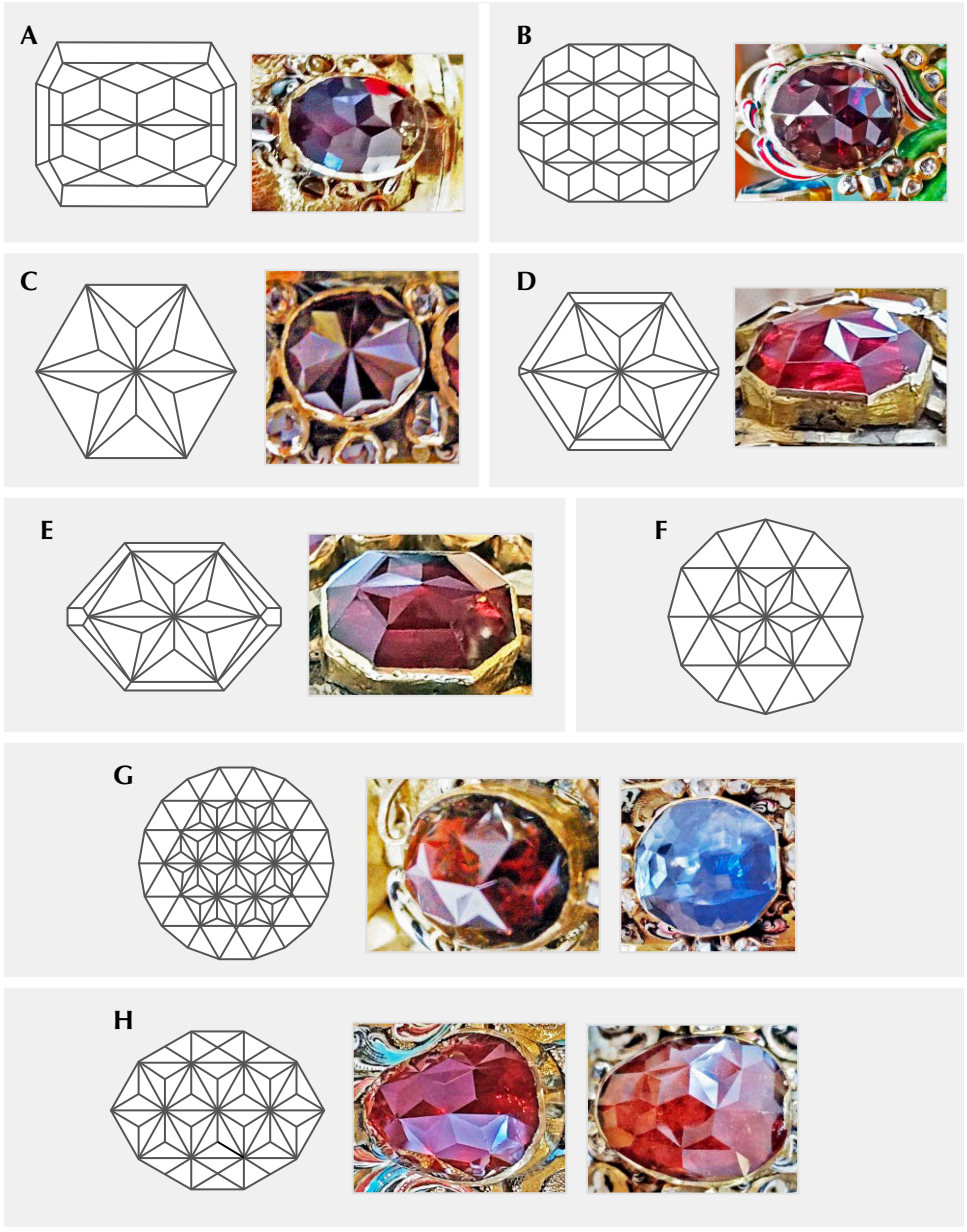

Figure 24. In group 9, the central rhombuses otherwise forming a six-rayed star could be split, i.e., subdivided into two components, along one direction (A, B) or along three directions (C–E). A similar principle could be applied to splitting the triangles in gemstones with expanded Dutch rose cuts (F–H). A: 13 × 10 mm garnet. B: 16 × 14 mm garnet. C: 7 × 7 mm garnet. D: 10 × 8 mm garnet. E: 11 × 8 mm garnet. G: 9 × 8 mm garnet (left) and 23 × 22 mm sapphire (right). H: two garnets, each measuring 13 × 9 mm. Drawings and photos by K. Schmetzer.

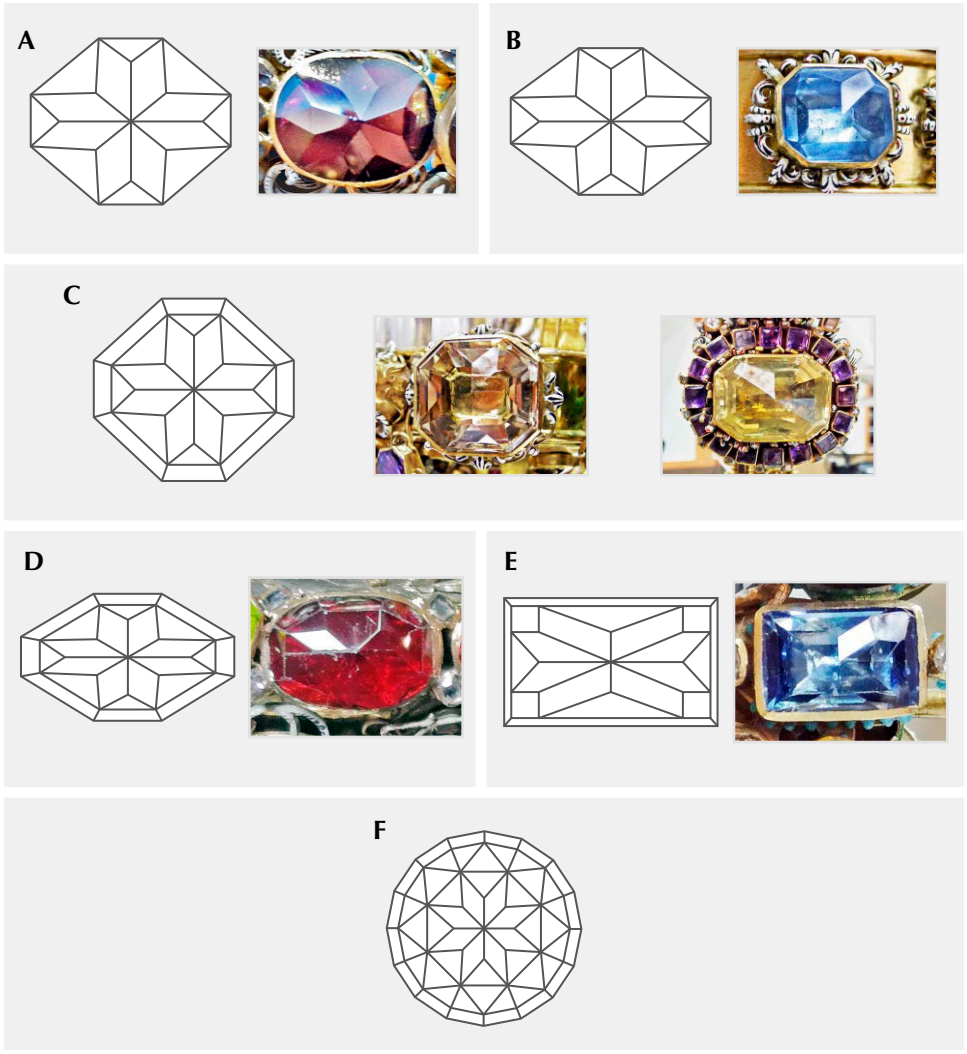

Figure 25. Domes topped by eight rhombuses or parallelograms reflected the signature feature of the so-called cross roses in group 10. Extending toward the girdle were additional triangular (A, B) or triangular plus step-cut facets (C–E). The potential complexity is illustrated by the sapphire drawn in F with a dome topped by eight kites. A: 16 × 12 mm garnet. B: 15 × 13 mm sapphire. C: Foil-backed quartz measuring 22 × 20 mm (left) and 28 × 20 mm (right). D: 12 × 9 mm garnet. E: 12 × 7 mm sapphire. Drawings and photos by K. Schmetzer.

Domes Topped with Rhombuses in Parallel Orientation (Group 11). Some stones were topped by a repeating pattern of numerous rhombuses in parallel orientation, terminating in triangular facets at the

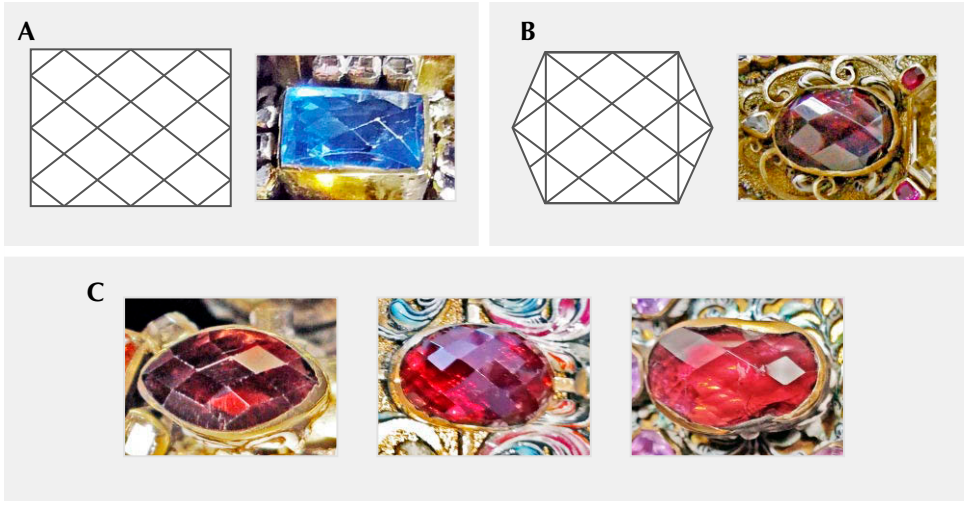

Figure 26. Repeating patterns of rhombuses in parallel orientation top the domes of group 11 gemstones with rectangular (A), hexagonal (B), or navette to oval (C) forms. A: 13 × 10 mm sapphire. B: 16 × 10 mm garnet. C: Garnets measuring 10.0 × 4.5 mm (left), 23 × 18 mm (center), and 13 × 8 mm (right). Drawings and photos by K. Schmetzer.

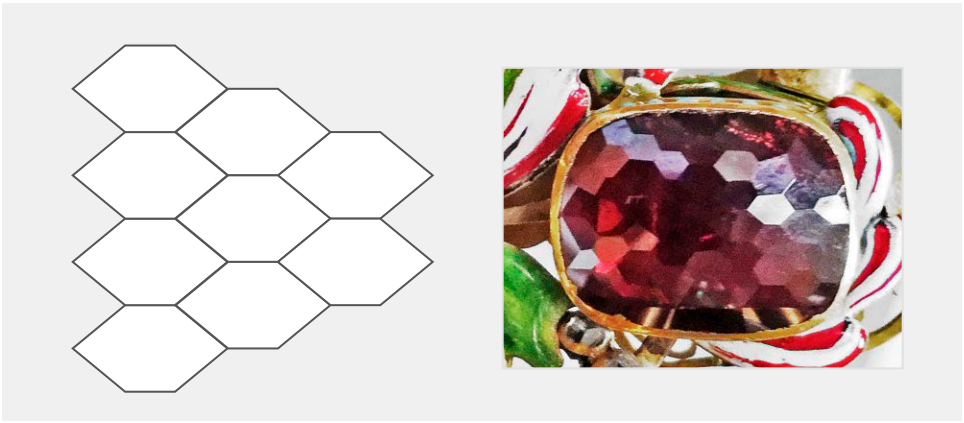

Figure 27. The one garnet in group 12, measuring 16 × 12 mm, was cut with small hexagonal facets covering the surface. Drawing and photo by K. Schmetzer.

girdles. The style led to rectangular (figure 26A), hexagonal (figure 26B), or marquise to oval forms (figure 26C).

Dome Topped with Small Hexagons (Group 12). One garnet was cut with numerous small hexagons covering the surface. These hexagons were slightly distorted, with small variances in size (figure 27).

Domes Cut with Mirror Symmetry (Group 13). The most complex cuts were observed in several samples with solely mirror symmetry. Some gems showed faceting arrangements with two perpendicular mirror planes (figure 28, A–D), while others displayed only one mirror plane (figure 28, E–G).

DISCUSSION AND CONCLUSIONS

The insignia and regalia from Limburg and Cologne exhibited a wide variety in the arrangement and design of the gemstone embellishment. Stones with the same cutting style (e.g., table, rose, or cabochon) were frequently grouped together to create attractive pat-

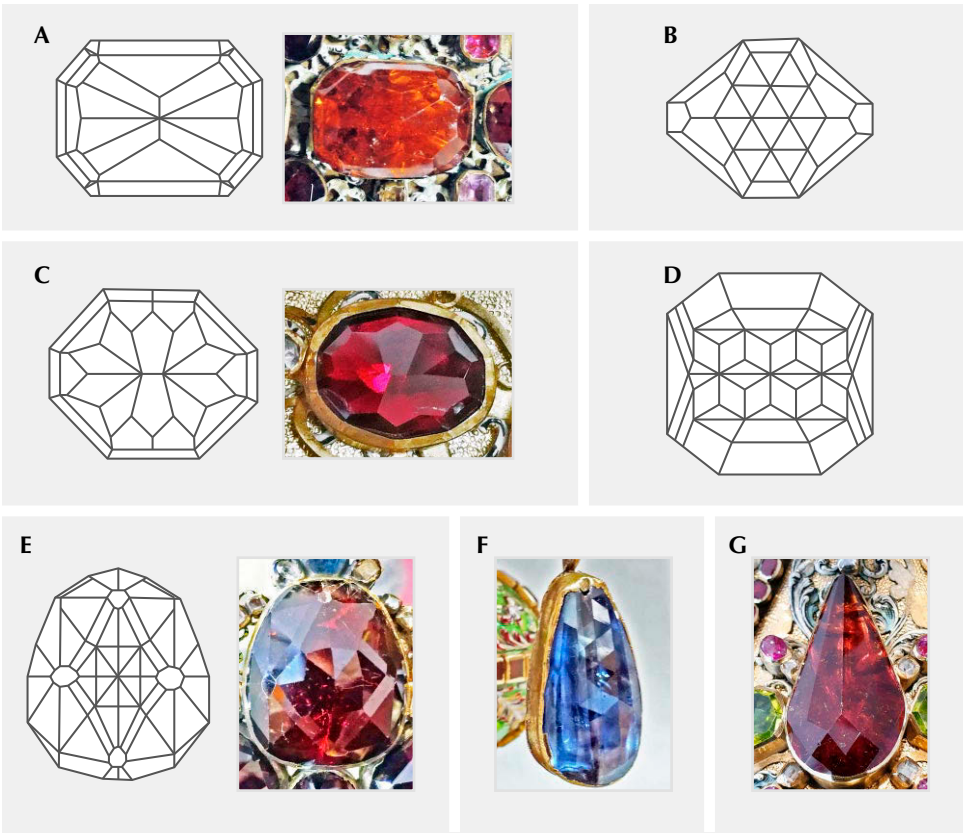

Figure 28. The small number of samples in group 13, including garnets and sapphires, offered the most complex cuts observed. They were characterized solely by mirror symmetry either along two perpendicular mirror planes (A–D) or along one mirror plane forming the longitudinal axis of the stones (E–G). A: 19 × 14 mm garnet. C: 13 × 10 mm garnet. E: 27 × 22 mm garnet. F: 26 × 14 mm sapphire. G: 35.0 × 12.5 mm garnet. Drawings and photos by K. Schmetzer.

terns, but groupings that mixed cutting styles were also common (figures 14, 29, and 30). While detailed description of the decorative arrangement is beyond the scope of this study, the cuts of the constituent gemstones offer notable insights about the practices of the time. Among the colored stones there were multiple table cuts, but the vast majority were similar step cuts with one or two rows of facets inclined to the table. In contrast, when surveying the rose cuts, defined for these purposes as gems without any central flat facet of substantial size, the range of creativity is striking.

The exacting nature of the cuts of colored stones in all sizes reveals the skill of the craftsmen in the second half of the seventeenth century (see the various examples in figures 17–28). The high symmetry and precise finish of the cuts, as observed in almost all samples of rose-cut gemstones studied in Limburg and Cologne, demonstrate what was considered beautiful according to the fashion of the Baroque era. Unfortunately, the historical record indicates that with the decline in popularity of rose-cut diamonds, the wide variety of colored stone rose cuts was lost as well, and only a small subset of standard cuts survived over the following centuries.

The most populous groups of colored stone rose cuts were groups 2 and 3, namely half-Dutch and full-Dutch roses and expanded Dutch roses. While other groups showed variations on the overarching theme, they tended to comprise a smaller number of examples with each cut, normally not exceeding five, with many variations only represented by three, two, or even a single gemstone. This indicates that these more complex cuts were less often produced, but it does not imply that a particularly extraordinary cut should be deemed unique. To cite a case in point, a cut with a dome topped by 10 (4 + 4 + 2) facets, as seen in figure 28C, was found in three garnet samples, evidencing an established rule or design.

If the rose cuts observed for colored stones are compared with those historically used for diamonds (see, e.g., Tillander, 1995), the half-Dutch and full-Dutch roses of group 2 readily find equivalents. Likewise having analogues in diamond jewelry of the Baroque era are the cuts summarized in group 5 (domes topped with four triangles meeting at right angles; figure 20) and group 11 (rhombuses in parallel orientation; figure 26). From other groups, certain variations are also known in diamonds, such as sample C of group 9 (dome topped with six split rhom-

Figure 29. The decorative groupings that embellished the regalia and liturgical insignia frequently mixed cutting styles. The examples here show rose-cut garnets surrounding a 12.0 × 11.5 mm step-cut garnet with a large table facet in the miter from Limburg (left) and a 19 × 17 mm rose-cut quartz surrounded by amethysts with varied forms and cuts in the monstrance from Cologne (right). Photos by K. Schmetzer.

Figure 30. The same overall pattern of gemstones—in this example consisting of five garnets, grouped together in one section of the foot of the Cologne monstrance—is prepared with samples showing a great variability in cutting style. The white arrow points to a garnet measuring 13 × 10 mm. Photos by K. Schmetzer.

buses three different orientations; figure 24) or sample A of group 4 (dome topped with eight triangles; figure 19). Conversely, other more complex cuts have no recognized parallel to date in diamonds. A logical explanation could be that such large pieces of rough material as found in quartz or garnet simply did not exist for diamonds, or at least was available in only a few extremely rare pieces.

ABOUT THE AUTHOR

Dr. Schmetzer is an independent researcher residing in Petershausen, near Munich, Germany.

ACKNOWLEDGMENTS

The author is grateful to the Catholic dioceses of Limburg and Cologne and the directors of the Limburg and Cologne museums, Dr. M. T. Kloft and Dr. L. Becks, for the opportunity to examine the regalia and insignia from the respective treasuries.

Appreciation is also expressed for assistance in practical work to the members of the museum's team in Limburg (M. Benecke, D. Müller, H. Müller, M. Scheidler, O. Teufer, and M. Vollmar) and to C. Baumsteiger in Cologne. Details concerning the restoration of the Cologne monstrance and the gemstones used were helpfully provided by goldsmith P. Bolg from Cologne and gemstone merchant A. Wintermantel and the company's present director, his son B. Wintermantel, from Waldkirch near Freiburg.

REFERENCES

Beitz E. (1928) Die Goldschmiede Christian Schweling zu Köln. *Wallraf-Richartz-Jahrbuch*, Vol. 5, pp. 95–100.

Beitz E. (1930) Christian Schweling der Aeltere, der Meister der Dommonstranz von 1658. In Kuphal, E. Ed., *Der Dom zu Köln. Festschrift zur Feier der 50. Wiederkehr des Tages seiner Vollendung am 15. Oktober 1880*. Verlag des kölnischen Geschichtsvereins e.V., Cologne, pp. 177–183.

Bolg P., Zieleskiewicz P. (1995) Der Domschatzraub 1975. Restaurierungs- und Wiederherstellungsbericht. *Kölner Domblatt*, Vol. 60, pp. 269–290.

Clasen C.-W. (1983) Die Wiederherstellung der Kölner Dommonstranz mit Hilfe der Photogrammetrie. *Jahrbuch der Rheinischen Denkmalpflege*, Vol. 29, pp. 123–134.

Clasen C.-W. (1989) Die goldene Dommonstranz von 1657/58. Ihr Schicksal und ihr Meister Christian Schweling. *Kölner Domblatt*, Vol. 54, pp. 123–158.

Clasen C.-W. (1993) *Peter Boy: Ein rheinischer Goldschmied und Emailmaler der Barockzeit und der Schatzfund von Perscheid*. Rhein-Merzbach, CMZ-Verlag, pp. 43–50.

De Bie A. (2014) The paradox of the Antwerp rose: Symbol of decline of token of craftsmanship? In K. Davids and B. De Munck, Eds., *Innovation and Creativity in Late Medieval and Early Modern European Cities*. Ashgate Publishing Company, Farnham, UK, pp. 269–293.

Eppler A., Eppler W. Fr. (1934) *Edelsteine und Schmucksteine*. Wilhelm Diebener G.m.b.H, Leipzig, 554 pp.

Falk F. (1975) *Edelsteinschliff und Fassungsformen im späten Mittelalter und im 16. Jahrhundert*. Verlag Wilhelm Kempter KG, Ulm, Germany, 150 pp.

Forsyth H. (2013) *The Cheapside Hoard: London's Lost Jewels*. Museum of London, London, 248 pp.

Gans M.H. (1961) *Juwelen en mensen*. J.H. de Bussy, Amsterdam, pp. 79–160.

Gilbertson A. (2007*) American Cut – The First 100 Years: The Evolution of the American Cut Diamond*. Gemological Institute of America, Carlsbad, California, 214 pp.

Kaiser M.J. (2003) Das Edelsteingewerbe in Freiburg und Waldkirch im Spiegel archäologischer und historischer Quellen. *Fundberichte aus Baden-Württemberg*, Vol. 27, pp. 1045–1172.

Klein G. (2005) *Faceting History: Cutting Diamonds & Colored Stones*. Published by the author, 242 pp.

Kloft M.T. (2016) *Dom und Domschatz in Limburg an der Lahn*. Karl Robert Langewiesche Nachfolger Hans Köster Verlagsbuchhandlung, Königstein im Taunus, 123 pp.

Kockelbergh I., Vleeschdrager E., Walgrave J. (1992) *The Brilliant Story of Antwerp Diamonds*. MIM n.v., Antwerp, 303 pp.

Kuhn H.W. (1976) Zur Geschichte des Trierer und Limburger Domschatzes. *Archiv für mittelrheinische Kirchengeschichte*, Vol. 28, pp. 155–207.

Kuhn H.W. (1989) Peter Boy. Goldarbeiter und Emailmaler des Barock. *Jahrbuch für westdeutsche Landesgeschichte*, Vol. 15, pp. 117–157.

Kuhn H. (1999) Der Frankfurter Goldarbeiter und Emailmaler Peter Boy (um 1650-1727) und seine Arbeiten für den Kurfürsten von Trier zu Ehrenbreitstein – Spurensuche nach einem vergessenen Meister. *Jahrbuch für westdeutsche Landesgeschichte*, Vol. 25, pp. 305–361.

Lenzen G. (1966) *Produktions- und Handelsgeschichte des Diamanten*. Duncker & Humblot, Berlin, 280 pp.

Long R., Steele N. (1979-1989) *Facet Design*. P/M Marketing, Seattle Faceting Books, Seattle, Washington. 7 Volumes.

Luthmer F. (1907) *Die Bau- und Kunstdenkmäler des Lahngebiets*. Kommissionsverlag von Heinrich Keller, Frankfurt, pp. 103–115.

Michel F. (1925) Der Silber- und Juwelenschatz der Trierer Erzbischöfe der Barockzeit. *Trierischer Volksfreund*, Gewerbeschau 1925, Vierte Sondernummer zur Rhein. Tausendjahrfeier, pp. 2–8.

Mösch M.T. (1995) Der Kölner Domschatzraub 1975. Zwanzig Jahre danach. *Kölner Domblat*t, Vol. 60, pp. 245–268.

The Munich Show (2017) Pressemitteilung (press release), https://munichshow.com/uploads/media/PRESSEMITTEILUNG_MunichShow2017.pdf

Ogden J. (2013) Gems and the gem trade in India. In A. Jaffer, Ed., *Beyond Extravagance: A Royal Collection of Gems and Jewels*. Assouline, New York, pp. 346–377.

Ogden J. (2014) Mughal gems in context. *InColor*, No. 26, pp. 36–47.

Ogden J. (2018) *Diamonds: An Early History of the King of Gems*. Yale University Press, New Haven, Connecticut, 388 pp.

Prim J.K. (2018) The rise of gem cutting and the occult in Renaissance Europe. https://medium.com/justin-k-prim/the-rise-of-gem-cutting-and-the-occult-in-renaissance-europe-f3535b78599b

Prim J.K. (2019) Fashioning fire from pebbles. The history of gem cutting in the Czech Republic. https://medium.com/justin-k-prim/fashioning-fire-from-pebbles-66d937273b94

Scarisbrick D. (1993) 17th-century diamond jewellery and the ornamental print. In A. Kinsbergen et al., Eds., *A Sparkling Age: 17th-Century Diamond Jewellery*. The Executive Board of the Province Council of Antwerp, Antwerp, pp. 23–36.

Schmetzer K., Gilg H.A. (2020) The late 14th-century royal crown of Blanche of Lancaster – history and gem materials. *Journal of Gemmology*, Vol. 37, No. 1, pp. 26–64.

Schrauf A. (1869) *Handbuch der Edelsteinkunde*. Carl Gerod's Sohn, Vienna, 252 pp.

Stranner H. (1953) *Edelsteine und Metalle in der Bijouterie*. Rascher Verlag, Zurich, 87 pp.

Tillander H. (1995) *Diamond Cuts in Historic Jewellery, 1381–1910*. Art Books International, London, 248 pp.

Trimborn H. (1940) Ein Beitrag zur österreichischen merkantilistischen Gewerbepolitik am beispiel der Bruderschaft der Borer und Balierer zu Freiburg und Waldkirch. Dissertation, Freiburg University, 80 pp.

Walgrave J. (1993a) Tendencies in 17th-century jewellery. In A. Kinsbergen et al., Eds., *A Sparkling Age: 17th-Century Diamond Jewellery*. The Executive Board of the Province Council of Antwerp, Antwerp, pp. 13–22.

Walgrave J. (1993b) Diamond cuts in the 17th century jewellery. In A. Kinsbergen et al., Eds., *A Sparkling Age: 17th-Century Diamond Jewellery*. The Executive Board of the Province Council of Antwerp, Antwerp, pp. 37–53.

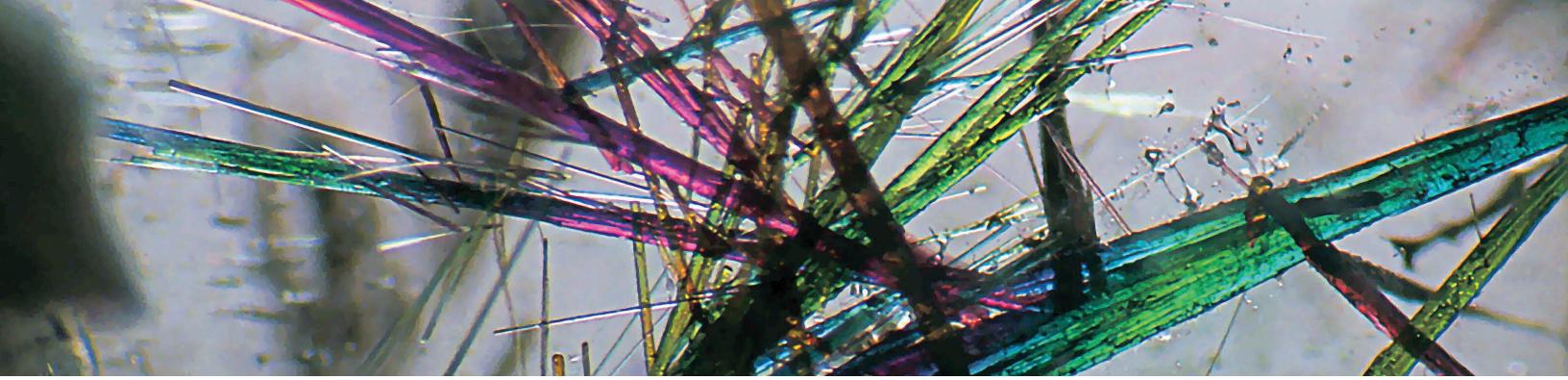

GIA®

Liddicoat Postdoctoral Research Fellowships in Mineralogy, Materials Science and Gemology at GIA

GIA (Gemological Institute of America®) invites qualified candidates to apply for the Richard T. Liddicoat Postdoctoral Research Fellowships at its Carlsbad, California and New York City locations. The one- to two-year fellowships encourage early career scientists to pursue full-time academic research in mineralogy, geology, physics, materials science and other fields related to gemology – the study of diamonds, colored gemstones, pearls and their treatment. Fellows are expected to conduct creative, independent, publishable research and collaborate with GIA scientists, outside research institutions and universities.

The fellowship includes a competitive annual stipend ($67,000+), research funding and approved travel subsidies. Benefits include health, dental and vision, and potential reimbursement of relocation expenses.

All applications will be reviewed after the deadline date and candidate selection will take place by end of September 2021. Applicants must have received their Ph.D. in a relevant field by the start date, and preferably within the last three years.

Applications are due by July 31, 2021. For more information visit **GIA.edu/research-careers**

About GIA

Established in 1931, GIA is the world's foremost authority on diamonds, colored stones and pearls. A public benefit, nonprofit institute, GIA is the leading source of knowledge, standards and education in gems and jewelry. For more information visit **GIA.edu**

An Equal Opportunity Employer

All employment decisions are made without regard to unlawful considerations of race, sex, religion, national origin, age, disability or any other legally protected status. Reasonable accommodations are available upon request.

Fluorescence Characteristics of Blue Amber from the Dominican Republic, Mexico, and Myanmar

Zhiqing Zhang, Xinran Jiang, Yamei Wang, Fanli Kong, and Andy H. Shen

Amber shows various luminescence phenomena under UV illumination. Amber with very strong blue fluorescence under sunlight or D65 illumination can appear blue to the unaided eye when placed on a black background. Amber showing this effect is highly sought after in the Chinese gem market and referred to as "blue amber." Almost all commercial blue amber is mined from the Dominican Republic, Mexico, and Myanmar. In this study, we collected and characterized the appearance, gemological properties, UV-visible light absorption spectra, and 3D fluorescence spectra of blue amber from these three producing areas. The results show that blue amber from the Dominican Republic generally emits much stronger fluorescence than the other two origins, with narrow triple-peak emissions near 450, 474, and 508 nm. Mexican and Burmese excitation-emission maps present several distinct emission and excitation wavelengths. Additionally, distinctive UV/visible/near-infrared absorptions at 412 and 441 nm appeared only in blue amber from the Dominican Republic. The combination of appearance, UV-Vis-NIR spectroscopy, and excitation-emission mapping may assist in the separation of blue amber from these three localities.

Amber is widely distributed around the world. It is of interest not merely as an important natural fossil resin witnessing the history of the earth and providing direct evidence for paleobiologists, but also as a widely loved organic gemstone. Transparent yellow amber from the Dominican Republic, Mexico, and Myanmar displaying a blue or greenish blue glow when viewed on a black background in normal sunlight is called "blue amber" in the Chinese gem trade. This paper focuses on amber displaying this characteristic and will refer to this material as blue amber. In the Guangzhou and Shenzhen amber trading centers, Dominican blue amber can be sold for up to thousands of Chinese RMB (around several hundred U.S. dollars) per gram, while Mexican material fetches only several hundred RMB (around several tens of U.S. dollars) per gram—even though they have a similar appearance.

Bellani et al. (2005) first described blue amber and studied the fluorescence emission, excitation, and optical absorption spectra of Dominican blue and non-blue (including yellow and red varieties) amber. They found that multiple emission fluorescence peaks at 449 nm, 476 nm, and 505 nm occurred in this blue amber, while only a broad fluorescence band was observed in non-blue amber. They further proposed that perylene (a polycyclic aromatic hydrocarbon, $C_{20}H_{12}$) was the fluorophore for Dominican blue amber by comparing the emission spectra and

In Brief

- Amber that shows strong blue fluorescence under daylight is called "blue amber" in the Chinese gem market. These can be classified into blue and blue-green groups.
- The main production areas are the Dominican Republic, Myanmar, and Mexico.
- 3D fluorescence spectroscopy showed distinct features among these groups and localities.
- The combination of appearance, UV-Vis-NIR spectroscopy, and excitation-emission mapping may assist in the separation of blue amber from these three localities.

See end of article for About the Authors and Acknowledgments.
Gems & Gemology, Vol. 56, No. 4, pp. 484–496,
http://dx.doi.org/10.5741/GEMS.56.4.484

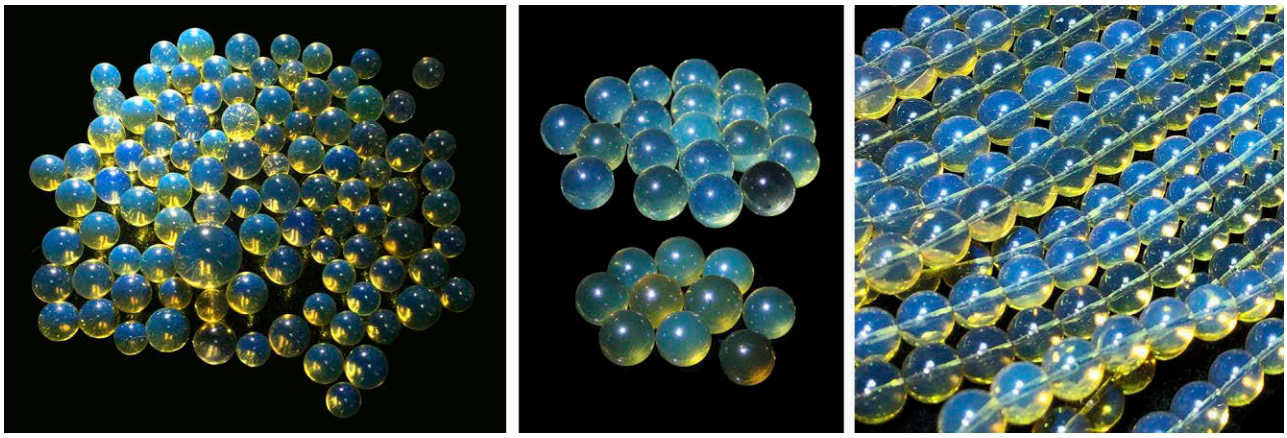

Figure 1. Commercial blue amber beads from the Dominican Republic (left, about 6–15 mm in diameter), Mexico (center, approximately 10 mm), and Myanmar (right, approximately 5 mm) have very similar appearances. The illumination source is a handheld D65 light. Photos by Y. Wang.

fluorescence lifetime with the fluorescence spectra documented in the handbook by Berlman (1971). Liu et al. (2014) found blue amber's fluorescence to be confined to the surface, and further illustrated that a black background could enhance the visibility of the fluorescence by reducing the amount of scattered light that reaches the eye. Chekryzhov et al. (2014) and Bechtel et al. (2016) discussed the luminescence properties and the hydrocarbon composition of blue amber from the Russian Far East, but they did not give a possible cause of the blue fluorescence. Recently, Jiang et al. (2017) analyzed the fluorescence emission wavelengths and optimal excitation wavelengths, aiming to distinguish Dominican from Mexican and Burmese blue amber. Additionally, the fluorescence properties of Baltic Sea and Ukrainian amber have been described using conventional and synchronous fluorescence spectrometers (Matuszewska and Czaja, 2002; Mysiura et al., 2017).

The main purpose of this work is to fully characterize blue amber from the Dominican Republic, Mexico, and Myanmar, as well as to compare their gemological properties, UV-Vis-NIR spectra, and 3D fluorescence spectra. To make the following discussion more applicable to practical identification workflow, we classify these amber samples according to their apparent fluorescence colors (blue, greenish blue, and non-blue) and then discuss the difference in EEM (also known as 3D fluorescence spectra, excitation-emission matrix, or excitation-emission mapping) from different origins in each category.

SAMPLES AND METHODS

Samples. For this study, we contacted merchants in the Chinese gem trade who dealt mainly with specific amber species and could provide samples with reliable origins as well as current market information. Figure 1 shows commercial blue amber beads from three sources. We tested a total of 247 amber specimens (including beads, fragments, and jewelry pieces) reportedly from the Dominican Republic (109), Mexico (47), and Myanmar (91).

Gemological Testing. Standard gemological and spectroscopic testing were all performed at the Gemmological Institute of China University of Geosciences (Wuhan). Specific gravity (SG) values were determined hydrostatically using a Sartorius BT 224 S balance. Refractive indices (RI) were measured with a GR-6 refractometer produced by Wuhan Xueyuan Jewelry Technology Co. Ltd. Reaction to long-wave ultraviolet light (LWUV: 365 nm) and short-wave ultraviolet light (SWUV: 254 nm) was observed using a standard handheld gemological 4W UV light source (mercury bulb), also made by Wuhan Xueyuan Jewelry Technology Co. Ltd. Samples and inclusions were observed and photographed using a Leica M205 A microscope and a Nikon D810 camera. For each bead, two sets of images were captured—one on a white background and the other on a black background, to show the difference in appearance.

UV-Vis-NIR Spectroscopy. UV/visible/near-infrared absorption spectra were measured in transmission mode with a PerkinElmer Lambda 650 S spectrophotometer. Spectral scans were collected from 250 to 800 nm with a speed of 266.75 nm/min and a data interval of 1.00 nm. The detector response was set at 0.2 s. To successfully perform transmission spectroscopy, the samples needed to be prepared as slices;

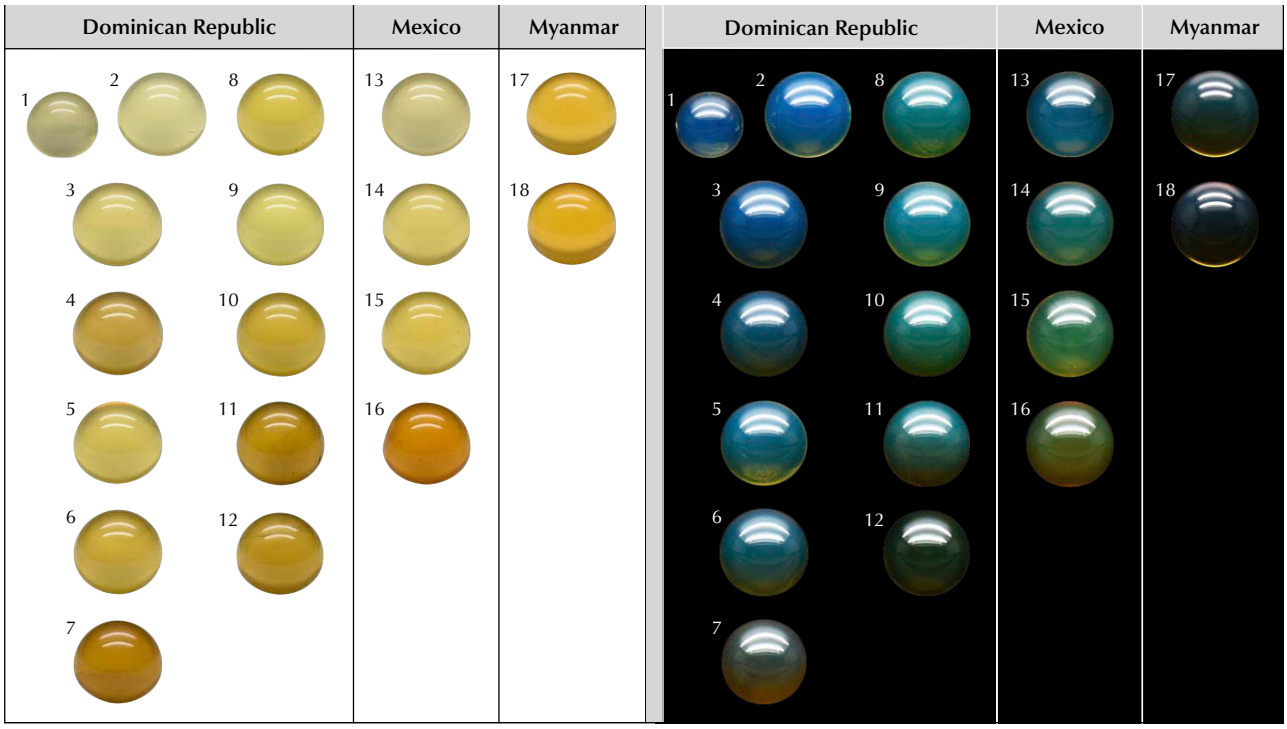

Figure 2. Assembled photos of selected samples representing various types of amber discussed in the text. The photos on the left were taken in a light box under D65 illumination with the samples placed on a standard white background, and those on the right were taken in a light box under D65 illumination with the samples placed on a black velvet background. All photos have variable magnification for optimal display. Samples 1–12 are from the Dominican Republic (B-type: 1–7, GB-type: 8–11, NB-type: 12); samples 13–16 are from Mexico (B-type: 13–14, GB-type: 15–16); and samples 17 and 18 are from Myanmar (B-type). Photos by Z. Zhang.

all slices were less than 0.5 mm in thickness. It is not possible to perform this type of destructive testing on samples intended for jewelry.

Fluorescence Spectroscopy. All fluorescence spectra were recorded at room temperature using a Jasco FP-8500 fluorescence spectrometer (see box A). 3D fluorescence spectral data (i.e., EEM) was collected with a 2000 nm/min scan speed. The excitation wavelengths varied from 220 to 500 nm, with a step size of 5 nm and an excitation bandwidth of 5 nm. The emission spectra were collected with a starting wavelength 10 nm longer than the excitation wavelength and up to 750 nm, with the bandwidth set to 5 nm and a data interval of 1 nm. The beam size was fixed with a 3 mm diameter aperture. In order to keep the illuminated area constant, the sample was placed in a fixed position in a sample holder with a 2 mm diameter opening (see figure A-2). Each EEM, made up of 57 individual emission scans, usually took about 20 minutes to collect. The final EEM spectra appeared similar to a contour map with color coding to indicate the strength of the fluorescence emission peaks or bands under various excitation wavelengths (see box B).

After identifying the main emission peaks, specific excitation wavelengths were chosen and finer-resolution emission scans were performed to obtain more detailed spectra for these specific excitation wavelengths. These scans were conducted with the excitation bandwidth set to 2.5 nm, emission bandwidth 1 nm, and the data interval 1 nm.

Data Collection. All data were recorded using Spectra Manager II software from Jasco. The same software package was used to construct the EEMs from 57 rows and 511 columns of data; higher-resolution emission spectra were drawn as typical two-dimensional plots using plotting software.

RESULTS

Standard Gemological Properties. All samples were colorless to yellow to orange under a standard D65 light when placed on a white background, but the Burmese samples tended to have a richer yellow color. However, when viewed on a black background

BOX A: FLUORESCENCE SPECTROMETER AND EXPERIMENTAL GEOMETRY

Fluorescence spectroscopy has been applied to study the fluorescence of liquids and solid-state luminescent materials. The instrument is called a spectrofluorometer, and it records detailed information about the fluorescence emission spectrum under different excitation wavelengths as well as the excitation efficiency of a particular emission wavelength. This is done by fixing the emission wavelength and scanning through different excitation wavelengths (thus producing what is known as an excitation spectrum).

In a typical spectrofluorometer instrument for analyzing fluorescing liquids, the measurement geometry for the excitation beam, the sample, and the emission beam is set at 90° (Lakowicz, 2006; figure A-1). In this mode, the excitation light travels through the sample and the collected emission light travels through the same distance in the sample. The emission measured is the accumulation of the luminescence along the whole optical path, which is greatly affected by self-absorption and secondary fluorescence. Liu et al. (2014) pointed out that amber's fluorescence occurs mainly on the surface; therefore, a front-surface geometry determination can substantially remove the self-absorption and secondary fluorescence effect (Parker, 1968; Birks, 1974; Airado-Rodriguez et al., 2011).

We performed our experiment using a Jasco FP-8500 spectrofluorometer equipped with a 150 W xenon lamp and a special accessory (EFA-833). This accessory provides a preferred geometry for this study: front-surface mode with an incident angle (between the incident excitation beam and the normal of the sample surface) of approximately 45° (schematic shown in figure A-2). At the same time, no sample pre-treatment is required, which makes this a truly nondestructive test.

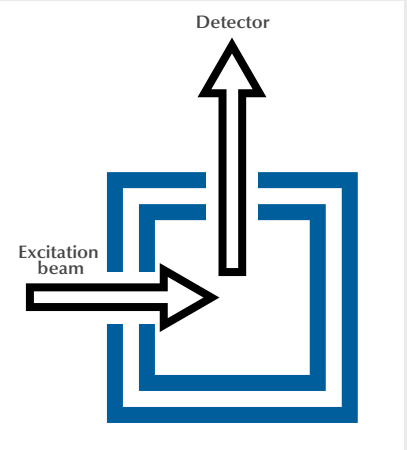

Figure A-1. Schematic of the geometric arrangement for observation of fluorescence in a classic spectrofluorometer (Lakowicz, 2006).

In the FP-8500 fluorescence spectrometer, the maximum emission intensity (I) is limited to 10000 arbitrary units (a.u.), and the actual measurement requires adjusting several measurement parameters such as the size of the slit on the accessory controlling the incident beam, the voltage on the photomultiplier (PMT), and other parameters. In our EEM measurements, all parameters were fixed manually so that the relative intensities of the fluorescence given out by each amber sample from the obtained spectra could be directly compared.

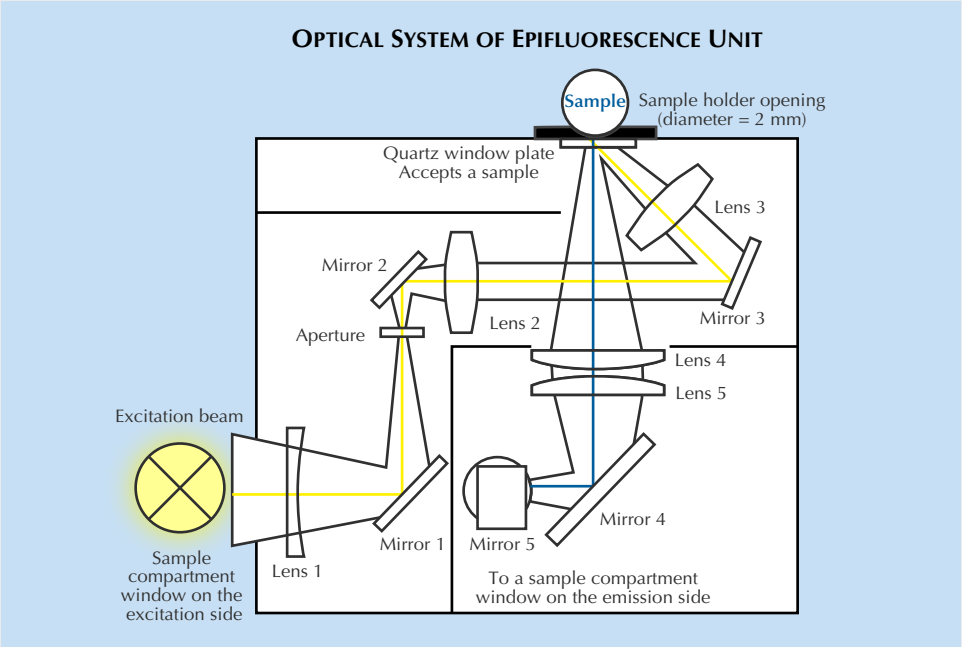

Figure A-2. Schematic of the EFA-833 optical accessory attached to the Jasco FP-8500 instrument used in this study (redrawn by Z. Zhang, from the Jasco FP-8500 handbook). We used a front-surface geometry to minimize the influence of self-absorption and secondary emission effects on measurements of solid samples. This geometry also accommodates gemstones.

BOX B: 3D FLUORESCENCE SPECTRA

3D fluorescence spectra are also known as excitation-emission matrices or excitation-emission maps (EEM). The data collection is conducted by starting with the shortest excitation wavelength and an emission scan from a wavelength 10 nm longer than the excitation wavelength to a set ending point. The excitation wavelength is increased by a set step size, and the emission scan is started again from a wavelength 10 nm longer than the new excitation wavelength to the ending wavelength. This is repeated until the set excitation wavelength range is complete. As shown in figure B-1, these data are commonly plotted in emission wavelength (nm) versus excitation wavelength (nm), with intensity (a.u.) as the third dimension, either plotted directly or referencing a color-coded contour map. In these maps, each horizontal cross section is an emission spectrum, which indicates the intensity distribution of emission wavelengths, measured at a single excitation wavelength. Each vertical cross section is an excitation spectrum, which shows the efficiency of emission by scanning through various excitation wavelengths, while holding constant at a single emission wavelength.

Some commonly encountered terms and their symbols for expressing characteristics of 3D fluorescence spectra used in the main text are presented in table B-1.

TABLE B-1. Summary of relevant terms and symbols.

Symbol	Meaning
λ_{em}	Emission wavelength
λ_{ex}	Excitation wavelength
$I_{\lambda em=450\ nm}$	Intensity of fluorescence at emission wavelength of 450 nm
$I_{\lambda em}$	Intensity of fluorescence at all emission wavelengths

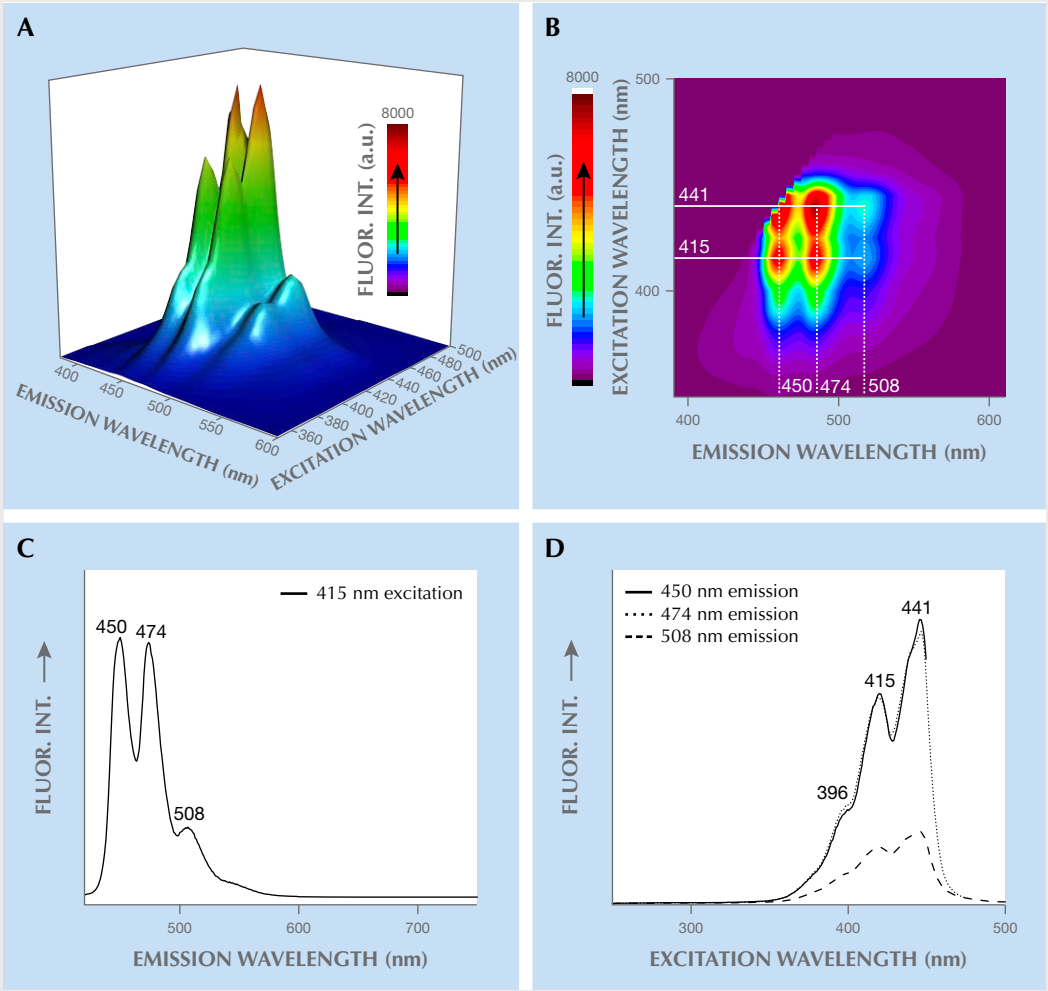

Figure B-1. The three-dimensional plot and contour map (A and B) from a Dominican blue amber fluorescence spectrum shows three extremal emission wavelengths at 450, 474, and 508 nm, and their corresponding optimal excitation wavelengths at 415 and 441 nm. Plots C and D present the emission curve and the excitation curves, respectively.

TABLE 1. Summary of gemological properties of all samples.

Locality	Dominican Republic	Mexico	Myanmar
Total no. of samples	109	47	91
No. of B-type	74	22	5
No. of GB-type	29	22	
No. of NB-type	6	3	86
Color observed on a white background	Colorless to yellow to orange	Colorless to yellow to orange	Yellow
Transparency	Transparent	Transparent	Transparent
SG	1.032–1.051	1.030–1.048	1.024–1.042
RI	1.54	1.54	1.54
Internal features	Usually clean. For all three sources, sporadic tiny red solid inclusions were observed. Some tiny bubbles were observed in Burmese samples.		
Fluorescence reaction	LWUV: Very strong to weak blue fluorescence SWUV: Weak blue fluorescence to inert	LWUV: Strong to weak blue fluorescence SWUV: Weak blue fluorescence to inert	LWUV: Medium violetish blue fluorescence SWUV: Weak violetish blue fluorescence to inert
Phosphorescence	Faint greenish yellow	Faint greenish yellow	Evident yellow

under a standard D65 light source, three types of color appearance were easily identified—blue fluorescence (B-type), greenish blue fluorescence (GB-type), and fluorescence that was too weak to see and thus labeled as non-blue amber (NB-type) (such as the examples seen in figure 2). Liu et al. (2014) attributed the color appearance change from yellow to blue to the superposition of the reflected light with its fluorescence. Most blue amber in the market has an evenly distributed blue or greenish blue color across the entire surface. Among all 247 samples we studied, we found that those from the Dominican Republic and Mexico included both B- and GB-types, while Myanmar had only B-type. NB-type amber occurred in all three sources.

Table 1 summarizes the samples by color appearance and the results of standard gemological testing. The RI values by spot measurement were all 1.54, while the SG values ranged from 1.032 to 1.051 for material from the Dominican Republic, 1.030 to 1.048 for material from Mexico, and 1.024 to 1.042 for material from Myanmar. When observed under the microscope, the samples were quite transparent, with a few tiny internal features. The fluorescence response was typically LWUV > SWUV, with or without the phosphorescence. Under LWUV illumination, Dominican and Mexican blue amber showed blue fluorescence, while the Burmese samples sometimes displayed a violetish blue fluorescence.

UV-Vis-NIR Spectroscopy. We collected in total 178 spectra from 81 Dominican amber samples (including 76 B- and GB-type, and 5 NB-type), 44 Mexican amber samples, and 53 Burmese amber samples. Typical UV-Vis-NIR absorption curves for blue amber are shown in figure 3. We noticed that the absorption edges of samples from all three origins were similarly located at about 400 nm. A tailing absorption from 400 to 500 nm indicates that when mixed-wavelength sunlight strikes blue amber, wavelengths shorter than 400 nm cannot penetrate deeply, while light between 400 and 500 nm may be able to penetrate a little deeper, resulting in a yellowish bodycolor. In Dominican blue amber samples, two distinctive absorption peaks occurred at 412 and 441 nm as well, thus further limiting the 400–450 nm light penetration for Dominican samples. These two peaks are distinctive features for blue amber from the Dominican Republic and were not detected in material from Mexico or Myanmar. However, both the size (or thickness) and the color of samples impact the detection results, so this test has its limitations in real-world gem testing.

Fluorescence Spectroscopy. A brief introduction to 3D fluorescence spectra (EEMs) and relevant terms and symbols are provided in box B.

After collecting 3D fluorescence spectra of all samples, totaling 247 EEM spectra, we found that the fluorescence intensity varied in different samples, while the excitation-emission maps had similar features for samples of the same type from the same origin. To describe blue amber fluorescence features in detail, we selected 18 samples (numbered and shown in figure

2), which had typical EEMs representing the various groups of all blue amber in this study. They included 11 pieces of B-type with different fluorescence intensity (samples 1–7 from the Dominican Republic, 13–14 from Mexico, and 17–18 from Myanmar); six beads of GB-type with different fluorescence intensity (samples 8–11 from the Dominican Republic and 15–16 from Mexico); and one non-blue amber (sample 12) from the Dominican Republic.

Fluorescence of B-Type Amber. Figure 4 compares the 3D fluorescence spectra and significant emission and excitation curves of B-type amber from the Dominican Republic, Mexico, and Myanmar.

From the EEMs of all Dominican B-type samples (74 specimens, figure 4A), we found that the fluorescence emission consisted of three peaks that were rather stable when excited by different excitation wavelengths. Figure 4B shows a typical emission spectrum using λ_{ex} = 415 nm; three main peaks at wavelengths of λ_{em} = 450, 474, and 508 nm are clearly visible. These three fluorescence peaks are in good agreement with those reported by Bellani et al. (2005), Chekryzhov et al. (2014), Liu et al. (2014), and Jiang et al. (2017). The observed fluorescence intensity $I_{\lambda em=450\ nm}$ is generally about the same as $I_{\lambda em=474\ nm}$, though it is sometimes a bit stronger. The strongest fluorescence emission can be excited by λ_{ex} = 415 and 441 nm, but the strongest λ_{em} is observed using 441 nm excitation (figure 4C). Additionally, λ_{em} can only be excited using λ_{ex} between 350 and 460 nm, thus explaining the somewhat inert reaction to SWUV.

Compared with their Dominican counterparts, all Mexican and Burmese B-type samples tended to have weaker $I_{\lambda em}$, as indicated by the lower maximum values for fluorescence intensity in their EEM spectra, as in figures 4A, 4D, and 4G. Their emission patterns were also rather different.

In Mexican B-type samples, shown in figure 4, D–F, when excited using λ_{ex} = 441 and 415 nm, one can see similar triple-peak patterns made up of 451, 476, and 514 nm emissions. Upon switching to a shorter excitation wavelength of λ_{ex} = 400 nm, two different emission bands appeared near 438 and 456 nm (figure 4E). Additionally, the most efficient excitation region in these samples was from 320 to 475 nm, which is rather far from the typical SWUV (254 nm radiation found in a handheld UV light source), thus resulting

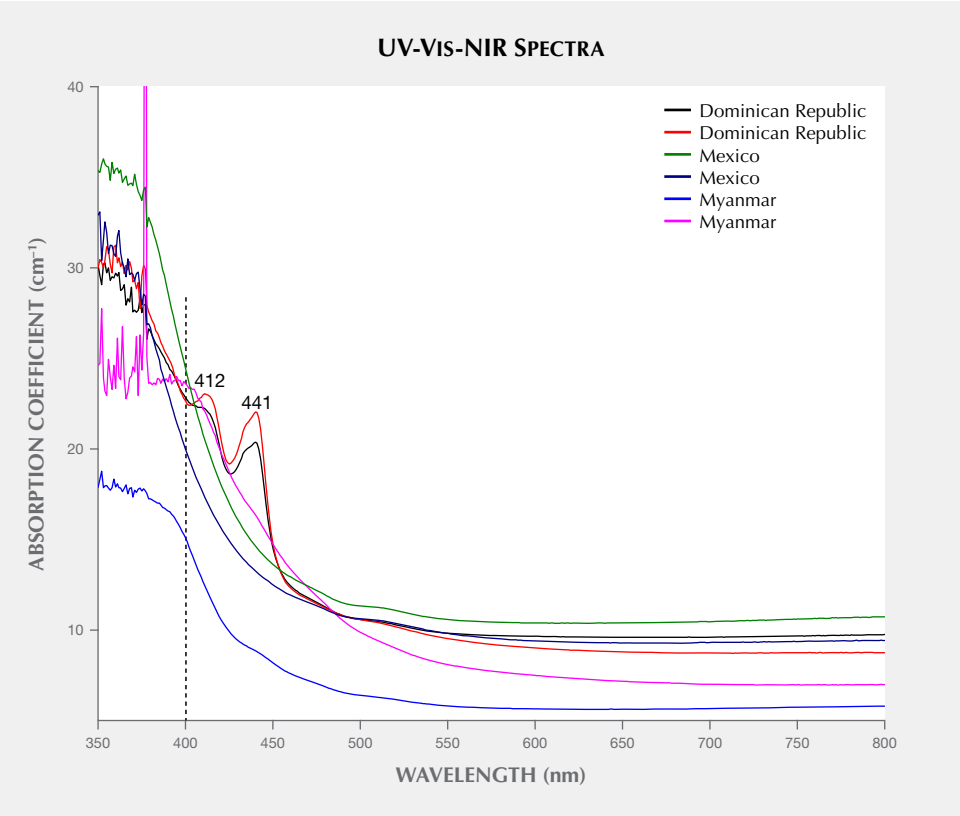

Figure 3. The absorption curves of blue amber from different origins show strong absorbance below 400 nm. While the absorption in the 400–500 nm range varies from origin to origin, the samples from the Dominican Republic showed distinctive absorption peaks at 412 and 441 nm.

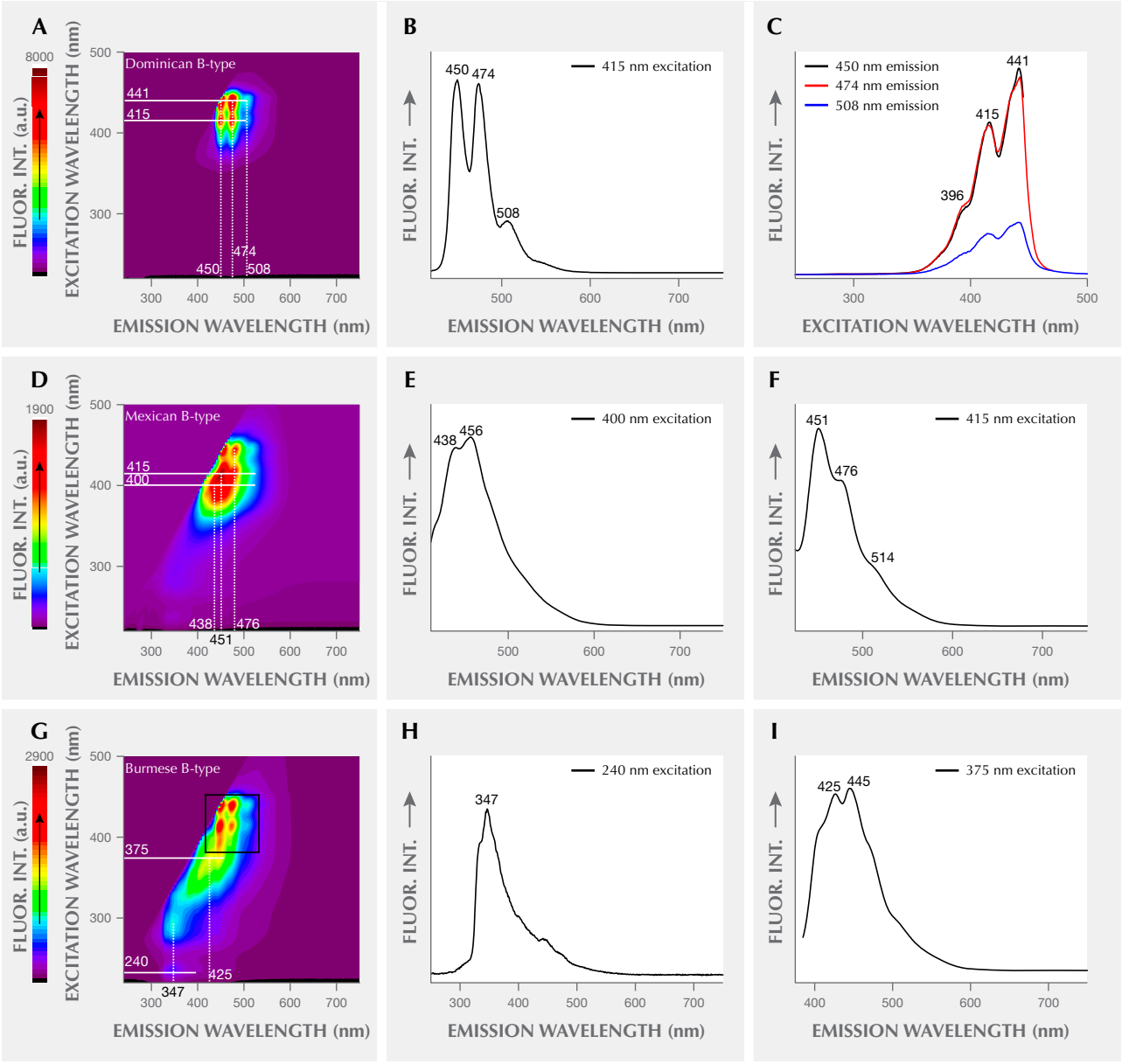

Figure 4. Representative EEMs of B-type amber from three different origins: sample 2 (A–C) from the Dominican Republic, sample 13 (D–F) from Mexico, and sample 17 (G–I) from Myanmar. The left column shows EEM spectra. Images B, E–F, and H–I are emission curves (horizontal sections in EEMs, with λ_{ex} = 415, 400, 375, or 240 nm, as labeled). Image C shows three main excitation curves (as vertical sections in EEMs; different lines are for the different emission peaks). The rectangular area in (G) highlights the EEM area in Burmese B-type sample 17, having a pattern similar to that seen in Dominican B-type amber.

in the very weak to inert fluorescence appearance under SWUV.

In Burmese B-type (seen in figure 4, G–I), a three-emission pattern similar to that of the Dominican B-type was observed in the longer excitation wavelengths (380–450 nm), indicated in figure 4G as the area outlined by a rectangle. The more interesting feature in these samples is in the shorter excitation wavelengths. Two unique emissions were observed: An additional emission peak at about λ_{em} = 425 nm (with a violet color) is at its maximum when excited with λ_{ex} = 375 nm (figure 4I); another λ_{em} at approximately 347 nm (in

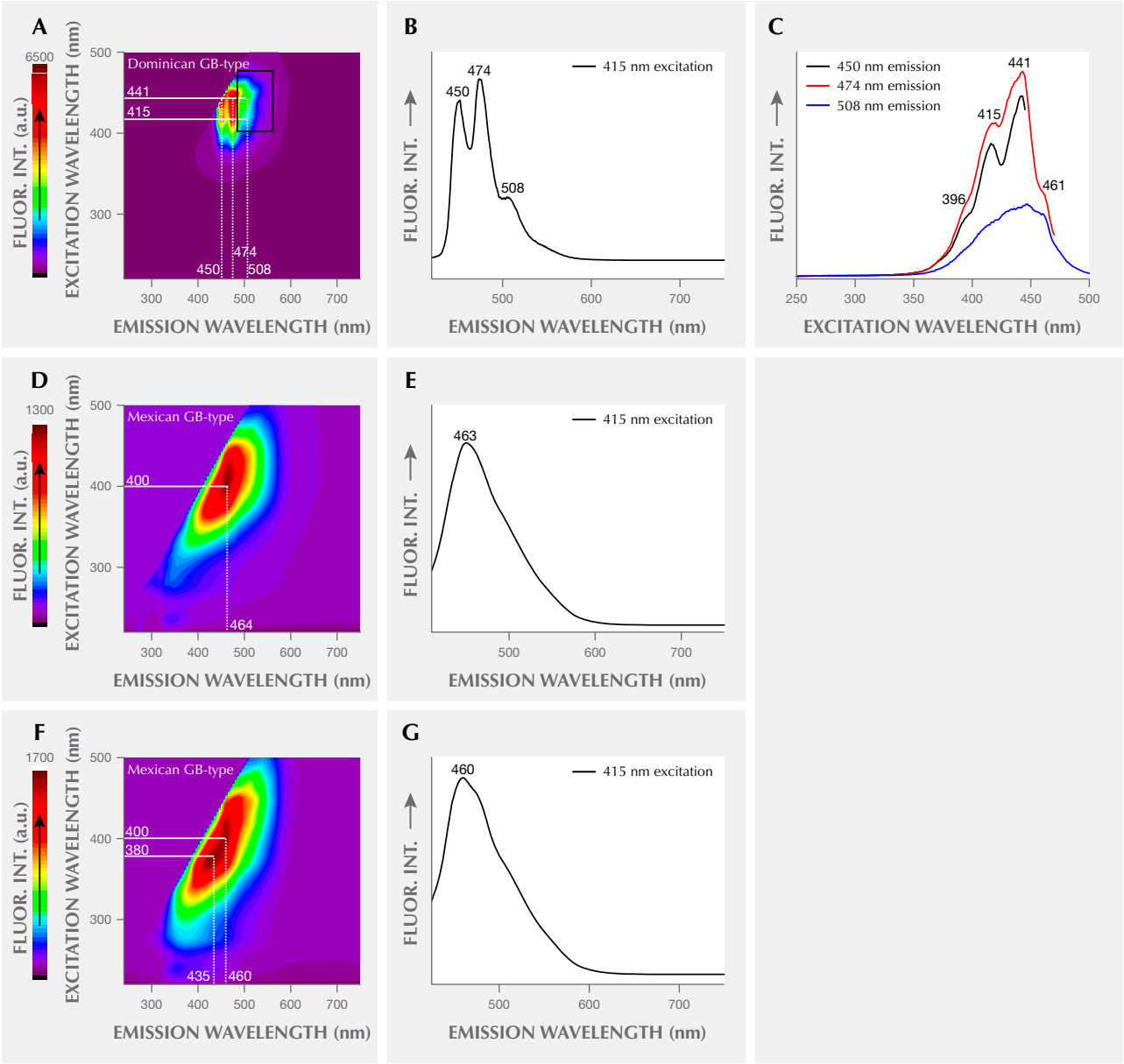

Figure 5. A–C: EEMs and emission and excitation curves show the fluorescence behavior of Dominican GB-type amber, sample 8. The rectangular section in A highlights the additional green fluorescence range. B shows the emission spectrum with λ_{ex} = 415 nm, while C gives the excitation spectra for three different fluorescence emissions, λ_{em} = 450, 474, and 508 nm. The EEMs in D and F and the emission curves with 415 nm excitation in E and G display the fluorescence characteristics of Mexican GB-type amber, samples 15 and 16. Their main emission wavelengths and optimal excitation wavelengths are labeled.

the ultraviolet region) was seen in a wide range of excitation wavelengths, including 240 nm (figure 4H) and from 270 to 330 nm. Again, these spectral features explain the observed weak response to handheld SWUV illumination, especially when compared to the response to LWUV illumination at 365 nm.

Fluorescence of GB-Type Amber. Figure 5 compares the EEM spectra and emission and excitation curves of GB-type amber from the Dominican Republic and Mexico.

In all Dominican GB-type amber, the EEM patterns are similar to those in B-type (for example, fig-

ures 4A and 5A). The major differences include: (1) $I_{\lambda em=474\ nm}$ is much higher than $I_{\lambda em=450\ nm,}$ regardless of the excitation wavelengths, and (2) a longer-wavelength emission tailing toward the green region (indicated by the rectangular area in figure 5A). This tailing varies as the excitation wavelength changes. This emission tailing enhances the green fluorescence, which explains the greener fluorescence appearance in the GB-type amber. Additionally, (3) another excitation extremum at λ_{ex} = 461 nm occurs in excitation curves (figure 5C).

As for Mexican GB-type, the EEMs of samples 15 and 16 (figure 5, D-G) display a broad emission range from the near-ultraviolet to the greenish yellow region (350 to 600 nm), which can be excited with a wide range of excitation wavelengths from 275 to 500 nm. The strongest emission in this material is around 435 nm and/or 464 nm.

Fluorescence of NB-Type Amber. Figure 6 displays the EEM pattern of Dominican NB-type amber. The highest $I_{\lambda em}$ of this amber is only 600, versus the much higher emission counts for B- and GB-type amber, showing maximum values of 8000 to 6500, respectively. This observation indicates that non-blue amber from the Dominican Republic has a much lower fluorescence strength than the other two types from the same locality.

The NB-type amber shows a weak broad emission band in the blue to yellow region (410 to 600 nm) with the highest peak at λ_{em} = 463 nm, best excited by 400 nm light. This is similar to Mexican GB-type amber, but the latter has stronger emission (maximum values of fluorescence intensity are 1300–1700 vs. 600 in Dominican NB-type; see figures 5D and 5F and figure 6A). Due to the wide excitation range and stronger emissions of Mexican GB-type, fluorescence can still be observed visually with sunlight, whereas it cannot in Dominican NB-type (sample 12).

DISCUSSION

In our UV-Vis-NIR absorption spectra (figure 3), the Dominican blue amber showed additional absorption peaks at 412 and 441 nm, which is consistent with the optimal excitation wavelengths for its blue fluorescence. This indicates that Dominican blue amber is very efficient at absorbing these two wavelengths and more likely to generate stronger fluorescence than its Mexican and Burmese counterparts.

When conducting fluorescence measurements, one needs to consider the effects of self-absorption and secondary fluorescence, which can cause errors in fluorescence spectral analysis. These two effects are related—self-absorption occurs when a sample under testing absorbs its own primary fluorescence (Birks, 1974; Lakowicz, 2006) and subsequently emits secondary fluorescence that is either similar to or different from the primary fluorescence. Such absorption may decrease the total amount of fluorescence or reduce a specific peak intensity measured

Figure 6. The 3D fluorescence contour map (A) and emission spectrum (B) of Dominican NB-type amber.

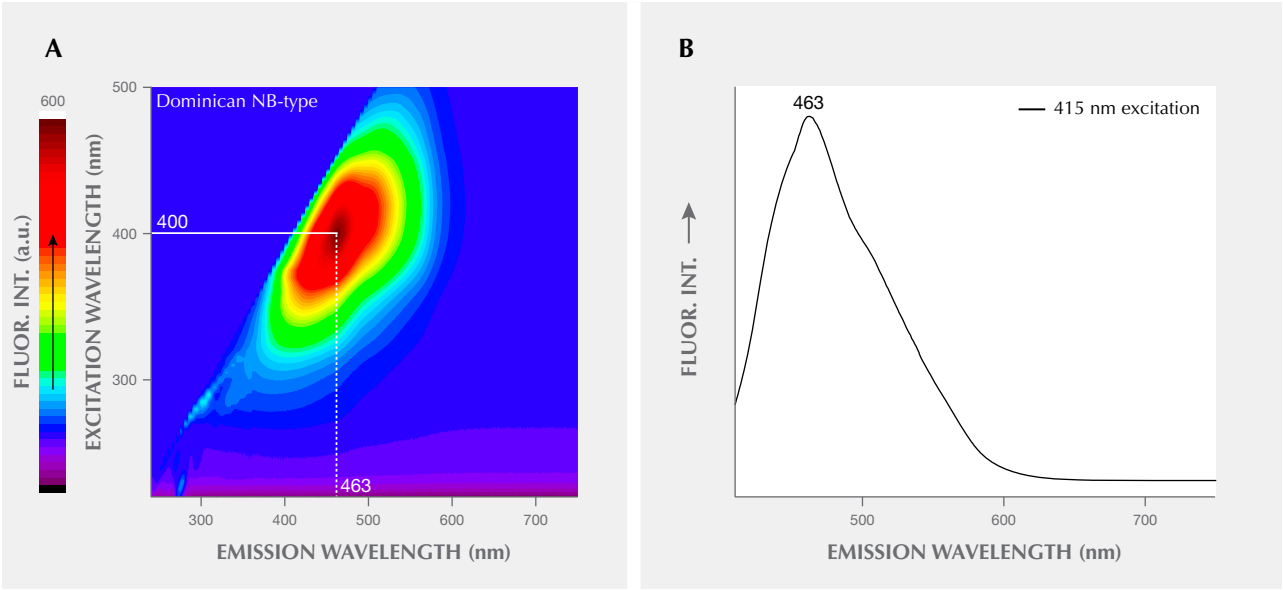

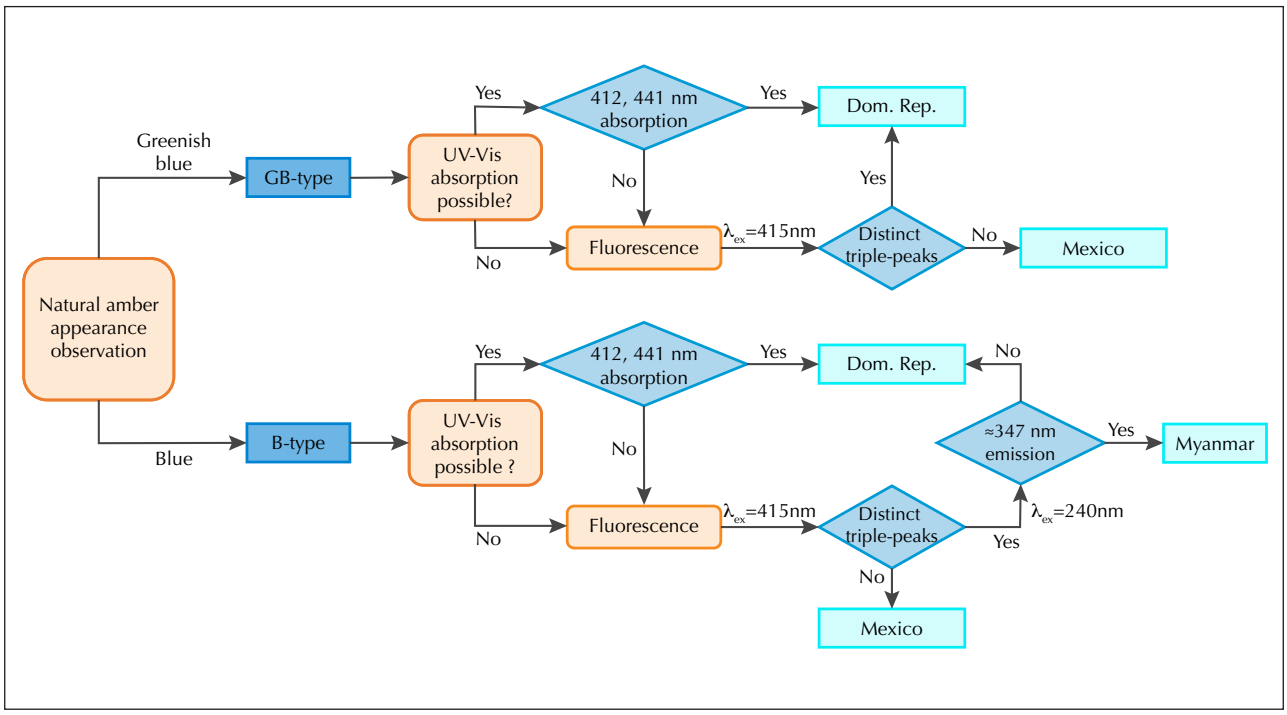

Figure 7. A preliminary flowchart illustrating the combination of visual appearance under D65 light on a black background, UV-Vis-NIR features, and fluorescence features to assist in determining geographic origin of blue amber. Even though clearly Mexican B-type material similarly shows 450, 474, and 508 nm features with 415 nm excitation, this is not a distinct triple peak.

by the instrument, and the secondary fluorescence may produce additional emission peaks or bands. These two effects are more often encountered in a typical fluorescence spectral measurement when the sample is a liquid and loaded in a standard cuvette with 1 cm optical path length. Fortunately, our experiment geometry (as described in box A) can minimize the possibility of self-absorption and secondary fluorescence. Liu et al. (2014) clearly indicated that the fluorescence only occurs on the amber's surface, not deep inside. In addition, our UV-Vis-NIR absorption spectra (figure 3) also showed that any light with wavelength <400 nm will be greatly absorbed and cannot penetrate the amber sample. Thus, the excitation light source is highly unlikely to travel deep into the amber sample to cause self-absorption and secondary fluorescence. Our geometry also ensures that the sample size will not directly influence the amount of fluorescence emission measured.

When we observe amber's fluorescence with the unaided eye, our eyes and brain are extremely sensitive to the fluorescence intensity variations, which allows us to classify the fluorescence response as inert, weak, medium, strong, or very strong. In the current experiment, by strictly controlling the EEM measurement parameters, we achieved a rough quantification of the fluorescence intensity—the intensity bar of the EEM can reflect the relative strength of each sample's fluorescence response. Nevertheless, this procedure may help us set up a future semi-quantitative fluorescence scale for very strong, strong, medium, weak, and inert responses.

Considering the similarities and differences in EEMs from different types of Dominican, Mexican, and Burmese blue amber, it seems possible that EEMs could be aid in separating geographic origin. Figure 7 shows a preliminary flowchart for this separation—by combining the appearance under D65 on a black background, the UV-Vis-NIR absorption (should such test be allowed), and the EEM fluorescence spectra. This summary is based upon the 247 samples we studied and will be further tested and expanded when more samples are available.

Determining the nature of the chemical compound that produces the different fluorescence features is an exceedingly difficult task due to the

structural complicacy resulting from polymerization and the low solubility of amber in most solvents. To date, only Bellani et al. (2005) proposed a possible candidate—perylene—for the triple-peak fluorescence features in Dominican blue amber. Chekryzhov et al. (2014) and Bechtel et al. (2016) excluded perylene for Russian Far East blue amber and proposed azulene ($C_{10}H_8$) as an alternative agent of fluorescence but did not confirm it. Material from the Russian Far East is not commercially available and therefore was not included in this study. Nevertheless, the exact fluorescing agent still has not been successfully extracted, nor has its structure been determined.

CONCLUSIONS

In this study, blue amber refers to amber that shows significant blue fluorescence under a standard D65 light source and, when placed on a black background, this material appears blue to greenish blue. This type of amber is known to come from the Dominican Republic, Mexico, and Myanmar, and material from all three origins exhibits similar gemological properties such as bodycolor, transparency, RI, SG, and internal features. However, their LWUV responses are different—Dominican and Mexican amber mostly show blue fluorescence, while Burmese material displays a violetish blue fluorescence. Blue amber from all three origins showed a similar response to SWUV—much weaker to inert, as compared to the LWUV responses.

We separated blue amber into two types according to their appearance in sunlight or D65 illumination when viewed against a dark background. One is B-type with a blue appearance, and the other is GB-type with a greenish blue appearance. All three origins produce amber that does not show enough blue fluorescence to change its appearance in D65 light; we classified this material as NB-type.

In their EEMs, a triple-peak emission pattern always occurs in Dominican blue amber (both B-type and GB-type). B-type and GB-type Dominican blue amber differ in that the GB-type amber has an additional green fluorescence component (~ 500 nm emission) and an additional 461 nm excitation maximum.

For Mexican B-type amber, the triple-peak features are merged into each other and additional emissions near 438 and 456 nm showed up when using <400 nm excitation. Mexican GB-type amber only has a broad emission feature with an emission center near 460 nm, similar to Dominican NB-type amber. However, Mexican GB-type amber has much stronger emission intensity than Dominican NB-type amber. Burmese B-type amber, in addition to displaying a triple-peak feature similar to Dominican material, has emissions in the violet-ultraviolet region, giving it a violetish appearance.

In the UV-Vis-NIR absorption spectra, in addition to the strong absorption edge just below the near-ultraviolet region (<400 nm) that blue amber from all three sources display, Dominican blue amber has two absorption peaks at 412 and 441 nm, which correspond to the most efficient excitation wavelengths in the EEM. This may explain why Dominican amber fluoresces with much more intensity. Combining the appearance, UV-Vis-NIR spectra, and EEMs, a possible workflow for discriminating blue amber from these three geographic origins is proposed (figure 7). Further study continues to identify the nature of the fluorescing agents and their relationship to the tree species that secrete the specific resins.

ABOUT THE AUTHORS

Ms. Zhang (zhangzhiqing@cug.edu.cn) is a PhD candidate at the Gemmological Institute, China University of Geosciences in Wuhan. Ms. Jiang is a postgraduate student at the Gemmological Institute, China University of Geosciences in Wuhan. Ms. Wang (wangym@cug.edu.cn, corresponding author) is associate professor at the Gemmological Institute, China University of Geosciences in Wuhan, and the director of CUG gem testing center in Guangzhou. Mr. Kong works in the Shenzhen BaoAn Century Amber Museum, China. Dr. Shen (shenxt@cug.edu.cn, corresponding author) is a distinguished professor at the Gemmological Institute, China University of Geosciences in Wuhan.

ACKNOWLEDGMENTS

All authors appreciate the financial support from the National Key R&D program of China (2018YFF0215400) and grants from the Center for Innovative Gem Testing Technology, China University of Geosciences in Wuhan, under grant number CIGTXM-201806. This is contribution CIGTWZ-2020032. The authors are grateful to all the generous merchants for supplying samples. Comments from three anonymous reviewers helped improve this article.

REFERENCES

Airado-Rodriguez D., Durán-Merás I., Galeano-Díaz T., Petter Wold J. (2011) Front-face fluorescence spectroscopy: A new tool for control in the wine industry. *Journal of Food Composition and Analysis*, Vol. 24, No. 2, pp. 257–264.

Bechtel A., Chekryzhov I.Y., Nechaev V.P., Kononov V.V. (2016) Hydrocarbon composition of Russian amber from the Voznovo lignite deposit and Sakhalin Island. *International Journal of Coal Geology*, Vol. 167, pp. 176–183, http://dx.doi.org/10.1016/j.coal.2016.10.005

Bellani V., Giulotto E., Linati L., Sacchi D. (2005) Origin of the blue fluorescence in Dominican amber. *Journal of Applied Physics*, Vol. 97, No. 1, pp. 016101, http://dx.doi.org/10.1063/1.1829395

Berlman I.B. (1971) *Handbook of Fluorescence Spectra of Aromatic Molecules*, 2nd ed. Academic Press, New York and London, 473 pp.

Birks J.B. (1974) Fluorescence parameters and their interpretation. *Journal of Luminescence*, Vol. 9, No. 4, pp. 311–314, http://dx.doi.org/10.1016/0022-2313(74)90044-1

Chekryzhov I.Y., Nechaev V.P., Kononov V.V. (2014) Blue-fluorescing amber from Cenozoic lignite, eastern Sikhote-Alin, Far East Russia: Preliminary results. *International Journal of Coal Geology*, Vol. 132, pp. 6–12, http://dx.doi.org/10.1016/j.coal.2014.07.013

Jiang W., Nie S., Wang Y. (2017) Fluorescence spectral characteristics of blue amber from Dominican Republic, Mexico and Myanmar. *Journal of Gems and Gemmology*, Vol. 19, No. 2, pp. 1–8, http://dx.doi.org/10.15964/j.cnki.027jgg.2017.02.001

Lakowicz J.R. (2006) *Principles of Fluorescence Spectroscopy*, 3rd ed. Springer, Boston, 954 pp, https://doi.org/10.1007/978-0-387-46312-4

Liu Y., Shi G., Wang S. (2014) Color phenomena of blue amber. *G&G*, Vol. 50, No. 2, pp. 134–140, http://dx.doi.org/10.5741/GEMS.50.2.134

Matuszewska A., Czaja M. (2002) Aromatic compounds in molecular phase of Baltic amber—synchronous luminescence analysis. *Talanta*, Vol. 56, No. 6, pp. 1049–1059, http://dx.doi.org/10.1016/S0039-9140(01)00610-5

Mysiura I., Kalantaryan O., Kononenko S., Zhurenko V., Chishkala V., Azarenkov M. (2017) Ukrainian amber luminescence induced by X-rays and ultraviolet radiation. *Journal of Luminescence*, Vol. 188, pp. 319–322, http://dx.doi.org/10.1016/j.jlumin.2017.04.045

Parker C.A. (1968) Apparatus and experimental methods. In C.A. Parker, Ed., *Photoluminescence of Solutions with Applications to Photochemistry and Analytical Chemistry*. Elsevier, Amsterdam, pp. 128–302.

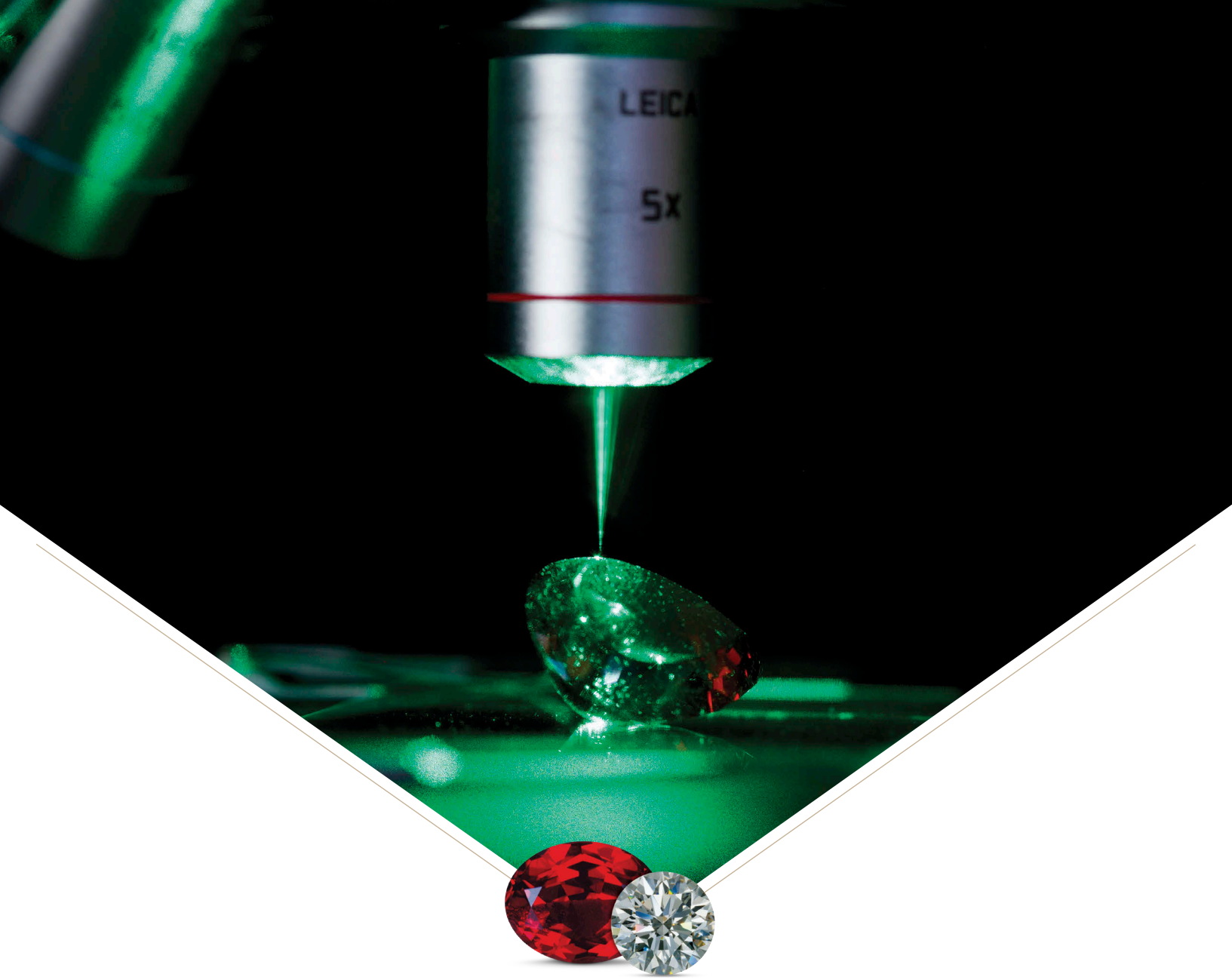

At GIA, gems endure even more pressure.

Science and discovery underpins everything we do. Since 1931, the Gemological Institute of America has been unearthing the truth about gems and creating industry standards. With unwavering commitment to accurate and unbiased methodologies, our dedicated research staff advances the knowledge the industry and consumers need to protect confidence in gems and jewelry. Our discoveries are one of the many reasons why GIA is the world's foremost authority on diamonds, colored stones and pearls.

Learn more about the many facets of GIA at GIA.edu

GIA®

The World's Foremost Authority in Gemology™

Ensuring the Public Trust Through Nonprofit Service Since 1931

BENEFICIATION EDUCATION INSTRUMENTS LABORATORY **RESEARCH**

Mineral Inclusions in Sapphire from Basaltic Terranes in Southern Vietnam: Indicator of Formation Model

Doan Thi Anh Vu, Abhisit Salam, Alongkot Fanka, Elena Belousova, and Chakkaphan Sutthirat

Sapphires in southern Vietnam have been discovered in alluvial gem fields derived from Cenozoic basalts. Several syngenetic mineral inclusions were identified by Raman spectroscopy and electron probe microanalysis; they were classified as ferrocolumbite, zircon, alkali feldspar (albite-anorthoclase-oligoclase), pyrochlore, hercynite spinel, and ilmenite (titanohematite series). Geochemical characteristics of these inclusions appear to have evolved from an alkaline felsic suite. Consequently, the original formation of these sapphires would be related to alkaline felsic magmatic processes before basaltic magmatism, which was derived from the deeper upper mantle, had passed through and transported the sapphires and their associated minerals to the surface via volcanic eruption.

Since the late 1980s, sapphire mines in southern Vietnam have supplied significant quantities of gem materials to the jewelry industry (figure 1). Commercial gem mines in southern Vietnam have been located in four main areas, including Dak Nong, Di Linh, Binh Thuan, and Krong Nang (figure 2) (Smith et al., 1995; Long et al., 2004; Garnier et al., 2005; Izokh et al., 2010; Vu, 2010, 2018). Specifically, the first discovery of abundant gem sapphires was in Dak Nong, followed by Di Linh, Binh Thuan, and Krong Nang, respectively. These sapphires accumulated in Upper-Pleistocene to Quaternary alluvial deposits.

In 2017, we carried out field trips in southern Vietnam encompassing Binh Thuan Province, Di Linh (Lam Dong Province), Dak Nong Province, and Krong Nang (Dak Lak Province), where sapphire samples were collected directly from the mines (see figure 2). Gem mining activities in these areas are conducted by a few local miners. Pits are dug with basic tools before washing and hand picking along streams by artisanal miners (figure 3), and mines worked by machinery (figure 4) can also be found. Sapphires in this region usually range from dark blue to bluish green, yellowish green to green, with rare yellow sapphire. The natural intense blue sapphire is the best known and has been specifically recovered from the Dak Nong and Di Linh gem fields (figure 1, left). Other colors such as bluish green and yellowish green to green are common, particularly in the Binh Thuan and Krong Nang gem fields, respectively (figure 1, right). However, these sapphire varieties are generally heat treated for color enhancement. In addition, trapiche-type sapphires (figure 5) are sometimes found in these gem fields.

In Brief

- Several syngenetic mineral inclusions were recognized in sapphires from southern Vietnam.
- Chemical compositions of these mineral inclusions indicated that they evolved from an alkaline felsic suite.
- Alkaline felsic melts were then proposed as the original formation environment of sapphire from basaltic terranes in southern Vietnam.

Gemological properties and chemical fingerprints of sapphire from southern Vietnam have identified this material as basaltic-type (Smith et al., 1995; Long et al., 2004; Garnier et al., 2005; Izokh et al., 2010; Vu, 2010, 2018). However, understanding of their formation remains unresolved. Inclusions in sapphire, including basaltic type, have become a highly interesting issue in the last decade. These inclusions may preserve significant information on chemical and

See end of article for About the Authors and Acknowledgments.
Gems & Gemology, Vol. 56, No. 4, pp. 498–515,
http://dx.doi.org/10.5741/GEMS.56.4.498

Figure 1. High-quality sapphires from southern Vietnam set in rings. Left: The center blue sapphire is approximately 8.8 ct, and the side stones range from 0.3 to 0.4 ct; all are from Di Linh. Right: An approximately 18 ct yellow sapphire from Binh Thuan surrounded by small diamonds. The yellow sapphire was heated to improve its color. Photos by Doan Thi Anh Vu.

physical conditions directly related to the original formation of the basaltic-type sapphire. Subsequently, various analytical techniques such as Raman spectroscopy, scanning electron microscopy

Figure 2. Map of Vietnam showing the distribution of Cenozoic basalts and the main sapphire mining areas in southern Vietnam with the four occurrences where samples were collected (Binh Thuan, Di Linh, Dak Nong, and Krong Nang); modified from Hoa et al. (2005), Lepvrier et al. (2008), Tri and Khuc (2011), and Hoang et al. (2018).

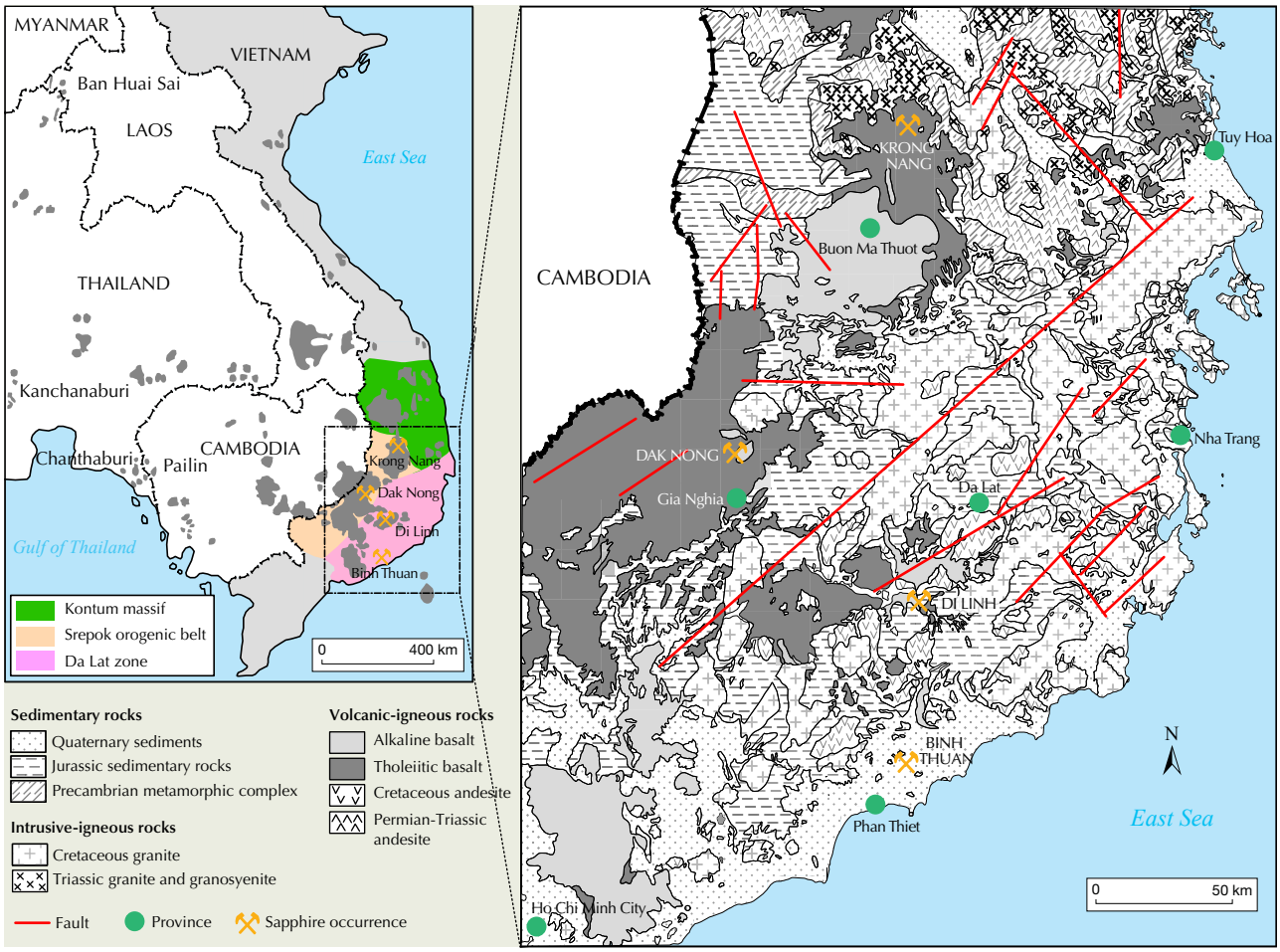

Figure 3. Left: Artisanal miners use crowbars and shovels to remove topsoil and dig through the gem-bearing layer in the Binh Thuan gem field. Right: Gem-bearing gravels are washed and sieved along the stream at Dak Nong. Photos by Doan Thi Anh Vu.

with energy-dispersive spectroscopy (SEM-EDS), and electron probe microanalysis (EPMA) have been applied for identification of inclusions in sapphire from southern Vietnam. For example, Smith et al. (1995) and Long et al. (2004) used SEM-EDS to identify various mineral inclusions in sapphires from Dak Nong and Phan Thiet, whereas Izokh et al. (2010) applied EPMA for chemical analyses of a few inclusions in sapphires from Dak Nong.

Although a variety of mineral inclusions in sapphires from southern Vietnam were previously reported, the chemistry of these inclusions has not been widely analyzed. Therefore, this study is focused on a wider variety of mineral inclusions and

Figure 4. In areas mined with machinery, backhoes were used to remove topsoil and reach the gem-bearing gravel layers prior to washing and sieving using a water pump in the gem fields of Binh Thuan (left) and Krong Nang (right). Photos by Doan Thi Anh Vu.

Figure 5. Trapiche-type sapphires, about 10 ct (left) and 9 ct (right), from Binh Thuan gem field. Photo by Doan Thi Anh Vu.

their chemical analyses using EPMA. These analytical data lead to a reconstruction of a genetic model of sapphire formation related to basaltic volcanism in this region. They also yield significant information for origin determination by gem testing laboratories.

GEOLOGICAL SETTING

Southern Vietnam geologically belongs to a large-scale structure of the Da Lat active continental margin (Da Lat zone) and the Indosinian polyepisodic orogenic belt (Srepok orogenic belt) (figure 2, left) (Tri and Khuc, 2011), which separated from Gondwana in the Devonian (Şengör et al., 1988; Hutchison, 1989; Metcalfe, 1988, 1996, 2009, 2011). Rock formations range widely: Precambrian basement rocks, Jurassic sedimentary rocks, late Mesozoic igneous rocks, and Cenozoic basaltic rocks (Hoa et al., 2005) (figure 2, right). The basement rocks in this area are composed of metamorphic complexes of granulites and gneiss granulite. A thick pile of Jurassic rocks covering the basement rocks is composed of sandstone, siltstone, and shale. These basement rocks and Jurassic rocks are intruded by a number of late Mesozoic rocks, including Triassic granite and granosyenite and Cretaceous granite.

The uppermost part of the area was eventually covered by Cenozoic basalts, which are directly associated with sapphires in southern Vietnam. These Cenozoic (Neogene-Quaternary) basalts range in age from 0.8 to 17.6 Ma (Hoang and Flower, 1998; Garnier et al., 2005) and appear to have been related to the most recent tectonic event, the opening of the East Sea after the Indian-Eurasian collision (from 35 to 17 Ma) (Barr and MacDonald, 1981; Rangin et al., 1995; Hoang and Flower, 1998; Lee et al., 1998). According to Hoang and Flower (1998), these basalts covering an area of about 23,000 km^2 with a thickness of several hundred meters erupted in two main episodes. The early stages mostly included tholeiite basalts, which erupted from extensional fissures trending along the NE-SW and NW-SE directions, derived from the lithosphere. On the other hand, the latter alkali basalts usually flowed along conjugate strike-slip faults originating from the asthenosphere. Only the alkali basalts in particular are associated with sapphire (Smith et al., 1995; Garnier et al., 2005; Izokh et al., 2010). According to Garnier et al. (2005), alkali basalts in Dak Nong are characterized by porphyritic olivine basalts that comprise olivine, clinopyroxene, plagioclase, and spinel. These compositions are associated with megacrysts, xenocrysts, and xenoliths of the mantle and lower crust. Mantle xenoliths embedded in Dak Nong basalts are recognized as garnet lherzolite and spinel lherzolite, while xenocrysts include olivine, Al-rich clinopyroxene, orthopyroxene, phlogopite, sapphire, and zircon. Lower crustal xenoliths usually contain plagioclase and quartz. The presence of mantle xenoliths, xenocrysts, and lower crustal xenoliths may indicate that crystallization of these minerals occurred at high pressure in a magma chamber close to the boundary between the upper mantle and lower crust.

MATERIALS AND METHODS

Over a thousand unheated, gem-quality rough sapphires were collected directly from the gem fields in southern Vietnam (Dak Nong, Di Linh, Krong Nang, and Binh Thuan) for this study. Most of the samples from the Dak Nong and Di Linh mines were collected by the first author over 20 years, while sapphires from Binh Thuan and Krong Nang were collected in 2001 and 2012, respectively. Moreover, more samples from all areas were collected by the authors during the field trip in 2017. These were initially investigated under a gemological microscope to find suitable samples containing mineral inclusions. Subsequently, a total of 274 sapphire samples (77 from Dak Nong, 75 from Di Linh, 45 from Krong Nang, and 77 from Binh Thuan) were then selected and polished to expose the inclusions.

These inclusions were then identified by a Renishaw InVia 1000 laser Raman spectroscope at the Gem and Jewellery Institute of Thailand (Public Organization) (GIT). Subsequently, they were analyzed for major and minor compositions using a JEOL JXA-8100 electron probe microanalyzer at the Depart-

ment of Geology, Faculty of Science, Chulalongkorn University. Operating conditions were set at 15 kV acceleration voltage and 24 nA filament current with 30 seconds of peak and background counts for each element prior to automatic ZAF calculation and reporting in oxide forms. The general detection limits of major and minor analyses obtained from EPMA are typically lower than 0.01 oxide wt.%. Various natural minerals and artificial standards were used for calibration. These included quartz, corundum, eskolaite, fayalite, manganosite, periclase, nickel oxide, wollastonite, jadeite, potassium titanium phosphate, strontium barium niobate, zirconium, yttrium phosphate, cerium phosphate, and neodymium phosphate for SiO_2, Al_2O_3, Cr_2O_3, FeO, MnO, MgO, NiO, CaO, Na_2O, K_2O, Nb_2O_5, ZrO_2, Y_2O_3, Ce_2O_3, and Nd_2O_3, respectively. Fe^{2+} and Fe^{3+} ratios of some specific minerals (e.g., spinel and ilmenite) were estimated by stoichiometric calculation as suggested by Droop (1987). Additionally, a total of four samples that contained zircon inclusions, one from each area, were analyzed for their rare earth elements (REE). These were analyzed using an Agilent 7700 quadrupole ICP-MS instrument, attached to a Photon Machines Excimer 193 nm laser ablation (LA) system at Macquarie University in Sydney, Australia. The analyses were carried out using the same laser conditions as for U-Pb dating. Detailed descriptions of analytical and calibration procedures were given by Belousova et al. (2002). These zircon inclusions were analyzed using a 2 Hz pulse rate with about 0.5 mJ beam energy per pulse, achieving a spatial resolution of about 30 µm. Quantitative results for the trace elements reported here were obtained through calibration of relative element sensitivities using NIST-610 standard glass as the external calibration standard. The BCR-2g and zircon 91500 and GJ-1 reference materials were analyzed within the run as an independent control on reproducibility and instrument stability. Zr content was used for internal calibration for unknown zircon samples (66 wt.% of ZrO_2 as the stoichiometric amount of this oxide in zircon). The precision and accuracy of the NIST-610 analyses were determined to be 1–2% for rare earth elements at the ppm concentration level. Typical detection limits (99% confidence) are provided in table 4.

RESULTS

The most common internal feature of sapphire from southern Vietnam was strong color zoning (figure 6A). Other features included parallel twin planes, needle-like inclusions (figure 6B), liquid-filled inclusions (figure 6C), and negative crystals (figure 6D). Based on Raman spectroscopic and EPMA analyses, 290 mineral inclusions were identified; they were mainly Nb-Ta oxides, followed by silicate and other oxide minerals. The types of mineral inclusions in each sample group are summarized in table 1. Mineral inclusions previously reported in sapphires from Thailand, Laos, and Cambodia are also compared in the same table. Columbite and zircon were the most

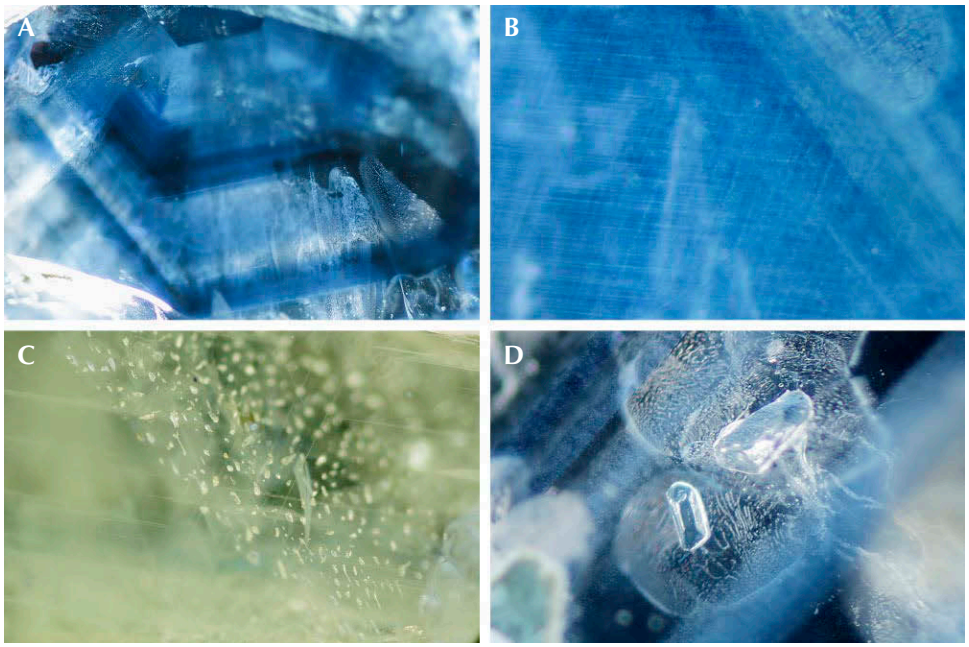

Figure 6. Typical internal features observed in sapphire from southern Vietnam: strong color zones (A), needle-like inclusions (B), liquid-filled inclusions (C), and negative crystals situated in healed fractures (D). Darkfield illumination. Photomicrographs by Doan Thi Anh Vu; magnified 50×.

TABLE 1. Summary of mineral inclusions found in sapphire from southern Vietnam, compared to those reported from basaltic gem fields elsewhere in Southeast Asia.

Area	Nb-Ta oxides	Silicate	Other oxides
Southern Vietnam			
Dak Nong	Columbite*[a] Pyrochlore*	Zircon*[a,b] Alkali feldspar*[a]	Spinel* Ilmenite* Unidentified iron*
Di Linh	Columbite*[c] Pyrochlore[c]	Zircon*[c] Alkali feldspar*[c]	Spinel*[c] Ilmenite[c] Unidentified iron*
Krong Nang	Columbite* Pyrochlore*	Zircon* Alkali feldspar*	Spinel* Unidentified iron*
Binh Thuan	Columbite*[c] Pyrochlore[c]	Zircon*[b,c] Alkali feldspar*[c]	Spinel*[c] Ilmenite[c] Unidentified iron*
Southeast Asia			
Chanthaburi (Thailand)	Columbite[d]	Zircon[d] Alkali feldspar[d]	Spinel[d,e]
Kanchanaburi (Thailand)	–	Zircon[f] Alkali feldspar[f]	Spinel[f] Ilmenite[f]
Ban Huai Sai (Laos)	Columbite[g]	Zircon[e,h] Alkali feldspar[h]	Spinel[e]
Pailin (Cambodia)	Pyrochlore[i]	–	Spinel[g]

**This study, using Raman and EPMA*
[a]Izokh et al. (2010), using EPMA
[b]Long et al. (2004), using SEM-EDS
[c]Smith et al. (1995), using SEM-EDS
[d]Promwongnan and Sutthirat (2019), using Raman and EPMA
[e]Saminpanya and Sutherland (2011), using EPMA
[f]Khamloet et al. (2014), using EPMA
[g]Sutherland et al. (1998b), using EPMA
[h]Sutherland et al. (2002), using EPMA
[i]Palke et al. (2019), using Raman

common inclusions in these sapphire samples, while alkali feldspar and spinel were often identified. Ilmenite, pyrochlore, and unidentified iron minerals were rarely detected. Details of these inclusions are provided below.

Columbite was the predominant mineral inclusion observed in sapphires from all gem fields in southern Vietnam, accounting for nearly 47% of the 290 mineral inclusions contained in the 274 samples. They generally formed as opaque black euhedral crystals with a rhombic prism with pyramidal shape and a truncated rhombic pyramid shape, ranging in sizes from <10 µm up to several millimeters (figure 7, A and B). They were often associated with zircon, with or without feldspar (figures 7C and 9B). Representative EPMA analyses of columbite inclusions

Figure 7. A: A larger prismatic columbite inclusion. B: Two truncated-rhombic columbite inclusions surrounded by healed fractures. C: A cluster of several tiny columbites with colorless feldspar and zircon inclusions. Darkfield illumination. Photomicrographs by Doan Thi Anh Vu; magnified 50×.

TABLE 2. Representative EPMA analyses of columbite inclusions found in sapphires from southern Vietnam, Thailand, and Australia.

Mineral phase analysis (wt.%)	Southern Vietnam								Thailand	Australia		
	Dak Nong		Di Linh		Krong Nang		Binh Thuan		Dak Nong[a]	Chanthaburi[b]	Lava Plains[c]	New England[d]
	DN63	DN68	DL70	DL74	KN25	KN54	PT11	PT73				
TiO_2	2.85	4.06	0.28	1.14	4.78	0.26	nd	12.04	na	0.43	3.57	3.03
FeO	12.32	12.73	15.24	12.35	21.35	15.99	15.96	15.29	15.90	9.79	16.59	17.44
MnO	6.45	6.81	14.64	8.12	0.70	6.55	3.77	4.27	2.93	1.58	2.99	2.19
MgO	0.52	1.38	0.16	2.93	0.77	0.09	nd	0.08	na	0.08	1.18	0.54
CaO	nd	0.05	0.01	0.02	nd	nd	nd	nd	na	0.42	0.03	0.00
Nb_2O_5	75.92	70.02	68.54	72.59	70.80	64.56	76.98	66.03	77.10	74.37	71.98	73.95
Ta_2O_5	0.74	4.45	1.76	1.57	0.50	1.21	3.78	0.46	3.61	0.25	2.98	2.38
ThO_2	nd	0.02	nd	nd	0.02	nd	nd	nd	na	0.85	0.01	na
UO_2	nd	0.08	0.09	nd	0.13	9.97	nd	0.04	na	3.50	0.12	na
ZrO_2	0.41	0.17	0.18	0.26	1.23	0.95	0.03	0.52	0.79	0.78	0.40	0.52
Y_2O_3	nd	nd	nd	nd	nd	0.16	nd	0.15	na	2.76	0.01	na
Nd_2O_3	nd	nd	nd	nd	nd	0.87	nd	nd	na	1.42	na	na
Sm_2O_3	nd	nd	nd	nd	nd	nd	nd	nd	na	0.72	na	na
Total (oxides)	99.2	99.78	100.90	98.98	100.28	100.60	100.53	98.87	100.40	98.61	99.94	100.43
Formula 3(O)												
Ti	0.060	0.086	0.006	0.024	0.099	0.006	–	0.247	–	0.010	0.075	0.064
Fe	0.288	0.299	0.365	0.290	0.494	0.404	0.377	0.348	0.376	0.243	0.388	0.407
Mn	0.152	0.162	0.355	0.193	0.016	0.168	0.090	0.098	0.070	0.040	0.071	0.052
Mg	0.022	0.058	0.007	0.123	0.032	0.004	–	0.003	–	0.004	0.049	0.022
Ca	–	0.002	0.000	0.001	–	–	–	–	–	0.013	0.001	0.000
Nb	0.957	0.888	0.888	0.923	0.886	0.882	0.984	0.813	0.985	0.997	0.909	0.933
Ta	0.006	0.034	0.014	0.012	0.004	0.010	0.029	0.003	0.028	0.002	0.023	0.018
Th	–	0.000	–	–	0.000	–	–	–	–	0.006	0.000	–
U	–	0.001	0.001	–	0.001	0.067	–	0.000	–	0.023	0.001	–
Zr	0.006	0.002	0.002	0.003	0.017	0.014	0.000	0.007	0.011	0.011	0.005	0.007
Y	–	–	–	–	–	0.003	–	0.002	–	0.044	0.000	–
Nd	–	–	–	–	–	0.012	–	–	–	0.019	–	–
Sm	–	–	–	–	–	0.000	–	–	–	0.007	–	–
Total (cations)	1.490	1.538	1.638	1.570	1.549	1.568	1.481	1.522	1.470	1.417	1.521	1.503
Mn/Mn+Fe	0.35	0.35	0.49	0.40	0.03	0.29	0.19	0.22	0.16	0.14	0.15	0.11
Ta/Ta+Nb	0.01	0.04	0.02	0.01	<0.01	0.01	0.33	<0.01	0.03	<0.01	0.02	0.02

Abbreviations: na = not analyzed; nd = not detected
[a]*Izokh et al. (2010)*
[b]*Promwongnan and Sutthirat (2019)*
[c]*Guo et al. (1996)*
[d]*Sutherland et al. (1998a)*

ranged between 65–77 wt.% Nb_2O_5, ≤4.5 wt.% Ta_2O_5, ≤12 wt.% TiO_2, ≤3 wt.% MgO, 12–21 wt.% FeO, and <15 wt.% MnO (table 2); The chemical formula of these columbite inclusions can be expressed as $(Fe_{0.373}Mn_{0.133}Mg_{0.133}Ca_{0.228}Ti_{0.091})(Nb_{0.938}Ta_{0.010}U_{0.001}Zr_{0.007})_2O_6$, which fits very well within the compositional range of ferrocolumbite (figure 8). Their compositions were also equivalent to those previously reported for sapphires from Dak Nong by Izokh et al. (2010) as well as from Lava Plains and New England in Australia (Guo et al., 1996; Sutherland et al., 1998b). Lower FeO contents of columbite inclusions in Bo Welu sapphire

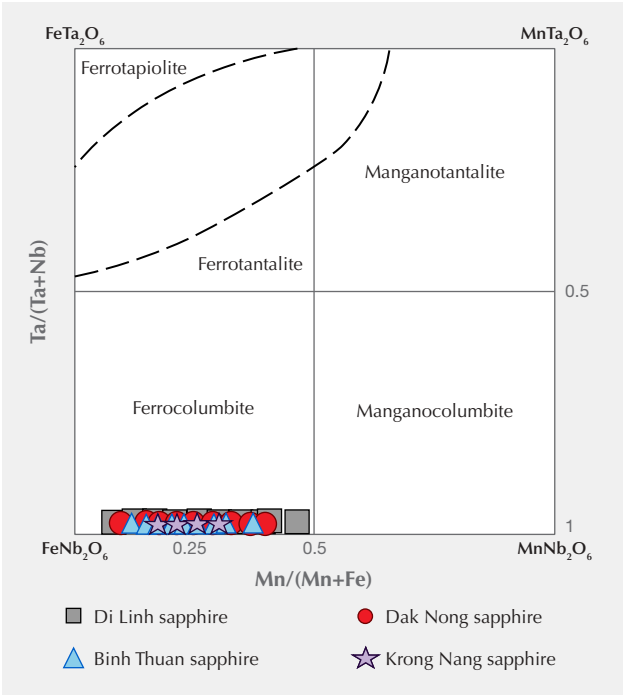

Figure 8. Quadrilateral compositional plots of ferrocolumbite inclusions found in sapphires from southern Vietnam. Various compositional fields and columbite–tapiolite miscibility gap were proposed by Černý and Ercit (1985).

from Chanthaburi, Thailand, were reported by Promwongnan and Sutthirat (2019). Ferrocolumbite inclusions in sapphire from southern Vietnam contained low Ta content, yielding a Ta/(Ta+Nb) ratio < 0.05 within a wide range of Mn contents (<15 wt.% MnO and Mn/(Mn+Fe) ratio <0.5) (figure 8), which may have derived from peralkaline complexes (peralkaline granite/syenite) (Mackay and Simandl, 2015).

Zircon was the second most abundant inclusion, representing about 22% of the mineral inclusions contained in the sapphire samples. These inclusions commonly formed as euhedral tetragonal prismatic or dipyramidal crystals (figure 9, A and B). Most of the zircons were colorless, but some had orange to orange-red colors. Their chemical compositions varied within narrow ranges of approximately 31–34 wt.% SiO_2 and 61–65 wt.% ZrO_2 (table 3). The hafnium contents showed a slightly wider range of about 1–4 wt.%, leading to Hf/Zr ratios of 0.01 to 0.04, which fall in the range of magmatic zircon, particularly syenite and granite zircons (Deer et al., 2013). Significant trace elements included <1.5 wt.% ThO_2, <1.8 wt.% UO_2, and <0.6 wt.% Y_2O_3; these elements appeared to be higher in zircon inclusions of Di Linh sapphire. On the other hand, these zircon inclusions yielded Th/U ratios >0.2, indicating a magmatic source (Williams and Claesson, 1987; Rubatto and Gebauer, 2000; Huong et al., 2016). These were similar in composition to zircon analyses previously reported from Dak Nong (Izokh et al., 2010) and other basalt-associated sources such as Ban Huai Sai in Laos, Kanchanaburi in Thailand, and Kings Plains and New England in Australia (Guo et al., 1996; Sutherland et al., 1998a; 2002; Khamloet et al., 2014), although the Y_2O_3 content of zircon inclusions from Bo Welu in Thailand (Promwongnan and Sutthirat, 2019) has recently been reported with a higher content. Total REE contents of representative zircon inclusions ranged from 1156 to 2710 ppm (table 4), more similar to those from syenite pegmatite (2043 ppm) and granitoid (1813 ppm) than those from carbonatite (600–700 ppm) (Belousova et al., 2002).

Alkali feldspar inclusions were sometimes observed in the sapphire samples, making up about 13% of the mineral inclusions. They generally presented subhedral or euhedral grains with small sizes ranging from about 40 µm, with some rare examples reaching 1 mm. These included crystals were commonly transparent and colorless (figures 7C and 9C).

Figure 9. A: Prismatic orange zircon inclusion. B: Colorless dipyramidal zircon inclusion surrounded by radial cracks, associated with black columbite inclusions. C: Tiny euhedral feldspar inclusions. Darkfield illumination. Photomicrographs by Doan Thi Anh Vu; magnified 50×.

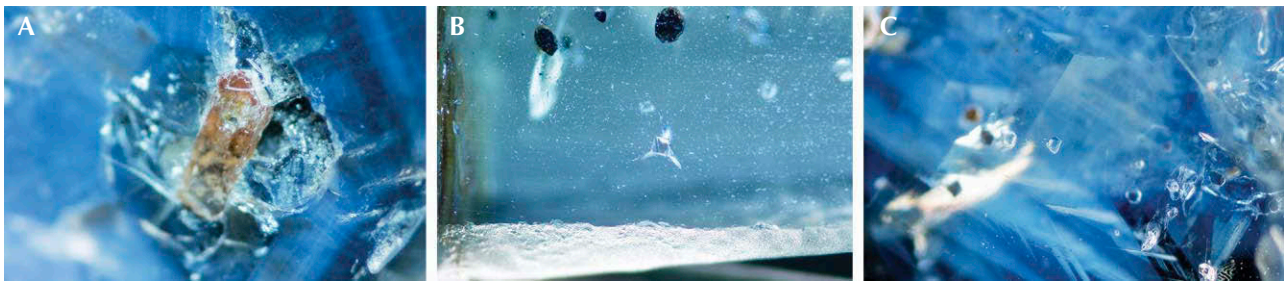

TABLE 3. Representative EPMA analyses of zircon inclusions found in sapphires from southern Vietnam, Laos, Thailand, and Australia.

Mineral phase analysis (wt.%)	Southern Vietnam									Laos	Thailand		Australia	
	Dak Nong		Di Linh		Krong Nang		Binh Thuan		Dak Nong[a]	Ban Huai Sai[b]	Chantha-buri[c]	Kancha-naburi[d]	Kings Plains[e]	New England[f]
	DN23	DN31	DL18	DL44	KN15	KN13	PT36	PT65						
SiO_2	32.16	32.43	34.34	32.59	33.84	33.43	31.19	33.86	32.34	31.23	33.63	34.14	32.12	31.48
TiO_2	0.03	0.02	nd	0.01	0.01	nd	0.06	nd	na	na	na	na	<0.01	0.00
Al_2O_3	0.27	0.30	nd	nd	nd	nd	0.28	0.01	na	0.01	0.01	0.17	0.02	0.44
FeO	nd	0.02	0.04	nd	nd	0.10	0.31	nd	na	na	0.07	0.04	0.20	0.13
MgO	0.02	0.01	nd	nd	nd	nd	0.02	0.01	na	0.01	na	na	<0.01	0.00
CaO	0.06	0.05	nd	nd	nd	0.01	0.01	nd	na	na	na	0.00	0.02	0.00
Na_2O	nd	nd	nd	nd	nd	nd	0.04	nd	na	na	na	na	na	0.00
K_2O	0.02	nd	nd	nd	nd	0.05	0.67	nd	na	na	na	na	na	0.00
ThO_2	0.03	0.31	0.11	1.40	0.32	0.03	0.13	0.09	0.76	0.18	1.21	na	0.49	0.11
UO_2	0.12	1.40	0.12	1.73	0.23	0.06	0.17	0.34	0.93	0.41	1.13	na	0.84	0.11
ZrO_2	64.47	61.44	62.20	61.00	63.98	63.29	63.78	62.02	63.96	64.02	59.39	62.40	63.78	64.84
HfO_2	1.62	3.70	2.51	3.08	2.00	2.82	2.62	3.85	2.44	3.58	2.62	3.50	2.88	2.58
P_2O_5	0.13	0.16	nd	0.22	0.08	0.09	0.32	0.23	na	0.25	0.57	na	0.34	na
Y_2O_3	0.02	0.08	0.27	0.56	0.05	0.07	0.28	0.03	na	0.80	0.85	na	0.34	0.46
Total (oxides)	98.93	99.91	99.60	100.58	100.52	99.96	99.87	100.42	100.43	100.55	99.57	100.25	101.04	100.15
Formula 4(O)														
Si	0.996	1.008	1.048	1.013	1.028	1.024	0.971	1.033	1.001	0.973	1.035	1.036	0.989	0.976
Ti	0.001	0.000	–	0.000	0.000	–	0.001	–	–	–	–	–	–	0.000
Al	0.010	0.011	–	–	–	–	0.010	0.000	–	0.000	0.000	0.006	0.001	0.016
Fe	–	0.000	0.001	–	–	0.003	0.008	–	–	–	0.002	0.001	0.046	0.003
Mg	0.001	0.001	–	–	–	–	0.001	0.000	–	0.000	–	–	–	0.000
Ca	0.002	0.002	–	–	–	0.000	0.000	–	–	–	–	0.000	0.001	0.000
Na	–	–	–	–	–	–	0.003	–	–	–	–	–	–	0.000
K	0.001	–	–	–	–	0.002	0.027	–	–	–	–	–	–	0.000
Th	0.000	0.002	0.001	0.010	0.002	0.000	0.001	0.001	0.005	0.001	0.008	–	0.003	0.001
U	0.001	0.010	0.001	0.012	0.002	0.000	0.001	0.002	0.006	0.003	0.008	–	0.006	0.001
Zr	0.974	0.931	0.925	0.924	0.948	0.945	0.968	0.923	0.965	0.972	0.891	0.923	0.957	0.980
Hf	0.014	0.033	0.022	0.027	0.017	0.025	0.023	0.033	0.022	0.032	0.023	0.036	0.025	0.023
P	0.003	0.004	–	0.006	0.002	0.002	0.008	0.006	–	0.007	0.013	–	0.009	–
Y	0.000	0.001	0.004	0.009	0.001	0.001	0.005	0.000	–	0.013	0.014	–	0.006	0.008
Total (cations)	2.004	2.003	2.002	2.001	2.000	2.003	2.028	1.999	2.000	2.002	1.995	2.002	2.001	2.008
Th/U	0.29	0.23	0.93	0.83	1.42	0.51	0.79	0.26	0.84	0.45	1.10	–	0.60	1.02
Hf/Zr	0.02	0.04	0.02	0.03	0.02	0.03	0.02	0.04	0.02	0.03	0.03	0.03	0.03	0.02

Abbreviations: na = not analyzed; nd = not detected
[a]*Izokh et al. (2010)*
[b]*Sutherland et al. (2002)*
[c]*Promwongnan and Sutthirat (2019)*
[d]*Khamloet et al. (2014)*
[e]*Guo et al. (1996)*
[f]*Sutherland et al. (1998a)*

Their chemical compositions were rather uniformly toward Na-rich feldspar between albite-anorthoclase-oligoclase ($Ab_{77–98}An_{<15}Or_{1–11}$, see table 5 and figure 10). However, feldspar in Krong Nang sapphires mostly plotted close to the junction of albite-anorthoclase-oligoclase compositions ($Ab_{82–86}An_{6–11}Or_{6–11}$),

TABLE 4. REE analyses (ppm) of representative zircons found in southern Vietnam sapphire, determined by LA-ICP-MS.

Element	Dak Nong	Di Linh	Krong Nang	Binh Thuan	Typical detection limits (99% confidence)
	DN05	DL46	KN08	PT05	
Y	1468.21	4220.35	1194.74	2868.13	0.004
La	0.02	nd	0.01	nd	0.004
Ce	2.79	12.00	1.65	13.33	0.003
Pr	0.01	0.06	0.02	0.0523	0.003
Nd	0.27	1.11	0.26	1.451	0.014
Sm	1.23	5.62	0.68	5.62	0.019
Eu	0.96	5.12	0.59	2.177	0.006
Gd	12.91	54.66	5.74	44.06	0.019
Tb	7.23	27.58	3.91	21.66	0.003
Dy	122.00	416.17	76.25	310.13	0.013
Ho	50.02	152.71	38.25	104.29	0.003
Er	258.30	672.98	258.42	442.14	0.009
Tm	60.40	134.11	83.73	89.21	0.003
Yb	566.33	115.50	1081.3	721.34	0.018
Lu	80.77	140.18	179.34	81.68	0.003
Total REE	1155.94	2710.22	1762.23	1815.47	

Abbreviation: nd = not detected

whereas Di Linh feldspar was divided into two groups: the first group close to the albite-anorthoclase boundary ($Ab_{82–85}An_{6–9}Or_{8–11}$) and the second one containing lower K content near the albite-oligoclase boundary ($Ab_{85–87}An_{7–11}Or_{4–5}$). Binh Thuan feldspar ranged between albite and oligoclase compositions, while most Dak Nong feldspar fell within albite composition ($Ab_{83–98}An_{1–10}Or_{1–8}$). These compositional ranges were wider than those previously reported, as only oligoclase was identified in sapphires from Dak Nong (Izokh et al., 2010) and from Ban Huai Sai in Laos (Sutherland et al., 2002), but An and Or components were narrower in range than those in Thai sapphires from Kanchanaburi ($An_{9–23}Or_{6–14}$) (Khamloet et al., 2014) and Chanthaburi ($An_{<14}Or_{7–17}$) (Promwongnan and Sutthirat, 2019) and Australian sapphires from Kings Plains ($An_{<14}Or_{7–17}$)

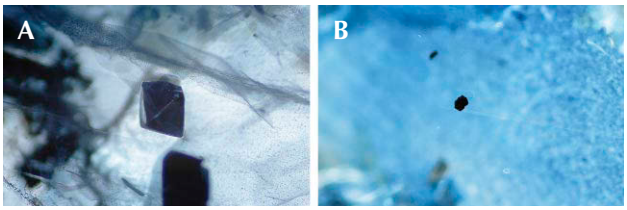

Figure 11. Inclusions of black octahedral hercynite spinel (A) and euhedral rhombohedral ilmenite (B). Darkfield illumination. Photomicrographs by Doan Thi Anh Vu; magnified 50×.

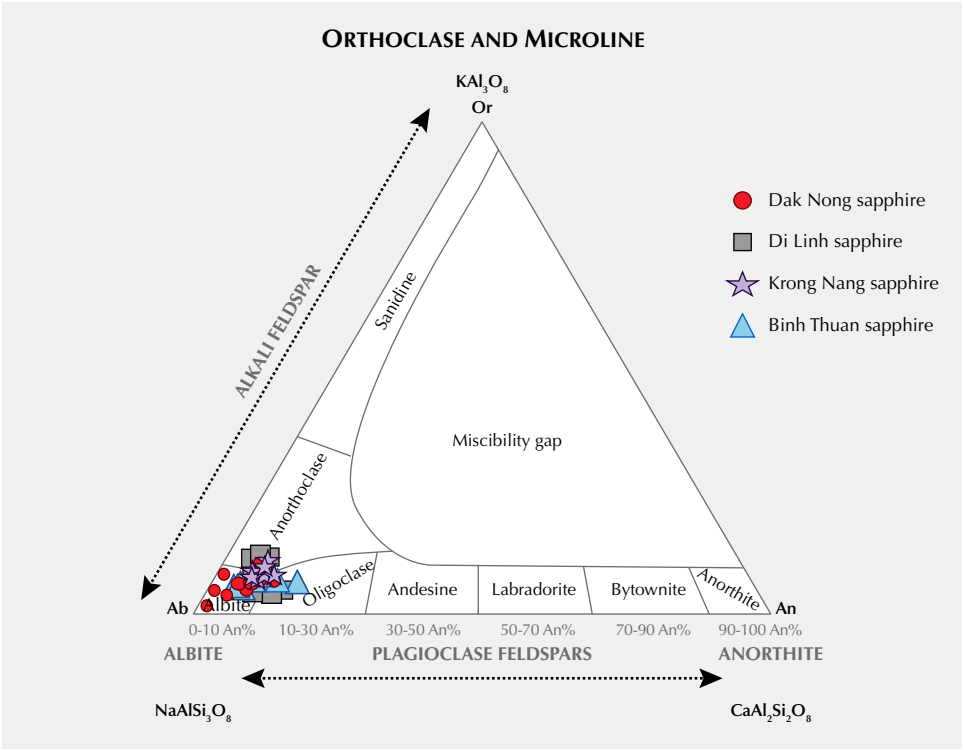

Figure 10. Ternary plot of An-Ab-Or in alkali feldspar inclusions in sapphires from southern Vietnam. Modified from N.N. Greenwood and A. Earnshaw, Chemistry of Elements *(1998), p. 357.*

TABLE 5. Representative EPMA analyses of feldspar inclusions in sapphires from southern Vietnam, Laos, Thailand, and Australia.

Mineral phase analysis (wt.%)	Southern Vietnam								Laos	Thailand		Australia	
	Dak Nong		Di Linh		Krong Nang		Binh Thuan		Dak Nong[a]	Ban Huai Sai[b]	Kanchanaburi[c]	Chanthaburi[d]	Kings Plains[e]	New England[f]
	DN41	DN34	DL27	DL34	KN53	KN37	PT01	PT23						
SiO_2	67.93	64.13	65.66	62.30	65.83	64.38	68.89	64.31	64.20	64.83	65.60	66.97	64.81	53.47
TiO_2	0.02	nd	0.01	0.02	0.01	0.01	nd	nd	0.00	na	0.01	0.02	na	0.00
Al_2O_3	19.06	21.92	23.72	23.73	22.86	21.79	19.70	22.39	22.10	21.45	21.50	21.40	18.56	29.28
FeO	0.03	0.06	0.03	0.19	0.09	0.07	nd	0.06	0.06	0.03	0.04	0.65	na	0.09
MnO	nd	nd	nd	nd	nd	nd	nd	nd	0.02	na	0.00	0.04	na	0.00
MgO	nd	nd	nd	nd	nd	nd	nd	nd	0.00	na	0.05	nd	na	0.00
BaO	0.07	0.01	0.03	0.06	0.07	nd	0.02	0.03	na	na	na	na	na	na
CaO	0.17	2.24	1.09	1.64	1.54	2.24	nd	2.98	3.13	1.96	2.59	0.73	<0.01	11.19
Na_2O	11.33	9.65	7.63	10.76	8.73	9.22	11.37	9.02	9.71	9.37	4.31	2.69	0.73	5.50
K_2O	0.22	1.15	1.60	1.02	1.70	1.44	0.32	1.43	0.82	1.53	6.52	8.47	15.50	0.48
Total (oxides)	98.83	99.16	99.76	99.72	100.84	99.15	100.31	100.22	100.10	99.17	100.62	100.97	99.60	100.01
Formula 8(O)														
Si	3.003	2.857	2.872	2.775	2.872	2.868	2.998	2.841	2.840	2.885	2.908	2.957	2.997	2.425
Ti	0.001	–	0.000	0.001	0.000	0.000	–	–	–	–	0.000	0.001	–	–
Al	0.993	1.151	1.223	1.245	1.175	1.144	1.010	1.166	1.152	1.125	1.124	1.114	1.011	1.565
Fe	0.001	0.002	0.001	0.007	0.003	0.003	–	0.002	0.002	0.001	0.002	0.024	–	0.003
Mn	–	–	–	–	–	–	–	–	0.001	–	–	0.001	–	–
Mg	–	–	–	–	–	–	–	–	–	–	0.003	0.000	–	–
Ba	0.001	0.000	0.000	0.001	0.001	–	0.000	0.001	–	–	–	0.000	–	–
Ca	0.008	0.107	0.051	0.078	0.072	0.107	–	0.141	0.148	0.093	0.123	0.035	–	0.544
Na	0.971	0.833	0.647	0.929	0.738	0.796	0.959	0.772	0.833	0.808	0.371	0.230	0.065	0.484
K	0.012	0.065	0.089	0.058	0.095	0.082	0.018	0.081	0.046	0.087	0.369	0.477	0.914	0.028
Total (cations)	4.991	5.016	4.884	5.095	4.957	4.999	4.986	5.003	5.023	5.000	4.899	4.893	4.988	5.048
Atomic (%)														
Albite	97.9	82.9	82.1	87.2	81.6	80.8	98.2	77.7	81.1	81.8	43.0	31.0	6.7	45.8
Anorthite	0.8	10.6	6.5	7.4	8.0	10.9	0.0	14.2	14.4	9.5	14.2	4.7	0.0	51.5
Orthoclase	1.3	6.5	11.3	5.4	10.5	8.3	1.8	8.1	4.5	8.8	42.8	64.3	93.3	2.7

Abbreviations: na = not analyzed; nd = not detected
[a]*Izokh et al. (2010)*
[b]*Sutherland et al. (2002)*
[c]*Khamloet et al. (2014)*
[d]*Promwongnan and Sutthirat (2019)*
[e]*Guo et al. (1996)*
[f]*Sutherland et al. (1998a)*

(Guo et al., 1996) and New England ($An_{<53}Or_{22–94}$) (Sutherland et al., 1998a).

Spinel inclusions accounted for about 4% of the mineral inclusions contained in the samples from southern Vietnam. They usually occurred as black cubic crystals (figure 11A). Spinel inclusions with compositions ranging between chromite-hercynite and magnetite-hercynite have been previously reported, on the basis of SEM-EDS analyses, in sapphires from Binh Thuan and Di Linh (Smith et al., 1995). However, EPMA analyses of spinel inclusions in this study revealed significant components of hercynite ($FeAl_2O_4$, $Hc_{78–100}$) and spinel ($MgAl_2O_4$, $Sp_{<23}$), whereas other components were negligible (table 6). The spinel inclusions' $Mg:Fe^{2+}$ ratios were mostly less than 1:4, falling into hercynite spinel (Deer et al., 2013). In comparison, these hercynite spinel inclusions contained a moderately lower spinel composition than those in

TABLE 6. Representative EPMA analyses of spinel inclusions in sapphires from southern Vietnam, Thailand, Cambodia, and Australia.

Mineral phase analysis (wt.%)	Southern Vietnam							Thailand	Cambodia	Australia
	Dak Nong		Di Linh	Krong Nang		Binh Thuan		Kanchanaburi[a]	Pailin[b]	New England[c]
	DN12	DN16	DL62	KN42	KN47	PT22	PT34			
SiO_2	nd	nd	0.01	nd	nd	nd	0.25	0.03	0.03	0.00
TiO_2	0.12	0.08	0.70	0.13	0.18	nd	1.91	0.07	0.26	0.13
Al_2O_3	60.99	60.93	60.76	60.31	60.11	61.18	61.58	59.52	63.00	57.04
Cr_2O_3	nd	nd	0.09	nd	nd	nd	nd	0.16	0.29	0.00
FeO_{total}	33.99	34.18	33.87	34.96	33.77	33.35	35.53	35.39	21.77	34.66
MnO	nd	0.89	0.34	0.05	1.18	0.53	1.44	0.22	0.15	0.48
MgO	4.02	4.29	4.62	3.17	4.31	4.60	0.08	5.85	13.50	6.09
ZnO	0.12	0.38	0.18	nd	0.51	0.93	0.07	0.14	na	0.69
CaO	0.06	nd	nd	nd	nd	nd	nd	0.00	<0.005	0.00
Total (oxides)	99.29	100.74	100.58	98.61	100.06	100.58	100.95	101.36	99.00	99.15
Formula 32(O)										
Si	–	–	0.002	–	–	–	0.056	0.007	0.006	0.00
Ti	0.020	0.014	0.117	0.023	0.030	–	0.321	0.011	0.042	0.022
Al	16.134	15.975	15.886	16.153	15.881	16.018	16.194	15.570	15.774	15.364
Cr	–	–	0.016	–	–	–	–	0.028	0.049	–
Fe^{3+}	0.000	0.000	0.000	0.000	0.078	0.000	0.000	0.412	0.000	0.779
Fe^{2+}	6.380	6.359	6.285	6.645	6.253	6.196	6.630	6.157	3.868	5.846
Mn	–	0.168	0.064	0.009	0.224	0.100	0.272	0.041	0.027	0.093
Mg	1.344	1.421	1.529	1.072	1.440	1.524	0.026	1.934	4.276	2.075
Zn	0.020	0.062	0.030	–	0.122	0.152	0.012	0.023	–	0.116
Ca	0.015	–	–	–	–	–	–	–	–	–
Total (cations)	23.913	23.999	23.929	23.901	24.029	23.991	23.526	24.183	24.041	24.296
ΣR^{2+}	7.759	8.010	7.907	7.726	8.040	7.973	6.956	8.155	8.171	8.131
ΣR^{3+}	16.154	15.989	16.022	16.175	15.989	16.018	16.571	16.028	15.870	16.165
Atomic (%)										
Spinel	17.3	17.7	19.3	22.5	13.9	19.1	0.4	23.9	52.5	26.2
Hercynite	82.2	79.4	79.5	77.5	86.1	80.3	99.6	76.1	47.5	73.8

Abbreviations: na = not analyzed; nd = not detected
Fe^{2+} and Fe^{3+} were recalculated from total FeO after the method of Droop (1987).
$\Sigma R^{2+} = Fe^{2+}+Mn+Mg+Zn+Ca$. $\Sigma R^{3+} = Ti+Al+Cr+Fe^{3+}$.
[a]*Khamloet et al. (2014)*
[b]*Sutherland et al. (1998b)*
[c]*Sutherland et al. (1998a)*

sapphires from Pailin in Cambodia or from New England in Australia, but nearly the same as those from Kanchanaburi in Thailand (see also table 6).

Ilmenite ($FeTiO_3$) was found in only two samples from Di Linh and one sample from Dak Nong. These inclusions were black, opaque, and euhedral (figure 11B), and their identity was confirmed by Raman spectroscopic identification. A previous study, based on SEM-EDS analysis, also recognized ilmenite in sapphires from Di Linh and Binh Thuan (Smith et al., 1995). The chemical composition of the ilmenite inclusions in this study clearly belonged to the titanohematite series (ilmenite-hematite, $Il_{54–49}He_{40–34}$) (table 7). The low Mn content (<0.15 wt.% MnO) of these titanohematites was closer to that from an igneous magma source (Lindsley, 1991) as reported from Sybille Monzosyenite (Fuhrman et al., 1988), and different from ilmenite with higher Mn originating from metamorphic rocks from Western Australia (Cassidy et al., 1988). Moreover, their Mn contents

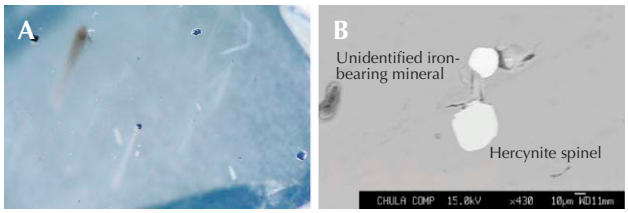

Figure 12. A: Several tiny unidentified iron-bearing minerals with cubic shape, shown in darkfield illumination. Photomicrograph by Doan Thi Anh Vu; magnified 50×. B: Backscattered electron image of unidentified cubic iron oxides and euhedral hercynite-spinel.

were similar to those of ilmenite in New England sapphires originating from silicate melt (Sutherland et al., 1998a) and different from those of ilmenite in Kanchanaburi sapphires from melt involved by subsequent contact metamorphism (Khamloet et al., 2014) (table 7).

Unidentified iron-bearing minerals were also observed in these sapphire samples. They presented as tiny black cubic crystals (less than 10 µm and a few around 30 µm) (figure 12A) with morphological forms similar to those identified for spinel inclusions. They were commonly associated with spinel inclusions and sometimes formed as composite inclusions (figure 12B). These iron-rich minerals contained up to 96% FeO and had aluminum contents ranging from 0.1 to 13% Al_2O_3 (table 8) and their Raman spectra indicated the presence of magnetite, with characteristic bands at 663 to 652 cm^{-1} (Faria et al., 1997). However, their atomic proportions, based on stoichiometric calculation as suggested by Droop (1987), yielded a $\Sigma R^{3+}/\Sigma R^{2+}$ ratio of almost 1:1, particularly Fe^{3+}/Fe^{2+} (see table 8), which was inconsistent with the formula of magnetite (Fe_3O_4), with an Fe^{3+}/Fe^{2+} ratio of 2:1. More details of these inclusions need to be worked out in the future.

Figure 13. A red cubic pyrochlore inclusion displaying halo and radial cracks in darkfield illumination. Photomicrograph by Doan Thi Anh Vu; magnified 50×.

TABLE 7. Representative EPMA analyses of ilmenite inclusions in sapphires from southern Vietnam, Thailand, and Australia.

Mineral phase analysis (wt.%)	Southern Vietnam			Thailand	Australia
	Dak Nong	Di Linh		Kanchanaburi[a]	New England[b]
	DN39	DL23	DL85		
SiO_2	0.11	0.10	nd	0.00	0.70
TiO_2	34.94	37.08	33.77	45.73	59.04
Al_2O_3	0.02	1.50	0.58	6.90	0.45
Cr_2O_3	nd	0.04	0.12	na	0.00
FeO_{total}	61.43	61.58	63.48	27.64	32.05
MnO	0.14	0.06	0.05	17.59	0.40
MgO	nd	0.18	0.64	0.98	1.85
ZnO	0.80	nd	nd	na	0.00
CaO	nd	0.01	nd	0.00	0.00
NiO	0.02	nd	0.03	na	na
Total (oxides)	97.46	100.54	98.67	98.84	94.57
Formula 3(O)					
Si	0.003	0.003	–	0.000	0.017
Ti	0.752	0.757	0.718	0.857	1.102
Al	0.001	0.048	0.019	0.202	0.013
Cr	–	0.001	0.003	–	0.000
Fe^{3+}	0.655	0.584	0.715	0.124	0.000
Fe^{2+}	0.814	0.814	0.786	0.452	1.330
Mn	0.003	0.001	0.001	0.371	0.008
Mg	–	0.007	0.027	0.036	0.068
Zn	0.017	–	–	–	0.000
Ca	–	0.000	–	0.000	0.000
Ni	0.000	–	0.001	–	–
Total (cations)	2.245	2.216	2.271	2.042	1.874
ΣR^{2+}	0.835	0.823	0.815	0.859	0.742
ΣR^{2+}	1.410	1.393	1.455	1.183	1.132
Atomic (%)					
Ilmenite	53.1	54.5	49.4	56.7	98.8
Magnetite	6.8	6.9	8.3	0.0	0.0
Hematite	38.7	33.7	39.8	29.9	0.0

Abbreviations: na = not analyzed; nd = not detected
Fe^{2+} and Fe^{3+} were recalculated from total FeO after the method of Droop (1987).
$\Sigma R^{2+} = Fe^{2+}+Mn+Mg+Zn+Ca+Ni$; $\Sigma R^{3+} = Ti+Al+Cr+Fe^{3+}$.
[a]Khamloet et al. (2014)
[b]Sutherland et al. (1998a)

TABLE 8. Representative EPMA analyses of unidentified iron-rich inclusions in sapphires from southern Vietnam.

Mineral phase analysis (wt.%)	Dak Nong		Di Linh		Krong Nang		Binh Thuan	
	DN73	DN89	DL14	DL50	KN05	KN19	PT17	PT18
SiO_2	0.33	0.02	nd	0.02	1.58	0.06	0.27	0.34
TiO_2	4.43	1.57	1.53	2.33	6.62	1.24	0.22	0.52
Al_2O_3	12.51	8.78	6.66	0.21	10.82	11.84	0.12	10.14
Cr_2O_3	0.18	nd	0.04	0.02	0.33	0.03	0.03	0.06
FeO_{total}	77.55	87.90	89.29	96.45	75.75	86.30	95.46	86.45
MnO	nd	0.14	1.49	0.41	0.08	0.18	1.81	1.57
MgO	0.98	0.18	0.29	1.36	0.15	0.37	0.88	0.05
ZnO	0.43	0.33	0.36	nd	0.31	0.51	nd	nd
CaO	0.12	nd	nd	nd	0.12	nd	nd	nd
NiO	0.02	nd	nd	0.03	0.10	nd	nd	nd
Total (oxides)	96.54	98.92	99.66	100.84	95.86	100.52	98.78	99.13
Formula 32(O)								
Si	0.110	0.001	–	0.008	0.523	0.020	0.104	0.116
Ti	1.106	0.051	0.405	0.645	1.648	0.310	0.063	0.133
Al	4.892	3.598	2.769	0.091	4.218	4.641	0.053	4.104
Cr	0.047	–	0.011	0.006	0.086	0.008	0.010	0.016
Fe^{3+}	9.753	12.429	13.148	14.925	8.501	11.658	15.700	12.266
Fe^{2+}	11.769	13.121	13.183	14.740	12.460	12.349	14.788	12.571
Mn	–	0.041	0.446	0.128	0.023	0.051	0.585	0.457
Mg	0.485	0.092	0.150	0.748	0.073	0.183	0.498	0.026
Zn	0.105	0.085	0.095	–	0.075	0.125	–	–
Ca	0.043	–	–	–	0.041	–	–	–
Ni	0.005	–	–	0.008	0.027	–	–	–
Total (cations)	28.315	29.784	30.206	31.299	27.676	29.345	31.801	29.690
ΣR^{2+}	12.407	13.339	13.874	15.624	12.699	12.708	15.871	13.054
ΣR^{3+}	15.908	16.078	16.333	15.667	14.453	16.617	15.826	16.519

Abbreviation: nd = not detected
Fe^{2+} and Fe^{3+} were recalculated from total FeO after the method of Droop (1987).
$\sum R^{2+} = Fe^{2+}+Mn+Mg+Zn+Ca+Ni$. $\sum R^{3+} = Ti+Al+Cr+Fe^{3+}$.

Pyrochlore was recognized as an inclusion in three sapphire samples from Dak Nong and a couple of samples from Krong Nang. They formed similarly red cubic crystals, which were commonly surrounded by radial cracks (figure 13). Based on SEM-EDS analysis, Smith et al. (1995) previously reported uranpyrochlore, $(Ca,U)_2(Ti, Nb, Ta)_2O_6$, in sapphires from Di Linh and Binh Thuan. EPMA analyses of pyrochlore in this study yielded a high U content (about 19–22% in ΣR^{2+}), a high Nb content leading to a Nb/Ta ratio ≥ 8, and a (Nb+Ta)/Ti ratio of about 2 (table 9), all within the compositional range of uranpyrochlore (Hogarth, 1977). These compositions were similar to those found in Australian sapphires from Anakie (Guo et al., 1996) and New England (Sutherland et al., 1998a).

DISCUSSION

It has been suggested that sapphire and ruby deposited within basaltic terranes could not have crystallized directly from basaltic magma (Coenraads, 1992; Levinson and Cook, 1994; Guo et al., 1996; Sutherland et al., 1998a, 2002, 2015; Khamloet et al., 2014; Promwongnan and Sutthirat, 2019). A corroded surface is a typical feature observed in basalt-associated sapphires, clearly indicating transport by the hot magma. This has also been reported for sapphires from Di Linh and Binh Thuan (Smith et al., 1995). A petrochemical study of sapphire-associated basalts from Dak Nong has also suggested that these xenocrystic sapphires may have formed in the boundary between the lower crust and upper mantle prior to corrosive transport in alkali basaltic magma

TABLE 9. Representative EPMA analyses of pyrochlore inclusions found in sapphires from southern Vietnam and Australia.

Mineral phase analysis (wt.%)	Southern Vietnam				Australia	
	Dak Nong		Krong Nang		Anakie[a]	New England[b]
	DN35	DN77	KN18	KN36		
SiO_2	0.23	0.37	0.55	0.33	na	0.00
TiO_2	11.67	11.20	10.59	11.63	11.48	10.14
FeO	1.68	1.38	1.54	1.57	1.51	0.30
MnO	0.37	0.19	0.08	0.03	na	na
CaO	6.86	6.63	6.26	6.89	5.58	5.49
Na_2O	4.33	5.11	4.44	5.24	4.27	5.92
K_2O	0.04	0.05	0.06	0.09	na	na
Nb_2O_5	33.61	32.24	33.88	33.03	32.99	38.48
Ta_2O_5	6.05	6.50	5.97	6.34	6.58	4.44
ThO_2	7.88	7.31	7.00	7.61	8.56	1.99
UO_2	22.28	23.06	23.83	22.32	21.80	30.88
ZrO_2	0.08	0.15	0.01	0.02	0.20	na
Y_2O_3	nd	0.08	0.12	0.08	0.66	na
Ce_2O_3	0.12	0.35	0.34	0.28	0.48	na
Nd_2O_3	0.14	0.17	nd	0.06	0.54	na
Total (oxides)	95.36	94.40	94.67	95.51	94.90	97.64
Formula 6(O)						
Si	0.016	0.026	0.039	0.023	–	0.000
Ti	0.605	0.591	0.557	0.601	0.607	0.518
Fe	0.097	0.081	0.090	0.090	0.089	0.017
Mn	0.022	0.011	0.005	0.002	–	–
Ca	0.506	0.498	0.469	0.508	0.420	0.400
Na	0.578	0.643	0.601	0.698	0.582	0.780
K	0.003	0.004	0.005	0.008	–	–
Nb	1.046	1.022	1.070	1.026	1.048	1.182
Ta	0.113	0.124	0.113	0.118	0.126	0.082
Th	0.123	0.117	0.111	0.119	0.137	0.031
U	0.341	0.360	0.370	0.341	0.341	0.467
Zr	0.003	0.005	0.000	0.001	0.007	0.000
Y	–	0.003	0.005	0.003	0.025	–
Ce	0.003	0.009	0.009	0.007	0.012	–
Nd	0.000	0.000	–	0.000	0.014	–
Total (cations)	3.460	3.498	3.444	3.546	3.411	3.477
ΣR^{2+}	1.674	1.719	1.651	1.767	1.628	1.694
Nb/Ta	9	8	9	9	8	14
(Nb+Ta)/Ti	2	2	2	2	2	2
$U/\Sigma R^{2+}$	20	21	22	19	21	28

Abbreviation: na = not analyzed; nd = not detected
ΣR^{2+} = Fe+Mn+Ca+Na+K+Th+U+Zr+Y+Ce+Nd
[a]*Guo et al. (1996)*
[b]*Sutherland et al. (1998a)*

(Garnier et al., 2005). Moreover, a hypothesis has recently been proposed that the original crystallization of alluvial Dak Nong sapphires would have taken place in the shallow crust within an iron-rich syenite melt in collaboration with carbonate-H_2O-CO_2 fluid phases, based on the geochemistry of syngenetic mineral inclusions (i.e., zircon, columbite, oligoclase, and Al-Ti-hematite) (Izokh et al., 2010).

Based on the results of this detailed study, the most common syngenetic mineral inclusions (ferrocolumbite, alkali feldspar, and zircon) were similar in composition to those in Dak Nong sapphires (Izokh et al., 2010) as well as alkaline felsic inclusion groups in other alluvial basalt-related sapphires (Guo et al., 1996). Although hercynite spinel and ilmenite (titanohematite) inclusions observed in this study were quite different from Al-Ti-hematite in Dak Nong sapphires (containing 85.6 wt.% Fe_2O_3, 11.9 wt.% Al_2O_3, and 1.57 wt.% TiO_2 as reported by Izokh et al., 2010), they still favored igneous sources instead of metamorphic sources. Although columbite and pyrochlore in the studied sapphires were chemically close to the inclusions Guo et al. (1996) proposed as representing a carbonatite assemblage, they were also similar to those found in alluvial basalt-associated sapphires from silicate melt origin (Sutherland et al., 1998a). Therefore, both columbite and pyrochlore may relate to silicate melts to indicate the original source of these sapphires.

Consequently, a unique mineral inclusion suite including alkali feldspar, zircon, hercynitic spinel, and ilmenite appears to have crystallized from alkaline felsic magma, which is relevant to the original source of sapphires from southern Vietnam. This magmatism should have taken place extensively prior to fractionated crystallization in the lower crust. This model agrees well with the genetic model proposed by Aspen et al. (1990), Sutherland et al. (1998a, 2009), Pin et al. (2006), Zaw et al. (2006), Upton et al. (2009), Khamloet et al. (2014), and Promwongnan and Sutthirat (2019).

Based on the geological setting in southern Vietnam, granite and granosyenite occurred in the Triassic and Cretaceous during orogenic periods due to Indosinian-Yangtze (South China) collision and Paleo-Pacific plate subduction, respectively (Carter et al., 2001; Nguyen et al., 2004; Tri and Khuc, 2011; Shellnutt et al., 2013). Subsequently, alkali basaltic magmas in southern Vietnam had probably been derived from garnet peridotite of the asthenosphere at high pressure (<4 GPa) and high temperature (about 1470°C) (Hoang and Flower, 1998), and mixed with recycling oceanic crustal materials from Paleo-Pa-

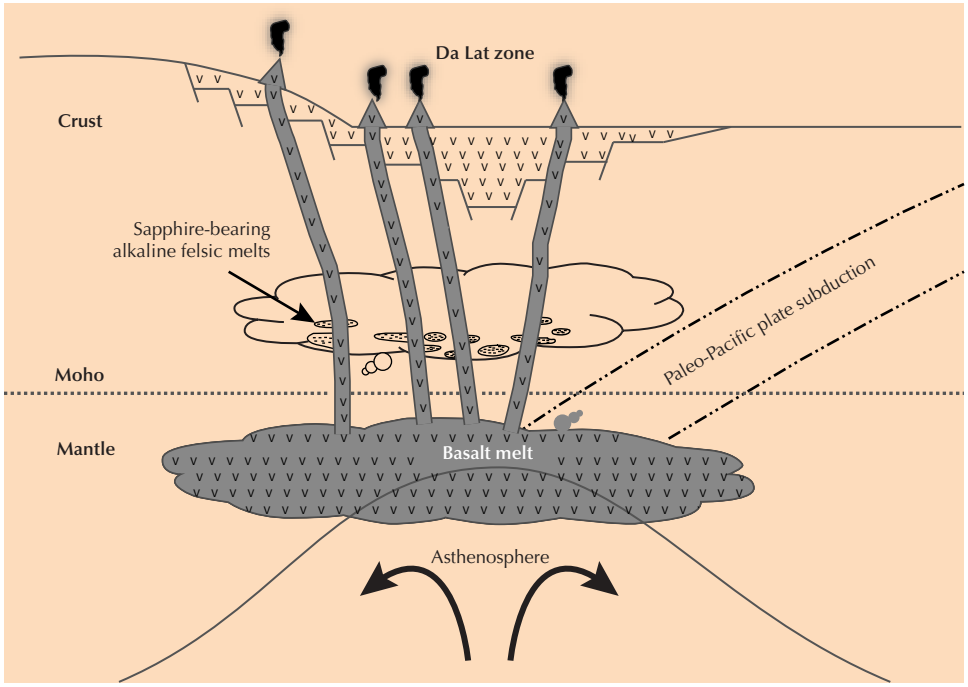

Figure 14. This illustration shows an alkaline felsic melt as the environment for sapphire origin, based on the alkali basalt and crustal evolution models for southern Vietnam (Hoang and Flower, 1998; Tri and Khuc, 2011; Anh et al., 2018).

cific plates that subducted beneath the Southeast Asian continental margin (Anh et al., 2018) during the early Tertiary Indian-Eurasian collision. Rising penetration at close to the Moho, an unconformity zone boundary between lower continental crust and upper mantle, located at about 32–75 km depth (Teng et al., 2013), the heat and volatility separated from these alkaline mafic melts caused the extensive melting of silicate rocks (granite and granosyenite) at lower-crust level with the formation of alkaline felsic melt (figure 14). Sapphires should have crystallized directly during the slow cooling of this alkaline felsic melt. Afterwards, the alkali basaltic magma from the asthenosphere of mantle rose and then brought these sapphires onto the surface via volcanic eruption.

CONCLUSIONS

Mineral inclusions including ferrocolumbite, zircon, alkali feldspar, hercynite spinel, ilmenite (titanohematite), and pyrochlore were identified in sapphires from the main deposits in southern Vietnam. On the basis of chemical composition, they can be mostly grouped into alkaline felsic suites. An alkaline felsic melt is proposed as the crystallization environment for the original formation of these sapphires. Detailed studies on U/Pb dating and trace analysis of zircon inclusions should be carried out to support time scale and original formation of the sapphire hosts. Moreover, unidentified iron-bearing inclusions may give more significant information related to the crystallization environment.

ABOUT THE AUTHORS

Mrs. Vu is a doctor's degree student in geology at Chulalongkorn University in Bangkok and a lecturer at the Faculty of Geology, University of Science, Vietnam National University in Ho Chi Minh City. Dr. Salam and Dr. Fanka are lecturers at the Geology Department, Faculty of Science, Chulalongkorn University. Dr. Belousova is a research fellow at the Department of Earth and Planetary Science, Macquarie University in Sydney. Dr. Sutthirat (chakkaphan.s@chula.ac.th) is a professor of earth sciences at the Geology Department, Faculty of Science, Chulalongkorn University and an academic advisor to the Gem Testing Laboratory of the Gem and Jewelry Institute of Thailand (GIT).

ACKNOWLEDGMENTS

The authors would like to thank all staff members of the Geology Department, Faculty of Science, Chulalongkorn University, for their support in sample preparation and analyses. This research is a part of PhD thesis of the first author who has been supported by the Scholarship Program for ASIAN Countries of Chulalongkorn University.

REFERENCES

Anh H.T.H., Choi S.H., Yu Y., Hieu P.T., Hoang N.K., Ryu J. (2018) Geochemical constraints on the spatial distribution of recycled oceanic crust in the mantle source of late Cenozoic basalts, Vietnam. *Lithos*, Vol. 296, pp. 382–395, http://dx.doi.org/10.1016/j.lithos.2017.11.020

Aspen P., Upton B.G.J., Dicken A.P. (1990) Anorthoclase, sanidine and associated megacrysts in Scottish alkali basalts: High pressure syenitic debris from upper mantle sources? *European Journal of Mineralogy*, Vol. 2, pp. 503–517, http://dx.doi.org/10.1127/ejm/2/4/0503

Barr S., MacDonald A. (1981) Geochemistry and geochronology of late Cenozoic basalts of Southeast Asia: Summary. *Geological Society of America Bulletin*, Vol. 92, No. 8, pp. 1069–1142, http://dx.doi.org/10.1130/0016-7606(1981)92%3C508:GAGOLC%3E2.0.CO;2

Belousova E., Griffin W., O'Reilly S., Fisher N. (2002) Igneous zircon: Trace element composition as an indicator of source rock type. *Contributions to Mineralogy and Petrology*, Vol. 143, No. 5, pp. 602–622, http://dx.doi.org/10.1007/s00410-002-0364-7

Carter A., Roques D., Bristow C., Kinny P. (2001) Understanding Mesozoic accretion in Southeast Asia: Significance of Triassic thermotectonism (Indosinian orogeny) in Vietnam. *Geology*, Vol. 29, No. 3, pp. 211–214, http://dx.doi.org/10.1130/0091-7613(2001)029

Cassidy K., Groves D.I., Binns R.A. (1988) Manganoan ilmenite formed during regional metamorphism of Archean mafic and ultramafic rocks from Western Australia. *Canadian Mineralogist*, Vol. 26, pp. 999–1012.

Cerný P., Ercit T.S. (1985) Some recent advances in the mineralogy and geochemistry of Nb and Ta in rare-element granitic pegmatites. *Bulletin de Minéralogie*, Vol. 108, pp. 499–532, http://dx.doi.org/10.3406/bulmi.1985.7846

Coenraads R. (1992) Sapphires and rubies associated with volcanic provinces: Inclusions and surface features shed light on their origin. *Australian Gemmologist*, Vol. 18, No. 3, pp. 70–78.

Deer W.A., Howie R.A., Zussman J. (2013) *An Introduction to the Rock-Forming Minerals*. Longman, Essex, UK, 696 pp.

Droop G.T.R. (1987) A general equation for estimating Fe^{3+} concentrations in ferromagnesian silicates and oxides from microprobe analyses, using stoichiometric criteria. *Mineralogical Magazine*, Vol. 51, No. 361, pp. 431–435, http://dx.doi.org/10.1180/MINMAG.1987.051.361.10

Faria D.L.A., Silva S.V., Oliveira M.T.M. (1997) Raman microspectroscopy of some iron oxides and oxyhydroxides. *Journal of Raman Spectroscopy*, Vol. 28, No. 11, pp. 873–878, http://dx.doi.org/10.1002/(SICI)1097-4555(199711)28:11%3C873:AID-JRS177%3E3.0.CO;2-B

Fuhrman M., Frost B.R., Lindsley D.H. (1988) Crystallization conditions of the Sybille Monzosyenite, Laramie Anorthosite Complex, Wyoming. *Journal of Petrology*, Vol. 29, No. 3, pp. 699–729, http://dx.doi.org/10.1093/petrology/29.3.699

Garnier V., Ohnenstetter D., Giuliani G., Fallick A.E., Trinh P., Quang V., Van L., Schwarz D. (2005) Basalt petrology, zircon ages and sapphire genesis from Dak Nong, southern Vietnam. *Mineralogical Magazine*, Vol. 69, No. 1, pp. 21–38, http://dx.doi.org/10.1180/0026461056910233

Guo J., O'Reilly S.Y., Griffin W.L. (1996) Corundum from basaltic terrains: A mineral inclusion approach to the enigma. *Contributions to Mineralogy and Petrology*, Vol. 122, No. 4, pp. 368–386, http://dx.doi.org/10.1007/s004100050134

Hoa T.T., Phuong N.T., Anh T.T., Van V.V., Y N.V., Hoang N., Thanh H.H., Anh P.L., Nien B.A., Hung T.Q., Dung P.T., Lam T.H., Hang H.V., Anh T.V., Chuong V.D., Hung P.V., Quan V.M. and eds. (2005) Study of forming conditions and distribution laws of precious and rare minerals related to magmatic activity in Central Vietnam and Tay Nguyen Highlands. *State-level Project, code DTDL-2003/07*, Vol. I, pp. 347 (in Vietnamese).

Hoang N., Flower M. (1998) Petrogenesis of Cenozoic basalts from Vietnam: Implication for origins of a 'diffuse igneous province'. *Journal of Petrology*, Vol. 39, No. 3, pp. 369–395, http://dx.doi.org/10.1093/petroj/39.3.369

Hoang T.H.A., Choi S.H., Yu Y., Pham T.H., Nguyen K.H., Ryu Y. (2018) Geochemical constraints on the spatial distribution of recycled oceanic crust in the mantle source of late Cenozoic basalts, Vietnam. *Lithos*, Vol. 296-299, pp. 382–395, http://dx.doi.org/10.1016/j.lithos.2017.11.020

Hogarth D.D. (1977) Classification and nomenclature of the pyrochlore group. *American Mineralogist*, Vol. 62, No. 5-6, pp. 403–410.

Huong L.T.T., Vuong B.T.S., Khoi N.N., Satitkune S., Wanthanachaisaeng B., Hofmeister W., Häger T., Hauzenberger C. (2016) Geology, gemmological properties and preliminary heat treatment of gem-quality zircon from the Central Highlands of Vietnam. *Journal of Gemmology*, Vol. 35, No. 4, pp. 308–318, http://dx.doi.org/10.15506/JOG.2016.35.4.308

Hutchison C.S. (1989) *Geological Evolution of South-east Asia*. Clarendon Press, Oxford, UK.

Izokh A.E., Smirnov S.Z., Egorova V.V., Anh T.T., Kovyazin S.V., Phuong N.T., Kalinina V.V. (2010) The conditions of formation of sapphire and zircon in the areas of alkali-basaltoid volcanism in Central Vietnam. *Russian Geology and Geophysics*, Vol. 51, No. 7, pp. 719–733, http://dx.doi.org/10.1016/j.rgg.2010.06.001

Khamloet P., Pisutha-Arnond V., Sutthirat, C. (2014) Mineral inclusions in sapphire from the basalt-related deposit in Bo Phloi, Kanchanaburi, western Thailand: Indication of their genesis. *Russian Geology and Geophysics*, Vol. 55, No. 9, pp. 1087–1102, http://dx.doi.org/10.1016/j.rgg.2014.08.004

Lee T., Lo C.H., Chung S.L., Chen C.Y., Wang P.L., Lin W.P., Hoang N., Chi C., Yem N. (1998) $^{40}Ar/^{39}Ar$ Dating Result of Neogene Basalts in Vietnam and its Tectonic Implication. *Mantle Geodynamics and Plate Interactions in East Asia*, *AGU Monograph*, Vol. 27, pp. 317–330, http://dx.doi.org/10.1029/GD027p0317

Lepvrier C., Vuong N.V., Maluski H., Thi P.T., Vu T.V. (2008) Indosinian tectonics in Vietnam. *Comptes Rendus Geoscience*, Vol. 340, No. 2, pp. 94–111, http://dx.doi.org/10.1016/j.crte.2007.10.005

Levinson A.A., Cook F.A. (1994) Gem corundum in alkali basalt: Origin and occurrence. *G&G*, Vol. 30, No. 4, pp. 253–262, http://dx.doi.org/10.5741/GEMS.30.4.253

Lindsley D.H. (1991) Experimental studies of oxide minerals. In D.H. Lindsley, Ed., *Oxide Minerals: Petrologic and Magnetic Significance. Reviews in Mineralogy*, Vol. 25, Mineralogical Society of America, pp. 69–106.

Long P.V., Vinh H., Garnier V., Giuliani G., Ohnenstetter D., Lhomme T., Schwarz D., Fallick A.E., Dubessy J., Trinh P.T. (2004) Gem corundum deposits in Vietnam. *Journal of Gemmology*, Vol. 29, No. 3, pp. 129–147, http://dx.doi.org/10.15506/JOG.2004.29.3.129

Mackay D., Simandl G. (2015) Pyrochlore and columbite-tantalite as indicator minerals for specialty metal deposits. *Geochemistry: Exploration, Environment, Analysis*, Vol. 15, No. 2-3, pp. 167–178, http://dx.doi.org/10.1144/geochem2014-289

Metcalfe I. (1988) Origin and assembly of South-east Asian continental terranes. *Geological Society, London, Special Publications*, Vol. 37, No. 1, pp. 101–118, http://dx.doi.org/10.1144/GSL.SP.1988.037.01.08

——— (1996) Pre-Cretaceous evolution of SE Asian terranes. *Geological Society, London, Special Publications*, Vol. 106, No. 1, pp. 97–122, http://dx.doi.org/10.1144/GSL.SP.1996.106.01.09

——— (2009) Late Palaeozoic and Mesozoic tectonic and palaeogeographical evolution of SE Asia. In E. Buffetaut, G. Cuny, J. Le Loeuff, and V. Suteethorn, Eds., *Late Palaeozoic and Mesozoic Ecosystems in SE Asia*. The Geological Society of London, Special Publication, Vol. 315, No. 1, pp. 7–23.

——— (2011) Palaeozoic-Mesozoic history of SE Asia. *Geological Society of London Special Publications*, Vol. 355, No. 1, pp. 7–35, http://dx.doi.org/10.1144/SP355.2

Nguyen T., Satir M., Siebel W., Chen F. (2004) Granitoids in the Dalat zone, southern Vietnam: Age constraints on magmatism and regional geological implications. *International Journal of Earth Sciences*, Vol. 93, No. 3, pp. 329–340, http://dx.doi.org/10.1007/s00531-004-0387-6

Palke A.C., Saeseaw S., Renfro N.D., Sun Z., McClure S. (2019) Geographic origin determination of blue sapphire. *G&G*, Vol. 55, No. 4, pp. 536–579, http://dx.doi.org/10.5741/gems.55.4.536

Pin C., Monchoux P., Paquette J.L., Azambre B., Wang P.C., Martin R.F. (2006) Igneous albititic dikes in orogenic lherzolites, Western Pyrenees, France: A possible source for corundum and alkali feldspar xenocrysts in basalt terranes. II. Geochemical and petrogenetic considerations. *Canadian Mineralogist*, Vol. 44, No. 4, pp. 817–842, http://dx.doi.org/10.2113/gscanmin.44.4.817

Promwongnan S., Sutthirat C. (2019) Mineral inclusions in ruby and sapphire from the Bo Welu gem deposit in Chanthaburi, Thailand. *G&G*, Vol. 55, No. 3, pp. 354–369, http://dx.doi.org/10.5741/GEMS.55.3.354

Rangin C., Huchon P., Le Pichon X., Bellon H., Lepvrier C., Roques D., Hoe N.D., Quynh P.V. (1995) Cenozoic deformation of central and south Vietnam. *Tectonophysics*, Vol. 251, No. 1-4, pp. 180–196, http://dx.doi.org/10.1016/0040-1951(95)00006-2

Rubatto D., Gebauer D. (2000) Use of cathodoluminescence for U-Pb zircon dating by ion microprobe: Some examples from the Western Alps. In M. Pagel et al., Eds., *Cathodoluminescence in Geosciences*, Springer, Berlin, pp. 373–400.

Saminpanya S., Sutherland F. (2011) Different origins of Thai area sapphire and ruby, derived from mineral inclusions and co-existing minerals. *European Journal of Mineralogy*, Vol. 23, No. 4, pp. 683–694, http://dx.doi.org/10.1127/0935-1221/2011/0023-2123

Sengör A.M.C., Altiuner D., Cin A., Ustaömer T., Hsü K.J. (1988) Origin and assembly of the Tethyan orogenic collage at the expense of Gondwana land. In M.G. Audley-Chalerles and A. Hallam, Eds., Gondwana and Tethys. *The Geological Society of London, Special Publication*, Vol. 37, No. 1, pp. 119–181, http://dx.doi.org/10.1144/GSL.SP.1988.037.01.09

Shellnutt J., Lan C.-Y., Long T., Usuki T., Yang H.-J., Mertzman S., Iizuka Y., Chung S.-L., Wang K.-L., Hsu W.-Y. (2013) Formation of Cretaceous Cordilleran and post-orogenic granites and their microgranular enclaves from the Dalat zone, southern Vietnam: Tectonic implications for the evolution of Southeast Asia. *Lithos*, Vol. s 182–183, pp. 229–241, http://dx.doi.org/10.1016/j.lithos.2013.09.016

Smith C.P., Kammerling R.C., Keller A.S., Peretti A., Scarratt K.V., Khoa N.D., Repetto S. (1995) Sapphires from southern Vietnam. *G&G*, Vol. 31, No. 3, pp. 168–186, http://dx.doi.org/10.5741/GEMS.31.3.168

Sutherland F., Hoskin P., Fanning C., Coenraads R. (1998a) Models of corundum origin from alkali basaltic terrains: A reappraisal. *Contributions to Mineralogy and Petrology*, Vol. 133, No. 4, pp. 356–372, http://dx.doi.org/10.1007/s004100050458

Sutherland F., Schwarz D., Jobbins E.A., Coenraads R., Webb G. (1998b) Distinctive gem corundum suites from discrete basalt fields: A comparative study of Barrington, Australia and West Pailin, Cambodia, Gemfields. *Journal of Gemmology*, Vol. 26, No. 2, pp. 65–85.

Sutherland F., Bosshart G., Fanning C., Hoskin P.W.O., Coenraads R. (2002) Sapphire crystallization, age and origin, Ban Huai Sai, Laos: Age based on zircon inclusions. *Journal of Asian Earth Sciences*, Vol. 20, No. 7, pp. 841–849, http://dx.doi.org/10.1016/S1367-9120(01)00067-0

Sutherland F.L., Zaw K., Meffre S., Giuliani G., Fallick A.E., Graham L., Webb G.B. (2009) Gem-corundum megacrysts from east Australian basalt fields: Trace elements, oxygen isotopes and origins. *Australian Journal of Earth Sciences*, Vol. 56, No. 7, pp. 1003–1022, http://dx.doi.org/10.1080/08120090903112109

Sutherland F.L., Piilonen P.C., Zaw K., Meffre S., Thompson J. (2015) Sapphire within zircon-rich gem deposits, Bo Loei, Ratanakiri Province, Cambodia: Trace elements, inclusions, U–Pb dating and genesis. *Australian Journal of Earth Sciences*, Vol. 62, No. 6, pp. 761–773.

Teng J., Zhang Z., Zhang Y., Pi J., Deng Y., Zhang X., Wang C.-Y., Gao R., Liu C. (2013) Moho depth, seismicity and seismogenic structure in China mainland. *Tectonophysics*, Vol. 627, pp. 108–121, http://dx.doi.org/10.1016/j.tecto.2013.11.008

Tri T.V., Khuc V. (2011) *Geology and Earth Resources of Vietnam*. General Department of Geology and Minerals of Vietnam, Ha Noi, Publishing House for Science and Technology, 634 pp.

Upton B.J.G., Finch A.A., Slaby E. (2009) Megacrysts and salic xenoliths in Scottish alkali basalts: Derivatives of deep crustal intrusions and small melt fractions from the upper mantle. *Mineralogical Magazine*, Vol. 73, No. 6, pp. 943–956, http://dx.doi.org/10.1180/minmag.2009.073.6.943

Vu D.T.A. (2010) Petrographical characteristics and genesis of corundum in Vietnam. University of Science, VNU-Ho Chi Minh City, 120 pp.

——— (2018) Gemological characteristics and the quality of sapphire from Krong H'Nang - Dak Lak. *Science and Technology Development Journal – Natural Sciences*, Vol. 1, No. T5, pp. 263–269, http://dx.doi.org/10.32508/stdjns.v1iT5.559

Williams I.S., Claesson S. (1987) Isotopic evidence for the Precambrian provenance and Caledonian metamorphism of high grade paragneisses from the Seve Nappes, Scandinavian Caledonides. *Contributions to Mineralogy and Petrology*, Vol. 97, No. 2, pp. 205–217, http://dx.doi.org/10.1007/bf00371240

Zaw K., Sutherland F.L., Dellapasqua F., Ryan C.G., Yui T., Mernagh T.P., Duncan D. (2006) Contrasts in gem corundum characteristics, eastern Australian basaltic fields: Trace elements, fluid/melt inclusions and oxygen isotopes. *Mineralogical Magazine* Vol. 70, No. 6, pp. 669–687, http://dx.doi.org/10.1180/0026461067060356

Lab Notes

Editors
Thomas M. Moses | Shane F. McClure

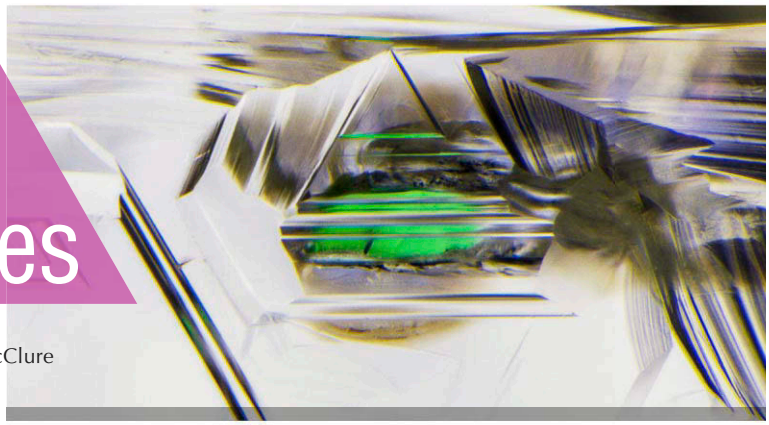

DIAMOND

Blue "Graining" in Green-Yellow Diamond

It is not uncommon for fancy-color diamonds to possess uneven color distribution. This is generally seen as diffuse concentrations of color that may arise from changes in growth environment, natural or artificial irradiation, or as linear graining. Color zoning from radiation is often diffuse and blue or green in color, whereas graining exists as sharp distinct lines and is typically brown, pink, or yellow in color. Blue color zones resembling graining, however, were recently observed in a 1.50 ct Fancy Intense green-yellow diamond (figure 1) at the Carlsbad laboratory.

The diamond was type IaAB and showed clear spectroscopic evidence of both high-pressure, high-temperature (HPHT) treatment and artificial irradiation. Under magnification, the stone showed reflective cubic graining and strong green luminescence with fiber-optic lighting. When immersed, it revealed a blue colored crown (created during the artificial radiation color treatment) and a yellow pavilion. This type of color zoning is unusual, as artificial radiation is typically done on the pavilion of faceted diamonds, not the crown. When viewed under magnification with diffused light, the stone displayed yellow and brown graining as well as peculiar blue grain lines (figure 2). Graining is associated with regions of planar lattice deformities, or plastic deformation that formed when the diamond was deep in the earth's mantle. Colored graining occurs when regions of plastic deformation coexist with clusters of lattice vacancies or complex nitrogen defects.

Figure 1. The 1.50 ct Fancy Intense green-yellow round brilliant diamond as seen from the crown.

Blue graining has rarely been seen as a cause of blue coloration in treated or untreated diamonds. Blue color is almost always a result of trapped boron atoms within the diamond lattice (type IIb; usually with a uniform color distribution) or exposure to natural or artificial radiation (usually with a patchy color). Given that no boron impurities were seen in the infrared spectra, radiation damage was most likely the cause of this blue "graining."

Figure 2. Blue "graining" was seen in this 1.50 ct HPHT-treated and irradiated Fancy Intense green-yellow diamond. Note the dark yellow graining also visible in this image. Field of view 4.90 mm.

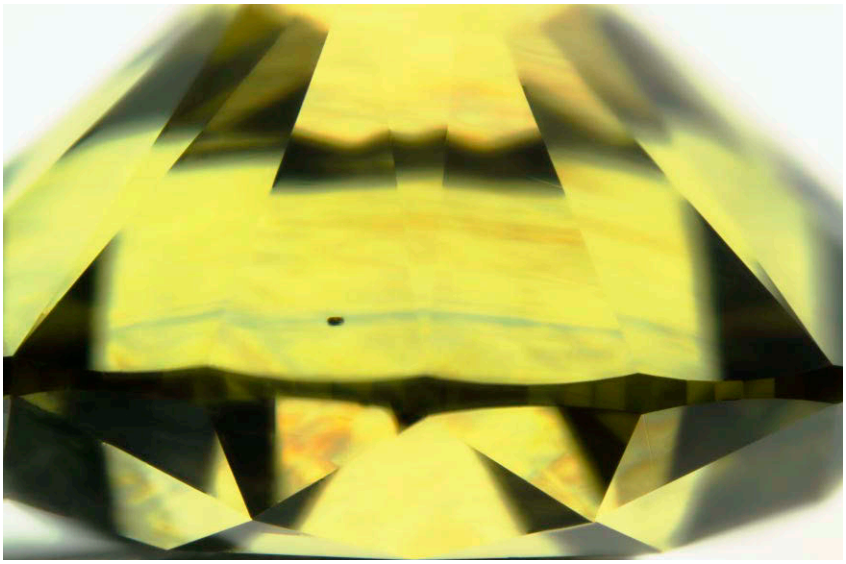

Editors' note: All items were written by staff members of GIA laboratories.

GEMS & GEMOLOGY, Vol. 56, No. 4, pp. 516–525.

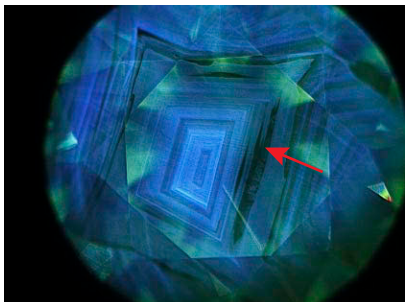

Figure 3. DiamondView imaging showed strong blue fluorescence and inert zones corresponding to nitrogen-rich and nitrogen-poor areas, respectively. The inert zone shown by the red arrow correlated with the blue "graining" seen in figure 2.

When diamonds are analyzed with DiamondView, nitrogen-rich areas often show strong blue fluorescence due to N3 defects while lower-nitrogen areas (type IIa) are sometimes inert. The diamond showed strong blue fluorescence in an octahedral growth pattern with streaky inert patches (figure 3). These inert streaks appeared to correspond with the location of the blue zone, as seen under magnification in diffused light. When viewed through the pavilion, the zoning on the crown has a grain-like appearance (figure 2).

We propose that the blue zone with a grain-like appearance formed during artificial irradiation treatment within a region of diamond containing very low nitrogen impurities. Initially, this stone likely had a brown color. HPHT treatment then influenced the bodycolor by destroying the initial brown color before creating most of the yellow component as well as green luminescence. When artificial irradiation treatment followed, we believe that vacancies were created in higher concentrations within the low-nitrogen regions to create the blue color zone. This is similar to the way type IIa diamonds are HPHT treated and irradiated to a blue color. This stone is a fine illustration of how inherent heterogeneities of impurity distribution within diamond can be differentially affected by treatments.

Britni LeCroy and Virginia A. Schwartz

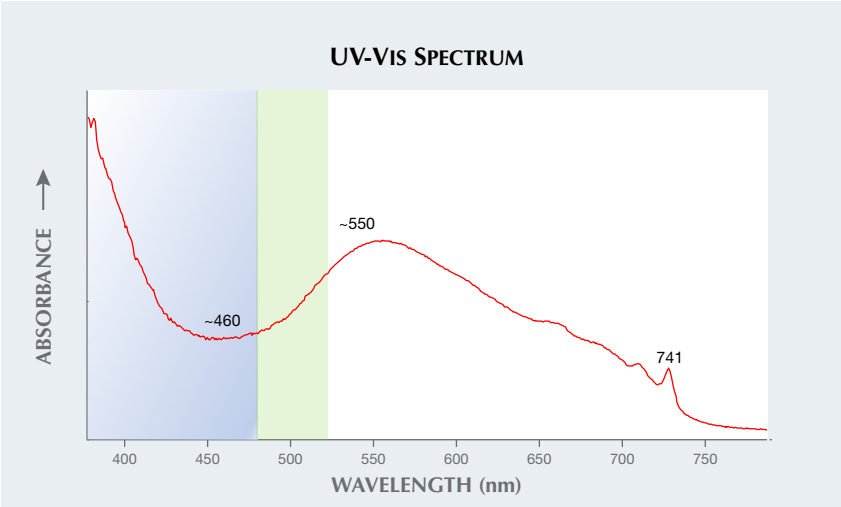

Figure 5. UV-visible spectrum collected from the 0.53 ct diamond showing the ~550 nm absorption band and blue transmission window at ~460 nm. Also observed is the GR1 peak at 741 nm.

Irradiated Blue Diamond

Blue is a very desirable color for diamond. A rare type of blue to violet hydrogen-rich diamond came from the recently closed Argyle mine in Australia ("Gray-to-blue-to-violet hydrogen-rich diamonds from the Argyle mine, Australia," C.H. van der Bogert et al., Spring 2009 *G&G*, pp. 20–37). Prior to the discovery of the Argyle mine, *G&G* reported on a rare 4.28 ct bluish gray diamond with the 550 nm band feature (R. Crowningshield, "Developments and Highlights at GIA's Lab in New York," Fall 1969 *G&G*, pp. 89–90).

Figure 4. The 0.53 ct Fancy Light blue pear-shaped diamond. The face-up color in this image does not appear blue or match the colorimeter image in figure 7 (right).

Recently submitted to the New York laboratory for identification was a 0.53 ct pear-shaped diamond graded as Fancy Light blue on GIA's color grading system (figure 4).

Gemological features typical of natural pink type Ia diamonds were observed under the microscope, including very strong graining or glide planes with a pink color. IR spectroscopy confirmed that this is a type Ia diamond. The unusual graining (haziness) seen in figure 4 contradicts the blue color of this diamond.

A UV-visible absorption spectrum collected from this diamond showed a broad band at about 550 nm, typical for this type of diamond and the pink color attributed to it (resulting from plastic deformation of the crystal lattice during growth or post-growth). A GR1 (general radiation damage) peak at about 741 nm was also observed. This radiation damage is responsible for the green and blue colors observed in some diamonds, both naturally colored and treated (figure 5).

This is a very unusual combination of spectral features in the same diamond. While the strong 550 nm band absorption creating a strong blue

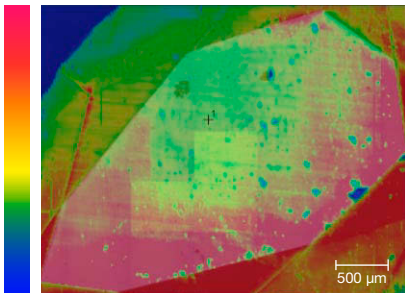

Figure 6. GR1 radiation damage (red) is concentrated on one side of the diamond table facets.

Figure 7. GIA colorimeter images captured the original Fancy Light pinkish purple color (left) and the treated Fancy Light blue color (right) of the 0.53 ct pear-shaped diamond.

transmission window at ~460 nm was responsible for the pink color, the relatively strong GR1 absorption and its side band caused the near-violet color. When mapped with a Raman photoluminescence microscope, this GR1 radiation damage could be seen concentrated on one side of the diamond (figure 6). This concentration of radiation damage, in conjunction with the absorption spectroscopy and gemological features, enabled the confident determination that this diamond had been artificially irradiated to create the desirable blue color. This is a great example of color engineering. Subsequent to this determination, a GIA records query search revealed that this diamond had a previous report with a Fancy Light pinkish purple color grade (figure 7).

Paul Johnson and Surjit Dillon Wong

Large Type IIa Diamond from Arkansas, USA

The GIA lab in Carlsbad recently had the opportunity to examine a truly "all-American" diamond. The 1.16 ct near-colorless cushion-cut stone was submitted for a grading report along with a certificate from Crater of Diamonds State Park in Arkansas, USA, indicating it was cut from a 2.73 ct rough diamond mined in July 2020 by William Dempsey. The diamond was reported to have been cut and polished domestically in North Dakota (figure 8). It was ultimately graded as H color (near colorless) with SI_1 clarity (due to an internal feather). Crater of Diamonds State Park is the only feedig diamond mine in the world where anyone with a prospector's spirit can search in hopes of finding a true gem (Summer 2020 Gem News International, "Finders, keepers: Field trip to Crater of Diamonds, USA," pp. 311–314). At 2.73 ct, the rough stone was exceptionally large for an Arkansas diamond, most of which come in significantly under 1 carat.

Researchers at GIA were excited to study this unique stone, especially with the prospect of analyzing inclusions that might shed light on the geological history of the Arkansas diamond deposit. However, the diamond turned out to be fairly clean with no crystalline inclusions. Somewhat unexpectedly, FTIR spectroscopy revealed the stone to be a type IIa diamond with no measurable nitrogen impurities. Type IIa diamonds are extremely rare among natural diamonds, and some have even been shown to grow much deeper in the earth than most type I diamonds (E.M. Smith et al., "Large gem diamonds from metallic liquid in Earth's deep mantle," *Science*, Vol. 354, No. 6318, pp. 1403–1405). The lack of inclusions in the stone was consistent with its type IIa character. Imaging with the DiamondView instrument showed relatively even blue fluorescence. Photoluminescence spectroscopy confirmed the natural origin of the diamond.

Discovering a type IIa gem diamond is remarkable enough, but uncovering one from a source in the United States, where few diamonds occur, is definitely a noteworthy event.

Aaron C. Palke and Christopher M. Breeding

Figure 8. A 1.16 ct type IIa diamond recovered in 2020 from Crater of Diamonds State Park in Arkansas.

Artificial GLASS Imitating a Paraíba Tourmaline

Recently the Carlsbad laboratory examined two transparent bluish green prisms for identification service (figure 9). The submitted prisms weighed 1.91 ct and 1.92 ct and contained eye-visible clusters of reflective brownish metallic crystal inclusions along with small cavities and minor abrasions. At first glance, these stones resembled either Paraíba tourmaline with copper inclusions or possibly emerald with pyrite inclusions.

Standard gemological testing revealed a single refractive index of 1.50 and a hydrostatic specific gravity of 2.43. Both stones fluoresced weak green to long-wave UV light and weak to medium green to short-wave UV light. Although the six-sided, trigonal prisms had well-formed "crys-

Figure 9. These two pieces of glass with copper inclusions, weighing 1.91 and 1.92 ct, appear to have been manufactured to imitate natural copper-bearing Paraíba tourmaline crystals.

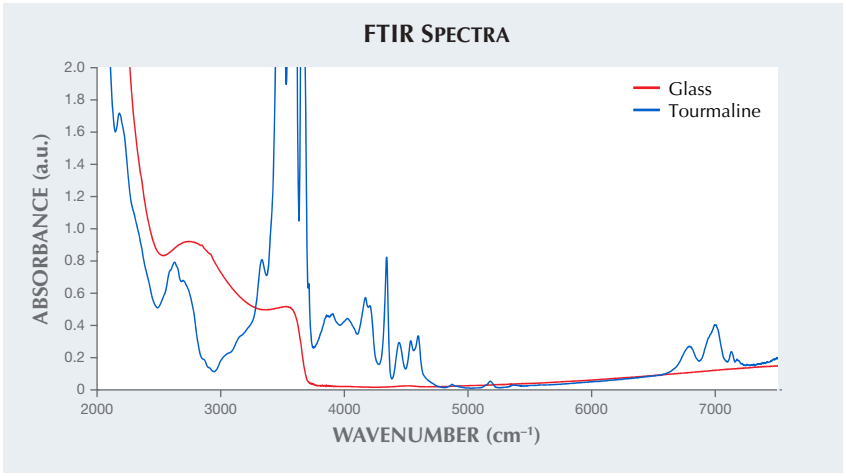

Figure 11. The FTIR spectrum of one of the glass imitations of tourmaline (red trace) was consistent with manmade glass, while the FTIR spectrum for tourmaline (blue trace) is distinctly different.

tal-like" shapes resembling tourmaline, the refractive index ruled out that material.

Microscopic examination with fiber-optic lighting showed trapped gas bubbles, flow structure, and a distinct boundary where two types of glasses, with and without metallic inclusions, were fused together. Areas of encapsulated glass exhibited a light yellow bodycolor and contained geometric metallic crystals and gas bubbles (figure 10). Due to the mixture of the fused glasses, it was obvious that the prisms were manmade.

Infrared spectroscopy confirmed our identification of manmade glass. The FTIR spectrum for manmade glass is very different than that of tourmaline (see figure 11). Further testing with EDXRF showed the presence of Cu, consistent with the copper color of the minute metallic crystal inclusions.

Figure 10. Areas of encapsulated goldstone glass exhibited a light yellow bodycolor and contained geometric copper crystals and gas bubbles. Field of view 3.52 mm.

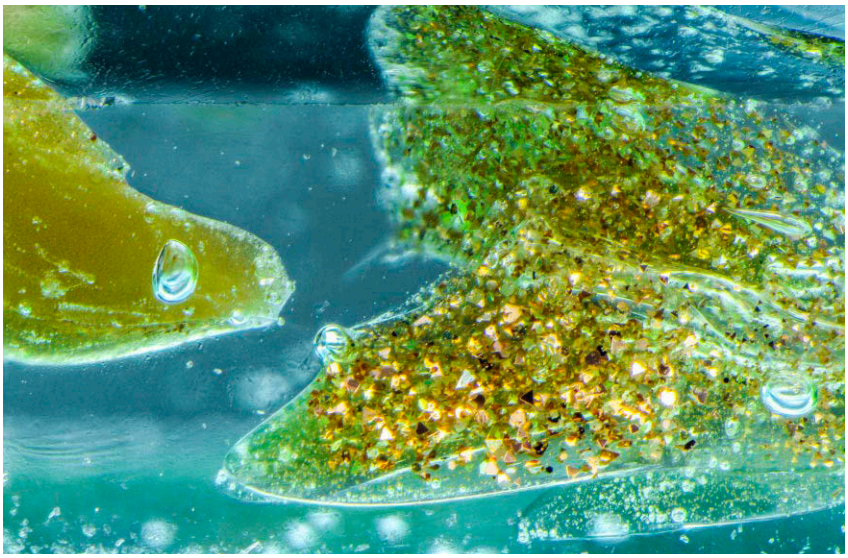

The rough "crystal-like" shape and fusion of two glass types, one with metallic inclusions and one without, present a more complicated type of manmade glass product. This sort of glass imitation using copper platelets to simulate a natural stone has been documented (see E.J. Gübelin and J.I. Koivula, *Photoatlas of Inclusions in Gemstones*, Vol. 1, 2005, Opinio Publishers, Basel, Switzerland, p. 433). The polish lines seen on the surfaces of both glasses clearly indicate that these were faceted to resemble a natural rough stone, and the trigonal outline and elongate shape suggest the goal was to imitate tourmaline, which has a similar appearance. The copper inclusions and neon bluish green color would further indicate that the manufacturer intended to imitate Paraíba-type tourmaline.

During this same time these glass imitations were examined, a natural copper-bearing tourmaline (figure 12) from Brazil was also submitted for a colored stone identification and origin service. This stone was notable because it had rare natural dendritic copper inclusions (figure 13) that the submitted glass imitation attempted to mimic.

It is unusual to see manmade glass cut to imitate a natural rough crystal with eye-visible inclusions. Paraíba tourmaline is one of the most expensive varieties of tourmaline and

Figure 12. Paraíba tourmaline with copper inclusions.

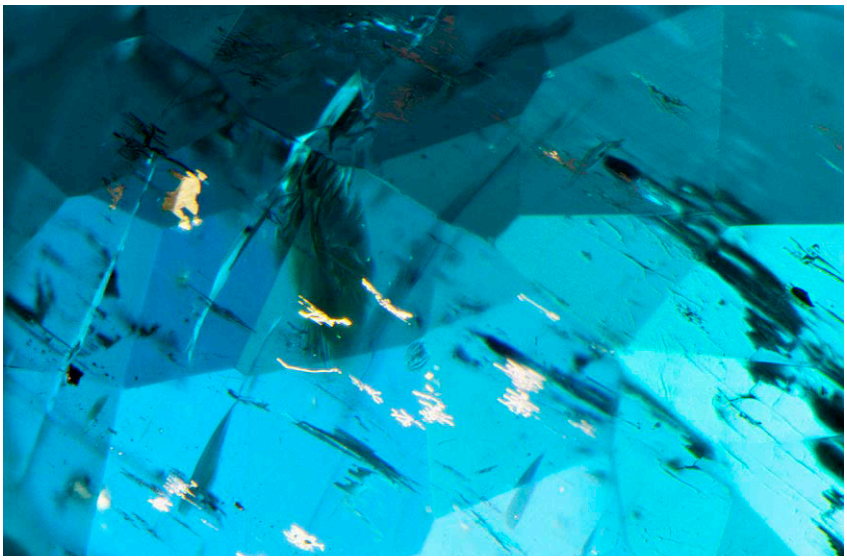

Figure 13. Native copper inclusions in natural Paraíba tourmaline. Field of view 2.82 mm.

well sought after since its discovery in the 1980s. These pieces of man-made glass were certainly interesting from a gemological perspective to demonstrate the variety of creative ways imitation gems are produced.

Amy Cooper, Jamie Price, and Heidi Breitzmann

Chromite Inclusions in Green Common OPAL

Recently the Carlsbad laboratory examined a mottled grayish green partially polished rough stone for identification services. The stone measured 21.01 × 16.13 × 15.50 mm and weighed 28.16 ct (figure 14). The stone showed a vitreous luster and prominent reddish orange staining in surface-reaching fractures and cavities.

Standard gemological testing revealed a refractive index of 1.450 measured on a polished flat surface and a specific gravity of 2.07 obtained hydrostatically. No play-of-color was

Figure 14. This 28.16 ct polished rough dark green common opal contained inclusions of chromite and is colored by chromium.

Figure 15. The chromite inclusions within the green common opal. Field of view 0.95 mm.

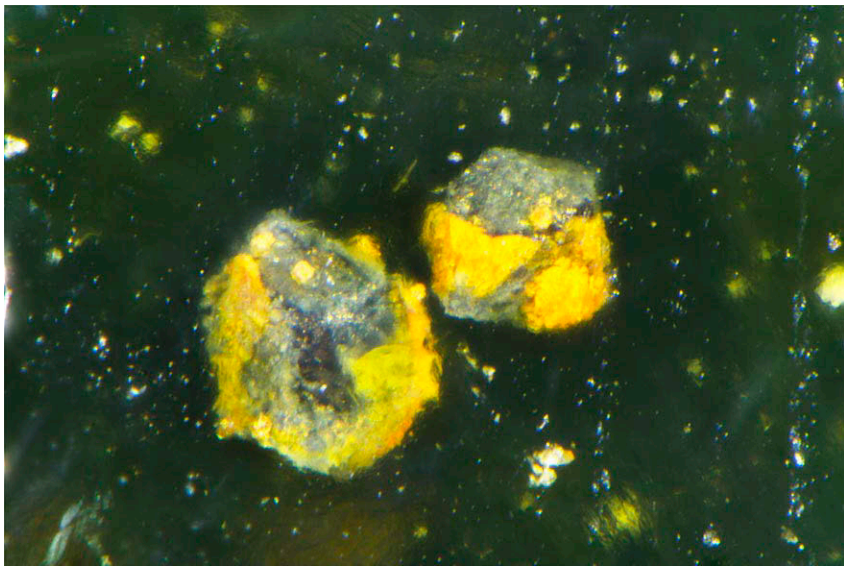

observed, and all properties were consistent with common opal. Weak chromium lines were seen with the handheld spectroscope as well as a weak pink Chelsea color filter reaction. Microscopic analysis using fiber-optic lighting showed minute mineral grains scattered throughout the opal. Several well-formed black opaque octahedral inclusions with yellow staining (figure 15) were confirmed by Raman spectroscopy to be predominantly chromite ($FeCr_2O_4$), a member of the spinel group (C. Klein and B. Dutrow, *The Manual of Mineral Science*, 23rd ed., 2007, pp. 387–388).

Additional information on the chromite inclusions and the green bodycolor of the opal was collected by further advanced testing with LA-ICP-MS (table 1) and Vis-NIR (figure 16). The visible-range spectrum shows a broad absorption band centered at 610 nm and a smaller band at 680 nm, which may result from minute inclusions of chromium-colored serpentine (E. Fritsch et al., "Cr^{3+}-green common opal from Turnali, north-eastern Turkey," *32nd International Gemmological Conference*, Interlaken, Switzerland, 2011, pp. 165–166). LA-ICP-MS trace element chemistry showed the black inclusions were predominantly a mixture of magnesiochromite (24.19 mol.%), chromite (42.94 mol.%), hercynite ($FeAl_2O_4$, 17.99 mol.%), and spinel ($MgAl_2O_4$, 10.12 mol.%). ICP data showed a high amount of chromium ranging from 936–1110 ppmw with an average of 1042 ppmw.

Although the location or geological occurrence of this particular sample is unknown, a previous publication on Turkish green common opal colored by Cr^{3+} discussed the occurrence in deposits of serpentinized peridotite with the color being attributed to minute inclusions of chromium-colored serpentine. This interesting common opal was a welcome gem material to study in the GIA lab.

Amy Cooper, Maxwell Hain, and Ziyin Sun

TABLE 1. LA-ICP-MS data of the inclusions in the green opal revealing they were consistent with the spinel group mineral chromite.

Oxides (wt.%)	Laser spot 1	Laser spot 2	Laser spot 3
MgO	7.32	6.99	7.38
SiO_2	0.02	0.38	0.05
Al_2O_3	14.39	14.64	14.21
TiO_2	0.04	0.04	0.04
Cr_2O_3	51.42	50.85	51.67
MnO	0.33	0.33	0.33
FeO[a]	22.55	23.60	22.54
Fe_2O_3	3.03	2.36	3.12
Others	0.89	0.80	0.64
Total	100.00	100.00	100.00
Atomic proportions on the basis of 4 oxygen atoms			
Mg	0.3639	0.3470	0.3662
Mn	0.0093	0.0094	0.0093
Fe^{2+}	0.6286	0.6572	0.6272
A-site[b] total	1.0018	1.0137	1.0027
Fe^{3+}	0.0760	0.0591	0.0782
Al	0.5652	0.5747	0.5572
Cr	1.3551	1.3389	1.3591
Ti	0.0010	0.0010	0.0011
Si	0.0008	0.0126	0.0017
B-site[c] total	1.9982	1.9863	1.9973
End member mol.%			
Chromite ($FeCr_2O_4$)	42.55%	43.70%	42.56%
Magnesiochromite ($MgCr_2O_4$)	24.64%	23.08%	24.85%
Spinel ($MgAl_2O_4$)	10.28%	9.90%	10.19%
Hercynite ($FeAl_2O_4$)	17.75%	18.76%	17.45%
Magnetite ($Fe^{2+}Fe^{3+}{}_2O_4$)	2.39%	1.93%	2.45%
Magnesioferrite ($MgFe_2O_4$)	1.38%	1.02%	1.43%
Others	1.02%	1.61%	1.06%

[a]*Initially, all iron is assumed to be ferrous, and the ferric amount was calculated out based upon assigning four corresponding oxygen atoms pfu.*
[b]*Four-fold coordination positions*
[c]*Six-fold coordination positions*
Detection limits (ppmw): Mg = 0.028, Al = 0.23, Si = 25.6, Ti = 0.13, Cr = 0.13, Mn = 0.048, Fe = 0.93

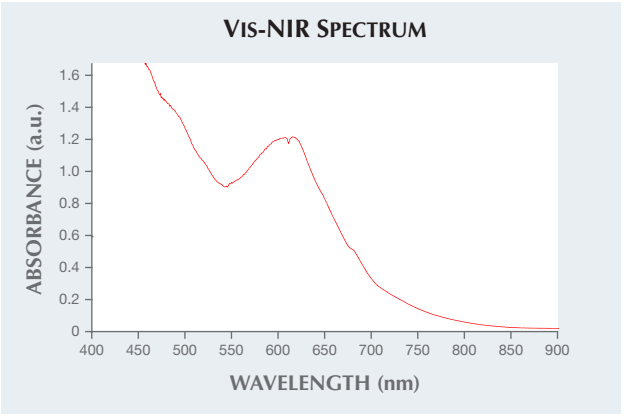

Figure 16. The visible-NIR-range spectrum shows a broad absorption band centered at 610 nm and a smaller band at 680 nm, which may result from minute inclusions of chromium-colored serpentine.

Rare Intense Purplish Pink Montana SAPPHIRE

Recently the Carlsbad laboratory received an intensely saturated purplish pink faceted sapphire for identification and origin report (figure 17). The faceted stone weighed 3.93 ct with measurements of 10.93 × 6.58 × 6.61 mm and had a hexagonal modified mixed-cut style. Standard gemological testing revealed a refractive index of 1.761 to 1.769, and a hydrostatic specific gravity of 3.99, both consistent with corundum. The stone fluoresced medium red to long-wave UV and weak red to short-wave UV.

Figure 17. These Montana sapphires are a 3.93 ct hexagonal modified mixed cut (left, examined for this study) and a 6.39 ct hexagonal rough (right).

Microscopic examination showed angular and oval shaped reflective films, short needles, intact crystals with decrepitation halos and fluid films (figure 18). Also present were dense bands of rutile silk interspersed with finer bands of silk (figure 19). These internal characteristics are typical for sapphires from secondary Montana deposits including Rock Creek, Missouri River, and Dry Cottonwood Creek (E.J. Gübelin and J.I. Koivula, *Photoatlas of Inclusions in Gemstones*, Vol. 3, Opinio Publishers, Basel, Switzerland, 2008, p. 226). The decrepitation halos, the unaltered bands of hexagonal rutile silk, and intact crystals showed no indications of heat treatment. Notably, decrepitation halos are not indicative of heat treatment for sapphires originating from magmatic environments, including Montana sapphires (Winter 2018 Lab Notes, pp. 434–435).

Advanced testing with laser ablation–inductively coupled plasma–mass spectrometry (LA-ICP-MS) was used to obtain the stone's trace element chemistry. The results indicated ranges of Mg (23.8–29.6 ppma), Ti (20.4–22.9 ppma), V (1.75–1.86 ppma), Cr (89.8–108 ppma), Fe (813–864 ppma), and Ga (10.9–11.6 ppma). The LA-ICP-MS trace element chemistry was consistent with Montana sapphires when compared to known sample material from the GIA colored stone reference collection. Chemical profiles for pink and purple sapphires as well as rubies from Montana have been documented (see Winter 2018 Lab Notes, pp. 434–435 and Summer 2019 Gem News International, pp. 286–288).

Figure 18. Reflective decrepitation halos and an unaltered orange crystal. Field of view 1.79 mm.

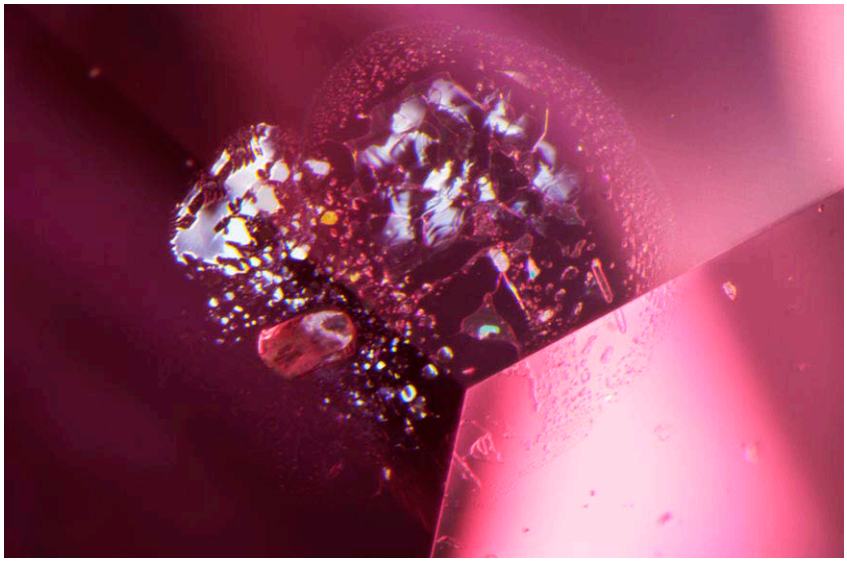

Sapphires from Montana are separated into two groups based on the geology of the deposit. Sapphires from secondary deposits include Rock Creek, Dry Cottonwood Creek, and Missouri River, while the only primary deposit is at Yogo Gulch. The inclusion features in this purplish pink sapphire are consistent with stones from Montana's secondary deposits. This sapphire is reported to be from the Rock Creek deposit. While Rock Creek is historically the most productive deposit in Montana in terms of overall volume of sapphires recovered, stones from this deposit continue to increase in popularity due to their unique colors and excellent clarity (J.C. Zwaan et al., "The origin of Montana's

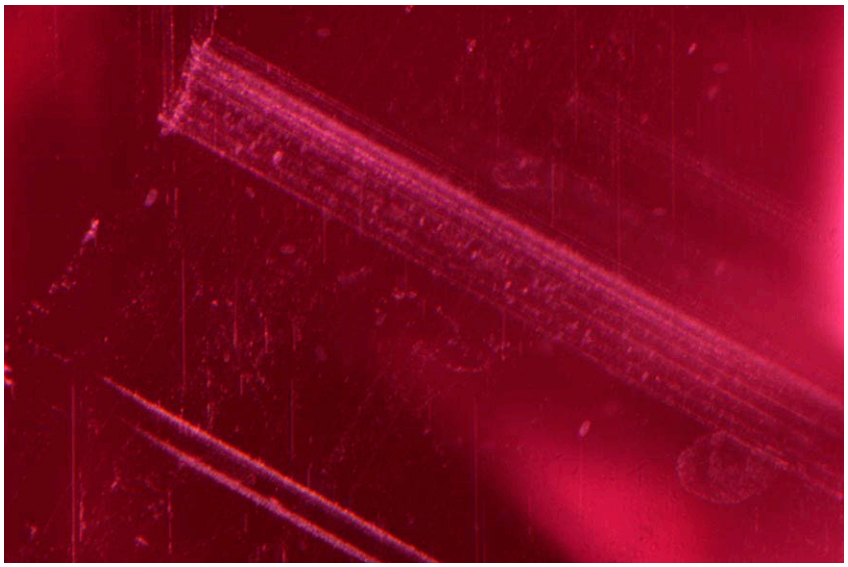

Figure 19. Dense bands of exsolution rutile with finer outer bands frequently seen in secondary Montana sapphires. Field of view 1.79 mm.

Figure 20. This M-color, 7.07 ct round brilliant is the largest CVD-grown diamond seen to date at GIA.

sapphires," Winter 2015 *G&G*, pp. 370–391). Typically, Montana sapphires are less than 2 carats in size. This lends to the rarity and exceptional qualities of this large 3.93 ct intense purplish pink unheated sapphire.

Amy Cooper and Aaron C. Palke

Largest CVD LABORATORY-GROWN DIAMOND Submitted to GIA

Chemical vapor deposition (CVD) diamond growth has greatly improved over the years. More CVD-grown diamonds are seen in the market today, and in recent years, larger CVD-grown diamonds are beginning to emerge. In 2016, the GIA laboratory in Hong Kong examined a 5.19 ct cushion, the largest CVD-grown diamond analyzed at GIA until now (Winter 2016 Lab Notes, pp. 414–416).

A larger CVD-grown diamond was recently submitted to the GIA laboratory in Carlsbad: a round brilliant with VS_2 clarity and M color weighing just over 7 carats (figure 20). This 7.07 ct CVD-grown diamond came to the Carlsbad laboratory undisclosed as CVD, but advanced testing correctly identified this diamond's origin. The largest reported faceted CVD-grown diamond is a 12.75 ct round brilliant ("IGI's Hong Kong lab certifies largest CVD grown diamond," IGI Press Room, November 23, 2020).

Microscopic investigation revealed grade setting graphitic inclusions just below the center of the table. Photoluminescence investigation showed characteristic growth features consistent with a CVD-grown diamond that was subsequently HPHT-treated, generally intended to reduce the brown coloration. With 514 nm excitation at liquid nitrogen temperature (–196°C), nitrogen-vacancy centers at 575 $[NV]^0$ and 637 $[NV]^-$ nm, along with a strong $[SiV]^-$ doublet at 736.6/736.9 nm were revealed (figure 21) determining this diamond as CVD-grown. When viewed through the DiamondView, growth layers were evident (figure 22), and the green fluorescence along with the lack of a 596/597 nm feature in the PL spectrum were indicative of post-

Figure 21. The photoluminescence spectrum collected with a 514 nm laser at liquid nitrogen temperature reveals the NV centers and silicon-vacancy center that are typically observed in CVD-grown diamonds.

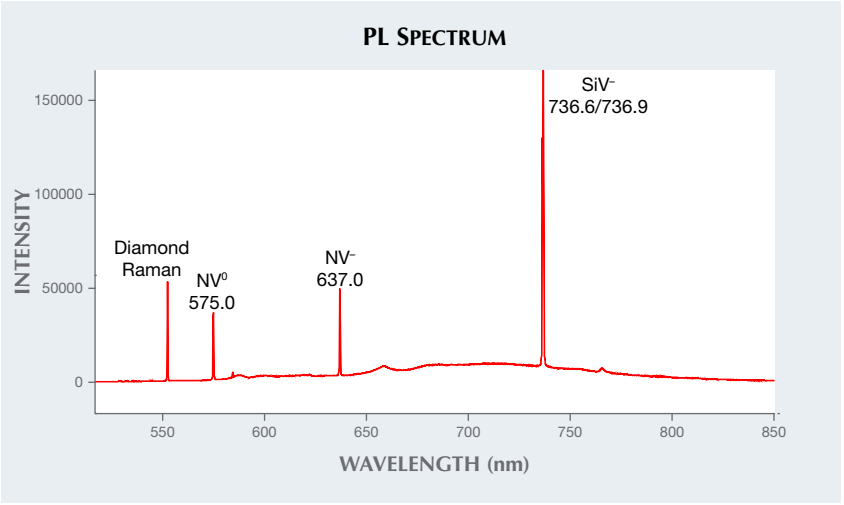

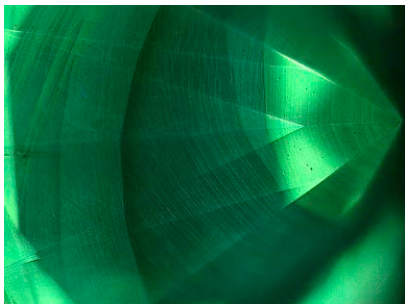

Figure 22. DiamondView fluorescence imaging shows the striations that are diagnostic of its CVD origin, and its coloring is consistent with post-growth HPHT treatment.

growth HPHT treatment (figure 22; Wang et al., "CVD synthetic diamonds from Gemesis Corp.," Summer 2012 *G&G*, pp. 80–97).

CVD-grown diamonds of these sizes are still a rarity, but with new technologies and advancements it is evident that larger laboratory-grown diamonds are becoming more prevalent.

Garrett McElhenny and Sally Eaton-Magaña

Unusual Absorption in a Blue Flux-Grown SYNTHETIC SAPPHIRE

The GIA laboratory in Bangkok analyzed a 0.52 ct blue flux-grown synthetic sapphire (figure 23). Standard gemological properties were typical for corundum. Observation in the microscope revealed various forms of flux or wispy fingerprints and platinum inclusions in a variety of shapes (figure 24). All of these inclusions are typical for Chatham synthetic sapphire (R. Kane, "The gemological properties of Chatham flux-grown synthetic orange sapphire and synthetic blue sapphire," Fall 1982 *G&G*, pp. 140–153).

Figure 23. A 0.52 ct blue flux-grown synthetic sapphire.

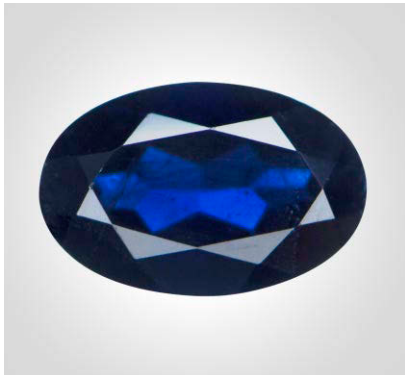

Figure 24. Platinum inclusions in a variety of shapes.

However, the most interesting feature of this stone was its UV-Vis-NIR spectrum (figure 25). The spectrum had the usual 377, 388, and 450 nm peaks related to Fe^{3+}, as well as the Fe^{2+}-Ti^{4+} broad band around 560 nm that is responsible for the blue color, but additionally featured an unexpected broad band around 800 nm. The broad band at 800 nm is typ-

Figure 25. UV-Vis-NIR spectra of faceted blue flux-grown synthetic sapphire. Estimated path length 2.51 mm.

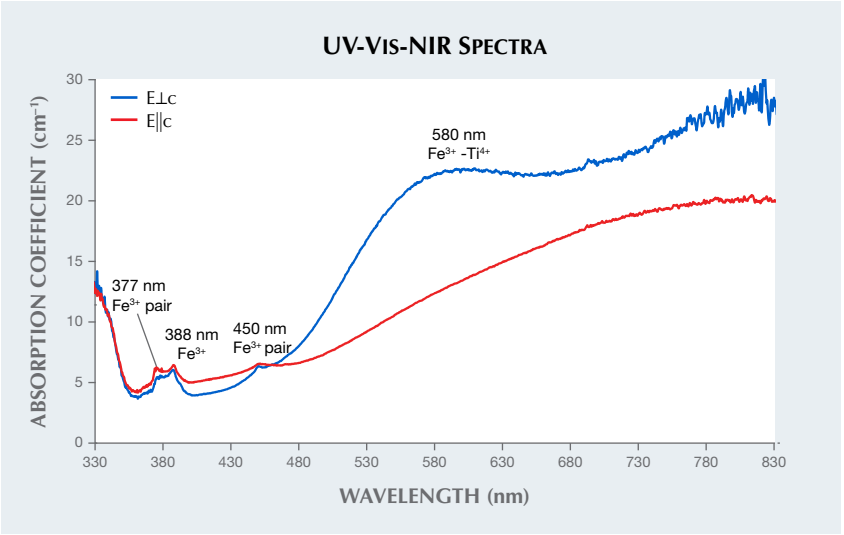

TABLE 2. LA-ICP-MS results in parts per million atomic (ppma) for the blue flux-grown synthetic sapphire.

	Be	Mg	Ti	V	Cr	Fe	Ga	Rh	Pt
Average	12.2	0.083	95	0.025	0.99	1299	0.51	1.3	1.08
SD (n = 3)	0.8	0.001	8	0.002	0.02	37	0.03	0.1	0.05
Detection limit	0.07	0.025	0.07	0.007	0.08	1	0.004	0.0004	0.001

ical for basalt-related, natural blue sapphire and can also be found in some heated metamorphic blue sapphire (Summer 2019 *G&G* Micro-World, pp. 264–265). However, it has never been reported in blue lab-grown sapphire, either flame-fusion or flux-grown.

We analyzed the trace element composition on the blue flux-grown synthetic sapphire using LA-ICP-MS. The results showed very low amounts of vanadium (V) and gallium (Ga), a combination that is a classic indicator of lab-grown corundum. Other trace elements such as titanium and iron were found at levels on average of about 95 ppma and 1299 ppma. Beryllium was also detected at 12 ppma (table 2), a trace element whose presence is unpredictable in laboratory-grown sapphire. The presence of rhodium (Rh) and platinum (Pt) is an indicator of flux-grown corundum, representing traces of the crucible in which the sapphire was grown.

Sudarat Saeseaw

PHOTO CREDITS
Diego Sanchez—1, 8, 9, 12, 20; Britni LeCroy—2; Virginia Schwartz—3; Jian Xin (Jae) Liao—4; Nathan Renfro—10, 13, 15, 18, 19; Angelica Sanchez—14, 17; Adam Steenbock—22; Nuttapol Kitdee—23; Charuwan Khowpong—24

Blue Apatite in Pyrope-Spessartine Garnet

The author recently had the opportunity to examine and facet a piece of garnet rough. The garnet, reportedly from Madagascar, was acquired from gem cutter and dealer Desmond Chan of Los Angeles. The rough was selected for the unusual blue apatite crystal nearly reaching the surface. Laser ablation–inductively coupled plasma–mass spectrometry (LA-ICP-MS) chemical analysis indicated the rough to be a pyrope-spessartine variety. When orienting the stone in preparation for faceting, the author wanted the apatite inclusion to be the main focus of the gemstone. After slow and careful execution, a cut-cornered mixed-cut faceted gem was achieved, with the apatite eye-visible just under the table facet (figure 1). Oblique fiber-optic illumination was used to observe the world inside the gemstone, revealing a scene consisting of the blue euhedral apatite crystal paired with numerous iridescent intersecting needles of rutile (figure 2). This is one of the most unusual inclusions the author has seen in a garnet, and it is also notable as the gem was faceted to showcase the inclusion rather than hide or remove it.

Jessa Rizzo
GIA, Carlsbad

Figure 1. This 5.33 ct red pyrope-spessartine garnet was faceted by the author to display the unusual blue apatite crystal within. Photo by Diego Sanchez.

CVD Landscape

Fluorescence is an integral part of diamond analysis that displays varying growth defects. Each color provides visual clues to the growth chemistries and defects formed. Gemologists use this data along with other spectroscopic features to determine a diamond's origin and treatment history. The

Figure 2. A blue apatite crystal associated with intersecting iridescent needles was showcased. Photomicrograph by Jessa Rizzo; field of view 2.90 mm.

About the banner: Platy inclusions of covellite appear a vibrant pink color in this quartz from Brazil. Photomicrograph by Nathan Renfro; field of view 3.83 mm. Stone courtesy of the John Koivula Inclusion Collection.

Editors' note: Interested contributors should contact Nathan Renfro at nrenfro@gia.edu and Stuart Overlin at soverlin@gia.edu for submission information.

Gems & Gemology, Vol. 56, No. 4, pp. 526–533.

Figure 3. GIA-grown rough CVD diamond weighing 5.8 ct, photographed under daylight conditions. Photo by Towfiq Ahmed.

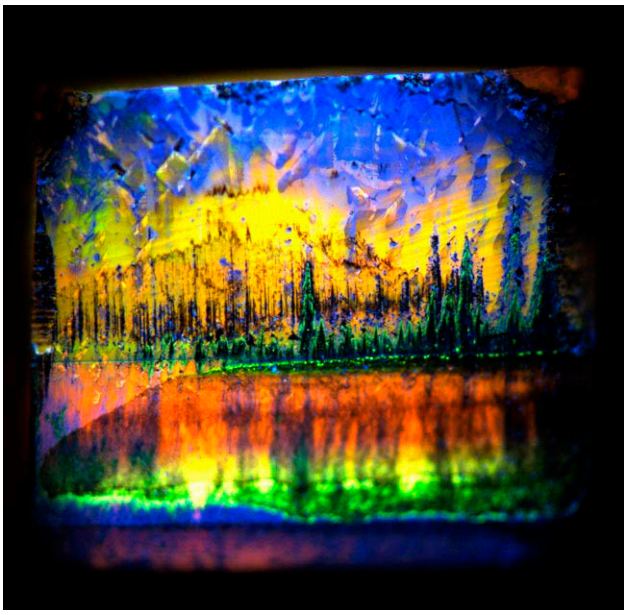

Figure 4. DiamondView fluorescence image of a 5.8 ct GIA-grown CVD block measuring 7 × 7 × 7 mm. Photomicrograph by Stephanie Persaud.

fluorescence features in this experimental CVD block grown by GIA (figure 3) are reminiscent of a landscape with trees reflecting into a lake during a sunset (figure 4, illuminated using a DiamondView equipped with a UV light).

CVD diamond technologies have improved vastly over the last decade. Researchers at GIA grew this CVD block over several growth runs to gain a better understanding of CVD diamonds. This block captures the essence of nature within a laboratory setting.

Stephanie Persaud
GIA, New York

Unmasking Emerald Filler

Of the treatments we see in the laboratory, fissure filling has become one of the most ubiquitous. We have observed this treatment in a variety of stones, including emerald, ruby, sapphire, spinel, tourmaline, tanzanite, and more. The filling of fractures minimizes their appearance, making the gems appear cleaner. Fissure filling can be detected

Figure 5. An emerald with irregularly shaped cavities, shown in darkfield illumination. Photomicrograph by E. Billie Hughes; field of view 4 mm.

Figure 6. When the same inclusion scene is lit with a long-wave ultraviolet flashlight, it becomes evident that the cavity contains a filler that fluoresces a chalky blue color in long-wave illumination. The irregular shapes can also be seen to contain rounded gas bubbles. Photomicrograph by E. Billie Hughes; field of view 4 mm.

with a variety of methods. One way is to examine the infrared spectrum, where some fillers display distinctive peaks. Another is the hot point method, where oils can be observed leaking out in droplets. Some fillers are unmasked with simple observation in the microscope, because they display flashes of color or because they include visible dyes.

In addition to these methods, another tool in our arsenal is the long-wave ultraviolet flashlight, which can be used in conjunction with the microscope. Because some fillers display a chalky fluorescence when illuminated with long-wave UV light, shining a long-wave UV flashlight at the specimen is a simple technique that helps us to not only to detect the filler, but also to see its exact location in the stone. This helps the gemologist gauge the extent of filling and its impact on the stone's overall appearance.

Figure 5 (see p. 527) offers a great example of this. This inclusion scene in emerald shows an irregular cavity. When illuminated with a long-wave UV flashlight (figure 6), it is immediately evident that the cavity is filled with a substance that displays a chalky blue fluorescence. Observation under long-wave UV light also makes it easier to observe gas bubbles in the filled areas.

E. Billie Hughes
Lotus Gemology, Bangkok

Inclusions in Kenyan Rubies from the John Saul Mine

Rubies from the John Saul mine have been available in the market since the 1970s. The gems are found in a pegmatite-like vein that intrudes an ultrabasic body within the country rock (Winter 1999 Gem News, pp. 213–215). While the mine has produced a large quantity of ruby with fine color, only a small part of the production is fine quality and suitable for faceting, with most of the samples being cut into cabochons. Production has declined, and the material is seen less nowadays.

The rubies have an inclusion scene that typically includes short, iridescent needles associated with dense clouds of particles, often in bands (figure 7). Negative crystals surrounded by a plane of thin films are also typical (figure 8). These are very similar to the inclusion scenes in rubies from Mogok (Myanmar) and other marble-hosted deposits. The fact that the color and fluorescence, which is dictated by the trace element chemistry, are also similar to marble-related deposits makes separating them from

Figure 8. A negative crystal surrounded by iridescent thin films. Photomicrograph by Charuwan Khowpong; field of view 1.20 mm.

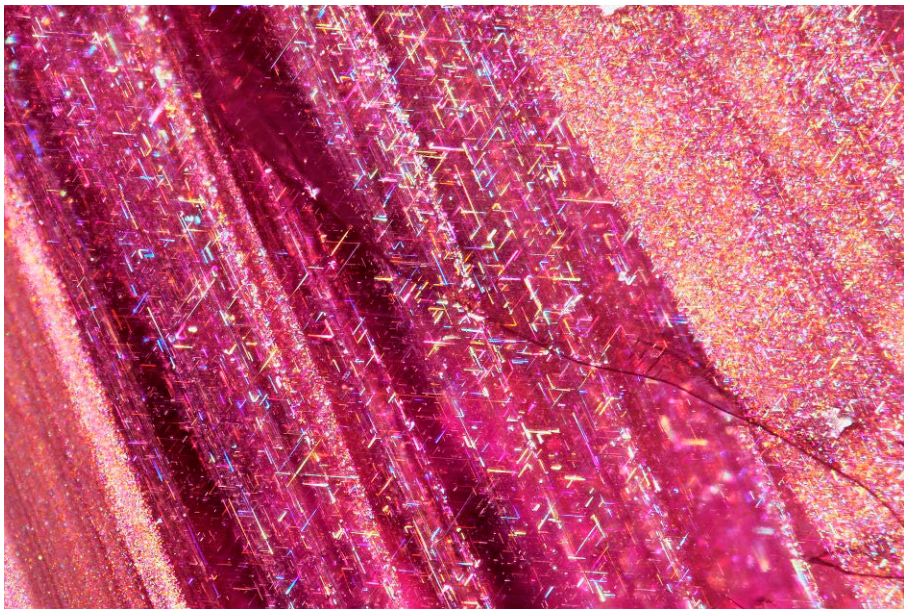

Figure 7. Bands of dense clouds of particles associated with iridescent short needles. Photomicrograph by Suwasan Wongchacree; field of view 1.75 mm.

Kenyan rubies even more challenging. This shows that similar inclusion scenes can form in very different geological environments and that the internal world of gemstones is not always a conclusive indicator of geographic origin.

Charuwan Khowpong
GIA, Bangkok

Uncommon Inclusion of Lazurite in Ruby from Mogok, Myanmar

A parcel of small rubies was received for identification at the S Gemmological Institute (SGI) gem lab in Yangon, Myanmar. Based on chemical, spectroscopic, and standard gemological testing, they were determined to originate from the Mogok Stone Tract in Myanmar. One faceted ruby contained a small blue crystal inclusion with what appeared to be a pyritohedron shape but an uncommonly seen bright blue color (figure 9). This inclusion was identified by Raman spectroscopy as lazurite.

A blue lazurite inclusion was previously reported to have been found in a 5.09 ct Burmese ruby and a 1.40 ct ruby from Namya, Myanmar (Spring 2012 Lab Notes, pp. 51–52). Also, blue lazurite mineral has previously been detected in 1.02 ct light gray Burmese spinel (Spring 2019 Micro-World, pp. 112–113).

According to the literature and our knowledge of inclusions in rubies from Mogok, this blue mineral is rare as an inclusion in Burmese rubies.

Thuzar Aung
S Gemmological Institute (SGI), Yangon, Myanmar

Figure 9. Lazurite inclusion in Mogok ruby from Myanmar (transmitted light and oblique illumination). Photomicrograph by Kyaw Thu; field of view 0.25 mm.

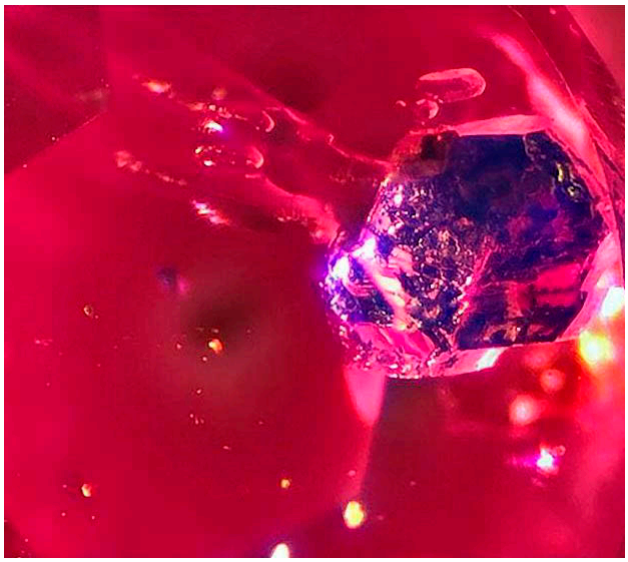

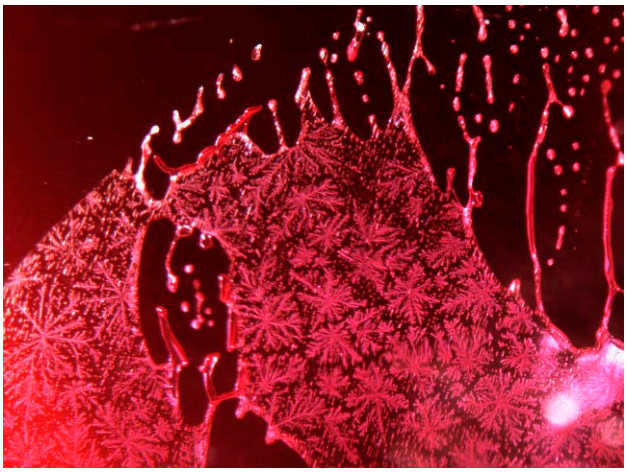

Figure 10. This partially healed fissure with a snowflake-like pattern is seen in a flux-heated Mong Hsu ruby. Photomicrograph by Nattida Ng-Pooresatien; field of view 1.3 mm.

Snowflake Inclusions in Mong Hsu Ruby

The two main sources of Burmese ruby today are Mogok and Mong Hsu. Mogok is the traditional source of gem-quality ruby. The rubies from Mong Hsu are generally not as high in quality as those from Mogok, and typically show distinctive zoning with dark violet cores, a cloudy appearance, and multiple fractures. As a result, most stones from this deposit are heat treated at moderate temperatures using flux to repair fractures, improve clarity, and remove any unwanted blue color. Unheated Mong Hsu rubies are generally considered quite rare.

The author recently examined a 0.79 ct sugarloaf cabochon of pigeon's blood ruby. Chemical analysis and gemological observation of internal features indicated that the origin of this stone was the Mong Hsu. Interestingly, microscopic examination with a combination of darkfield and oblique fiber-optic illumination revealed an open fissure with a snowflake-like pattern of flux residue (figure 10). The pattern is formed by the crystallization or devitrification of the glassy flux residue.

The snowflake is a symbol of the winter season and a traditional image associated with the Christmas holiday. This partially healed fissure resembling snowflakes is the first such feature the author has encountered in flux-heated ruby.

Nattida Ng-Pooresatien
GIA, Bangkok

Metal Sulfide Crystal in a Sapphire

The author recently examined a faceted sapphire from Sri Lanka. Gemological analysis confirmed that it was unheated. The sample contained a crystal that, when examined under the microscope using darkfield illumination and oblique fiber-optic illumination, exhibited a highly re-

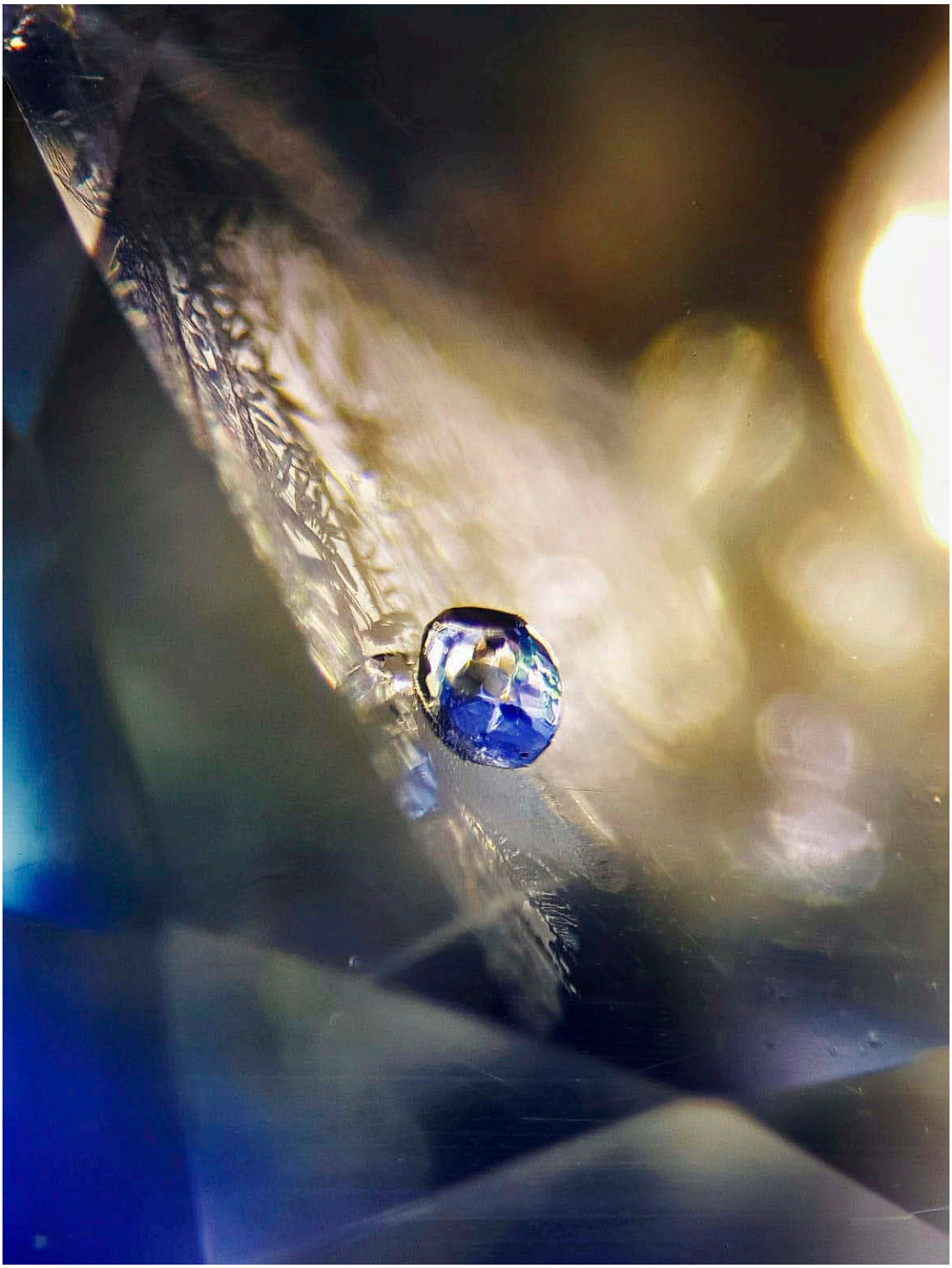

Figure 11. A rounded metal sulfide crystal displays a metallic luster within an unheated sapphire. Photomicrograph by Muzdareefah Thudsanapbunya; field of view 2.3 mm.

flective surface. The observations of the metallic luster and rounded appearance (figure 11) suggested that this inclusion was most likely an iron sulfide.

Iron sulfides are found as opaque mineral inclusions with metallic luster in corundum. The iron sulfides usually seen in corundum are pyrite (FeS_2) and pyrrhotite ($Fe_{1-x}S$)

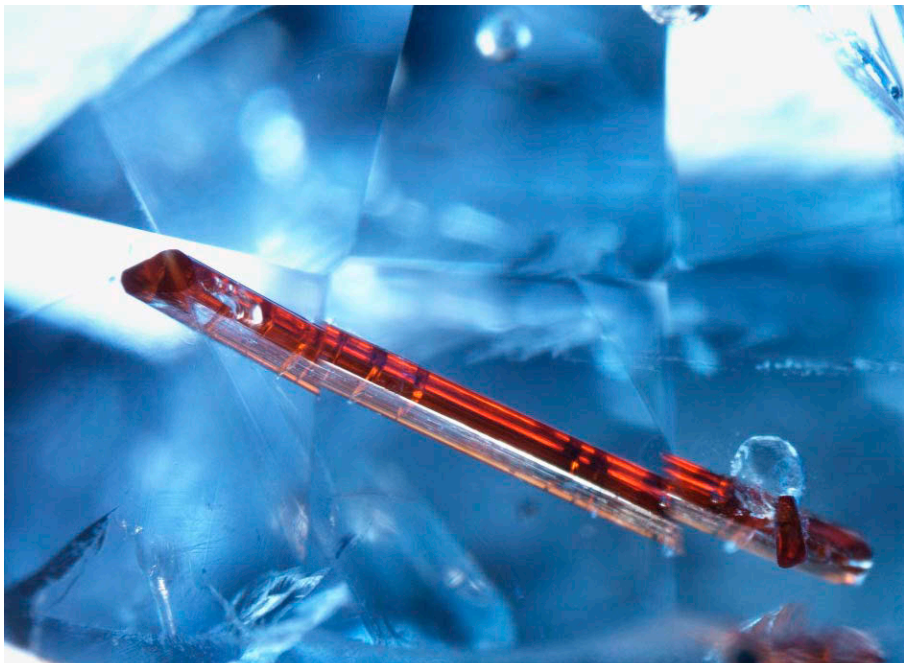

Figure 12. The elongated orange transparent rutile crystal observed in the faceted blue sapphire from Afghanistan. Photomicrograph by Nattida Ng-Pooresatien; field of view 3.0 mm.

(E.J. Gübelin and J.I. Koivula, *Photoatlas of Inclusions in Gemstones*, Vol. 3, Opinio Publishers, Basel, Switzerland, 2008, p. 285). Also present was a partially healed fracture, or fingerprint, next to this crystal, which made for an interesting inclusion scene.

Muzdareefah Thudsanapbunya
Bangkok

Elongated Rutile Crystal in Blue Sapphire from Afghanistan

Rutile, titanium dioxide (TiO_2), is a tetragonal mineral that generally occurs in corundum as silk (exsolution-formed needles), dust-like exsolution particles, or macroscopic crystal inclusions. Rutile crystals can have orange to deep red-brown coloration, and the crystal shapes can be rounded or euhedral.

The author recently examined a 4.24 ct faceted transparent blue sapphire from Afghanistan. The stone contained dusty flake-like inclusions, naturally healed fractures, lathe-like inclusions, twinning, rounded colorless crystals identified as apatite (RRUFF R040098), and an unusual long prismatic orange crystal identified as rutile (RRUFF R040049). This rutile crystal shape (figure 12) is not typical for corundum, particularly in blue sapphire.

Titapa Tanawansombat
GIA, Bangkok

Zircon in Jadeite Jade

One translucent green bangle bracelet recently examined by the author contained an interesting inclusion. The material was identified as dyed and polymer-impregnated jadeite jade using standard gemological testing and advanced spectroscopy, including UV-Vis, Raman, and infrared. This material would be classified as C-type jade in the trade.

Microscopic examination revealed a surprisingly well-formed transparent brownish crystal inclusion (figure 13). Raman analysis of the doubly terminated tetragonal prism revealed it to be "high" zircon ($ZrSiO_4$). To confirm this, the full width at half maximum (FWHM) of the internal stretching mode at 1008 cm^{-1} was calculated as 6.05 cm^{-1}, indicating a high level of crystallinity, as this band is known to broaden as metamictization occurs (L. Nasdala et al., "Metamictization and U-PB isotopic discordance in

Figure 13. This doubly terminated tetragonal crystal in jadeite jade was identified as "high" zircon using Raman spectroscopy. Photomicrograph by Tyler Smith; field of view 2.90 mm.

Figure 14. This aquamarine crystal plays host to several orange garnet crystals. Photo by Angelica Sanchez.

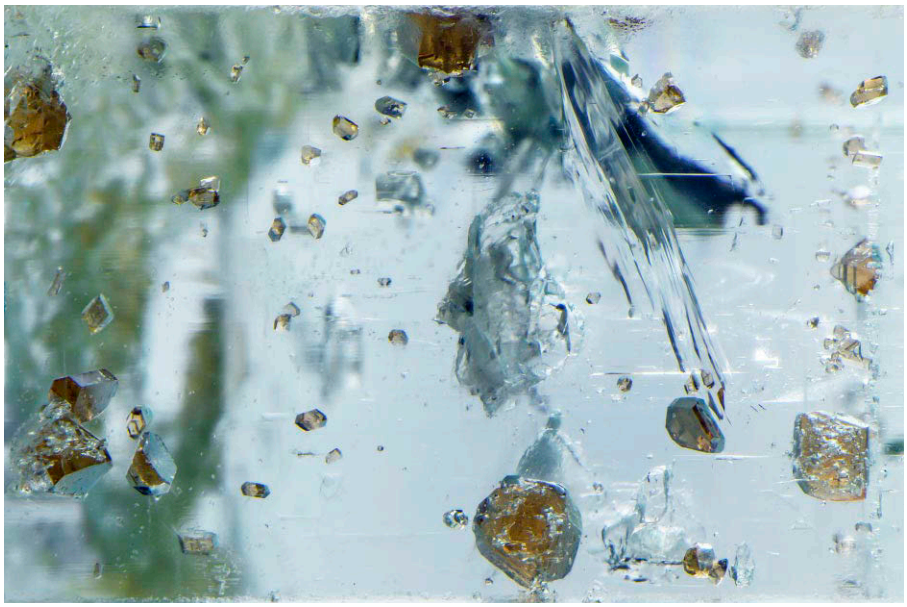

Figure 15. The garnets in the aquamarine were identified by Raman analysis as spessartine. Photomicrograph by Nathan Renfro; field of view 9.40 mm.

single zircons: A combined Raman microprobe and SHRIMP ion probe study," *Mineralogy and Petrology*, Vol. 62, 1998, pp. 1–27).

Although interstitial zircon grains are not uncommon in jadeites, such a euhedral crystal is rarely observed and is especially unexpected considering the various treatments its host had undergone.

Emily Jones
GIA, New York

Quarterly Crystal: Garnets in Aquamarine

For this quarterly crystal, we examined a transparent light blue-green hexagonal prism of aquamarine beryl terminated with a flat pinacoid (figure 14). The crystal weighed 26.16 ct with corresponding measurements of 25.93 × 11.64 × 9.08 mm. This aquamarine reportedly came from the Shigar Valley in the Skardu district, Gilgit-Baltistan territory of Pakistan, an area known to produce gemmy aquamarine crystals.

Magnification revealed numerous intense orange syngenetic garnet crystals near the base of the aquamarine. Raman analysis of the well-formed garnets identified them as spessartine (figure 15).

Garnet inclusions in beryl are rare. Having the opportunity to study this euhedral crystal gives us further insight into the pegmatitic origin of this aquamarine and its locality.

John Koivula
GIA, Carlsbad

Karen V. Smit and Steven B. Shirey

What Have Diamond Ages Taught Us?

The mantle below the oldest crustal rocks of Earth's continents has been attached to the crust since the time the crust formed. This fact is known from isotopic age dating, and it generally means that three billion-year-old crust will be underlain by three billion-year-old mantle. Welded together with the stable continental crust as a unit known as a craton (see detail below), this mantle—known as the subcontinental lithospheric mantle—has been isolated from mantle convection for billions of years. This lithospheric mantle is recognized as an important carbon reservoir, is where the majority of diamonds are stored in the earth, and has been the source of nearly all age-dated diamonds.

The subcontinental lithospheric mantle was depleted of volatiles like carbon and water during its initial formation by the igneous processes of melt generation and migration. Later subduction from ocean basins away from and below the continents carried carbonate and water in altered ocean floor rock to great depths in the mantle where it warmed up, melted, and/or released fluid. Over time the lithospheric mantle became gradually re-enriched in carbon and water by the infiltration of these fluids and melts. With the use of diamond age determinations, we are dating these re-enrichment processes because diamonds grow from these fluids and melts, thereby giving us a glimpse of ancient geodynamic processes.

The story of how and why diamonds become stored in the lithospheric mantle has only emerged in the last 35 years as techniques to determine diamond ages have been developed (see Spring 2019 Diamonds from the Deep). This edition focuses on the geologic lessons that have been learned from diamond ages. We examine the large-scale tectonic processes that have created lithospheric diamonds. These diamonds have become a key way to look at continent evolution and carbon cycling between the crust and mantle over the past 3.5 billion years (figure 1).

Diamonds, Their Ages, Cratons, and Continent Evolution

A worldwide association between the most ancient and stable portions of continents—cratons—and diamond occurrences has long been known (e.g., Kennedy, 1964; Clifford, 1966; Gurney and Switzer, 1973; Boyd and Gurney, 1986). Even though early work recognized the association of diamonds with ancient cratons of at least 1.5 Ga age (Kennedy, 1964; Clifford, 1966), common usage of the term craton evolved to refer simply to portions of Earth's continental crust that have long-term stability. Such portions presently show exceptionally little earthquake activity, no recent rifting or mountain building, and may contain rocks that range in age from as young as 1 billion years to as old as 4 billion years (Pearson et al., in press, 2021). However, just because such regions are now stable diamond storehouses does not mean that they always were so. Indeed, diamond dating allows us to look at just how continent collision or deep mantle upwelling processes—the antithesis of geologic stability—can create diamonds in the first place.

This updated definition of the term craton uses teleseismic (meaning from distant earthquakes across the globe) studies to establish the thickness of the stable lithospheric mantle that lies below the continental crust. Its thickness is established through fast seismic shear wave speeds in global seismic velocity models. In the updated definition, cratons are regions of the earth's continental crust that are underlain by 150–200 km of lithospheric mantle as a keel providing long-term stability since at least 1 Ga. Using this updated definition, around 63% of exposed continental crust and 18% of Earth's surface are cratons.

The first harzburgitic-garnet-inclusion-based diamond ages—which were more than 3 billion years old—proved that diamonds originate in continental mantle and that it too must be very old in order to store them (Richardson et al., 1984). These old ages, along with the strong spatial association of diamond occurrences with old continental crust and the high pressure/temperature conditions of diamonds and their host rocks, all led to the understanding that diamonds form and reside in the subcontinental lithospheric mantle (e.g., Boyd et al., 1985; Boyd and Gurney, 1986; Haggerty, 1986).

Diamonds have formed through nearly all of Earth's history, in distinct episodes that can often be linked to larger-scale tectonic processes (Richardson et al., 2004; Shirey and Richardson, 2011; Howell et al., 2020) and are likely forming today. Diamonds, and their ages, are the ideal time-resolved samples that can provide an overview of continent formation and evolution from deep in the mantle well below the crust (the crust-mantle boundary is typically around 40 km). A classic example is how the creation, assembly, and modification of the Kaapvaal-Zimbabwe craton in southern Africa is reflected in the age, chemistry, and geographic dis-

Gems & Gemology, Vol. 56, No. 4, pp. 534–541.

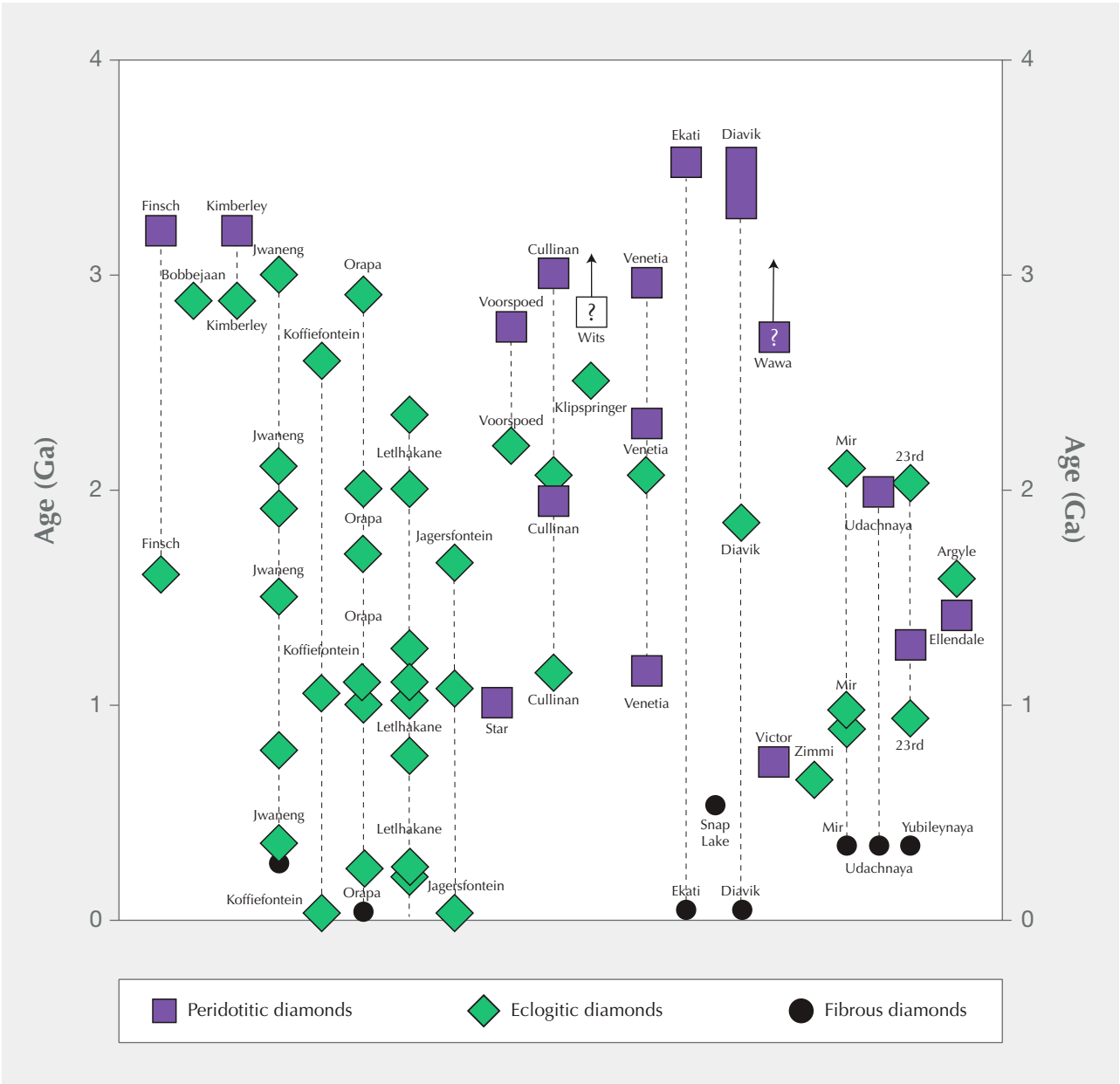

Figure 1. Age plot for all the diamond mines that have supplied enough diamonds on which to do age studies. This diagram summarizes all the known diamond growth events through time. Diamond mines typically have more than one age, may have both eclogitic and peridotitic diamonds, and may use different isotopic dating methods (Rb-Sr, Sm-Nd, Re-Os; see Spring 2019 Diamonds from the Deep). Diamond formation is associated with large-scale tectonic processes and has become a key way to look at continent evolution and carbon cycling between the crust and mantle over the past 3.5 billion years. Diamonds that occur in the Wawa and Witwatersrand conglomerates are undated, but minimum ages are given based on conglomerate age. Modified and updated from Howell et al. (2020).

tribution of multiple generations of diamonds formed and stored in its lithospheric mantle (Shirey et al., 2002, 2004).

Diamonds and Formation of the First Continents

The formation of the first continents involved the production of melt or magma in an Earth hotter than today's Earth. Direct melting of the mantle produced the earliest basaltic and komatiitic crust, leaving behind a buoyant residue. Subsequent remelting of this basalt was necessary to produce the silica-rich, granite-like rocks, termed felsic, that are hallmarks of the continental crust. The surface exposures of igneous rock on continents are composed of at least 50% high-silica rock, yet when basalt melts, less than

1/5 of the volume of melt is felsic. Therefore the amount of initial basalt that was available must have been huge and the amount of buoyant, depleted mantle even more huge—perhaps up to 10–20× the volume of granite. It is some of this abundant buoyant mantle residue that is thought to have become trapped underneath the crust to become nascent continental mantle. Where diamond ages play a role in the story is in using the oldest ages to understand how and when the buoyant mantle was produced and collected.

Active debate among research scientists about the stabilization of the thick buoyant continental mantle compares some form of horizontal tectonic processes—similar to modern subduction and accretion—to vertical tectonic processes that are similar to the upwelling of mantle plumes that occur beneath ocean islands like Hawaii and Iceland today. Both geodynamic scenarios would generate the abundant basaltic melt needed to eventually make the continental crust, but each scenario has different implications for the styles of early mantle convection, the release of Earth's excess heat, and the recycling of constituents from Earth's hydrosphere.

The oldest known diamonds to inform us about these earliest craton formation processes are the 3.5 Ga diamonds from the Diavik and Ekati mines on the Slave craton (Westerlund et al., 2006; Aulbach et al., 2009). Compositions of high-Ni sulfide inclusions related to mantle peridotite in Ekati diamonds are best explained by some surface material being recycled back into the mantle (Westerlund et al., 2006). However, diamond evidence for the lack of atmospherically modified sulfur isotopes (Cartigny et al., 2009) and the presence of very depleted peridotites deep in the continental mantle here suggest that the continental lithosphere was assembled in a way that did not involve substantial surface material. To accommodate these complexities and evidence from the overlying crust that can be explained by localized subduction, a hybrid model of localized subduction-like melting at the craton margin followed by plume-upwelling and underplating has been proposed (Aulbach et al., 2019). Is this subduction similar to modern plate tectonics, while an even earlier vertical upwelling regime is waning, as Aulbach et al. (2019) has suggested? Only future research can resolve the question.

Diamonds and Evidence for the Onset of Modern Plate Tectonics (Wilson Cycle)

The global database for diamond ages from all studies shows that prior to 3.1 Ga, only peridotitic diamonds formed, whereas after 3.0 Ga, eclogitic diamonds became prevalent (figure 1). Shirey and Richardson (2011) suggested that the prevalence of eclogitic diamonds after 3.0 Ga resulted from the capture of eclogite and diamond-forming fluids in mantle lithosphere via subduction and continental collision. From this observation and early continental assembly patterns, they suggested that the evident continental collision was preceded by rifting and comprised the first full cycle of ocean basin opening and closure, known as a Wilson Cycle, starting at about 3.2 Ga. The significance of identifying the earliest Wilson Cycle is that it is the form of plate tectonics we have today.

The regional pattern of diamond ages and the inclusion types seen in the Kaapvaal-Zimbabwe craton (figure 2) support the operation of the Wilson Cycle because they suggest that a piece of ocean floor was underthrust westward beneath the extant continental mantle as an ocean basin closed. When this underthrusting occurred, fluids transported by hydrated and carbonated oceanic crust were released into the overlying continental mantle crystallizing the predominant diamond type, the 2.9 billion-year-old eclogitic sulfide bearing diamonds found in diamond mines west of the suture between the two cratonic blocks (Kimberley, Jwaneng, and Orapa; Richardson et al., 2001, 2004; Shirey et al., 2013; figure 2). This mantle geologic history is in full agreement with the crustal magmatic history of the two cratonic blocks, because diamond ages have permitted us to correlate the geologic processes happening in the mantle with those that were happening in the crust at the same time.

Diamonds and Continent Growth at Their Margins: Subduction and Mountain Building

There are many examples worldwide where diamond formation is associated not just with old cratons (e.g., diamond formation in old enriched lithosphere; Richardson et al., 1984) but rather with deformed regions known as mobile belts, produced during continent collision. These mobile belts are zones of intense deformation in the crust that result from crustal thickening—a process known as orogeny that forms mountain chains around the world such as the Appalachians or the Himalayas. In the older mobile belts, the mountains have since been worn away by billions of years of erosion, and diamonds give us a look at the preserved mantle in the root zone of mountain belts that would not otherwise be seen.

The best example of a diamond deposit associated with collisional mountain building is the Argyle mine in Australia, where "subduction along the Kimberley craton edge generated the world's biggest diamond deposit" (Stachel et al., 2018). The Argyle mine has been a famous supplier of pink and red diamonds (Shigley et al., 2001) and, over its three-decade life, was known for its exceptionally high diamond abundances (Rayner et al., 2018). Argyle occurs within the Proterozoic Halls Creek orogen (1.92–1.83 Ga; Hancock and Rutland, 1984). The Argyle eclogitic diamonds formed "shortly" after continent collision, at 1580 ± 30 Ma (Richardson, 1986), likely within Archean mantle (Luguet et al., 2009). After their formation, the diamonds resided in the high-temperature, high-deformation region near the base of the lithosphere (figure 3). This region near the convecting mantle provided the ideal conditions to im-

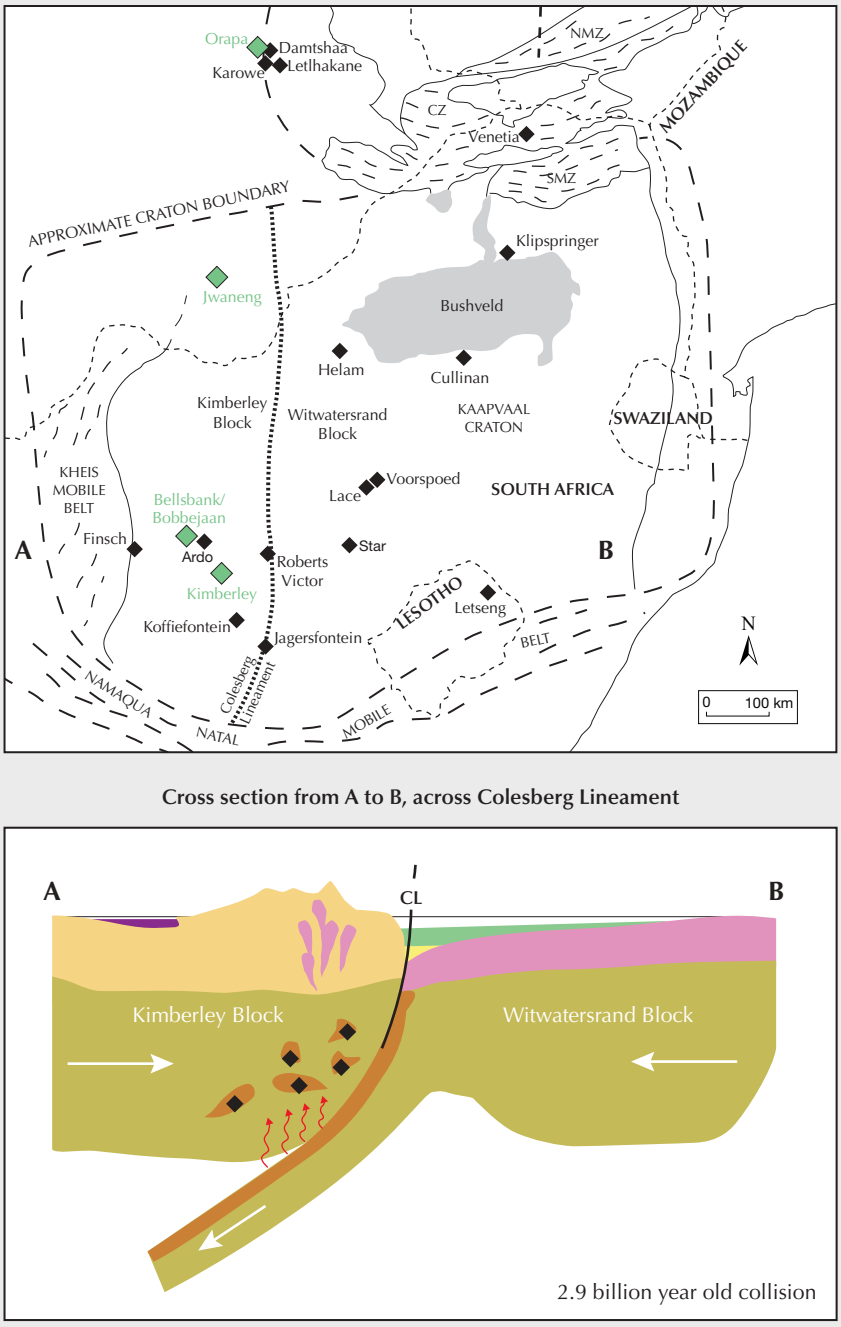

Figure 2. In the Kaapvaal craton (boundary shown by dashed line), some diamond formation occurred during continental collision. The top panel shows the Bellsbank/Bobbejaan, Kimberley, Jwaneng, and Orapa diamond localities (green), all with abundant to common 2.9 Ga diamonds. Diamonds of this age are thought to be derived from fluids (small squiggly arrows) associated with westward subduction along the Colesberg Lineament (CL), as shown in the lower panel (Shirey et al., 2013). The mantle is shown in olive, and the crust is in shades of pink, buff, and brown. Bold arrows show the direction of continental collision.

part strain to some of the diamonds resulting in the platelet degradation that causes their pink and brown colors (Stachel et al., 2018; Eaton-Magaña et al., 2019).

There are many other worldwide diamond localities that have allowed us to link diamond formation to collisional processes along the edge of an ancient continent. In Siberia, for example, lherzolitic and eclogitic diamonds formed in association with orogenesis related to the 1.8–1.2 Ga Angara and Akitkan orogens (Cherepanova and Artemieva, 2015, and references therein). In West Africa, diamonds from Zimmi formed at ~650 Ma (Smit et al., 2016) due to subduction and collision along the Rokelide orogen on the SW margin of the Man craton (700–550 Ma; Lytwyn et al., 2006). Other examples occur at the margins

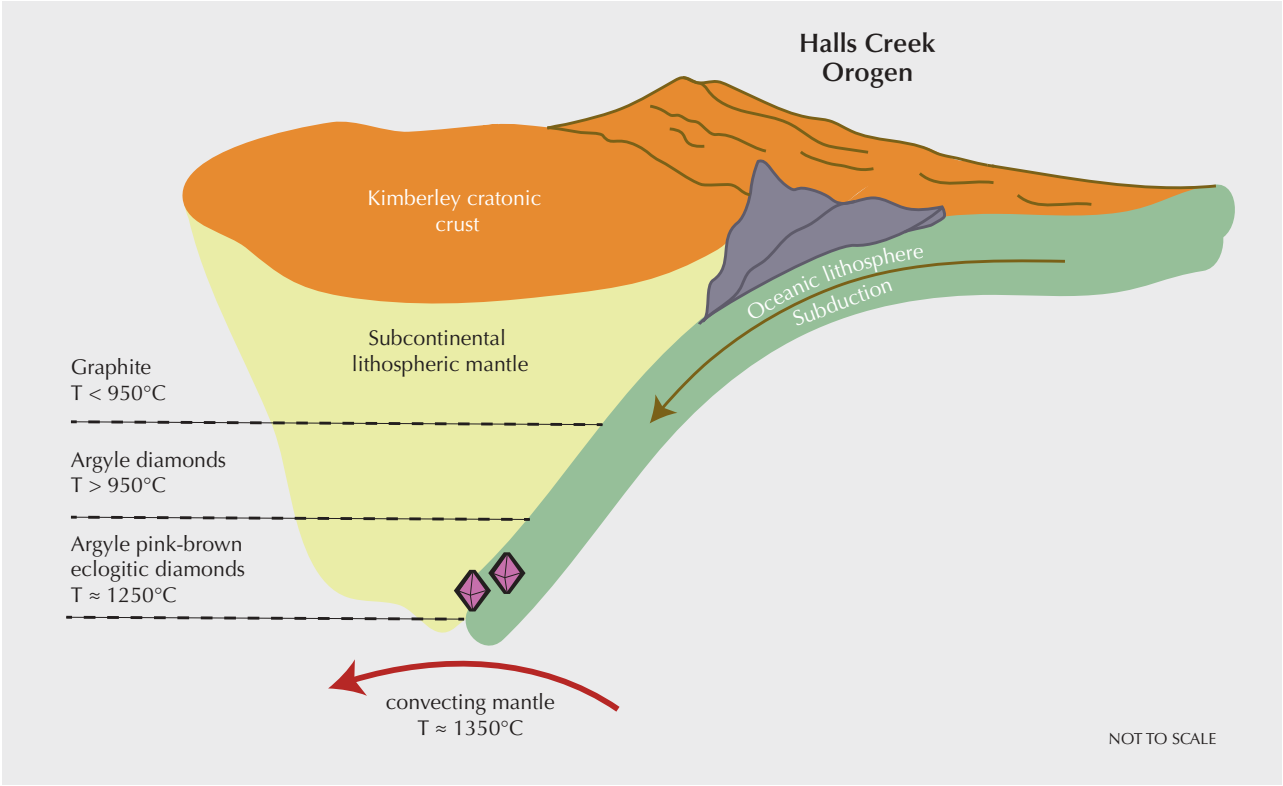

Figure 3. Formation of the pink-brown eclogitic diamonds at Argyle—the world's largest diamond deposit. After their formation, Argyle pink-brown diamonds resided in the high-temperature, high-deformation region near the base of the lithosphere (Viljoen, 2002; Stachel et al., 2018), which provided the ideal conditions to strain the diamonds, induce platelet degradation, and produce their pink and brown colors.

of the Slave (Canada), Kaapvaal (southern Africa), and Wyoming (United States) cratons.

A typical feature of diamonds forming in these mobile belts seems to be the existence of lithospheric mantle caught up in the collision process. An interesting and essential geologic question is whether the diamonds are older diamonds that survived in the lithospheric mantle through tectonic reworking, or diamonds forming at the time of deformation from inherited older carbon, or diamonds formed from carbon newly introduced into the continental mantle during deformation. Similarly, as researchers we want to know if there is mantle newly added during the collision process or whether much older mantle is involved. Answers to these questions cannot be obtained without the age constraints from diamond dating. In the end, incorporation of craton-margin areas to diamond exploration targets has expanded the limits suggested by Clifford (1966) and will continue to contribute to the finding of new economic diamond deposits.

What Do Diamond Ages Show Us About Where Diamonds Are Forming Today?

There is no reason to think that diamonds aren't still forming right now. Based on our knowledge of the age association of diamonds with global plate tectonic processes, we can make a few predictions about where diamonds might be forming today. Most of Earth's mantle is at the right pressure and temperature conditions for diamond formation as long as carbon-bearing fluids and melts are reduced enough to keep carbon from combining with oxygen—the most abundant element in the mantle.

Active subduction zones are obvious candidates for the mobilization of carbon into either the lithospheric or sublithospheric diamond-forming regions of the deeper Earth (figure 4). In oceanic subduction settings, conditions are often too oxidizing to be diamond friendly. The thermal paths of the hotter subducting slabs dictate that they may lose their water and carbon to island arc volcanism at conditions too oxidizing for diamonds to form. Additionally, at these relatively shallow depths, the only magmas available for transport of diamonds to the surface are basalts (not kimberlites) that will be destructive to any diamonds since they are too oxidizing, and/or diamonds may be graphitized due to slow eruption. In other words, diamonds might be forming at depth in normal oceanic subduction zones today, but we may never see them survive to the earth's surface.

Diamonds with relatively young ages have come from two geologic settings, suggesting that these are settings where diamonds may be forming today.

The first is in continental arcs where subduction can impinge directly against the base of the subcontinental mantle keel or can transfer fluids from the slab to the base of the continental mantle keel without triggering diamond-destroying basaltic magmatism. This is the process discussed above to produce many of the 2.9 Ga Kaapvaal diamonds and some of the other continent margin diamonds. Recent work has shown that only 200 million years ago, eastward subduction of the Farallon slab under the Slave craton released diamond-forming fluids that produced thick, fibrous diamond overgrowths on preexisting 3.5 and 1.8 billion-year-old monocrystalline diamonds (Weiss et al., 2015). Today, the best chance for diamond formation are the few places where subduction occurs against lithospheric mantle, despite the amount of subduction taking place around the margins of the Pacific Ocean. Diamond formation may be continuing today along the western margin of North America, where the Farallon/Juan de Fuca plates are being subducted eastward. Another possible environment is where the Nazca plate is being subducted below South America.

A second geological environment where we might find diamonds forming today is at the deeper reaches of subduction of oceanic lithosphere. We have evidence for diamonds forming between 400 and 700 km due to the deep subduction of cold slabs, which has carried carbon and volatiles into the transition zone and lower mantle. In this environment, the famous CLIPPIR (Smith et al., 2016, 2017) and type IIb blue diamonds (Smith et al., 2018) have crystallized from the mantle portion of the slab, whereas other diamonds have crystallized from carbonated oceanic crust (Walter et al., 2011; Regier et al., 2020).

Although modern diamond formation may be taking place in these regions, there is no definitive way for us to prove it without access to the diamonds. We need to wait for kimberlite or lamproite to erupt through the lithosphere and bring diamonds and their associated mantle rocks to the surface.

Diamonds forming in sublithospheric regions (300–700 km) have an additional complication in that they first need to be brought to shallower regions that can be sampled by kimberlites and lamproites. This is thought to happen through either mantle convection or upwelling plumes, which may take millions of years.

Since the last kimberlitic eruption was around 10,000 years ago (see Summer 2019 Diamonds from the Deep), we may have a long wait!

Figure 4. Geologic block diagram interpreted from seismic data showing modern-day subduction against the South American continental lithosphere, forming the Andes Mountains. Although diamonds could theoretically be forming in the mantle wedge anywhere between a depth of 160 and 300 km, local mantle conditions should also be reducing enough for elemental carbon to survive without being converted to carbon dioxide. Reproduced from Ward et al. (2016), with permission from John Wiley and Sons.

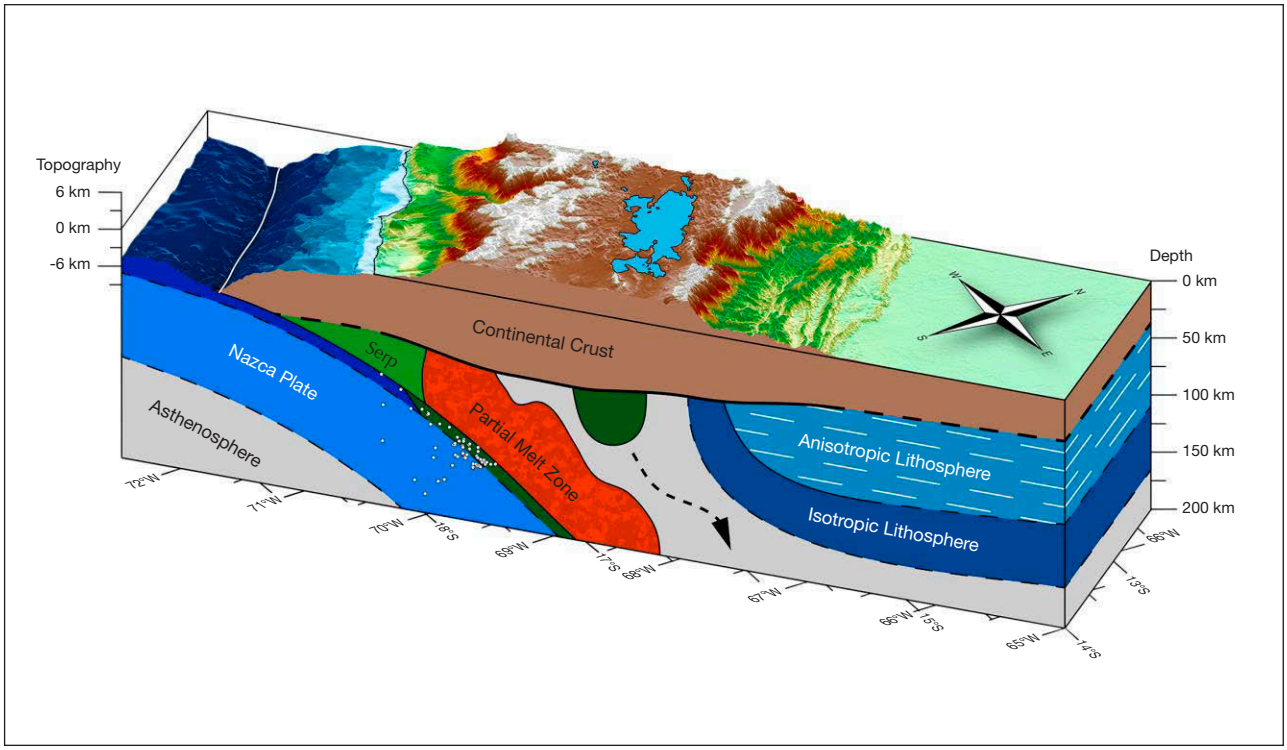

REFERENCES

Aulbach S., Stachel T., Creaser R.A., Heaman L.M., Shirey S.B., Muehlenbachs K., Eichenberg D., Harris J.W. (2009) Sulphide survival and diamond genesis during formation and evolution of Archaean subcontinental lithosphere: A comparison between the Slave and Kaapvaal cratons. *Lithos*, Vol. 112S - Proceedings of the 9th International Kimberlite Conference, pp. 747–757, http://dx.doi.org/10.1016/j.lithos.2009.03.048

Aulbach S., Hofer H.E., Gerdes A. (2019) High-Mg and low-Mg mantle eclogites from Koidu (West African craton) linked by Neoproterozoic ultramafic melt metasomatism of subducted Archaean plateau-like oceanic crust. *Journal of Petrology*, Vol. 60, No. 4, pp. 723–754, http://dx.doi.org/10.1093/petrology/egz011

Boyd F.R., Gurney J.J. (1986) Diamonds and the African lithosphere. *Science*, Vol. 232, No. 4749, pp. 472–477, http://dx.doi.org/10.1126/science.232.4749.472

Boyd F.R., Gurney J.J., Richardson S.H. (1985) Evidence for a 150-200 km thick Archaean lithosphere from diamond inclusion thermobarometry. *Nature*, Vol. 315, No. 6018, pp. 387–389, http://dx.doi.org/10.1038/315387a0

Cartigny P., Farquhar J., Thomassot E., Harris J.W., Wing B., Masterson A., McKeegan K., Stachel T. (2009) A mantle origin for Paleoarchean peridotitic diamonds from the Panda kimberlite, Slave Craton: Evidence from ^{13}C-, ^{15}N- and $^{33,34}S$-stable isotope systematics. *Lithos*, Vol. 112S, pp. 852–864, http://dx.doi.org/10.1016/j.lithos.2009.06.007

Cherepanova Y., Artemieva I.M. (2015) Density heterogeneity of the cratonic lithosphere: A case study of the Siberian Craton. *Gondwana Research*, Vol. 28, No. 4, pp. 1344–1360, http://dx.doi.org/10.1016/j.gr.2014.10.002

Clifford T.N. (1966) Tectono-metallogenic units and metallogenic provinces of Africa. *Earth and Planetary Science Letters*, Vol. 1, No. 6, pp. 421–434, http://dx.doi.org/10.1016/0012-821X(66)90039-2

Eaton-Magaña S., Ardon T., Smit K.V., Breeding C.M., Shigley J.E. (2019) Natural-color pink, purple, red, and brown diamonds: Band of many colors. *G&G*, Vol. 54, No. 2, pp. 352–377, http://dx.doi.org/10.5741/GEMS.54.2.352

Gurney J.J., Switzer G.S. (1973) The discovery of garnets closely related to diamonds in the Finsch pipe, South Africa. *Contributions to Mineralogy and Petrology*, Vol. 39, No. 2, pp. 103–116, http://dx.doi.org/10.1007/BF00375734

Haggerty S.E. (1986) Diamond genesis in a multiply constrained model. *Nature*, Vol. 320, No. 6057, pp. 34–38, http://dx.doi.org/10.1038/320034a0

Hancock S.L., Rutland R.W. (1984) Tectonics of an early Proterozoic geosuture: The Halls Creek orogenic sub-province, northern Australia. *Journal of Geodynamics*, Vol. 1, No. 3-5, pp. 387–432, http://dx.doi.org/10.1016/0264-3707(84)90017-6

Howell D., Stachel T., Stern R.A., Pearson D.G., Nestola F., Hardman M.F., Harris J.W., Jaques A.L., Shirey S.B., Cartigny P., Smit K.V., Aulbach S., Brenker F.E., Jacob D.E., Thomassot E., Walter M.J., Navon O. (2020) Deep carbon through time: Earth's diamond record and its implications for carbon cycling and fluid speciation in the mantle. *Geochimica et Cosmochimica Acta*, Vol. 275, pp. 99–122, http://dx.doi.org/10.1016/j.gca.2020.02.011

Kennedy W.Q. (1964) The structural differentiation of Africa in the Pan-African (+/-500 m.y.) tectonic episode. *Annual Report of the Research Institute of African Geology*, University of Leeds, pp. 48–49.

Luguet A., Jaques A.L., Pearson D.G., Smith C.B., Bulanova G.P., Roffey S.L., Rayner M.J., Lorand J.-P. (2009) An integrated petrological, geochemical and Re-Os isotope study of peridotite xenoliths from the Argyle lamproite, Western Australia and implications for cratonic diamond occurrences. *Lithos*, Vol. 112S - Proceedings of the 9th International Kimberlite Conference, pp. 1096–1108, http://dx.doi.org/10.1016/j.lithos.2009.05.022

Lytwyn J., Burke K., Culver S. (2006) The nature and location of the suture zone in the Rokelide orogen, Sierra Leone: Geochemical evidence. *Journal of African Earth Sciences*, Vol. 46, No. 5, pp. 439–454, http://dx.doi.org/10.1016/j.jafrearsci.2006.08.004

Pearson D.G., Scott J.M., Liu J., Schaeffer A., Wang L.H., van Hunen J., Szilas K., Chacko T., Kelemen P.B. (in press, 2021) Deep continental roots and cratons. *Nature*.

Rayner M.J., Jacques A.L., Boxer G.L., Smith C.B., Lorenz V., Moss S.W., Webb K., Ford D. (2018) The geology of the Argyle (AK1) diamond deposit, Western Australia. *Society of Economic Geologists - Special Publication*, Vol. 20, pp. 89–117.

Regier M.E., Pearson D.G., Stachel T., Luth R.W., Stern R.A., Harris J.W. (2020) The lithospheric-to-lower-mantle carbon cycle recorded in superdeep diamonds. *Nature,* Vol. 585, pp. 234–238.

Richardson S.H. (1986) Latter-day origin of diamonds of eclogitic paragenesis. *Nature,* Vol. 322, No. 6080, pp. 623–626, http://dx.doi.org/10.1038/322623a0

Richardson S.H., Gurney J.J., Erlank A.J., Harris J.W. (1984) Origin of diamonds in old enriched mantle. *Nature,* Vol. 310, No. 5974, pp. 198–202, http://dx.doi.org/10.1038/310198a0

Richardson S.H., Shirey S.B., Harris J.W., Carlson R.W. (2001) Archean subduction recorded by Re-Os isotopes in eclogitic sulfide inclusions in Kimberley diamonds. *Earth and Planetary Science Letters*, Vol. 191, No. 3-4, pp. 257–266, http://dx.doi.org/10.1016/S0012-821X(01)00419-8

Richardson S.H., Shirey S.B., Harris J.W. (2004) Episodic diamond genesis at Jwaneng, Botswana, and implications for Kaapvaal craton evolution. *Lithos*, Vol. 77, No. 1-4, pp. 143–154, http://dx.doi.org/10.1016/j.lithos.2004.04.027

Shigley J.E., Chapman J., Ellison R.K. (2001) Discovery and mining of the Argyle diamond deposit, Australia. *G&G*, Vol. 37, No. 1, pp. 26–41, http://dx.doi.org/10.5741/GEMS.37.1.26

Shirey S.B., Richardson S.H. (2011) Start of the Wilson Cycle at 3 Ga shown by diamonds from subcontinental mantle. *Science*, Vol. 333, No. 6041, pp. 434–436, http://dx.doi.org/10.1126/science.1206275

Shirey S.B., Harris J.W., Richardson S.H., Fouch M.J., James D.E., Cartigny P., Deines P., Viljoen F. (2002) Diamond genesis, seismic structure, and evolution of the Kaapvaal-Zimbabwe craton. *Science*, Vol. 297, No. 5587, pp. 1683–1686, http://dx.doi.org/10.1126/science.1072384

Shirey S.B., Richardson S.H., Harris J.W. (2004) Integrated models of diamond formation and craton evolution. *Lithos*, Vol. 77, No. 1-4, pp. 923–944, http://dx.doi.org/10.1016/j.lithos.2004.04.018

Shirey S.B., Cartigny P., Frost D.J., Keshav S., Nestola F., Nimis P., Pearson D.G., Sobolev N.V., Walter M.J. (2013) Diamonds and the geology of mantle carbon. *Reviews in Mineralogy and Geochemistry*, Vol. 75, No. 1, pp. 355–421, http://dx.doi.org/10.2138/rmg.2013.75.12

Smit K.V., Shirey S.B., Wang W. (2016) Type Ib diamond formation and preservation in the West African lithospheric mantle: Re-Os age constraints from sulphide inclusions in Zimmi diamonds. *Precambrian Research*, Vol. 286, pp. 152–166, http://dx.doi.org/10.1016/j.precamres.2016.09.022

Smith E.M., Shirey S.B., Nestola F., Bullock E.S., Wang J., Richardson S.H., Wang W. (2016) Large gem diamonds from metallic liquid in Earth's deep mantle. *Science*, Vol. 354, No. 6318, pp. 1403–1405, http://dx.doi.org/10.1126/science.aal1303

Smith E.M., Shirey S.B., Wang W. (2017) The very deep origin of the world's biggest diamonds. *G&G*, Vol. 53, No. 4, pp. 388–403, http://dx.doi.org/10.5741/GEMS.53.4.388

Smith E.M., Shirey S.B., Richardson S.H., Nestola F., Bullock E.S., Wang J., Wang W. (2018) Blue boron-bearing diamonds from Earth's lower mantle. *Nature*, Vol. 560, No. 7716, pp. 84–87, http://dx.doi.org/10.1038/s41586-018-0334-5

Stachel T., Harris J.W., Hunt L., Muehlenbachs K., Kobussen A.F., EIMF (2018) Argyle diamonds: How subduction along the Kimberley craton edge generated the world's biggest diamond de-

posit. In A.T. Davy et al., Eds., *Special Publications of the Society of Economic Geologists*.
Viljoen K.S. (2002) An infrared investigation of inclusion-bearing diamonds from the Venetia kimberlite, Northern Province, South Africa: Implications for diamonds from craton-margin settings. *Contributions to Mineralogy and Petrology, Vol. 144*, No. 1, pp. 98–108, http://dx.doi.org/10.1007/s00410-002-0385-2
Walter M.J., Kohn S.C., Araujo D., Bulanova G.P., Smith C.B., Gaillou E., Wang J., Steele A., Shirey S.B. (2011) Deep mantle cycling of oceanic crust: Evidence from diamonds and their mineral inclusions. *Science*, Vol. 334, No. 6052, pp. 54–57, http://dx.doi.org/10.1126/science.1209300
Ward K.M., Zandt G., Beck S.L., Wagner L.S., Tavera H. (2016) Lithospheric structure beneath the northern Central Andean Plateau from the joint inversion of ambient noise and earthquake-generated surface waves. *Journal of Geophysical Research: Solid Earth*, Vol. 121, No. 11, pp. 8217–8238, http://dx.doi.org/10.1002/2016JB013237
Weiss Y., McNeill J., Pearson D.G., Nowell G.M., Ottley C.J. (2015) Highly saline fluids from a subducting slab as the source for fluid-rich diamonds. *Nature*, Vol. 524, No. 7565, p. 339, http://dx.doi.org/10.1038/nature14857
Westerlund K., Shirey S., Richardson S., Carlson R., Gurney J., Harris J. (2006) A subduction wedge origin for Paleoarchean peridotitic diamonds and harzburgites from the Panda kimberlite, Slave craton: evidence from Re-Os isotope systematics. *Contributions to Mineralogy and Petrology*, Vol. 152, No. 3, pp. 275–294, http://dx.doi.org/10.1007/s00410-006-0101-8

Gem News International

Contributing Editors
Emmanuel Fritsch, *University of Nantes, CNRS, Team 6502, Institut des Matériaux Jean Rouxel (IMN), Nantes, France* (fritsch@cnrs-imn.fr)
Gagan Choudhary, *Gem Testing Laboratory, Jaipur, India* (gagan@gjepcindia.com)
Christopher M. Breeding, *GIA, Carlsbad* (christopher.breeding@gia.edu)

COLORED STONES AND ORGANIC MATERIALS

New emerald locality in Southern California. Located about 60 miles east of San Diego, a new emerald deposit has been discovered in the Julian Mining District (figure 1). This area is known for pegmatite mines and hydrothermal mineral deposits; however, none of those are known to have produced emeralds to date. The emeralds (example shown in figure 2) were all collected by author RE and son Bruce Edley near the surface and are embedded in a biotite schist host rock. Most of the recovered single crystals have a translucent dark green color and inclusions, and they are typically smaller than 2 cm. A few light-colored green beryl crystals have been recovered from a nearby pegmatite. Their formation was likely correlated with metamorphic and hydrothermal processes associated with regional tectonism.

Figure 1. A map of California with an inset showing the San Diego area and marking the emerald locality (star).

Figure 2. An example of an emerald cluster found in a new deposit in Julian, California. Specimen size is 20 × 10 × 9 mm. Photo by Myke Clarkson.

Samples were analyzed at the Natural History Museum of Los Angeles County and sent to GIA for species confirmation using laser ablation–inductively coupled plasma–mass spectroscopy (LA-ICP-MS). We performed Raman and X-ray fluorescence (XRF) hyperspectral mapping and powder X-ray diffraction (not shown) to determine mineralogy

Editors' note: Interested contributors should send information and illustrations to Stuart Overlin at soverlin@gia.edu or GIA, The Robert Mouawad Campus, 5345 Armada Drive, Carlsbad, CA 92008.

Gems & Gemology, Vol. 56, No. 4 pp. 542–554.

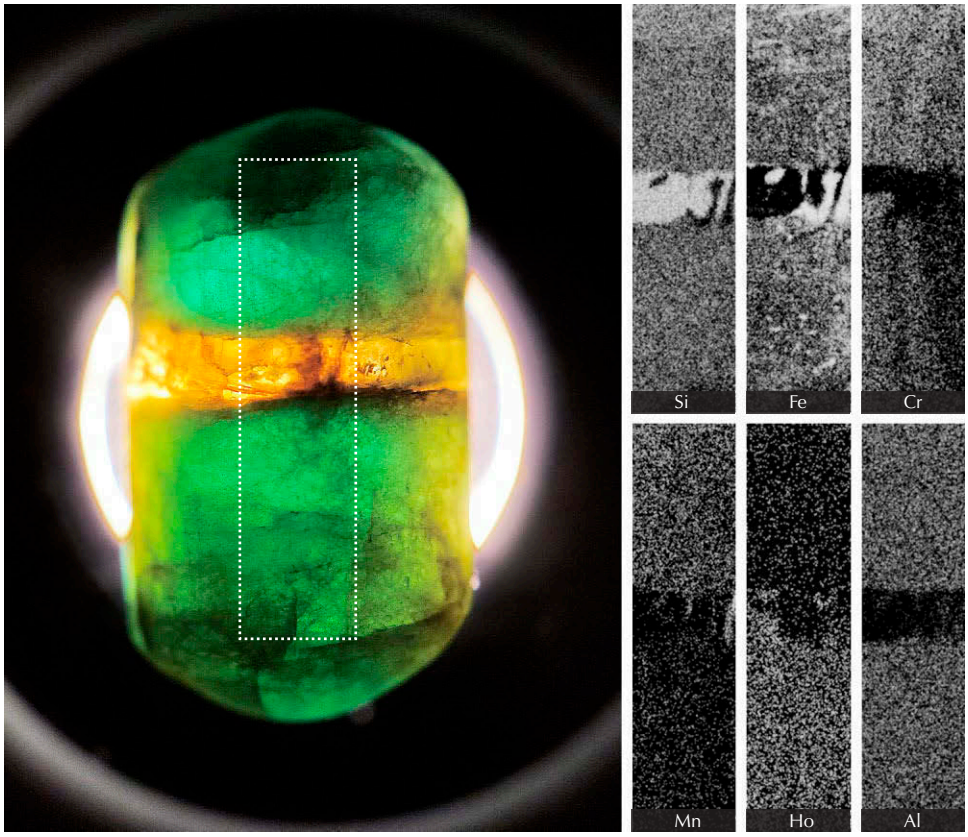

Figure 3. Left: A 3.16 ct polished pill-shaped emerald, seen in transmitted light, was one of the best examples of emerald with citrine from this locality. Photo by Aaron Celestian. Right: Element maps of the outlined area on the specimen. Brighter areas indicate higher concentrations.

and elemental composition. Raman analysis on a polished pill-shaped gem (figure 3, left) identified beryl and quartz to confirm our observation of the rare combination of emerald and citrine. Raman further identified dolomite and hematite inclusions. XRF element maps (figure 3, right) show silicon (Si), chromium (Cr), magnesium (Mg), iron (Fe), aluminum (Al), and holmium (Ho) content. Of the approximately 425 carats of emeralds that have been recovered, about 5–10% contain macro-citrine inclusions, representing a unique aspect of this deposit.

The distribution of trace elements in the pill-shaped emerald indicates a complex series of events. The emerald is cross-cut by a layer of citrine. Half of the gem is enriched in trace holmium (below the citrine), where holmium is inversely correlated with manganese. Chromium-rich areas run perpendicular to the citrine, but align on either side of the citrine, suggesting that the emerald formed as a single crystal. The patterns of holmium and manganese hint toward secondary geochemical processes that may be related to later citrine emplacement, though the origin of these processes is unknown. The unusual mineral associations and elemental distribution demonstrate the geologic complexity of the deposit, and further work is needed to unravel its full history.

Aaron J. Celestian (acelestian@nhm.org)
Natural History Museum of Los Angeles County
Richard Edley
Banning, California

Update on inclusions in emeralds from Davdar, China. We recently had the opportunity to examine emeralds containing unknown solid inclusions and numerous multiphase inclusions reportedly from Davdar, China. Three green transparent rough samples were acquired from the former mine owner Guimin Wong. They weighed 0.55 0.45, and 0.50 ct, respectively, with a diameter from 4.0 to 5.0 mm, a refractive index of 1.578 ± 0.002–1.584 ± 0.001, and SG ranging from 2.64 to 2.76. They were inert to both long- and short-wave UV radiation. Inclusion features of Davdar emeralds have been reported previously in the literature.

Very few mineral species have been identified as inclusions in this emerald—these include feldspar (plagioclase) (S. Saeseaw et al., "Three-phase inclusions in emerald and their impact on origin determination," Summer 2014 *G&G*, pp. 114–132; S. Saeseaw et al., "Geographic origin determination of emerald," Winter 2019 *G&G*, pp. 614–646) and to a lesser extent tourmaline, mica, scheelite, and fluorite (D. Marshall, "Geological work," *InColor*, Spring 2009, p. 29). Black rounded crystals were observed in some of the Davdar emeralds we studied. Previous studies noted the presence of black minerals as well but did not identify them (S. Saeseaw et al., 2014, 2019). We revealed the black mineral to be magnetite via Raman microspectrometry (figure 4). This is potentially the first time magnetite has been identified in Davdar emeralds, though it has been identified in emeralds from other regions (referenced

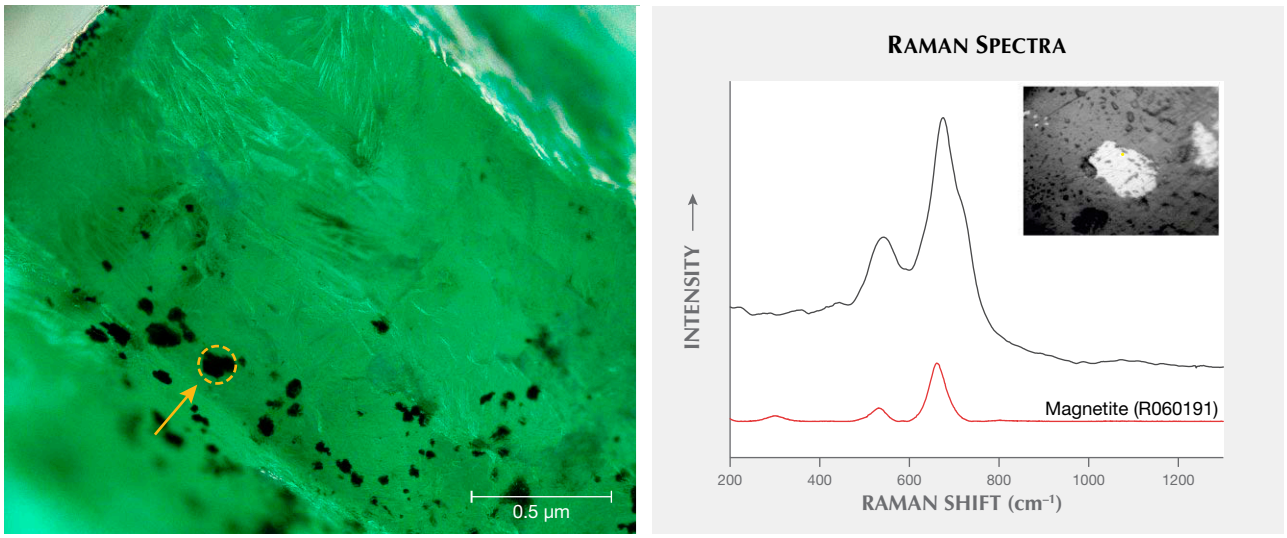

Figure 4. Left: A Davdar emerald hosted numerous black mineral inclusions identified by laser Raman microspectrometry as magnetite. Right: The Raman spectrum of the inclusions is shown along with the Raman reference spectrum for magnetite in the RRUFF database. Spectra are offset for clarity. Inset photomicrograph by Di Cui.

above). Magnetite as a black iron oxide inclusion is commonly seen in emeralds from Zambian and Brazilian localities and other schist-hosted origins (again, see Saeseaw et al., 2019).

Multiphase inclusions occur commonly in Davdar emeralds with solid phases (mainly halides such as halite assumed by D. Marshall et al., "Conditions for emerald formation at Davdar, China: Fluid inclusion, trace element and stable isotope studies," *Mineralogical Magazine*, Vol. 76, No. 1, 2012, pp. 213–226). Since previous studies reported that some birefringent phases did not dissolve during heating (again, see Marshall et al., 2012), we hoped to learn the solid phase identity in fluid inclusions. Comprehensive microscopic and Raman spectroscopic analyses indicated the presence of dolomite and likely calcite daughter inclusions (figures 5 and 6). As the solubility of a carbonate such as calcite seems to show an inverse solubility with respect to temperature (see B. Coto et al., "Effects in the

Figure 5. Left: Solid-rich fluid inclusions in Davdar emerald. One of the solid phases was determined to be dolomite. Right: The corresponding spectrum (red) showed peaks from both the host beryl (black) and the reference spectrum for dolomite in the RRUFF database (blue). Photomicrograph by Di Cui.

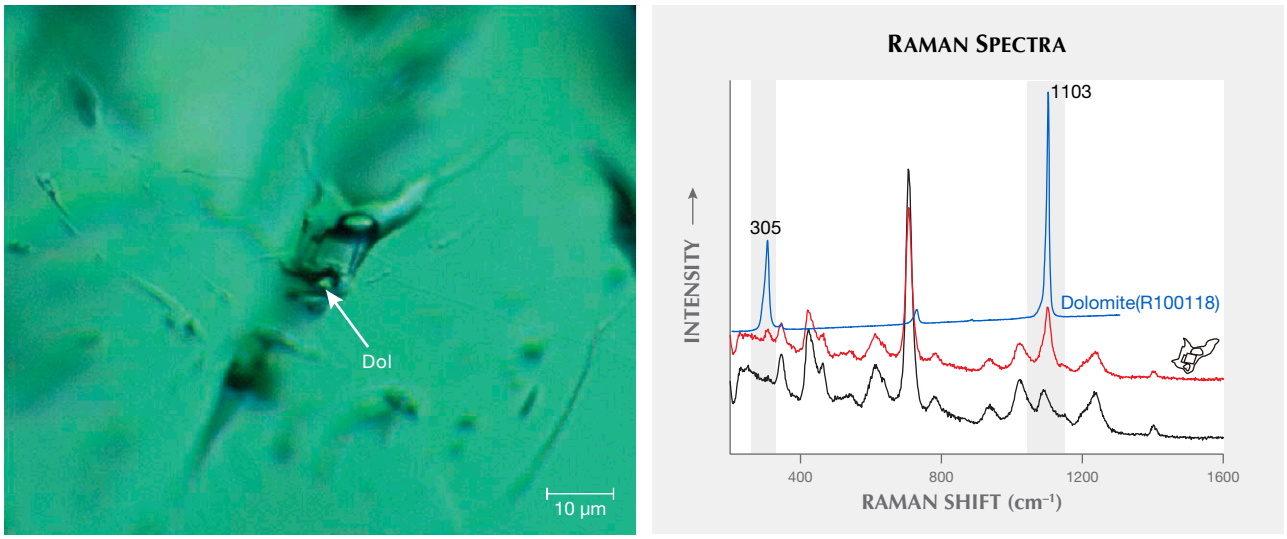

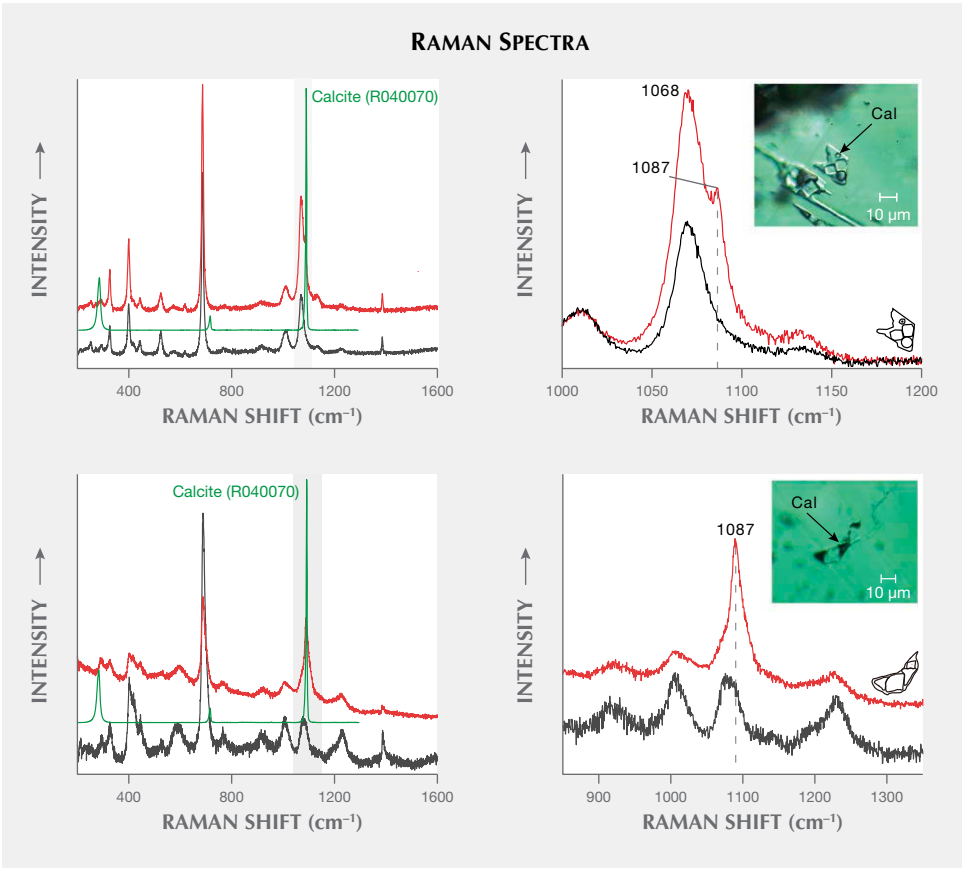

Figure 6. Two daughter crystals in separate inclusions were identified as likely calcite based on comparison with Raman reference spectra from the RRUFF database. The top and bottom left images show the spectra of the two daughter inclusions (red), the host beryl (black), and the RRUFF calcite reference spectrum (green). The dominant calcite peak at 1087 cm^{-1} matches with weak peaks in both daughter crystals. The top and bottom right images show the weak 1087 cm^{-1} peak corresponding to calcite under magnification. Photomicrographs by Di Cui.

solubility of $CaCO_3$: Experimental study and model description," *Fluid Phase Equilibria*, Vol. 324, 2012, pp. 1–7), the first identified dolomite daughter crystals could be attributable to the phases that were insoluble with increasing temperature and added more constraints to fluid inclusions in Davdar emeralds.

As far as we are aware, the carbonate phase could simply refer to the local geologic background and the host rock lithology, which mainly consisted of sandstone and dolomitic limestone. Study of the inclusions showed interesting results due to the genetic environment of the Davdar emerald mine. In addition to the daughter chloride such as halite, the identified dolomite mineral defined the complex multiphase assemblage for the Davdar fluid inclusion population.

Di Cui, Zongting Liao, Lijian Qi, and Zhengyu Zhou
School of Ocean and Earth Science
Laboratory of Gem and Technological Materials
Tongji University

Dendritic inclusions in nephrite from Dahua, China. Since the 2010s, with the discovery of nephrite ore deposits in Luodian County, Guizhou Province, a significant amount of nephrite has been mined in the town of Yantan in Dahua Yao Autonomous County, located in the northwest of the Guangxi Zhuang Autonomous Region (Z. Yin et al., "Nephrite jade from Guangxi Province, China," Fall 2014 *G&G*, pp. 228–235). Previously we reported on the nature of the chlorite inclusions found in this nephrite, and here we identify the chlorite as penninite.

The discovery of Dahua nephrite has eased the increasingly tight nephrite supply situation in China. Owing to its large reserves, the deposit has vast potential for future development. This material is of high quality and comes in a diverse array of colors including white, gray, light green, dark green, light yellow, and black. All bodycolors have been found to contain distinctive dendritic inclusions (figure 7). Dahua nephrite is popular with consumers, thus bringing huge economic benefit to the locality.

Dahua nephrite is mainly distributed around the river near the Yantan hydropower station. The ore body occurs in the limestone formed at the Qixian stage of the Paleozoic Permian system. The magmatic rocks in the area are basic intrusive rocks, divided into diabase and gabbro. The ore bed containing the nephrite is composed of dark gray stratified limestone of low to medium thickness, interspersed with fine calcite veins (B. Wang et al., "Gemmological and mineralogical characteristics of nephrite from Guangxi," *Journal of Gems and Gemmology*, Vol. 14, No. 3, 2012, pp. 6–11). The samples were tested by standard gemological methods, polarizing microscopy, environmental scanning electron microscopy (ESEM), X-ray diffraction (XRD), Raman spectroscopy, laser ablation–inductively

Figure 7. The nephrite samples with dendritic inclusions from Dahua County. Photos by Zuowei Yin.

coupled plasma–mass spectrometry (LA-ICP-MS), and energy-dispersive spectroscopy (EDS). We conducted the tests at the National Key Lab of the China University of Geosciences in Wuhan.

The refractive index of Dahua nephrites ranged from 1.60 to 1.63. The average hydrostatic specific gravity was 2.99, and the Mohs hardness was about 6.5. These properties were very similar to those of the samples previously tested, which had a spot RI of 1.61–1.62 and a hydrostatic SG of 2.88–2.90 (Yin et al., 2014).

The Raman spectra (peaks at 225, 370, 676, 1029, and 3677 cm^{-1}), infrared spectra, and X-ray powder diffraction (characteristic lines at 3.1189, 8.3968, 3.2702, and 2.7007 Å) were consistent with tremolite, showing that the main composition mineral of Dahua nephrite is tremolite with good crystallinity. Chemical composition analysis showed that the $Mg^{2+}/(Mg^{2+} + Fe^{2+})$ value of nephrite samples from Dahua was 0.973, identifying the main mineral as tremolite.

The REE distribution pattern of Dahua nephrite had an average value of Σ REE and LREE/HREE of 5.32 and 2.60, respectively, indicating that Dahua nephrite is slightly enriched in light rare earth elements. The δCe of the samples ranged from 0.21 to 0.91, with an average value of 0.47, in-

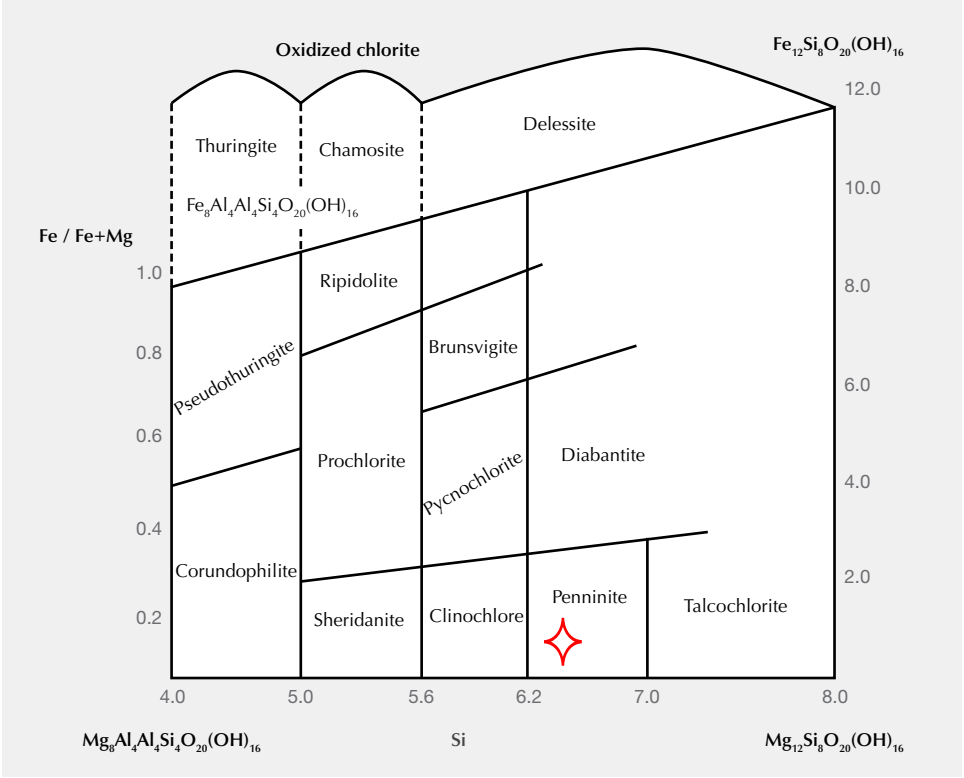

Figure 8. EDS compositional analysis showed that the chlorite inclusion in Dahua nephrite was penninite. From the chlorite classification system in Hu et al. (2019).

dicating a negative Ce anomaly. This suggests that Dahua nephrite was formed in a sedimentary metamorphic environment, with high oxygen fugacity and a single source of nephrite ore-forming fluid. The average δEu value of the samples was 0.71 in the range of 0.12–2.01, indicating a negative Eu anomaly. The negative Eu anomaly in this area may be due to the separation and crystallization during the ore-forming process of nephrite.

Most nephrite in Dahua has dendritic inclusions whose colors are mainly brownish yellow, brownish green, and black distributed in the form of branches, clumps, and the like. These "variegated" inclusions were actually determined to be penninite (belongs to the chlorite group) using modern techniques including routine gemstone testing, X-ray powder diffraction, scanning electron microscope, and EDS. According to the composition determined by EDS testing, we calculated the atomicity of Si with O_{20} as a reference. The results were as follows: The number of Si atoms was 6.4, and Fe^{2+}/Fe + Mg was 0.16, indicating that the chlorite inclusion was a type of penninite (red cross in figure 8, from the chlorite classification scheme in Y. Hu et al., "Related studies on characteristic altered mineral chlorite," *West-China Exploration Engineering*, No. 11, 2019, pp. 132–134).

The variegated chlorite inclusions in Dahua nephrite are very useful identifying characteristics. With the exception of Luodian nephrite, which contains similar inclusions, such distinctive dendritic inclusions have yet to be discovered in white nephrite deposits; therefore, it is potentially a significant tracer for origin. The Dahua nephrite contains penninite, a type of chlorite (i.e., hydrothermally metamorphosed tremolite) (Yin et al., 2014). As an inclusion unique to Dahua nephrite, penninite serves as an important reference for origin tracing.

Zuowei Yin (yinzuowei1025@163.com), Wenwei Wang, and Quanli Chen
Gemological Institute, China University of Geosciences Wuhan, China

SYNTHETICS AND SIMULANTS

Spectral analysis of resin imitation ivory. The application of spectroscopic techniques in solving gemological challenges is becoming more routine since more data is needed than standard gemological testing can provide. For example, resin is composed of a variety of complicated chemical components and, while basic testing can identify whether the material is resin, further detailed examination must be undertaken to obtain the specific chemical composition.

A client submitted three "ivory" items for identification, a bead bracelet and two seal stamps (figure 9). This case is similar to the "resin imitation ivory with a pseudo 'engine-turned' structure" reported previously (Fall 2019 Lab Notes, pp. 419–421). Standard gemological testing revealed an RI of 1.54 (spot) and an SG of 1.23, with parallel linear striations, all very similar to the properties obtained from the samples in the case referenced above. Natural ivory normally indicates an RI of 1.54 (spot) and an SG of 1.85, with Schreger lines. By comparing with this case, further examinations were taken by the following procedures.

FTIR and Raman spectroscopy were used to analyze the differences between resin imitating ivory and natural ivory reference samples with a known provenance. These results were compared with those of the client's submissions.

As shown in figure 10 (top), mid-FTIR reflectance spectra from the natural ivory of known provenance revealed peaks at 1044, 1447, and 1559 cm^{-1} (related to biogenic hydroxyapatites); 1658, 2850, and 2919 cm^{-1} (consistent with collagen); and 3310 cm^{-1} (from CO_3^{2-}) (Z. Yin et al., "A comparison of modern and fossil ivories using multiple techniques," Spring 2013 *G&G*, pp. 16–27). The client's resin imitations revealed peaks at 702, 1126, 1284, 1380, 1462, and 1730 cm^{-1}, characteristic of ester group alkyd resins (figure 10, bottom) (S.M. Cakić et al., "Investigation of the curing kinetics of alkyd-melamine-epoxy resin system," *Progress in Organic Coatings*, Vol. 73, No. 4, 2012, pp. 415–424), and 2932 cm^{-1}, consistent with CH stretch-

Figure 9. The "ivory" items submitted for identification: a bracelet (left) consisting of 16 beads, 13.4 mm diameter each, and two seal stamps (right) measuring 20 × 80 mm each. Photos by Lai Tai-An Gem Lab.

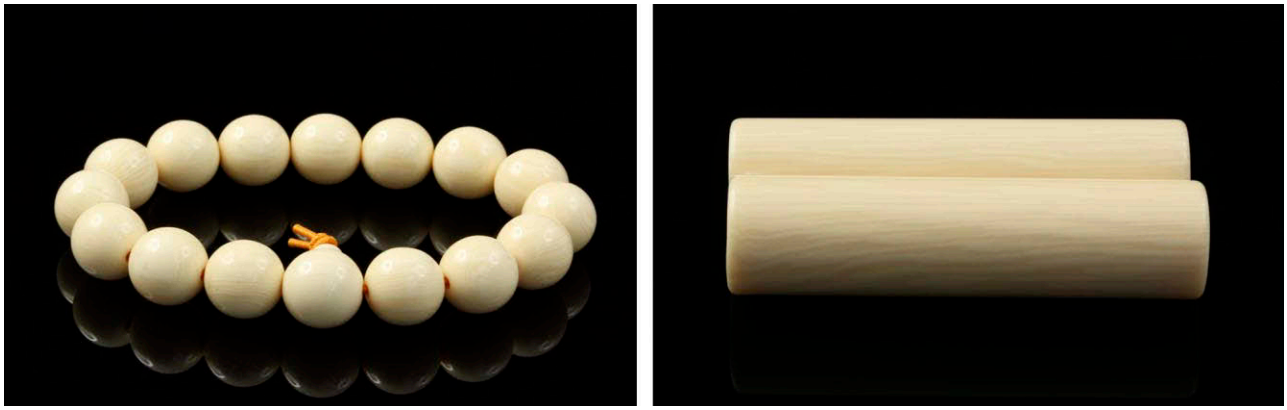

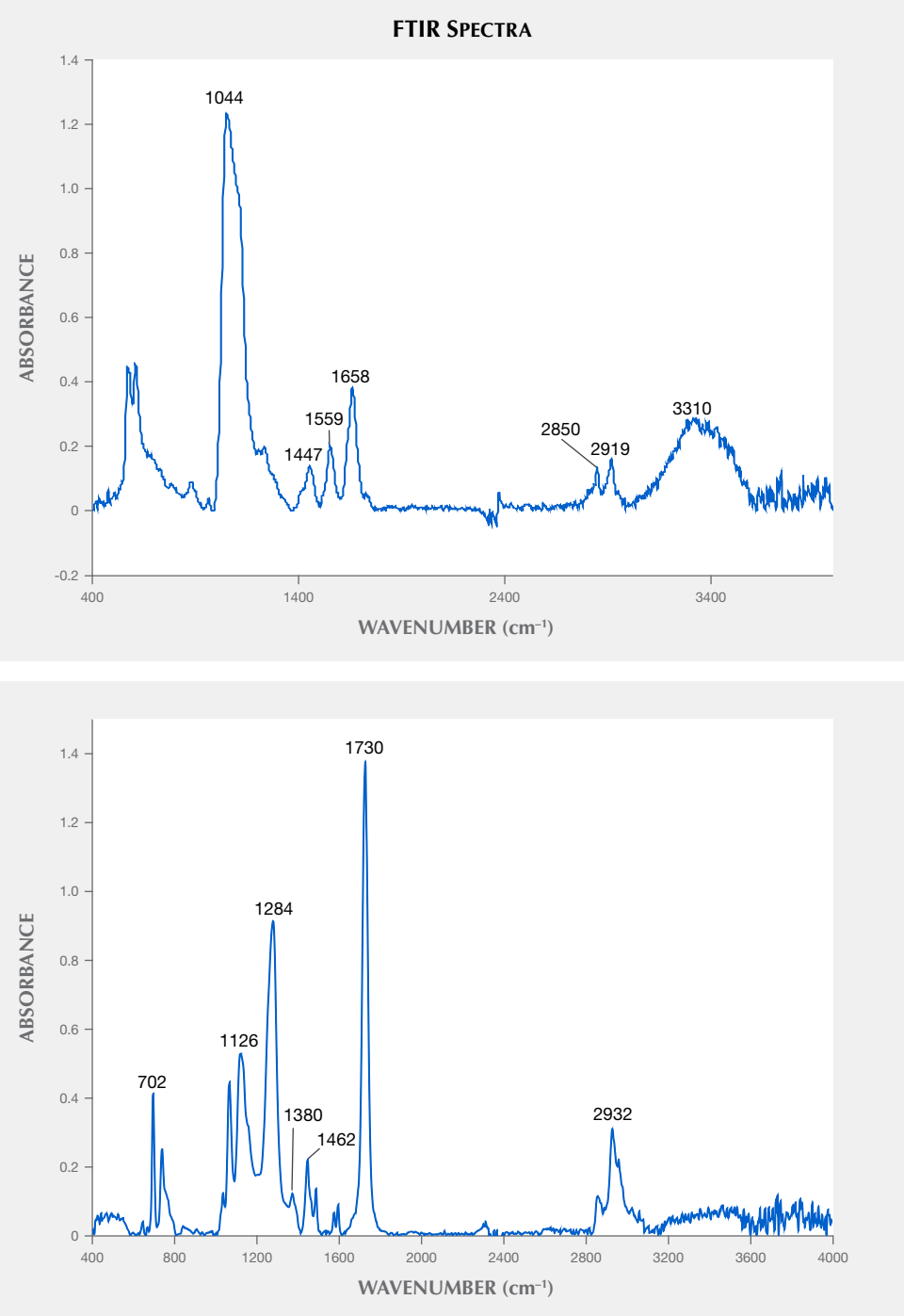

Figure 10. FTIR spectra of natural ivory (top) and this object "resin imitation ivory" (bottom) revealed different peaks.

ing. These results were significantly different from those obtained from known samples of ivory, as detailed above.

Raman analysis of the natural ivory revealed peaks at 428, 586, 852, 961, 1244, and 1664 cm^{-1} (figure 11, top), whereas the submitted resin samples displayed peaks at 621, 650, 1001, 1038, 1162, 1186, 1449, 1599, and 1724 cm^{-1} (figure 11, bottom). The spectra from each were sufficiently different to allow a quick and accurate separation.

These spectral comparisons provide readers with a reference when separating ivory from some resins. However, it is still important to apply standard gemological testing techniques during the initial examination while staying alert to the continual developments likely taking place with resin imitations. Spectral analysis plays an essential role in the differentiation process, especially in cases where more care may be needed.

Larry Tai-An Lai (service@laitaian.com.tw)
Lai Tai-An Gem Laboratory, Taipei

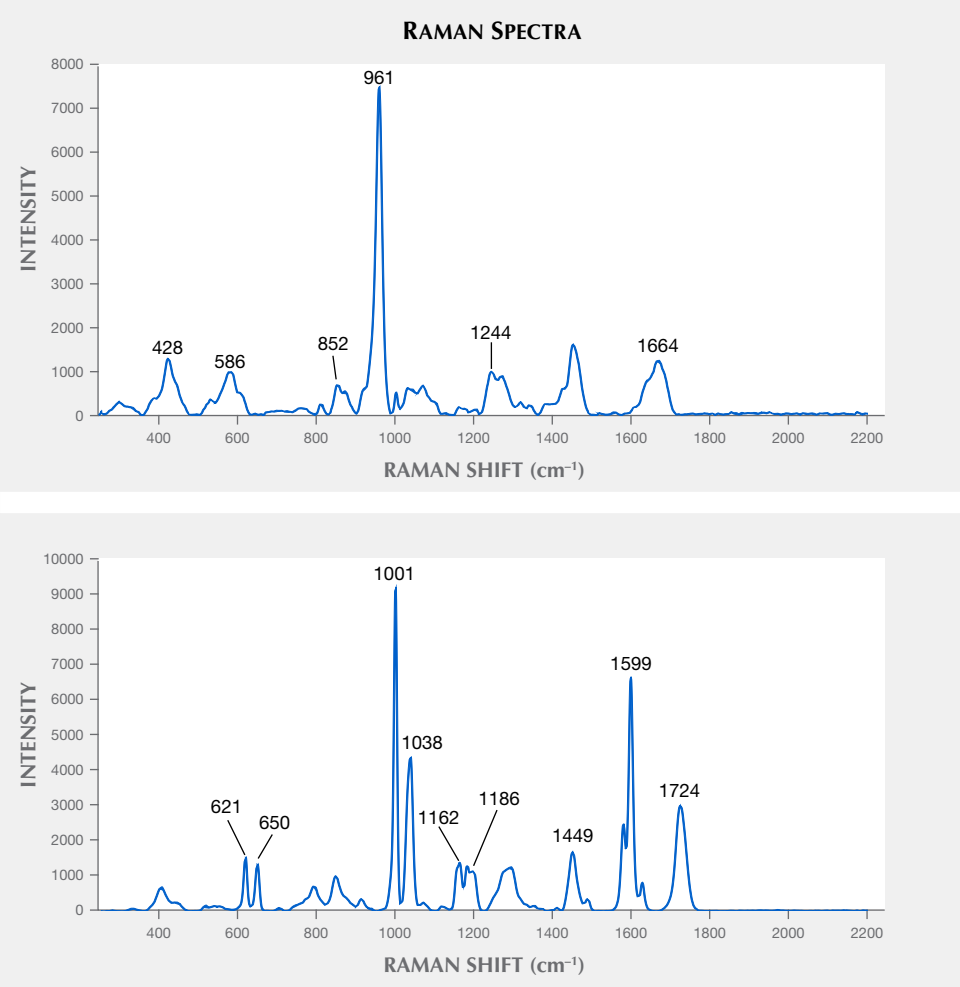

Figure 11. Raman spectra comparing natural ivory (top) and "resin imitation ivory" (bottom) also revealed significant differences.

A new phantom quartz imitation: Laser-engraved rock crystal. Phantom quartz generally refers to a rock crystal with inclusions of prismatic or pyramidal growth zonation, which represents early crystal faces covered by minerals, such as clinochlore, clay minerals, limonite, or fuchsite. Recently, a new type of phantom quartz imitation has appeared in the market, most of which is sold in the form of beads, pendants, or crystal spheres. A package of these imitation phantom quartz products was sent to the Taiwan Union Lab of Gem Research (TULAB) for identification services (figure 12).

Figure 12. The "phantom quartz" pendant was later confirmed to be natural quartz with three-dimensional laser engraving. Photo by Shu-Hong Lin.

These samples submitted as phantom quartz had a powdery white growth zonation in the form of a hexagonal pyramid. The host crystal was confirmed to be natural quartz by infrared absorption spectroscopy. The samples had an abnormal appearance for phantom quartz, of which the internal growth zonation was composed of regular and oriented small cracks (figure 13). Similar inclusions are often found in crafts made of glass or synthetic quartz engraved with a laser. According to the client, one of these

Figure 13. The internal growth zonation was composed of a regular network of small crack clusters around a central black point, presumably due to laser impact. Photomicrograph by Yu-Ho Li; field of view 2.14 mm.

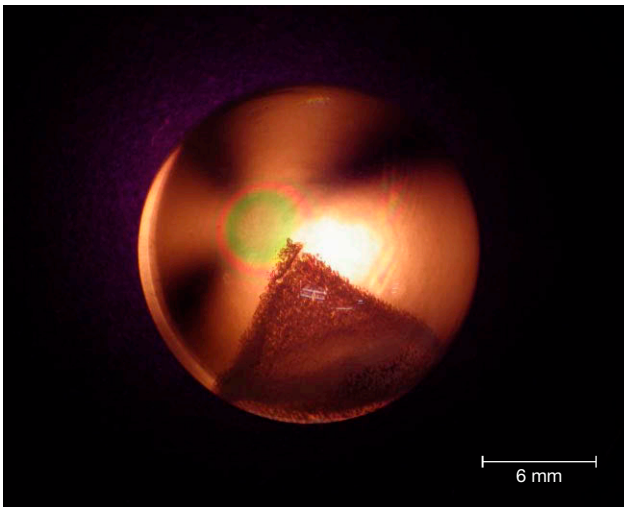

Figure 15. Crossed polarizers revealed that the bull's eye, indicating the optic axis, was nearly perpendicular to the axis of the engraved "phantom." Photo by Shu-Hong Lin.

samples had fractures along the ridgeline of the apparent pseudo-hexagonal pyramid (figure 14), which were possibly self- propagated due to the internal stress from the oriented small cracks.

In a true phantom, the axial direction of the host crystal is identical to that of the phantom crystal inside; however, the interference images through a polariscope revealed that the c-axis direction of these phantom quartz products was mostly inconsistent with what appeared to be their internal growth zonation (figure 15). In consideration of the morphological characteristics of inclusions as well as the interference images, these phantoms are imitations made of natural "rock crystal" with artificial growth zonation produced by laser engraving, irrespective of the crystallographic orientation of the host crystal.

Although internal laser engraving can imitate the appearance of a phantom quartz inclusion, such products can be easily identified through a microscope and a polariscope. More controversially, the internal stress generated by the regular and oriented cracks seems to reduce the toughness of the host crystal; therefore, consumers should be aware of the risk of such imitations.

Shu-Hong Lin
Institute of Earth Sciences, National Taiwan Ocean University
Taiwan Union Lab of Gem Research, Taipei
Yu-Ho Li
Institute of Earth Sciences, National Taiwan Ocean University
Huei-Fen Chen
Institute of Earth Sciences and Center of Excellence for Oceans
National Taiwan Ocean University

Figure 14. Left to right: A schematic diagram, a bottom view, and a top view of an imitation phantom crystal. The six fractures (red dashed lines) along the ridgeline of the pseudo-hexagonal pyramid in this imitation phantom quartz sphere were reportedly formed without any external force or heat treatment. The diameter of this sphere is 17.68 mm. Photos by Shu-Hong Lin.

TREATMENTS

Rhodium-plated iron meteorites. The annual Tucson Gem and Mineral Show has been a reliable source for the niche and the unusual, as seen with the rhodium-plated iron meteorites (figure 16) acquired by author BL at the 22nd Street Show in February 2020. The 28.53 ct mounted pendant and 36.69 ct loose slab were initially suspected to be imitations due to the abnormally high metallic luster and bright white color compared to typical polished and etched iron meteorites. However, chemical analysis of elements in the mounted sample using laser ablation–inductively coupled plasma–mass spectrometry (LA-ICP-MS) identified the specimens as authentic etched iron meteorites with layers of plated metals including nickel, copper, and rhodium.

Meteorites can be classified into three broad categories: stone, iron, and stony iron. The latter two groups are utilized within the gem and jewelry industry. The iron group consists of metallic meteorites composed primarily of iron with varying nickel content, a mineral intergrowth of low-nickel kamacite and high-nickel taenite. The iron group can be further categorized as hexahedrites (containing less than 6% nickel), octahedrites (6–13% nickel), and ataxites (more than 13% nickel) (O.R. Norton, *The Cambridge Encyclopedia of Meteorites*, 2002, pp. 184–198). When cut, polished, and etched with nital (a mixture of nitric acid and ethanol), the acid dissolves the isometric kamacite and taenite crystals at different rates, revealing a unique pattern dependent on the crystal's grain size. Octahedrites reveal a coarse pattern with a range of crystal widths known as a Widmanstätten structure (again, see figure 16). These lines and structures act like a fingerprint, as no two etched meteorites reveal the exact same pattern. Etched iron meteorites can also be easily classified by the size of their kamacite bands. Octahedrites show a width of banding ranging from 50 mm to < 0.2 mm. The pendant and slab showed an average band width of 0.50 mm and 2.68 mm, respectively, both well within the octahedrite threshold.

The pendant sample was analyzed with LA-ICP-MS spectrometry, and results were plotted and compared to a confirmed natural, non-plated octahedrite meteorite (figure 17). The x-axis shows time lapsed as the laser began drilling from the surface (starting at 40 seconds), therefore also representing depth. The y-axis shows the weight percent of the elements present. These include iron (Fe), nickel (Ni), copper (Cu), and rhodium (Rh) and represent the multiple layers of plating. The non-plated meteorite showed a steady amount of Fe (approximately 93 wt.%) and Ni (approximately 6 wt.%) throughout the total elapsed time from the beginning of analysis. The plated meteorite showed an initial thin peak of rhodium, quickly followed by a slightly wider peak of nickel. As these peaks began to flatten, a broad band of copper became visible. Near the 96 second mark, the graph of the plated meteorite began to resemble the non-plated meteorite, with approximately 92 wt.% Fe and 8 wt.% Ni. This analysis proved the material to be a genuine octahedrite meteorite with platings of Cu, Ni, and Rh. In order to achieve a final surface plating of rhodium to a metal, various under-platings are usually required. Through this technique of measuring the chemistry of the plated layers by LA-ICP-MS, gemologists were able to determine the identity of the subsurface material, as well as the composition of the various platings through a minimally destructive process. The pits or craters created by the laser are generally small (50 µm in diameter) and therefore impossible to visibly detect without magnification (L.A. Groat et al., "A review

Figure 16. The meteorite pendant (left) measured 27.02 × 12.75 × 2.59 mm and weighed 28.53 ct. The meteorite slab (right) measured 27.67 × 28.06 × 1.71 mm and weighed 36.69 ct. The intricate banding seen in these plated meteorites would both be categorized as Widmanstätten patterns, features of octahedrite iron meteorites. Photo by Angelica Sanchez.

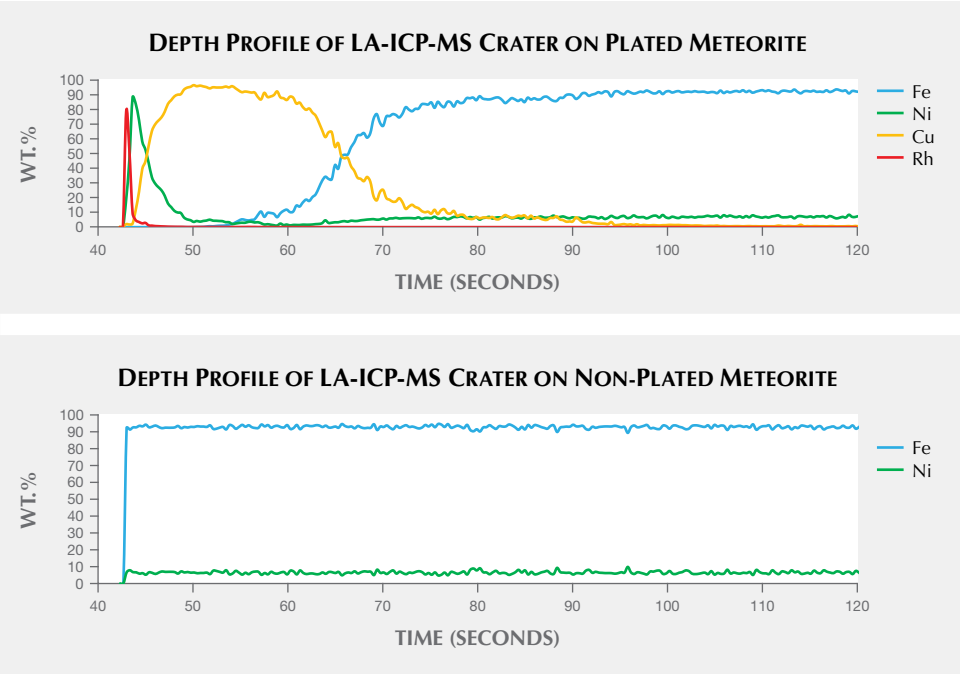

Figure 17. The profile of the plated meteorite (top) shows initial peaks of rhodium and nickel followed by a broad band of copper. Near the 96-second mark, the graph begins to resemble the profile of the non-plated meteorite (bottom) with >90 wt.% Fe and <10 wt.% Ni. This proves the material to be a genuine octahedrite meteorite with platings of Cu, Ni, and Rh.

of analytical methods used in geographic origin determination of gemstones," Winter 2019 *G&G*, pp. 512–535). Utilizing LA-ICP-MS to analyze metallic platings and subsurface materials is a method not previously explored by the authors. This study could offer insight into using LA-ICP-MS technology in new ways in the gem and jewelry industry.

Iron meteorites are prone to rusting due to their high iron content, as even slight humidity within air causes rapid corrosion. To slow this process, the stones are commonly kept in humidity-controlled environments, moisture absorbent silica gel, or coated with oil or hard clear lacquer. Rhodium plating offers an attractive luster and color to the surface; however, its essential function in this instance is to prevent moisture from altering the iron. Unfortunately, rust spots can be seen on the edges of both samples where the plating failed to adhere. Rhodium is a member of the platinum metal group, which is characterized by high stability, good resistance to corrosion, and a high melting point. While it is too brittle to be used for solid jewelry, rhodium has become a popular plating material, as it has a brighter color than silver or platinum.

Meteorites are popular collectibles with wide usage as jewelry. Etched iron meteorites can be found as watch dials and bezels, beads, hololith rings, and pendants. As this specialized material becomes more common, consumers should be aware of potential imitations or treatments such as these rhodium-plated examples.

Britni LeCroy, Ziyin Sun, and Dylan Hand
GIA, Carlsbad

Oiled tanzanite. Over the past five years, gemologists at Bangkok's Lotus Gemology have seen increasing numbers of what we might call "non-traditionally" oiled gems. This is particularly true of, but not limited to, Burmese gems such as ruby, sapphire, and spinel. But it is important to note that any gem with surface-reaching fissures can be oiled, often with dramatic improvements in apparent clarity. Cuprian and rubellite tourmalines are also frequently enhanced in this way.

Figure 18. This large 115 ct tanzanite was found to contain oil (left). After removal of the oil (center and right), highly reflective fissures became obvious. This clearly demonstrates how oiling a gem can have a radical impact on its appearance. Photos by Chanon Yimkeativong.

Figure 19. GIA consultant Nicholas Sturman presented on freshwater pearls during the conference. Photo by Lin Chen.

Recently we received a faceted tanzanite weighing more than 100 carats for testing. As is our practice for non-emeralds exhibiting fissure-filling clarity enhancement, we photograph the gem and then allow the client to re-submit the stone after filler removal. Figure 18 clearly shows the dramatic effect that fissure filling with oil/resin can have on gems such as tanzanite, even where the refractive index of the filler does not closely match that of the gem.

Richard Hughes
Lotus Gemology, Bangkok

CONFERENCE REPORT

2020 World Pearl Congress. The World Pearl Congress was held November 13–15, 2020, in Shanxiahu Town, a division of the Chinese city of Zhuji. Known as "China's pearl capital," Shanxiahu Town is known for cultivating, processing, trading, and researching pearls, especially freshwater pearls. The town produces nearly 80% of China's pearls and is currently home to more than 2,500 pearl companies. This event was organized by CIBJO, the Gems and Jewelry Trade Association of China, the Zhejiang Provincial Committee of China Council for the Promotion of International Trade, and the Shaoxing Municipal People's Government.

The event consisted of a series of activities, presentations, and exhibitions focused on pearls. Despite the global pandemic, more than 400 attendees who live in China and represent a number of professions and industries attended this meeting in person, while several international and domestic speakers delivered a series of talks via prerecorded videos. Presentations included: "Freshwater Pearls from a Laboratory Perspective" (**Nicholas Sturman**, GIA consultant) (figure 19), "An Overview of the

Figure 20. The new World Freshwater Pearl Museum was recently opened in Zhuji, China. Photos by Lin Chen.

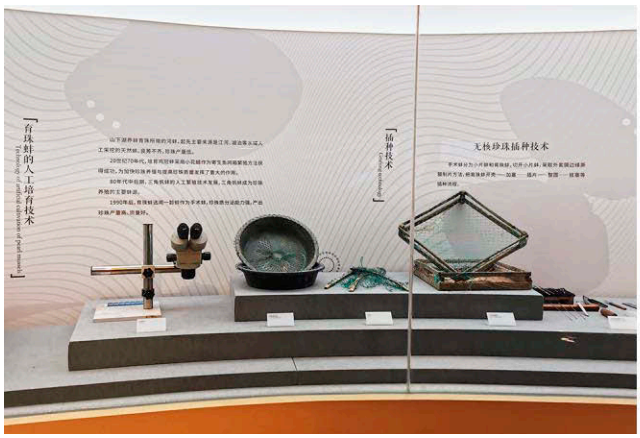

Global Pearl Industry" (**Kenneth Scarratt**, CIBJO Pearl Commission president), "Development of Quality and Detection of Pearls" (**Taijin Lu**, NGTC chief scientist), "The Importance of Design to the Pearl Industry" (**Paloma Sanchez**, independent designer), among many others. In addition, the World Freshwater Pearl Museum was also unveiled (figure 20), with exhibitions detailing the rich history of pearl culturing in China, pearl cultivating and processing techniques, and varieties of freshwater pearls and pearl jewelry.

According to several sources at the meeting, the global pandemic caused little disruption to the production of freshwater cultured pearls, as the harvest usually takes place at the end of the year and the government's fast control of the virus minimized the impact. However, the export of freshwater cultured pearls has been significantly affected, and dealers are trying to boost domestic sales with more emphasis on a strong online presence. Among different sales methods, livestreaming has become an ever more popular way to sell pearl jewelry in China (figure 21). From January to November 2020, online sales of pearls in Zhuji were valued at 11.85 billion yuan (US$1.8 billion), a year-over-year increase of 18.5%, according to Sina Finance.

Chunhui Zhou and Lin Chen
GIA, New York

ANNOUNCEMENT

American Gem Society upcoming events. The American Gem Society (AGS) will hold virtual and in-person educational events at the newly announced Confluence, slated for April 26. This event aims to provide industry professionals with content specifically designed to increase sales and refocus business strategy. Katherine Bodoh, CEO of AGS and AGS Laboratories, is pleased to offer a selection of programs that speak to "vital subjects our members need to reach new heights in their professional development." Members will also have access to AGS PRO, a learning portal filled with an array of relevant topics from leading experts in the field.

Conclave, which normally takes place each April, has been rescheduled for September 12–14, 2021. It will be held at the Sheraton Dallas Hotel in Dallas, Texas.

ERRATUM

The print version of the Spring 2020 article by Emily Dubinsky et al. ("A Quantitative Description of the Causes of Color in Corundum," pp. 2–28) contained several incorrectly colored gemstones and areal color density circles for various chromophores. To display the correct colors, we have included a reprint of the Spring 2020 article with this issue, accompanied by a wall chart.

Figure 21. Livestreaming has become one of the most popular ways for online selling of pearls in China, as shown in this Ruans store in Zhuji. Photo by Lin Chen.